VERA Virtual Environment for Reactor Applications

ORNL/SPR-2023/3094

MPACT Verification and Validation Manual Version 4.4

November 7, 2023

Aaron Graham[1], Mehdi Asgari[1], Thomas Downar[2], Brendan Kochunas[2], Yuxuan Liu[2], and Shane Stimpson[1]

[1]Oak Ridge National Laboratory
[2]University of Michigan

OAK RIDGE National Laboratory

U.S. DEPARTMENT OF ENERGY

ORNL is managed by UT-Battelle LLC for the US Department of Energy.

ORNL/SPR-2023/3094

MPACT VERIFICATION AND VALIDATION MANUAL VERSION 4.4

Aaron Graham[1], Mehdi Asgari[1], Thomas Downar[2], Brendan Kochunas[2],
Yuxuan Liu[2], and Shane Stimpson[1]

[1]Oak Ridge National Laboratory
[2]University of Michigan

Date Published: November 7, 2023

Prepared by
OAK RIDGE NATIONAL LABORATORY
Oak Ridge, TN 37831-6283
managed by
UT-Battelle, LLC
for the
US DEPARTMENT OF ENERGY
under contract DE-AC05-00OR22725

MPACT Verification and Validation Manual Version 4.4

Revision Log

Revision	Date	Affected Pages	Revision Description
0	06/24/2022	All	New template and updates for VERA 4.3 Release. Previous revisions are superseded by this new document number and format.

Document pages that are:

Export Controlled:	None
IP/Proprietary/NDA Controlled:	None
Sensitive Controlled:	None
Unlimited:	All

MPACT Verification and Validation Manual Version 4.4

Approvals:

Aaron Graham, Product Software Manager	**Date**
Bob Salko, Independent Reviewer	**Date**

CONTENTS

LIST OF FIGURES

LIST OF TABLES

ABBREVIATIONS

ARI	all rods in
ARO	all rods out
BWR	boiling water reactor
CZP	cold zero power
HFP	hot full power
HZP	hot zero power
NEM	nodal expansion method
PLR	part length rod
PWR	pressurized-water reactor
SENM	source expansion nodal method
TIP	transverse in-core probe
VERA	Virtual Environment for Reactor Applications

1. INTRODUCTION

As the VERA SQA plan requires, it is the responsibility of the University of Michigan (UM) and Oak Ridge National Laboratory (ORNL), as co-owners of MPACT, to ensure that verification and validation activities are performed and documented in a V&V manual with supporting publications and CASL technical reports which can be provided for reference and distribution within VERA. This document provides the current revision of the MPACT verification and validation (V&V) manual and describes the current state of MPACT V&V and updates the plans for future MPACT V&V activities. The following sections provide an overview of the V&V process used in MPACT, as well as a summary of the status of each component of V&V in the code.

2. CODE VERIFICATION AND SOLUTION VERIFICATION

The overarching objective of verification is to establish that a model implemented in the code accurately represents the developer's conceptual description and the solution of the model. The verification activities in MPACT have been designed to address this general objective and to encompass both the verification of the source code itself, as well as the verification of the solution. Source code verification activities in MPACT have been focused on identifying mistakes in the source code by establishing comprehensive software testing practices, whereas the solution verification activities within MPACT have been focused on evaluating the numerical error in the solution.

The following section addresses the code verification and summarizes the current status of the source code verification activities, followed by mesh convergence analysis [7]. More rigorous tests are performed using the method of exact solutions (MES) and the method of manufactured solutions (MMS).

2.1 SOURCE CODE TESTING

Unit testing and regression testing are the two principal components of source code testing in MPACT. Unit testing is a software testing method by which individual units of source code are tested to determine whether they are fit for use. In contrast, regression testing seeks to uncover new software bugs or regressions in existing functional and nonfunctional areas of the code after changes have been made to the source. The following subsections describe the unit and regression testing practices in MPACT.

2.1.1 Unit Testing

The overall goal of unit testing is to isolate each part of the program and demonstrate that the individual parts are correct. The testing in MPACT was designed to verify the smallest testable part of an application, and each test case was designed to be independent from the others. In MPACT, the practice has been for developers to create unit tests for all functions and methods while the code is being written. When the tests pass, that phase of the code development is considered complete. However, if a unit test fails, then a bug is considered to be either in the changed code or the tests themselves, and that phase of the code development process is continued. The unit tests accelerate the process of correcting the bug by allowing the location of the fault or failure to be easily traced [8].

During MPACT development, unit testing has served the important role of finding problems early in the development cycle. All unit testing in MPACT is run repeatedly as the larger code base is developed via an automated process. This has simplified the process of locating a fault or failure, because the unit tests have alerted the development team of the problem before the code is handed off to testers or users.

2.1.1.1 MPACT Unit Test Example

One of the principal unit tests implemented in the MPACT code is the solution of the mono-energetic flux for a purely absorbing 1D homogeneous medium with fixed boundary conditions. The test problem shown in Figure 2.1 is a square medium with 4×4 modules and 2×2 pins. Each pin itself has a mesh of 4×4, and the modules are 2×2 cm nodes, which makes problem domain 8×8 square. The north and south surfaces have a reflective boundary, whereas the west and east surfaces are a vacuum.

The boundary angular surface flux is set to a fixed value (which is 2 for this test) on the west side of the rays. The external source is set to zero, resulting in the analytical solution given in the following equation, which is loaded into a specific variable in the code from an external file.

$$\psi^{out} = \psi^{in} e^{-\Sigma_t s} \tag{2.1}$$

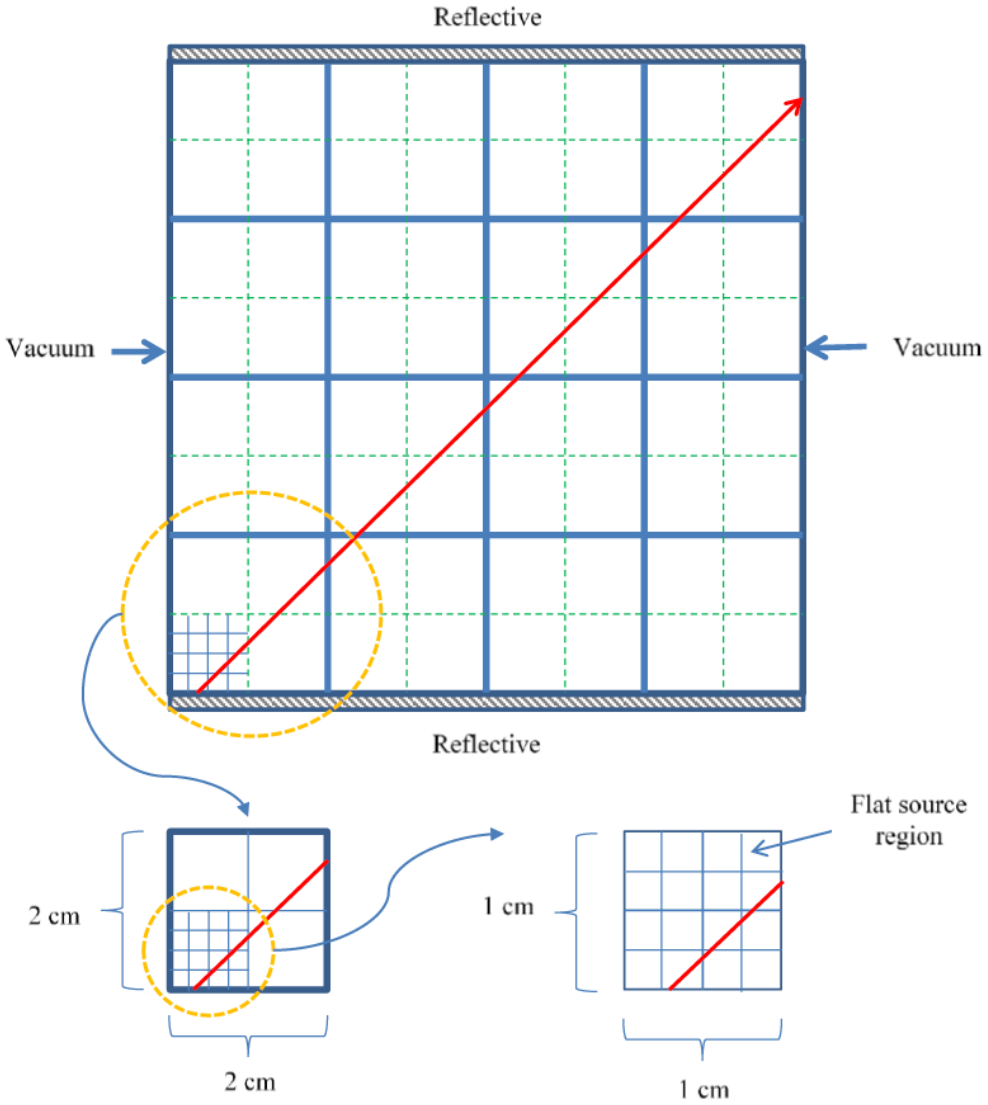

Figure 2.1. Unit test problem description.

The focus of this unit test is the product quadrature sweeper module of the MOC solver in the code. The sweeper loops through angles in the azimuthal quadrature set, which is the "Chebyshev" quadrature for this problem. For each angle in the azimuthal quadrature set, the long rays are swept, and the modular rays are looped through for each long ray. For each modular ray, the angles are swept in the polar quadrature set, which is the Gauss quadrature for this problem.

The code fragment for the unit test is given below. Similar testing is repeated for different types of boundary conditions applied to different surfaces.

```
!Test sweep for mono-energetic with fixed boundary in purely absorbing 1D
  homogeneous medium
!Test all faces
!
!West face, Mono-Directional
!Standard Sweep

COMPONENT_TEST('sweep(1,3,0.0_SRK) (Mono-Directional)')
```

```
!Clear volumetric source
testSource%qext=0.0_SRK
CALL testMOCSweeperType%setExtSource(testSource)

!Set boundary source on west face and make it mono-directional
CALL readRef2dSolution(1)
CALL testMOCSweeperType%setFluxVal(0.0_SRK)
DO iang=1,1
DO i=1,UBOUND(testMOCSweeperType%phiang(1)%angle(iang)%face(1)%angflux,DIM=2)
testMOCSweeperType%phiang(1)%angle(iang)%face(1)%angflux(:,i)=2.0_SRK
ENDDO
ENDDO
testMOCSweeperType%longRayDat%bcType=PERIODICBC
testMOCSweeperType%longRayDat%bcType(1)=VACUUMBC
testMOCSweeperType%longRayDat%bcType(3)=VACUUMBC
testMOCSweeperType%updateBC%bcType(1:4)=testMOCSweeperType%longRayDat%bcType

CALL testMOCSweeperType%sweep(1,3,0.0_SRK) !Sweep

!Test scalar flux
bool=ALL(ref2dsol*PI .APPROXEQ. testMOCSweeperType%phis(:,1))
ASSERT(bool,'testMOCSweeperType%sweep(1,3,0.0_SRK) (Mono-Directional)')
```

2.1.1.2 MPACT Unit Testing Statistics

MPACT unit testing provides living documentation of the overall code system. Below is a summary table of the current code statistics, with footnotes explaining the automated testing sequences. The data shown are for the MPACT Reflects code relevant to VERA-CS (i.e., MPACT built under VERA with weekly testing and coverage).

Since unit testing only tests the functionality of the units themselves, it is recognized that unit testing will not catch every error in the program. Specifically, unit testing will not identify integration errors or broader system-level errors (such as functions performed across multiple units or non-functional test areas such as performance). Therefore, unit testing is performed in conjunction with regression testing, which is described in the next section.

Table 2.1. MPACT code testing statistics (1/31/2019)

Metric	MPACT_libs	MPACT_Drivers	MPACT_exe
Unit tests	139	6	0
Regression tests	0	0	110
Coverage	75.9%	59.9%	58.3%
Lines of code	114,637	5,042	576

2.1.2 Regression Testing

The primary objective of regression testing is to provide a series of functional tests that can be repeatedly performed during code development. This allows code output to be compared against previously recorded outputs to ensure that new features and enhancements do not alter the reproducibility of existing features. Regression testing has served the important role during MPACT development to ensure that changes in one part of the code do not introduce new faults in other parts of the code.

As described in the previous section, unit tests were designed in MPACT to exercise individual functions or subroutines, whereas regression tests are more comprehensive and are designed to provide functional tests to exercise significant sections of the program with various inputs. MPACT regression testing targets key features that the user will need when applying the code to practical LWR problems. In addition, new regression tests in MPACT are sometimes added as part of the process of performing software fixes to the code. The best practice used in MPACT is that when a bug is located and fixed, a test is recorded that exposes the bug, and the test is rerun regularly after subsequent changes to the program. Both unit and regression testing are used to rerun previously completed tests to determine whether previously fixed faults have re-emerged. During code development, the MPACT developer can also systematically select the appropriate minimum set of tests needed to adequately cover a particular change. After the developer's change is complete, all MPACT tests are then performed as part of the MPACT regression testing.

The current practice in MPACT is to document all unit and regression testing with comments in the source code. However, consistent with the VERA SQA requirements, the plan is for all MPACT tests to be documented and subjected to configuration control with the following information:

1. The author or owner of the test;
2. The purpose of the test, including whether the test is a regression test, a verification test, or a performance test, for example;
3. The requirement or feature being tested; and
4. The pass/fail criteria for the test.

The regression tests in MPACT are also implemented as a scripted series of program inputs with a driver layer that links to the code without altering the code being tested. An automated system is in place to re-run all regression tests nightly, and a report is prepared documenting any failures. These tests are compared to previous solutions from MPACT to ensure consistent answers. The specific acceptance criteria are provided in the document entitled "MPACT Software Test Plan, Requirements, and Test Report" [9].

2.1.2.1 Sample MPACT Regression Test Problem

The essential features of a regression test problem can be demonstrated by one of the current regression tests in MPACT. One of the continuously run regression tests in MPACT is a 3×3 pin cell problem as shown in Figure 2.2. The pin-cells are stacked 2 nodes tall with the radial pin pitch of 1.26 cm and the axial node height of 5 cm. The central location of the 3×3 array is occupied by a guide tube, whereas the other cells are fuel pins. The pins are composed of fuel, helium gap and zirconium cladding, and the guide tube is also zirconium.

All the boundaries in the problem are reflective, and the Chebyshev-Yamamoto quadrature set is used with 1 polar and 8 azimuthal octants. A ray spacing of 0.08 cm is used with flux tolerance of 1e-4 and eigenvalue tolerance of 1e-4. The problem is performed with a 60-group library set with 4 subgroups for the resonance self-shielding. The solution for this problem is stored for comparison with the expected k-effective of 1.17933 and pin powers as shown in Figure 2.3.

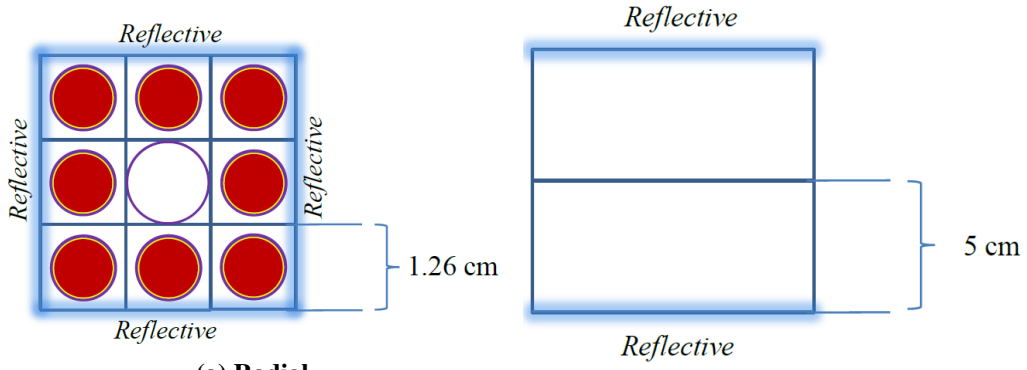

(a) Radial **(b) Axial**

Figure 2.2. Regression test problem: 3×3 pin cell.

0.99180	1.00820	0.99180
1.00820	0.00000	1.00820
0.99180	1.00820	0.99180

Figure 2.3. Regression test problem solution.

2.1.2.2 MPACT Regression Test Suite

As part of the MPACT regression test plan, a comprehensive regression test matrix was developed [1] to identify the key features of the code that require test coverage and for which regression tests must be run to ensure capability coverage testing of these features. The test matrix from that plan is shown in Figure 2.4 and now provides the roadmap for the development of regression testing in MPACT.

The rows and columns include an identical feature list, so only the top half of the test matrix is filled in. The diagonal of the matrix should be implicitly covered via unit testing of each individual feature. Grayed out boxes represent mutually exclusive features; for example, it is not possible to run with both quarter and full symmetry at the same time. The matrix contains an "X" to indicate the features that should be tested together in order to have sufficient functional coverage. Finally, the cells shaded in light blue represent tests that currently exist in the test suite.

Because of the substantial methodological and functional improvements to the code during the last few years, the requirement to rebaseline the entire regression and validation suite has become a formidable task which has made it more difficult to make improvements to the code. One of the improvements to the MPACT code development process this past year was to streamline the process of rebaselining the code and to provide diagnostics on the significance of any code modification and its impact on several code performance metrics. The following section describes a new MPACT regression test harness. More detail is available in the report by Collins [1].

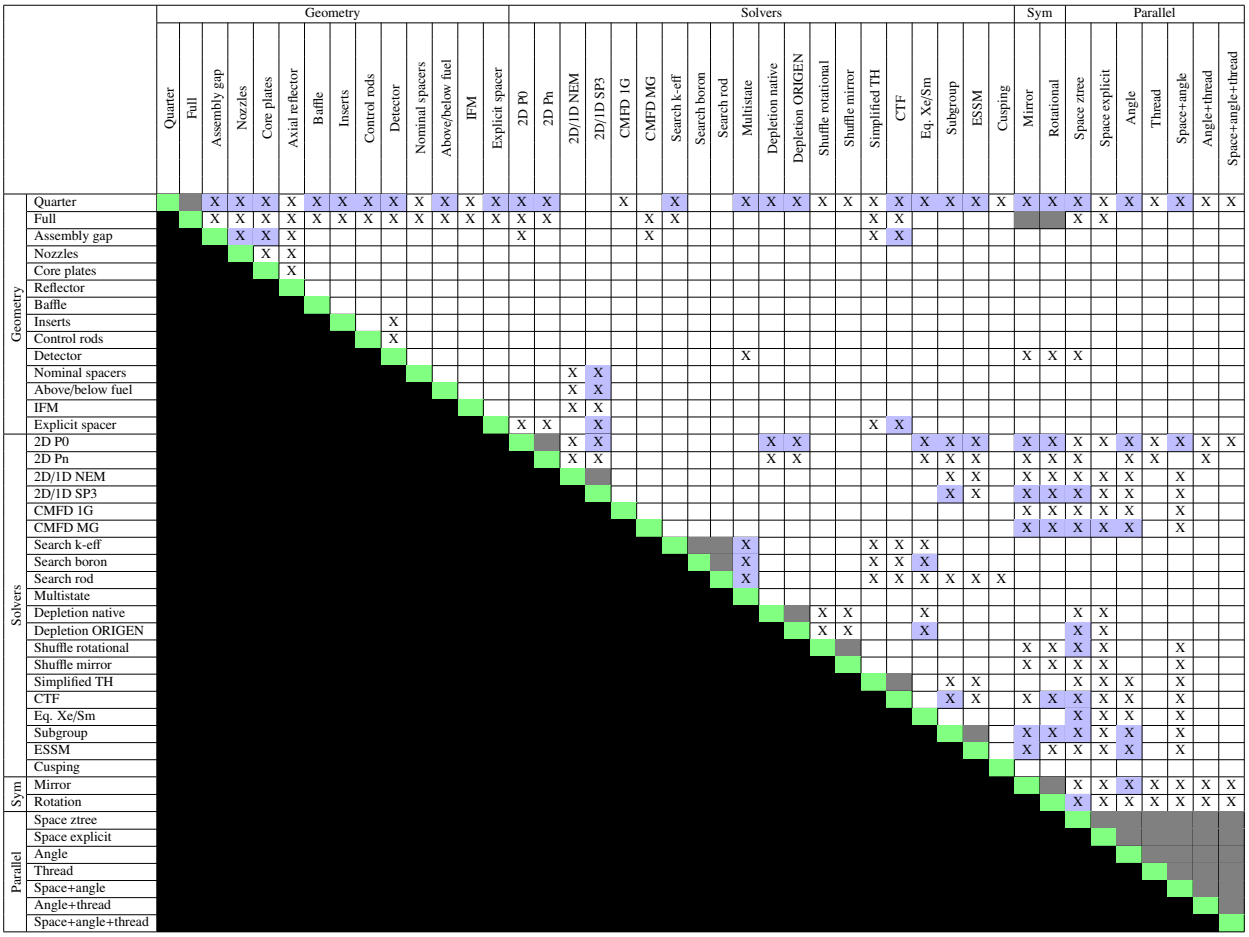

Figure 2.4. MPACT regression suite matrix [1]

2.1.2.3 MPACT Regression Test Harness

A Python script MPACTdiff was developed to provide the capability to simplify the process. The MPACTdiff script works with the MPACTdiff executable which is used by the regression and validation test suite to ensure that the MPACT solution is unchanged between commits. This is achieved by checking the difference between key parameters (k-eff, critical boron concentration, pin powers, and fuel temperature) with a "gold standard" HDF5 file. This HDF5 file is very similar to the VERA Common Output specification, except all of the gold standard values are stored in an "EXPECTED" directory in the file structure. There is also a "REFERENCE" directory that can store experimental data, analytic solutions, or continuous energy Monte Carlo solutions. MPACTdiff.exe compares the MPACT solution to the "EXPECTED" solution in the gold standard file, and it has tight tolerances to ensure the answer has not changed. The expected values for the key parameters are summarized in Figure 2.5.

The MPACTdiff Python script automates the process of collecting all test results into a single location and provides both tabular and visual comparisons to both the "EXPECTED" solution and the "REFERENCE" solution when it is available. This script has several capabilities that can be exposed through the command prompt or through an experimental GUI. The inputs for MPACTdiff can be found by running the script and providing the `--help` option.

```
usage: MPACTdiff.py [-h] [-g] [-pe [Plot Name]] [-pr [Plot Name]]
[-t [Table Name]] [-r Message Path] [-tr Message Path]
```

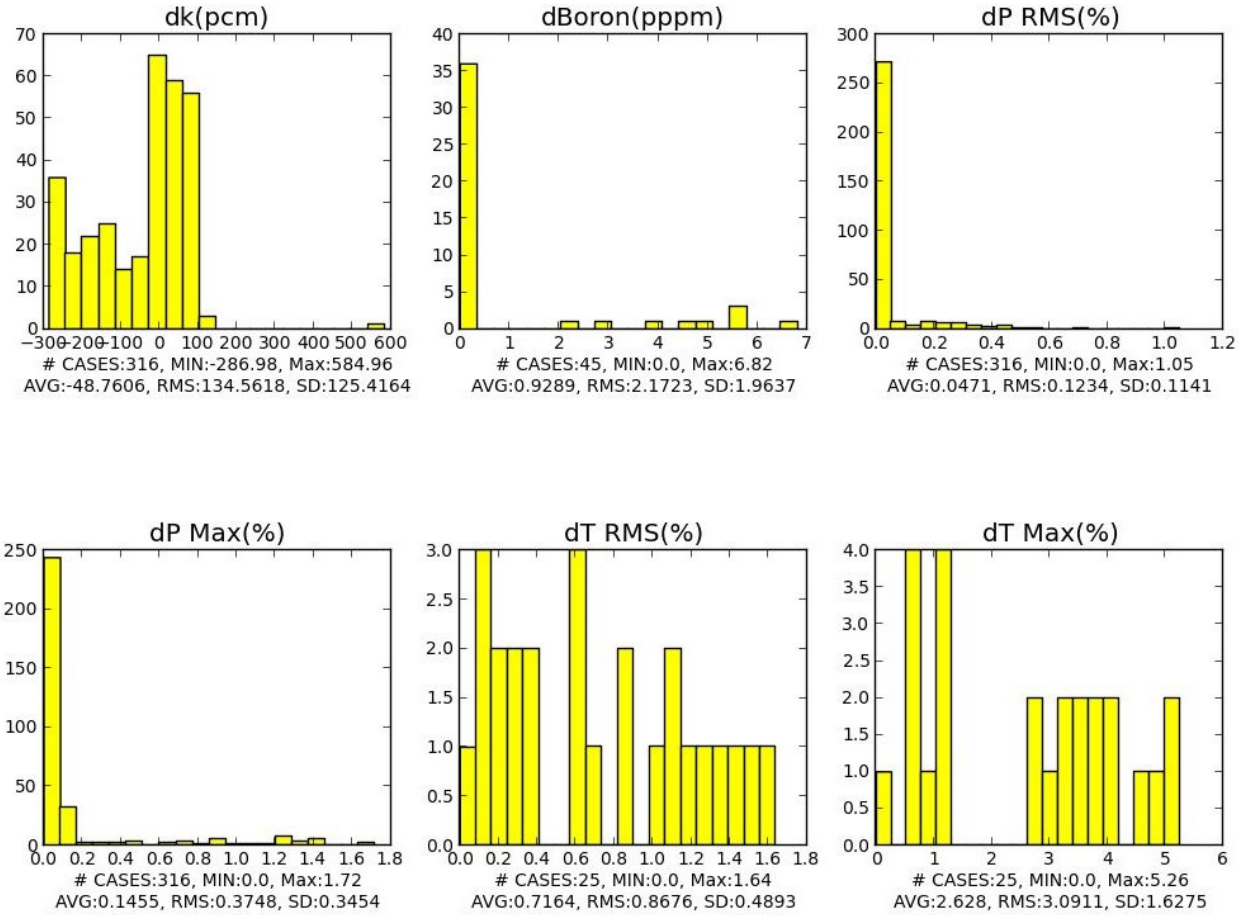

Figure 2.5. EXPECTED rebaseline summary.

```
optional arguments:
-h, --help            show this help message and exit
-g, --gui             enable GUI - experimental feature
-pe [Plot Name], --plot-expected [Plot Name]
plotted expected vs current solution
-pr [Plot Name], --plot-reference [Plot Name]
plotted reference vs current solution
-t [Table Name], --export-table [Table Name]
export table of expected and reference results
-r Message Path, --rebaseline Message Path
rebaseline tests given a rebaseline message and path
-tr Message Path, --test-rebaseline Message Path
perform rebaseline logic but does not rebaseline
code, only tells you what it will change
```

The script requires that the user call it from the top-level directory of tests to be compared. This provides the ability to analyze the whole test suite or just a subset of the suite based on the directory from which the script is run. Various options can be run from the command line. The `--plot-expected` and `--plot-reference` flags both take an optional name for the figure generated and will generate a histogram of all of the test

cases, as shown in Figure 2.6.

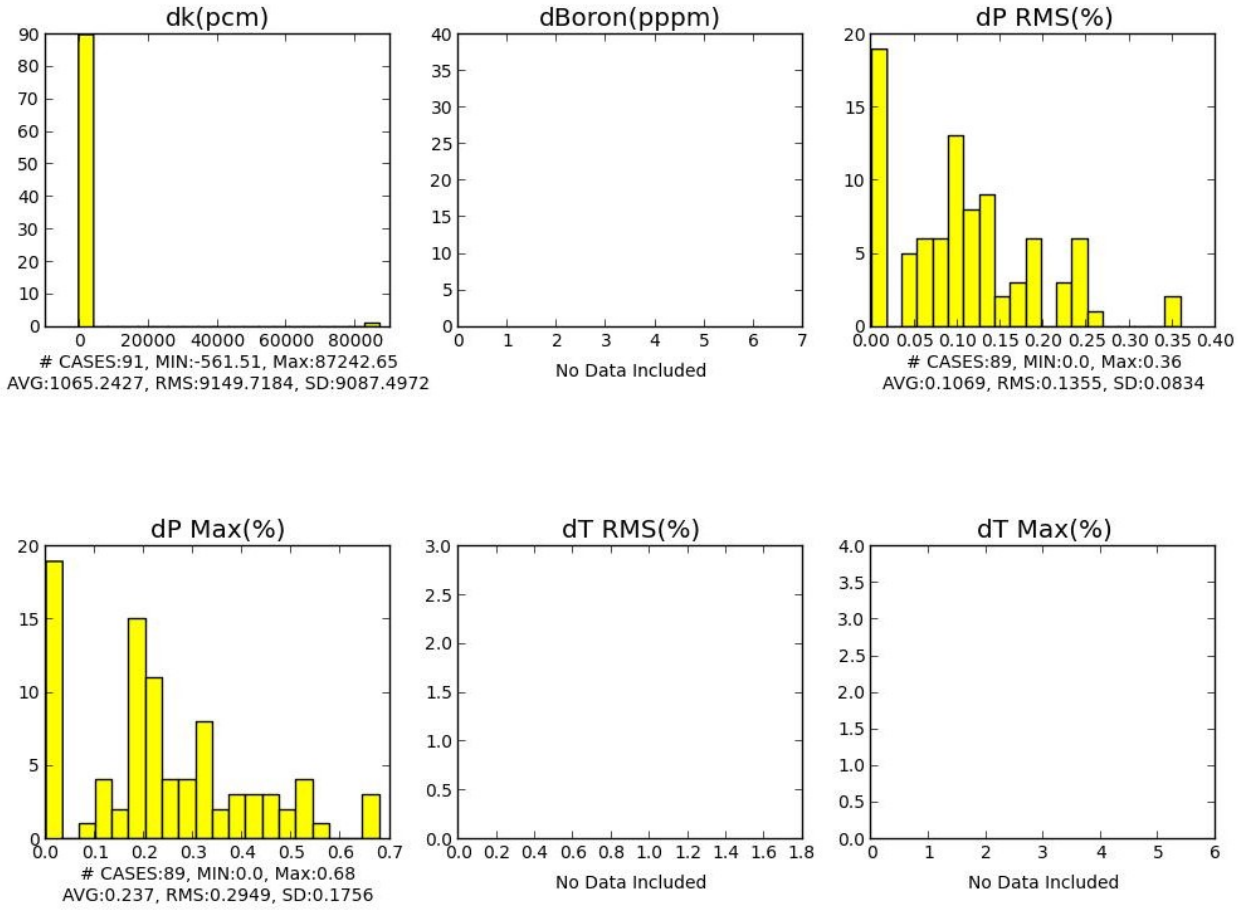

Figure 2.6. REFERENCE Rebaseline summary.

The `--export-table` flag will output a table of all the expected and reference results to a file. Although these results are always printed to standard output when the script is run, this option is included to simplify archiving the solution. Any of these options can be used in conjunction with the `--gui` flag, which will create a python interactive GUI to allow the user to view the histograms in real time and run the rebaseline script interactively. This feature is still considered experimental because instabilities have been observed, depending on the version of wx python that is used. The rebaseline component of the script can also be enabled from the command line using the `--rebaseline` command with two required arguments, a message stating what changed to require a rebaseline, and the path to the MPACT repository so the script can update the gold files. If a user chooses to observe the impact of change to rebaseline without actually modifying a gold standard file, then the `--test-rebaseline` flag can be used with the same arguments. This feature will perform all of the logical tests, but instead of changing a file, it will just print to the screen what would have changed. This helps the user gain confidence when using the capability and ensure that there are no errors while running the script.

The rebaseline process can be summarized in the following 5 steps:

1. Loops over all cases that have “EXPECTED” solutions

2. Ensures that the difference in the solution is greater than a small tolerance (0.02 in any quantity of interest)
   (a) If not, go to next case
3. Looks for a gold standard file that matches the test name
   (a) Error messages are printed if there are no or multiple gold standard files found (duplicate gold standard names are no longer allowed, even in unique folders. Either of these will result in this case being skipped)
4. Creates a new folder in gold standard file called `/OLD/EXPECTED_<date>`
   (a) Creates `change_date` and `change_description` fields and populates them using the message provided on the command line or through the GUI
   (b) For each state, creates a folder `STATE_<state>` and puts all of the quantities of interest into that folder
5. Copies the solution from the test output into the "EXPECTED" solution in the gold standard file

Once this process is completed, the developer proceeds to the MPACT repository and commits all of the changes, reruns the configure/build/test sequence, and then finally pushes the code changes.

MPACTdiff.py provides the developer with the ability to rebaseline MPACT whenever any change is made. Updates of the gold standard files should be minimized, but when necessary, a methodical process should be followed that involves critical questioning of the results and that ensures the changes are expected to minimize errors in the code base. To provide this assurance, a procedure for rebaselining MPACT is outlined below. A rebaseline of the tests requires formal approval of the designated MPACT product leads at UM and ORNL. The proposed workflow for applying a rebaseline is as follows:

1. Developer creates a ticket to perform work
2. Developer performs the work
3. Developer runs MPACTdiff.py and exports the table, and attaches the expected and reference figures files to the tickets
4. The UM and ORNL product leads both approve the rebaseline after reviewing the results (both product co-leads will be given sufficient time to review changes)
5. The developer runs the rebaseline script and pushes to a branch
6. The product lead at the corresponding institution merges the branch into the master and pushes

To implement this testing feature, a suite of regression tests was developed that mimic the capability required to perform the VERA Progression Problems with minimal computational expense. This significantly adds to the coverage of capabilities in the MPACT test matrix, and the matrix has been updated based on these features. The motivation for this is that problems 4, 5, 7, 8, 9, and 10 of the VERA Progression Problems all require significant computational resources to complete. Therefore, it is not feasible to run these cases on a nightly or weekly basis with the computing resources available.

Problems 1 and 2 (pin cells and lattices) have been present in the MPACT test suite for a few years. Problems 3, 4, and 6 have been added more recently, and because they push the limits of the computing power available on the test machines, they are only run on a nightly or weekly basis. Several key code features are introduced in each progression problem, resulting in a significant need for a quick running test to verify that functionality is maintained throughout the code development process. Therefore, a set of problems termed "Mini Progression Problems" was developed [1]. The purpose of these problems was to replace the more computationally intensive problems with smaller, faster running problems covering the same code features:

- The standard 47-group library was replaced with an 8-group test library
- The standard 17×17 pin assemblies were replaced with 5×5 pin assemblies
- A standard 193-assembly core was replaced with a 69-assembly core
- The core was shortened from 12 to 8 feet
- The MPACT parameters were coarsened to 0.08 cm ray spacing, 4 azimuthal angles per quadrant, and one polar angle

As an example, Figure 2.7 shows the center slice of the mini-core problems. The slice has 3 enrichment zones, PYREX rods in some of the fuel, and a baffle surrounding the core. All of these problems were designed so they could be performed on 32 cores or less and run as part of the automated test suite, including a full cycle depletion and shuffle.

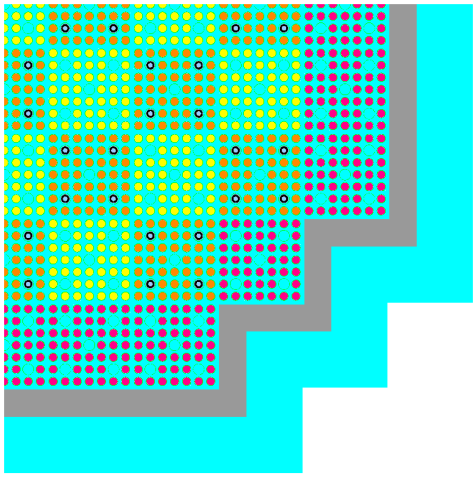

Figure 2.7. Mini Progression Problem 5 center slice.

2.1.2.4 Mesh Convergence Analysis

The method of characteristics (MOC) is one of the essential solution algorithms in MPACT. However, the MOC solver is a nonstandard discretization method, and the solution sensitivity to the various discretization parameters is not yet well understood. A better understanding of mesh convergence is also an essential first step in applying the method of manufactured solutions. The work described here used the various VERA benchmark cases to evaluate the sensitivity of k-eff to the MOC discretization parameters for selected VERA benchmark cases. The difference between k-eff for the specific case and k-eff for the most highly resolved case was used as the metric of performance. The MOC discretization parameters varied, including the flat source region (FSR) mesh (the number of radial and azimuthal discrete regions), the order of the quadrature set (the number of azimuthal and polar angles), and the ray spacing. The selected VERA benchmark cases covered pin cell problems (left) and assembly problems (right) as shown in Figure 2.8.

The detailed results are provided in the thesis by Wang [7], but selected conclusions from the sensitivity studies are given in Tables 2.2 and 2.3 below, and some of the findings are summarized as follows:

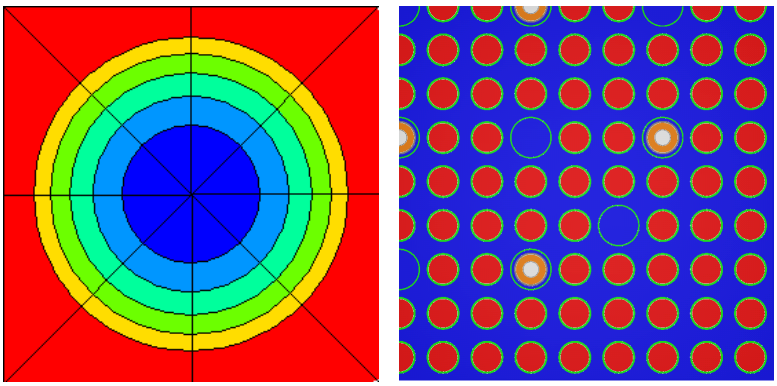

Figure 2.8. VERA benchmark problems for mesh convergence study (pin cell and assembly).

Table 2.2. Sensitivity study for VERA Benchmark Problem 1a (regular pin cell).

MOC Parameter	Sensitivity	Observations
FSR mesh	Slight (±20 pcm)	Adequate accuracy is obtained as long as the FSR mesh is not too coarse—3 rings in fuel and 2 rings in moderator for radial discretization, and 8 slices for azimuthal discretization are suggested.
Angular quadrature	Moderate (±100 pcm)	k-diff changes drastically when quadrature set order is changed—16 azimuthal angles in (0, PI/2) and 3 polar angles in (0, PI/2) are suggested.
Ray spacing	Moderate (±100 pcm)	k-diff oscillates with ray spacing, but after ray spacing decreases to 0.01 cm, the amplitude of oscillation is bounded within ±50 pcm range, so 0.01 cm is suggested.

1. For all cases, the sensitivity of k-eff to the FSR mesh is low as long as the FSR mesh is not too coarse and the ray spacing resolves the smallest region (i.e., the IFBA coating). The conclusion is that 3 rings in fuel and 2 rings in moderator for radial discretization and 8 slices for azimuthal discretization are sufficient given a sufficiently fine ray spacing.
2. For all cases, the sensitivity of the results to the quadrature set is moderate, and a reasonable set is 16 azimuthal angles per quadrant and 3 polar angles per hemisphere. In problems involving a very thin region, a higher quadrature set order may be needed.
3. The sensitivity of k-eff to the ray spacing is stronger, and the ray spacing must be comparable to the thickness of the smallest region, such as an IFBA coating, in order to get adequate accuracy.
4. There are nonlinear relationships among the MOC parameters and their impact on k-eff, which makes it difficult to determine an optimum set of MOC parameters that will hold for all cases, especially when accounting for computational time. For example, the FSR mesh is not a continuously changing variable, and k-eff oscillates with the ray spacing and the number of azimuthal angles, which means that the change in k-eff caused by a change in either of these quantities is a function of the other variable.
5. If there were better corrections for the IFBA region (or any other thin regions of interest, such as the peripheral fuel region) that could considerably reduce the sensitivity of k-eff to the ray spacing and angular quadrature set, then a coarser ray spacing and possibly less azimuthal angles could be used to reduce the computational cost while still retaining adequate accuracy.

Table 2.3. Sensitivity study for VERA Benchmark Problem 1e (IFBA pin cell).

MOC Parameter	Sensitivity	Observations
FSR mesh	Slight (±20 pcm)	k-diff is only slightly sensitive to FSR mesh as long as the ray spacing is decreased to a value comparable to the IFBA coating thickness (0.001 cm). Moreover, to have the right dependency behavior (k-diff barely depends on azimuthal discretization) a ray spacing at least as small as 0.002 cm (twice the coating thickness) should be used. Otherwise, k-diff drastically depends on the number of azimuthal zones used, which is unphysical in an "zimuthally symmetric" case. Again, 3 rings in fuel and 2 rings in moderator for radial discretization and 8 slices for azimuthal discretization are suggested.
Angular quadrature	Moderate (±100 pcm)	k-diff is sensitive to quadrature set order. It changes profoundly when quadrature set order changes, similar to vera_1a. However, it is not easy to find an order after which the oscillation will be bounded within a small range when the ray spacing is not small enough, which indicates a greater sensitivity to quadrature set order in the IFBA pin case. 28 azimuthal angles must be used to bound k-diff within a ±50 pcm range. Roughly, 16 azimuthal angles and 3 polar angles are acceptable.
Ray spacing	High (> ±500 pcm)	k-diff is very sensitive to ray spacing: (i) when ray spacing is too large, it triggers an abnormal dependency on FSR azimuthal mesh as mentioned earlier; (ii) only after the ray spacing decreases to the coating thickness (0.001 cm) should the k-diff fall into an acceptable range, although the k-diff vs. ray spacing curve level off earlier in some cases.

6. Overall, sensitivities of k-eff to the FSR mesh, angular quadrature, and ray spacing are mitigated in problems with a larger computational domain. However, large problems involving very thin regions show stronger sensitivity to MOC parameters than those without very thin regions.

This study is aimed at evaluating the sensitivity of k-diff to the MOC parameters for selected VERA benchmark cases, where k-diff is the difference between k-eff for the specific case and k-eff for the most highly resolved case. The input space of MOC parameters included the FSR mesh (the number of radial and azimuthal discretization), the order of the quadrature set (the number of azimuthal and polar angles), and the ray spacing.

The selected VERA benchmark cases covered small pin cell problems, relatively larger assembly problems, and problems involving very small regions such as an IFBA coating. The overall conclusions from the sensitivity studies are given in Tables 2.4 and 2.5 below based on the detailed sensitivity reports for each of the VERA cases, which are attached as appendices to this report.

Table 2.4. Sensitivity study for VERA Benchmark Problem 2a (17×17 assembly).

MOC parameter	Sensitivity	Observations
FSR mesh	Slight (±20 pcm)	k-diff is only slightly sensitive to FSR mesh; adequate accuracy is obtained as long as the FSR mesh is not too coarse: 3 rings in fuel and 2 rings in moderator for radial discretization, and 8 slices for azimuthal are suggested.
Angular quadrature	Moderate (±100 pcm)	k-diff is still sensitive to the quadrature set order, although to a smaller extent. Order 16 and 3 are suggested, after which the amplitude of oscillation is bounded, and going to higher order up to 32 only results in another 50 pcm accuracy at most.
Ray spacing	Moderate (±100 pcm)	k-diff is much less sensitive to ray spacing: the maximum accuracy gained by reducing ray spacing from 0.08 to 0.005 cm is only 35.2 pcm in this input space, average accuracy gain being 16.8 pcm. Therefore, for a problem that does not involve very thin regions, ray spacing as large as 0.08 cm or even larger is quite acceptable if k is the only concern. Note that it is possible that the local pin power resolution still requires smaller ray spacing. The ray spacing dependency of the k-diff vs. the number of azimuthal angles curve pattern is less profound because k-diff is less sensitive to ray spacing.

Table 2.5. Sensitivity study for VERA Benchmark Problem 2l (17×17 IFBA assembly).

MOC Parameter	Sensitivity	Observations
FSR mesh	Slight (±20 pcm)	k-diff is only slightly sensitive to FSR mesh; adequate accuracy is obtained as long as the FSR mesh is not too coarse: 3 rings in fuel and 2 rings in moderator for radial discretization, and 8 slices for azimuthal discretization are suggested. However, this is only true when the ray spacing is below 0.01 cm, which is ten times the thickness of the IFBA coating. This threshold value was formerly 0.001 cm in Problem 1e, indicating lower sensitivity of k-diff to ray spacing in larger problems.
Angular quadrature	Moderate (±100 pcm)	k-diff is still sensitive to the quadrature set order, although to a smaller extent. Order 16 and 3 are suggested, after which the amplitude of oscillation is bounded, and going to higher order only results in another 10 pcm accuracy. This value was formerly 50 pcm in Problem 1e, indicating mitigated sensitivity to angular quadrature in this larger problem.
Ray spacing	High (> ±500 pcm)	k-diff is less sensitive to ray spacing: the average accuracy gained by reducing ray spacing from 0.005 to 0.0001 cm is only 50 pcm in this input space, the average accuracy gain being 24 pcm when ray spacing is reduced from 0.003 to 0.0001 cm. Therefore, when k is the only concern, a ray spacing as large as 0.005 cm, which is relaxed 5 times from the value 0.001 cm required by a single IFBA pin in Problem 1e, would be acceptable. The ray spacing dependency of the k-diff vs number of azimuthal angles curve pattern is barely seen, which is a result of the mitigated sensitivity to the number of azimuthal angles and ray spacing.

2.2 CODE VERIFICATION USING THE METHOD OF EXACT SOLUTIONS

The MES is applied to problems with analytic solutions. The method typically involves consulting the literature for published solutions. The exact solution is a closed form mathematical expression that gives values of the solution at all locations in space and time. The problem with an exact solution can be modeled using the code, and then the numerical solutions can be compared against the exact solution. If the error is smaller than the acceptance criteria, then the code is verified. Grid refinements analysis can also be performed using the same problem, and the convergence rate can be observed and compared against the mathematical expectation.

Benchmark Problem 3.4 in Barry Ganapol's analytical benchmark book [2] is shown to be an excellent code verification test problem that can be modeled using MPACT without special coding. It can be included in the MPACT regression suite.

2.2.1 Ganapol Benchmark Description

The Ganapol benchmark problem is an analytic (or "semi-analytic" as Ganapol explains on page xxii) benchmark based on the exact solution of the singular integral equation that describes the cylindrical transport problem. This solution methodology is a complex sequence of steps as described in detail in Ganapol's book [2].

The configuration is a homogeneous right circular cylinder that is infinite in height:

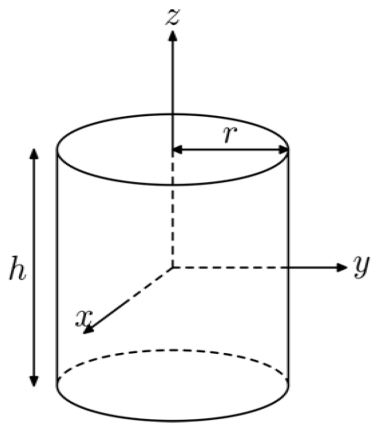

Figure 2.9. Ganapol benchmark problem configuration [2].

The homogeneous cylinder has a radius of $r = R$ and a height of $h \to \infty$, with a total cross section of Σ_t and c secondary neutrons per collision, where $c = \left(\Sigma_s + \nu\Sigma_f\right)/\Sigma_t$. The radius r is given in terms of mean free paths (MFPs), so the physical radius is r/Σ_t. Benchmark results are given for several cases:

(a) Uniform isotropic source: the scalar flux $\phi(r)$ is tabulated for selected values of $c < 1$

(b) Critical rod: the critical radius is tabulated as a function of $c > 1$

(c) Critical rod: the scalar flux $\phi(r)$ is tabulated for critical rods as a function of $c > 1$

2.2.2 MPACT Benchmark Problem

Cases (b) and (c) were chosen for the MPACT benchmark cases. This report presents the MPACT results for case (b) and beyond, including the convergence behavior with respect to certain discretization variables such as the radial discretization, ray spacing, and polar angular discretization. A separate report will be

prepared for case (c). The critical rod problems were chosen because they exercise the 2D MOC solver and the eigenvalue solver.

Table 3.4.3(a), as presented in Figure 2.10, gives the benchmark results for the critical rod problem. These results were extracted from the work by Ganapol [2]. Table 3.4.3(a) gives the critical rod radius as a function of c. The tabulated results are correct, with the last digit known to ±1 unit: hence, within 8 decimal points. This table shows the agreement with previously tabulated benchmark results, the shaded results indicate the digit that is not in agreement with Ganapol's [2] results.

Table 3.4.3(a). Critical radii comparisons

c	*R* (Ref. 3)	*R* (Ref. 10)
1.01E+00	1.312551649E+01	1.312551647E+01
1.02E+00	9.04325485E+00	----------
1.05E+00	5.41128829E+00	----------
1.10E+00	3.57739130E+00	3.57739129E+00
1.20E+00	2.28720926E+00	----------
1.30E+00	1.72500292E+00	1.72500292E+00
1.40E+00	1.39697859E+00	----------
1.50E+00	1.17834085E+00	1.17834085E+00
1.60E+00	1.02083901E+00	----------
1.80E+00	8.07426618E-01	----------
2.00E+00	6.68612867E-01	6.6861287E-01

Figure 2.10. Table 3.4.3(a) from Ganapol [2].

2.2.3 MPACT Results

Since MPACT is used for LWR lattices, special input processing would be needed to model the isolated cylinder. To avoid this, the cylinder is modeled as a fuel pin inside a nonscattering square bounding box—a void or a pure absorber—with vacuum boundaries. The angular flux along the rays starting at the bounding box boundaries will remain at zero until the ray intersects the rod, at which time the scattering and fission sources within the rod will begin to contribute to the solution.

The critical rod cases give the critical rod size as a function of c. To avoid adding special coding in MPACT to include an outer iteration to converge on the critical rod radius, MPACT solved for the eigenvalue k for each of the critical rod radii given in Table 3.4.3(a), where cross sections are chosen to yield the tabulated c. For each of these cases, MPACT should yield $k = 1$ to some precision.

Table 2.6 gives the MPACT eigenvalues for the values of c in Table 3.4.3(a). All cases were run with the following data:

- Bounding box side length = 30 cm
- Ray spacing = 0.0005 cm
- Number of radial rings = 160
- Number of azimuthal slices = 32
- Quadrature set = CHEBYSHEV-GAUSS 32 24
- Convergence criterion = 1e-7 for both k and ϕ

Table 2.6. MPACT k vs. critical rod radius

c	R	$\nu\Sigma_f$	k	error [pcm]
1.01	13.125516490	0.41	0.9999757	-2.43
1.02	9.043254850	0.42	0.9999783	-2.17
1.05	5.411288290	0.45	0.9999837	-1.63
1.1	3.577391300	0.50	0.9999895	-1.05
1.2	2.287209260	0.60	0.9999968	-0.32
1.3	1.725002920	0.70	1.0000006	0.06
1.4	1.396978590	0.80	1.0000020	0.20
1.5	1.178340850	0.90	1.0000004	0.04
1.6	1.020839010	1.00	0.9999968	-0.32
1.8	0.807426618	1.20	0.9999864	-1.36
2.0	0.668612867	1.40	0.9999621	-3.79

It is assumed that the reference value of k is known to within .01 pcm. The resulting ks are all within a few pcm, demonstrating excellent agreement with the benchmark results for the infinite rod. This is a stringent code verification problem because it is an actual transport solution being computed by MPACT, *not* a manufactured solution. These cases, or a subset of them, could easily be included in the MPACT regression test suite.

2.2.4 Mesh Convergence

The mesh convergence analysis for three discretization parameters is discussed in this section, including radial discretization, ray spacing, and polar angular discretization.

2.2.4.1 Radial convergence

The $c = 1.01$ critical rod case is used as an example. The following set of discretization parameters is used for the radial convergence analysis.

- Bounding box side length = 30 cm
- Ray spacing = .0005
- Number of azimuthal slices = 32
- Quadrature set = CHEBYSHEV-YAMAMOTO 16 3
- Convergence criterion = 1e-7 for both k and ϕ

The results are plotted as a convergence curve in Figure 2.11, which shows a nice second order radial convergence (up to 160 rings) for $c = 1.01$.

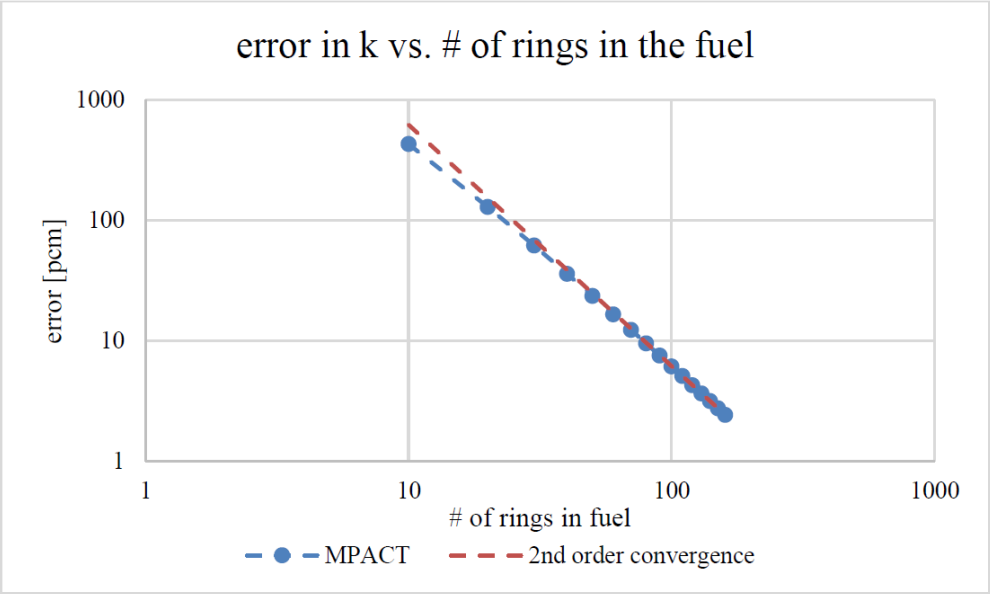

Figure 2.11. Ganapol radial convergence.

2.2.4.2 Ray spacing convergence and polar angle convergence

The convergence curve for eigenvalue *k* vs. ray spacing and polar angular discretization are plotted in Figure 2.12 and Figure 2.13, respectively. More details about this work are described in Appendix A.

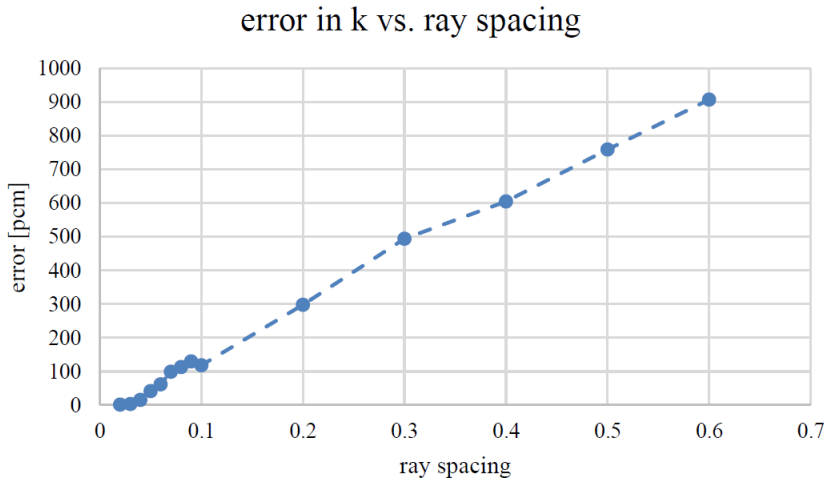

Figure 2.12. Ganapol convergence with respect to ray spacing.

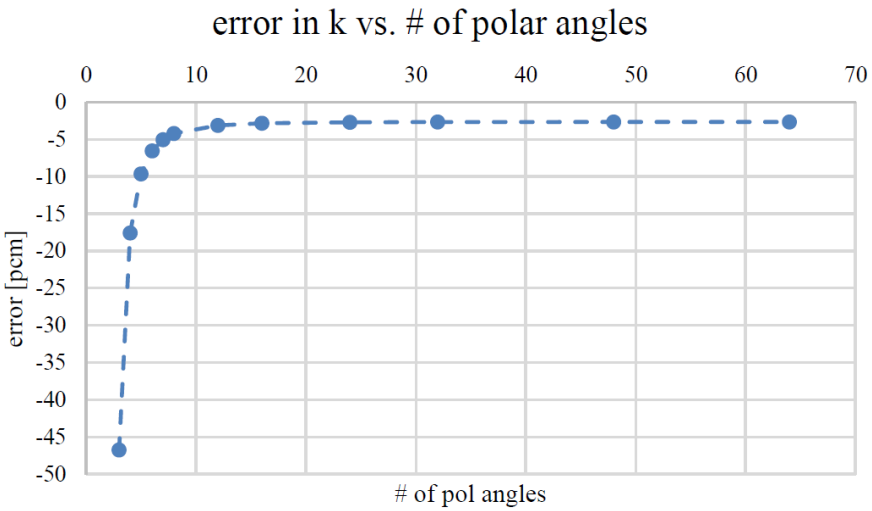

Figure 2.13. Ganapol convergence with respect to the number of polar angles.

2.2.5 Summary

Ganapol's benchmark problem 3.4 [2] has been used as a code verification test for MPACT. The bare rod configuration of problem 3.4 was changed to mimic a square lattice by surrounding the rod with a bounding box with a nonscattering material. Vacuum boundary conditions were imposed on the surface of the bounding box, and several critical rod cases were analyzed with MPACT using the tabulated critical rod radius as a function of c, the mean number of secondaries per collision. MPACT agreed with all cases to within a few pcm. The convergence behavior was studied. The radial rate of convergence is shown to be second order, which is consistent with second order flat-source approximation. The convergence curves with respect to ray spacing and polar angle quadrature set order were obtained, both of which converge to the analytic solution nicely.

2.3 CODE VERIFICATION USING THE METHOD OF MANUFACTURED SOLUTIONS

MMS was first applied in MPACT in FY15, and a methodology was developed for its application. MMS has been an effective code verification method for assessing the correctness of numerical algorithms and software implementation in a wide range of engineering applications. It has considerable flexibility in verifying computational functionalities of a computer code and has been used for the radiation transport code, but it has had mixed success in applications to the Boltzmann transport equation, primarily because of the complexity of coupled errors in space and angle. MMS has been applied to eigenvalue problems on a limited basis, published research on applying MMS to multiphysics problems is minimal. In this effort, a technique was developed to verify the method of characteristics (MOC) as implemented in MPACT for source and eigenvalue problems. This technique decoupled the angular error from the spatial error, enabling assessment of the convergence rate with spatial resolution. The angular error removal technique was also applicable to eigenvalue problems. Additionally, two independent approaches were applied to MMS eigenvalue problems: one using an inhomogeneous manufactured source, and the other using manufactured cross sections. Comprehensive tests were developed with a variety of solution structures to verify the theoretical convergence rates. Numerical results showed that both the eigenvalue, k, and the cell-averaged scalar fluxes exhibit orders of accuracy consistent with theoretical predictions. This section describes the work performed using MMS to analyze MOC, including the angular error removal technique. Ongoing work to implement MMS in MPACT and apply it to the OECD C5G7 Benchmark is also discussed.

The principal objective for applying the MMS to MPACT was to use a well-established method to complement the mesh convergence analysis as part of the code verification. Specifically, the mesh convergence analysis of the MOC-based solver in MPACT can provide insight for the code verification, but it has limitations because MOC is a nonstandard discretization method, and the solution sensitivity to the various discretization parameters is not yet well understood. MMS provides a more flexible technique with an analytically derived source term that can be discretized and used to solve the fixed source problem in MPACT. As discussed in a paper by Oberkampf and Trucano [10], MMS can be used to verify several numerical aspects of the code, such as the mathematical correctness of the numerical algorithms and the absence of coding errors that affect the orders of accuracy in the software implementation. MMS was used successfully with other transport codes [11] and is being investigated for implementation in MPACT. This section provides an update on the investigation of MMS for MPACT, and then, future plans are presented to implement MMS in MPACT.

2.3.1 Background

The essential concept behind MMS is that instead of solving a specified problem with a prescribed boundary and initial conditions, one can assume a solution beforehand and substitute it into the governing equation that the software will solve. The equation is then balanced by evaluating the resultant manufactured source. The boundary and initial conditions can be obtained by evaluating the manufactured solution at the boundary and at the initial time. The software is then used to solve the system with the manufactured source, boundary, and initial conditions. The computer code can be verified by comparing the numerical and manufactured solutions and observing the expected rate of the error's convergence with systematic grid refinements. The neutron Boltzmann transport equation with a fixed source can be presented as

$$(L+T)\,\psi = S\psi + Q\,, \tag{2.2}$$

where L, T, S, and Q represent leakage, collision, in-scattering, and external source operators, respectively, and ψ is the neutron angular flux.

Application of MMS to a fixed-source problem is straightforward. Start with an assumed solution ψ_{MMS}, and evaluate the manufactured source and boundary conditions:

$$Q_{MMS} = (L+T-S)\,\psi_{MMS} \tag{2.3}$$

$$\psi_{Bndy} = \psi_{MMS}|_{Bndy}\,, \text{ for incoming direction.} \tag{2.4}$$

The continuous source and boundary conditions presented above can be discretized by cell-averaging over a spatial cell and evaluating at angles defined in the applied quadrature set.

For example, in planar geometry discretized in J slab intervals $x_{j-1/2} < x < x_{j+1/2}\,,\ j = 1, ..., J$, as shown in Figure 2.14, and the discretized source (for flat source approximations) and boundary conditions can be expressed as

$$Q_{MMS,j,n} = \frac{1}{\Delta x_j}\int_{j-1/2}^{j+1/2} Q_{MMS}\,(x,\mu_n)\,dx \tag{2.5}$$

$$\psi_{LB,n} = \psi_{MMS}\,(x=0,\mu_n)\,,\quad \mu_n > 0 \tag{2.6}$$

$$\psi_{RB,n} = \psi_{MMS}\,(x=X,\mu_n)\,,\quad \mu_n < 0\,, \tag{2.7}$$

where μ_n is from the applied quadrature set $(\mu_n, \omega_n)\,,\ n \in [1, ..., N]$. More details about MMS in linear source MOC can be found in our published work [12, 13].

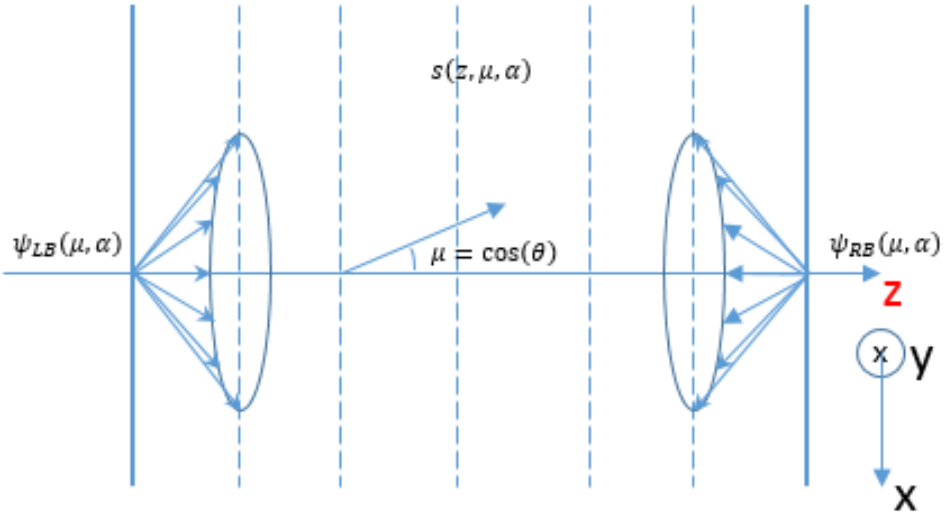

Figure 2.14. Planar geometry with azimuthal symmetry.

This problem is then modeled and solved with a series of refined grids. The RMS error is defined as

$$E_{RMS} = \sqrt{\frac{1}{J} \cdot \sum_{j=1}^{J} \left(E_j\right)^2} = \sqrt{\frac{1}{J} \cdot \sum_{j=1}^{J} \left(\phi_j - \phi_{MMS,j}\right)^2}\,, \tag{2.8}$$

where ϕ_j is the cell-averaged scalar flux, and $\phi_{MMS}\ (x)$ is the corresponding manufactured scalar flux:

$$\phi_{MMS,j} = \frac{1}{\Delta V_j} \int_{V_j} \int_{4\pi} \psi_{MMS}\left(\underline{r}, \hat{\Omega}\right) d\Omega dV\,. \tag{2.9}$$

The order of accuracy (OoA), or rate of convergence, measures the rate of error reduction with refined grids and can be calculated as

$$p = \frac{\log\left(\frac{E_{grid1}}{E_{grid2}}\right)}{\log\left(r\right)}\,, \tag{2.10}$$

where *r*ssi the ratio of the mesh size of grid 1 to that of grid 2, known as the *grid refinement ratio*. When equations with more than one independent variable are discretized, the discretization errors propagate and interact through the numerical algorithm, concealing the expected rate of convergence with respect to one variable when its grid is refined. A method was developed to remove the angular error from the MOC solution and to isolate the spatial grid discretization errors for its rate of convergence. Application of MMS to fixed source and eigenvalue problems is described in Appendix B. The following section describes the application of more direct interest, which is the use of MMS for 2D MOC, in which the 2D multigroup C5G7 benchmark problem is used.

2.3.2 Application of MMS to the C5G7 Problem to Verify a 2D Multigroup Neutron Transport Solver

As part of this milestone, methods to extend the range of problems to which MMS can be applied have been investigated. In this demonstration, MMS was applied to the C5G7 benchmark problem [14], which has the typical heterogeneity and complex geometry encountered in practical PWR nuclear fuel assemblies. The test framework developed as a result involves two useful tests. The first test is a consistency test in which

the converged solution of an eigenvalue problem is used to formulate a fixed-source problem. The second is the MMS test, in which an analytical solution is assumed, and the corresponding MMS source is used to verify the fixed source solver. This can be extended to the more challenging eigenvalue problem, in which the neutron flux distribution and the eigenvalue for verifying the eigensolver are assumed.

2.3.2.1 Consistency Test

An eigenvalue problem is solved first. Once the eigensolver converges to a solution pair ψ_{conv}, k_{conv}, the fission source $\frac{1}{k_{conv}} F\psi_{conv}$ is constructed and output to a data file, which is subsequently used in the fixed-source problem with the same geometric and material configurations. This fixed-source problem is modeled, and it is expected that the fixed source solver will return the same solution as the eigensolver upon convergence.

The consistency test is straightforward, but it is an important test to perform. It is also a convenient way to verify the fixed source solver if MMS capabilities (e.g., general fixed source and general boundary condition capabilities) are not present for a full-scale MMS test.

2.3.2.2 Application of MMS to a 2D Multigroup Fixed-Source Problem

For 2D, the multigroup Boltzmann transport equation with isotropic scattering and a fixed source, takes the following form,

$$\eta \frac{\partial \psi_g(x,y,\eta,\xi)}{\partial x} + \xi \frac{\partial \psi_g(x,y,\eta,\xi)}{\partial y} + \Sigma_{t,g}(x,y) \cdot \psi_g(x,y,\eta,\xi) \tag{2.11}$$

$$= \frac{1}{2\pi} \sum_{g'=1}^{G} \Sigma_{s,g\leftarrow g'}(x,y) \cdot \phi_{g'}(x,y) + q_g(x,y,\eta,\xi) \ , \quad g = 1,...,G \ . \tag{2.12}$$

Given a MOC solver that is intended to solve the above equation with prescribed boundary conditions, the steps for applying MMS to verify the correctness of the fixed source solver are shown below.

First, assume an analytical solution, such as

$$\psi_g(x,y,\eta,\xi) = \psi_{MMS,g}(x,y,\eta,\xi) \ , \ g = 1,...,G \ . \tag{2.13}$$

The corresponding scalar flux is

$$\phi_g(x,y) = \int_{-1}^{1} d\eta' \int_{-\sqrt{1-\eta'^2}}^{\sqrt{1-\eta'^2}} \frac{\psi_{MMS,g}(x,y,\eta',\xi')}{\sqrt{1-\eta'^2-\xi'^2}} d\xi' \ , \ g = 1,...,G \ . \tag{2.14}$$

Second, substitute the assumed solutions into the multigroup equation, as defined in Eq. (2.11). The equation will be balanced by an inhomogeneous MMS source, which can be expressed as in Eq. (2.15):

$$q_{MMS,g}(x,y,\eta,\xi) = \eta \frac{\partial \psi_g(x,y,\eta,\xi)}{\partial x} + \xi \frac{\partial \psi_g(x,y,\eta,\xi)}{\partial y} \tag{2.15}$$

$$+\Sigma_{t,g}(x,y) \cdot \psi_g(x,y,\eta,\xi) - \frac{1}{2\pi} \sum_{g'=1}^{G} \Sigma_{s,g\leftarrow g'}(x,y) \cdot \phi_{MMS,g'}(x,y) \ . \tag{2.16}$$

To get the discrete form of the manufactured source, the analytical form as defined in Eq. (2.15) is averaged over every FSR indexed by region ID i and is evaluated at each discrete angle (η_m, ξ_m) defined in the applied quadrature set:

$$q_{MMS,g,j,m} = \frac{1}{V_i} \int_{V_i} q_{MMS,g}(x,y,\eta_m,\xi_m)\, dxdy \ . \tag{2.17}$$

For the first two terms (i.e., the leakage terms of the manufactured source in Equation 2.15), the analytical form can be obtained using external software or a script or one can calculate the derivative by hand. However, it would be a substantial challenge to average the analytical leakage terms over every FSR region, unless a simple solution were assumed, in particular one with zero derivatives. (This is what we did, as we will see later.) The discrete form of the third term—the collision term—can be obtained by first having the code output the total cross section for all FSR regions as a vector and then performing an element-wise product of the cross section vector with the discrete MMS solution vector. The scattering source term is even more complicated. However, it is not necessary to expend the effort to compute scattering terms because the MOC code already accumulates these terms in its iterative approach to solve the eigenvalue problem. Specifically, the existing code infrastructure can be used to calculate the scattering sources. To use the existing infrastructure, the discrete MMS solution should be used to initialize the first iteration of the fixed source solver. This is a singular iteration because it must halt after one iteration, and once the in-scattering source and self-scattering source are accumulated, they are output to a data file. This file can be processed to generate the discrete MMS source.

The third step is to obtain the boundary conditions for the manufactured problem. This is achieved by straightforward evaluations of the assumed solutions at the problem boundaries, which are carried out for all energy groups,

$$\psi_g\left(x,y,\eta,\xi\right)|_{Boundary} = \psi_{MMS,g}\left(x,y,\eta,\xi\right)|_{(x,y)\in dV}\ ,\ \left(\eta\overrightarrow{i}+\xi\overrightarrow{j}\right)\cdot\overrightarrow{n}<0\ , \tag{2.18}$$

where ∂V is the boundary of the system V, $\overrightarrow{n}$ is the surface normal, and angle (η,ξ) represents the direction of flight of neutrons.

In MOC, the boundary conditions are defined using the entering fluxes associated with the sets of characteristic rays that sweep through the geometry. Each set of the rays is characterized by an angle (η_m,ξ_m) defined in the applied quadrature set. If the variable l_m is used to index each ray characterized by angle (η_m,ξ_m), then the discrete boundary condition can be expressed, as shown below:

$$\psi_{g,m,J_m} = \frac{1}{2}\psi_{MMS,g}\left(x_{l_m},y_{l_m},\eta_m,\xi_m\right)\ , \tag{2.19}$$

where (x_{l_m},y_{l_m}) are the coordinates of the entry point for the characteristic ray l_m. A factor of 1/2 accounts for the fact that one neutron travels along only one direction with either a positive or negative polar angle. This implies that the capability of accepting a more general prescribed incoming angular flux can be implemented. For cases in which the boundary flux distribution is an even function of the angular variables (η,ξ), the existing reflective boundary condition can be used.

The discrete MMS source and boundary conditions, along with the geometry and materials configurations, are modeled using the fixed source solver under verification. If the solver converges to the assumed MMS solution, then the fixed source solver is verified.

2.3.3 Demonstration and Numerical Results

For demonstration purposes, the OECD/NEA C5G7 benchmark problem was selected. The problem geometry, material, and cross section library are the same as those defined in the C5G7 benchmark report [14]. The problem configuration is shown in Figure 2.15.

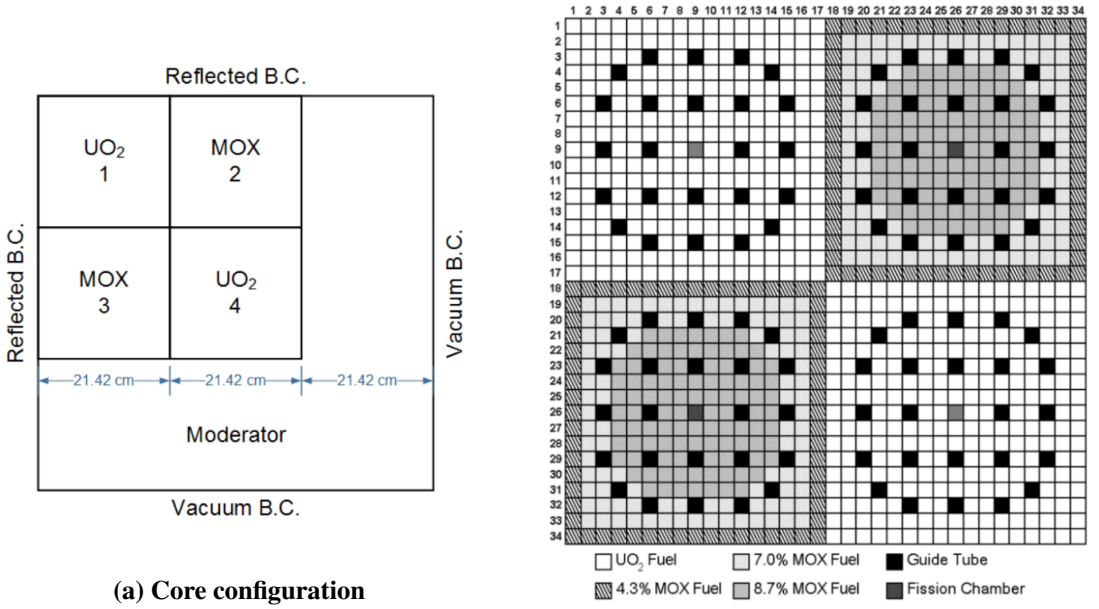

(a) Core configuration

(b) Pin cell compositions and numbering scheme

Figure 2.15. Problem configuration for the C5G7 benchmark problem solution.

2.3.3.1 Numerical Results for the Consistency Test

As noted above, we start with an eigenvalue calculation with the C5G7 configuration with the MOC-based code MOCC [15]. MOCC is an emulator for the production code MPACT [16], and it has the same solution strategy as MPACT. The objective is to prove the concept by implementing MMS for C5G7 in MOCC and then to use this experience to implement the C5G7 MMS test into MPACT.

The converged eigenvalue for the MOCC eigenvalue calculation was 1.18642. The converged scalar flux for the first energy group (fast) and the last energy group (thermal) are shown in Figure 2.16

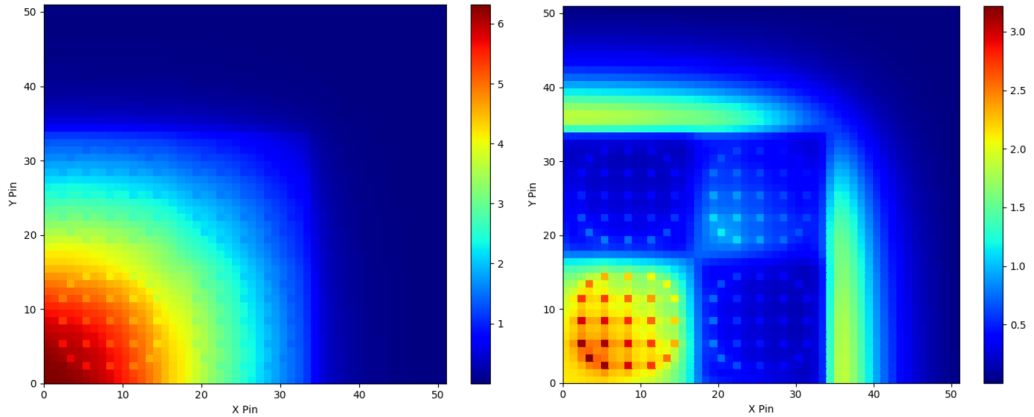

(a) The scalar flux of group 1

(b) The scalar flux of group 7

Figure 2.16. Scalar flux C5G7 eigenvalue calculation.

The fission source distribution is shown in Figure 2.17 in a pin-homogenized form for visualization. The fission source is used as the fixed source for the subsequent fixed source calculation. The plot shows the drastic spatial variation of this source.

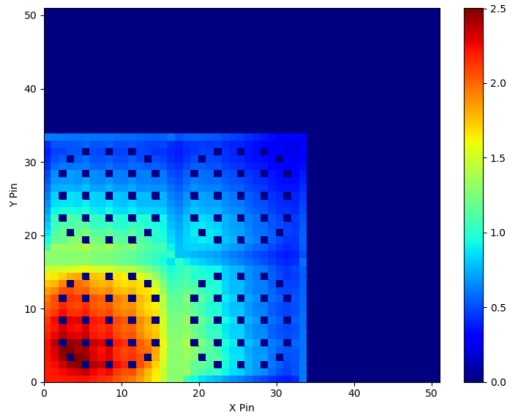

Figure 2.17. Fission source distribution from eigenvalue calculation.

The fixed-source problem is modeled with MOCC. The relative error of the scalar flux of the first energy group is plotted in Figure 2.18, in which the error is 1E-8. The relative error of the scalar flux of the thermal energy group can be close to 1E-5. The close-to-zero error indicates that the scalar flux from the fixed-source problem converges to the same solution as in the eigenvalue calculation. Therefore, the consistency of the inner workings between the eigensolver the fixed source solver in MOCC is verified.

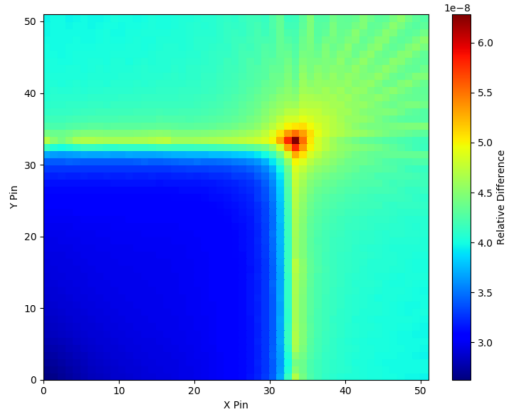

Figure 2.18. The relative error of the converged group one scalar flux from the fixed-source problem.

2.3.3.2 Demonstration with the C5G7 problem using a constant solution

A constant manufactured solution is selected to demonstrate the feasibility of applying MMS to a fixed-source problem for realistic applications.

Assume a constant angular flux for each group,

$$\psi_g(x, y, \eta, \xi) = \psi_{MMS,g}(x, y, \eta, \xi) = \frac{1}{2\pi}, \; g = 1, ..., 7 . \tag{2.20}$$

The scalar flux can be obtained

$$\phi_{MMS,g}(x, y) = 1 \tag{2.21}$$

with this:

$$q_{MMS,g}(x,y,\eta,\xi) = \eta\frac{\partial\psi_{MMS,g}(x,y,\eta,\xi)}{\partial x} + \xi\frac{\partial\psi_{MMS,g}(x,y,\eta,\xi)}{\partial y} \tag{2.22}$$

$$+ \Sigma_{t,g}(x,y)\cdot\psi_{MMS,g}(x,y,\eta,\xi) - \frac{1}{2\pi}\sum_{g'=1}^{G}\Sigma_{s,g\leftarrow g'}(x,y)\cdot\phi_{MMS,g'}(x,y) \tag{2.23}$$

$$= \Sigma_{t,g}(x,y)\cdot\frac{1}{2\pi} - \frac{1}{2\pi}\sum_{g'=1}^{G}\Sigma_{s,g\leftarrow g'}(x,y)\cdot 1 \tag{2.24}$$

$$= \frac{1}{2\pi}\cdot\left(\Sigma_{t,g}(x,y) - \sum_{g'=1}^{G}\Sigma_{s,g\leftarrow g'}(x,y)\right). \tag{2.25}$$

Because the MMS source is independent of angle, it can be treated as an isotropic external source when the manufactured problem is modeled:

$$Q_{MMS,g}(x,y) = \Sigma_{t,g}(x,y) - \sum_{g'=1}^{G}\Sigma_{s,g\leftarrow g'}(x,y)\ . \tag{2.26}$$

The MMS source can be discretized in the following form,

$$Q_{MMS,g,i} = \Sigma_{t,g,i} - \sum_{g'=1}^{G}\Sigma_{s,g\leftarrow g',i}\ , \tag{2.27}$$

where i is the FSR region index.

Note that the discontinuity in the MMS source from one FSR region to its neighbor is caused by the discontinuity in materials and is necessary for the solver to converge to a flat solution. The discrete boundary condition takes the following form:

$$\psi_{g,m,l_m} = \psi_{g,l_m}(\eta_m,\xi_m,\mu_m) = \frac{1}{4\pi}\ ,\ g = 1,...,7\ . \tag{2.28}$$

An easy way to implement this boundary condition is to modify the vacuum boundary condition code by replacing the zero incoming angular flux with constant $1/4\pi$.

The discrete MMS source and boundary conditions constitute a well-defined MMS problem. With the geometry and materials information from the C5G7 benchmark, the MMS problem can be modeled using the code under verification. The constant-in-space solution does not trivialize this MMS test case, because the complexity in geometry and materials is retained, and all routines involved are exercised. This complicated manufactured source drives the solver to converge to a flat solution, so this is a challenging test problem. This test helps verify the correctness of the fixed source solver.

2.3.3.3 Numerical results for the MMS fixed source problem

The fuel pins are spatially discretized with five rings in the fuel region, three rings in the moderator region, and eight azimuthal slices. Non-fuel pins in the moderator assemblies are meshed with 3×3 square subregions.

A "dummy" input with the spatial discretization outlined above is used to generate the scattering source and the collision term which are output to a data file. The data file is processed with an external script for

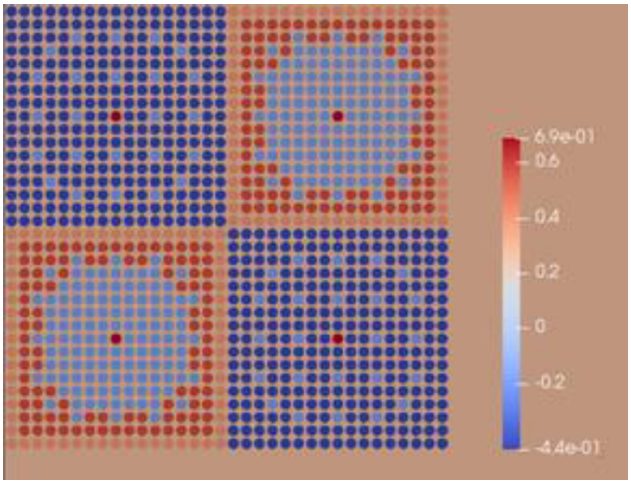

Figure 2.19. Manufactured source corresponding to a flat manufactured solution.

calculation of the MMS source. For example, the MMS source for the first energy group is presented in Figure 2.19.

As seen in Figure 2.19, with a flat MMS solution, the spatial variation of the MMS source coincides with material boundaries, which is expected. When the assumed solution is non-flat in space, the spatial variation of the MMS source will vary on the level of the FSR. In modeling the manufactured problem, Chebyshev-Gauss quadrature is used with eight azimuthal angles and two polar angles in each quadrant. Ray spacing is taken as 0.05 cm. A maximum of 100 source iterations is performed, with a 2.37E-8 convergence criterion on the root-mean-square (RMS) error between the scalar fluxes of two consecutive iterations:

$$e_{100} = \sqrt{\frac{\sum_{i=1}^{n_{reg}} \sum_{g=1}^{G} \left(\phi_{i,g,new} - \phi_{i,g,old}\right)^2}{n_{reg} \cdot G}} \leq 2.37 \times 10^{-8} \, . \tag{2.29}$$

Figure 2.20 shows the error in pin flux for energy groups 1 and 7. It can be seen that the errors are close to zero, which is also true for energy groups 2–6. This indicates that the numerical solution converges to the MMS solutions, thus passing the MMS test and verifying the fixed source solver. It is expected that the error in the moderator region is larger than the fuel region as a result of more scattering. It is also expected that the error in the lower energy group (right) is larger than the higher energy group (left) because of increased upscattering near low energy groups.

Note that the drastic spatial variation in MMS source, even with negative values in some regions as seen in Figure 2.19, does not affect the convergence of the scalar flux to the MMS solution. This strong spatial variation drives the fixed source solver to converge to a solution that is flat in space.

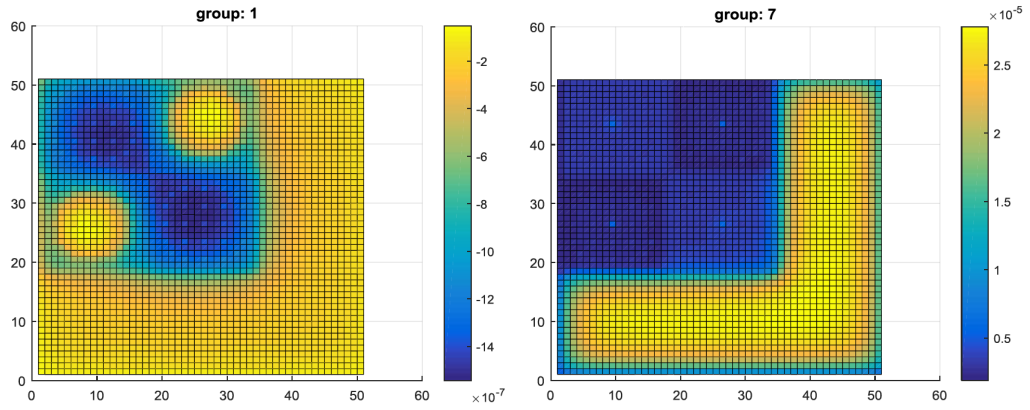

Figure 2.20. Error in pin flux for energy groups 1 (left) and 7 (right).

2.3.4 Summary and Conclusion on MMS

The applicability of MMS for the verification of a 1D S_N neutron transport code was demonstrated, including both source and eigenvalue problems. It was shown that errors from different approximations in each independent variable (e.g., diamond difference in space, discrete ordinate in angle) are separable and can be isolated from the overall error so that the order of accuracy with respect to each variable can be determined as the corresponding grid is refined. Two different approaches were developed to apply MMS methods to eigenvalue problems: the traditional manufactured source (MS) approach, and an alternative manufactured cross section (MXS) approach. A systematic method was used to ensure convergence to the correct manufactured eigenvalue and eigenfunction with both approaches. The manufactured source approach requires an angularly dependent fixed source necessitating minor changes to the fixed source in the eigensolver, whereas the manufactured cross section approach requires extra modifications in the data structure storing the fission cross section. The numerical results demonstrate that both k and the cell-averaged or cell-edged scalar flux show the same order of accuracy, which is as expected from the S_N method.

As for applying MMS to MOC, a systematic analysis of the order of accuracy for spatial discretization of the MOC method in a slab geometry was performed with flat source and linear source approximation. It was shown that including scattering source does not degrade the order of accuracy and that the order of the error in the first spatial moment of the angular flux is two orders higher than that in the zeroth spatial moment of the angular flux. Both theoretical prediction and experimental results show that the flat source approximation is second order accurate and that the linear source approximation has a fourth order accuracy.

Some preliminary studies of the application of MMS in 2D MOC have shown that the angular error still must be removed from the total error with the same technique developed in Sn 1D. To be consistent with MPACT, modularized angles, rather than the original angles defined in the quadrature set, should be used in the angular error removal process. Initial studies have also shown that the spatial error decreases and stagnates with the spatial grid refinements, which justified the idea of first simplifying the problem to 1D MOC and then adding the complexity of 2 angles before tackling the 2D MOC completely.

MMS methods are also applied to the C5G7 benchmark problem, which is a realistic reactor configuration with typical heterogeneity and complex geometry encountered in actual PWR nuclear fuel assemblies. The overall test framework included a consistency test and the application of MMS to the C5G7 problem with a fixed source. The consistency test is straightforward, but it is an important test to perform, as it verifies that the fixed source solver is consistent with the eigenvalue solver. The successful application of MMS to the C5G7 problem with an assumed flat solution verifies that the fixed source solver for this realistic reactor configuration can be verified using MMS. Work is ongoing to extend this to the eigenvalue problems. The

test framework established here extends the MMS range of applicability considerably. Work is in progress to implement the consistency test and the MMS test in the MPACT reactor code as part of the code verification and overall quality assessment effort for MPACT.

2.4 SOLUTION VERIFICATION IN 2D PIN GEOMETRY

The second solution verification exercise performed was a convergence analysis with 2D pin geometry (i.e., no grid refinements in the axial direction). The purpose of this study was to better understand the convergence behavior of terms 2 through 6. Two separate sets of calculations are performed. The first set is by Lindsay Gilkey under the direction of Nathan Andrews at Savannah National Laboratory (SNL), and the second set is by Jipu Wang under the direction of Bill Martin and Tom Downar at the University of Michigan (UM). Both sets of calculations include a re-coarsening analysis of five parameters of interest: radial division, azimuthal division, ray spacing, polar angle, and azimuthal angle. Additionally, the calculations performed by Andrews and Gilkey include a uniform mesh refinement study akin to the 3D assembly study presented in Section 0, and calculations with self-shielding turned off to isolate the effect of this factor. Although trend behaviors are consistent, there are some small differences between the UM and SNL calculations that are not fully understood, but they might be related to different code versions, different convergence criteria for k-eff and flux, or different cross section libraries. Table 2.7 shows the number of elements used for each of the five parameters of interest. The total number of elements varies six orders of magnitude from the xcoarse to the xfine case.

Table 2.7. Grid used for uniform refinement in 2D pin geometry

Andrews and Gilkey	**Uniform refinement 2D pin**				
	Number of elements				
	xcoarse	**coarse**	**medium**	**fine**	**xfine**
Radial division	**8**	**16**	**32**	**64**	**128**
Fuel	4	8	16	232	64
Gap	1	1	1	1	1
Clad	1	1	1	1	1
Moderator	4	8	16	32	64
Azimuthal division	**4**	**8**	**16**	**32**	**64**
Ray spacing N	63	125	250	500	1000
Ray spacing h	0.008	0.004	0.002	0.001	0.0005
Polar angle	**2**	**4**	**8**	**16**	**32**
Azimuthal angle	**2**	**4**	**8**	**16**	**32**
NTotal	8×10^3	2.56×10^5	8.19×10^6	2.62×10^8	8.39×10^9

The results of the uniform mesh refinement study performed by Andrews and Gilkey are shown in Figure 2.21, with self-shielding active (SS=On) and turned off (SS=Off). With self-shielding turned off, Richardson extrapolation cannot be applied, because the solution is not monotonically convergent. This is a major difference from the 3D assembly calculation, where convergence is observed. However, when self-shielding is turned off, monotonic convergence is observed. In this case, the Richardson extrapolation shows an order of convergence of 2.29. This can be compared to the 3D assembly order of converge of 2.75 with self-shielding activated. Another difference is that Walker's results at assembly level converge from above, whereas the current results at pin level converge from below. This suggests that the magnitude of compensating terms in the Richardson expansion differ between the assembly-level analyses and the pin-level analyses.

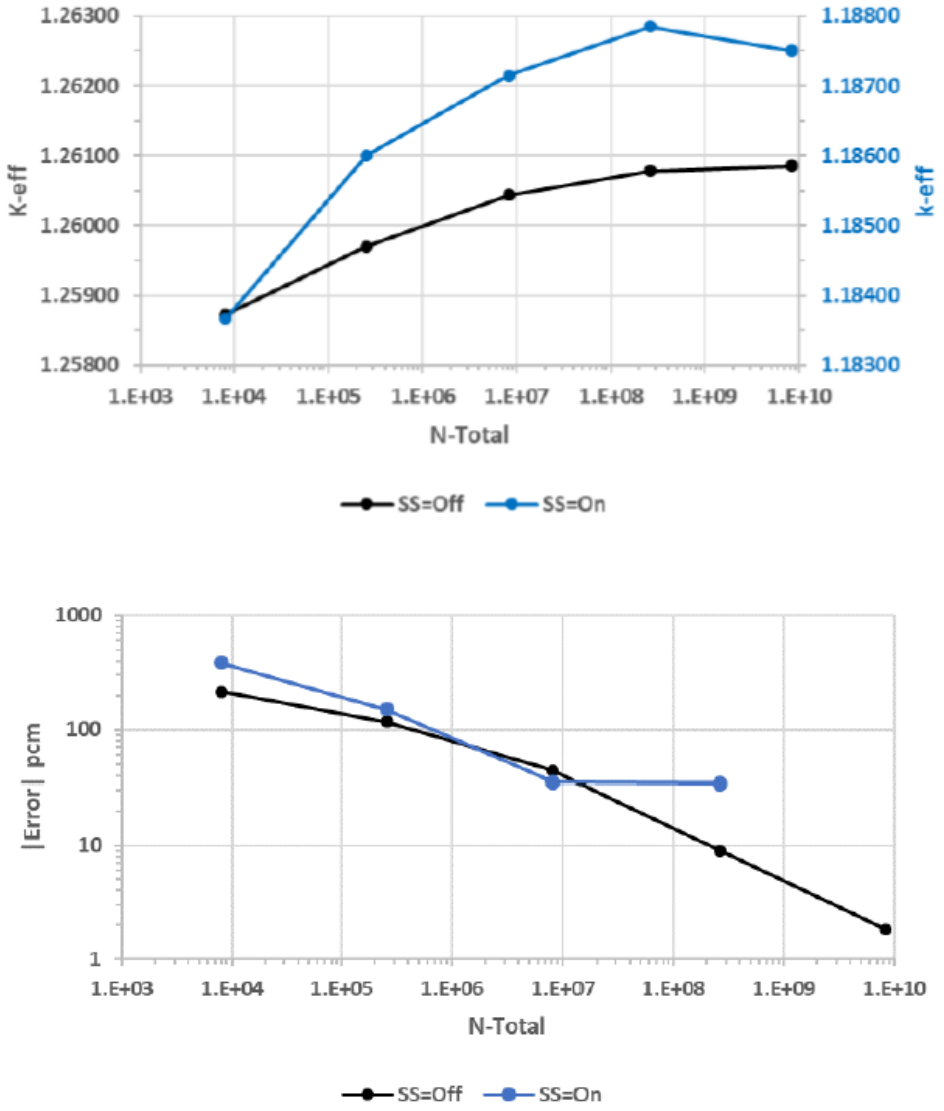

Figure 2.21. Uniform grid refinement 2D pin geometry

The impact of the self-shielding correction is again clearly indicated in Figure 2.22, which shows the re-coarsening analysis of the radial division term in the fuel and moderator. When the self-shielding is turned on, monotonic convergence is not observed. This can especially be seen in the analyses of Wang. When self-shielding is turned off, MPACT is monotonically convergent, with an order of convergence of 1.51. This indicates that the number of radial rings within the fuel has a significant effect on the multiplication constant that is calculated within MPACT. Andrews conducted additional sensitivity studies and clearly demonstrated that the non-monotonicity inserted by self-shielding is confined entirely to the fuel, with no sensitivity in the moderator.

Appendix C provides a summary description of self-shielding. To understand the impact of self-shielding calculation on the convergence behavior, it is noted that generally, a grid refinement study solves the SAME problem, defined by geometry, material, sources, and boundary condition, but only with different grid resolution. However, for each grid refinement, the self-shielding calculation produces an updated set of multi-group cross sections to account for the self-shielding effects. The inclusion of the self-shielding calculation

in MPACT results in a slightly different problem to be solved. In order to reveal the rate of convergence concerning each independent discretization parameter via a consistent grid refinement, results from calculations with self-shielding turned off are included. The results verified that turning self-shielding off gives more monotonic convergence curves.

Self-shielding has attributes analogous to mesh-dependent sub-grid models that sometimes appear in other disciplines (e.g., turbulence modeling). However, there has been a move away from such models in other disciplines because the results are typically calibrated to a specific grid, and the "model" is neither convergent nor predictive when one moves away from the calibrated grid.

The convergence observed during the re-coarsening of the azimuthal division term was significantly better, as shown in Figure 2.23. With self-shielding turned on and off, convergence behavior was observed in the analyses performed. Analysis of the Andrews and Gilkey results shows an order of convergence of 1.26 with self-shielding turned off, and 1.11 with self-shielding turned on. For all cases, the total range in k-eff from the xfine to the coarse grid is less than 10 pcm, indicating that this term is not a major driver of error in results.

The re-coarsening study performed on the ray spacing term is show in Figure 2.24. The coarsest grids resulted in MPACT crashing, because the coarsest ray spacings did not guarantee at least one ray segment in each FSR, which is required by the MOC. Monotonic convergence behavior was observed in all three cases when the ray spacing was reduced to below 0.02 cm. However, non-monotonic behavior was observed as the ray spacing was increased for the coarsest meshes when self-shielding was activated. Because of the numerical errors noted above, it is not known if the smear behavior would be observed with self-shielding deactivated. The error observed in all cases compared to the most refined cases was below 10 pcm, except for some coarse grids in the non-monotonic region. Unfortunately, these coarsest meshes are indicative of the defaults used by MPACT when not user specified. Note that the default ray spacing of 0.05 is not in the convergent region, but it results in a k-eff that is very close to the converged values. However, users should be cautious that refinement to 0.03 might introduce errors up to 40 pcm, where error reduction might have been expected because of refinement.

The azimuthal angle term shows the largest range of results for any of the parameters isolated in this analysis. For the default of 8 angles, the error is approximately 150 pcm, which exceeds the threshold of concern. It is not until 32 or more angles have been used that the error associated with this term decreases to near 10 pcm. For the Andrews and Gilkey cases, The Richardson extrapolation calculates the order of convergence to be 1.94 with self-shielding turned off. Of all the terms isolated, the azimuthal angle term is the most dominant, having the largest impact on the overall convergence of the problem. Monotonic convergence was observed for this term when examining the results provided by Andrews and Gilkey. Wang's results also showed convergence, but with small oscillations of 1 pcm, which are too small for concern and may be an artifact of other sources of numerical errors in the solutions.

The results of the MPACT cases for isolating the azimuthal angle are in Figures 2.25 and 2.26. Figure 2.25 shows the isolation when only an even number of angles is used, and Figure 2.26 shows both odd and even angles. A clear difference in the results can be observed. When an odd number of angles is used, saw-toothed behavior is observed. This was hypothesized to be caused by the direction of characteristic rays aligning with the boundary between meshes, particularly the boundary that runs from the center to the corner of the pin cell. However, further studies using four azimuthal slices per radial division show that this hypothesis is not significant for the saw-tooth behavior. It is believed that the local oscillation has to do with the angle modularization and the change in ways that characteristic rays interact with FSR mesh caused by the change in the number of azimuthal angles used. This needs further study.

The final term isolated was the polar angle; results for this are in Figure 2.27. This analysis showed that with self-shielding turned on, there is monotonic convergence behavior. However, with self-shielding turned off,

convergence behavior is not as straightforward and may only be monotonic for the finest grids. Significantly more error can be associated with this term when self-shielding is active. The fewest number of angles results in an error of over 100 pcm when self-shielding is used.

A summary of the results obtained from the three sets of calculations performed is provided in Table 2.8. Convergence rates can only be quantified when monotonic convergence is observed, which limits this discussion to the case with self-shielding turned off. The order of convergence (p) is the highest for ray spacing and the lowest for the number of azimuthal divisions modeled. Lacking guidance from theory or expectations established through code verification, these convergence rates are reasonable, suggesting that there is no large code implementation or algorithm concern.

Table 2.8. Summary of solution verification in 2D pin geometry

	Convergence study in pin geometry						
	Andrews: SS=Off			**Andrews: SS=On**		**Wang: SS=On**	
	k-extrap	**p**	**Range (pcm)**	**k-extrap**	**Range (pcm)**	**k-extrap**	**Range (pcm)**
Resolved	1.26086			1.18750		1.18727	
Uniform refinement	1.26088	2.29		1.18750			
Radial divisions	1.26087	1.51	30		52		-16
Azimuthal divisions	1.26085	1.26	6		7		6
Ray spacing	1.26086	3.26	-8		-9		-11
Azimuthal angle	1.26089	1.94	-128		-161		-190
Polar angle	1.26086	1.66	-4		-9		-9

The columns labeled “Range” are intended to estimate the error contribution of each term to the total error on a (near) default grid. Range is defined as k-eff on the near default grid minus k-eff on a fully refined grid. There are two differences from the default grid. First, the ray spacing for a default grid is 0.05 cm, whereas the coarsest grid here that did not bomb the code was 0.016 cm. Second, the Yamomoto quadrature with N=2 is the default for polar angles, whereas tradition quadrature was used here.

Note that values for the range can be either positive or negative, depending on whether the term is converging from above or below, respectively. Consequently, there are compensating terms in the Richardson expansion. These compensating terms can be exploited to minimize the total error, but the practitioner is cautioned that a grid optimized in this manner might not be optimal for significantly different models.

The azimuthal angle is the dominant term. Of the five terms isolated, it is the only term with an error range larger than 100 pcm. This suggests that a default of N=8 azimuthal angles/octant should be increased to 16 angles/octant, at least for pin level calculations. That would reduce the error associated with the azimuthal term to about -47 pcm and the total error to about -15 pcm, primarily because of the compensating effect of the radial division term.

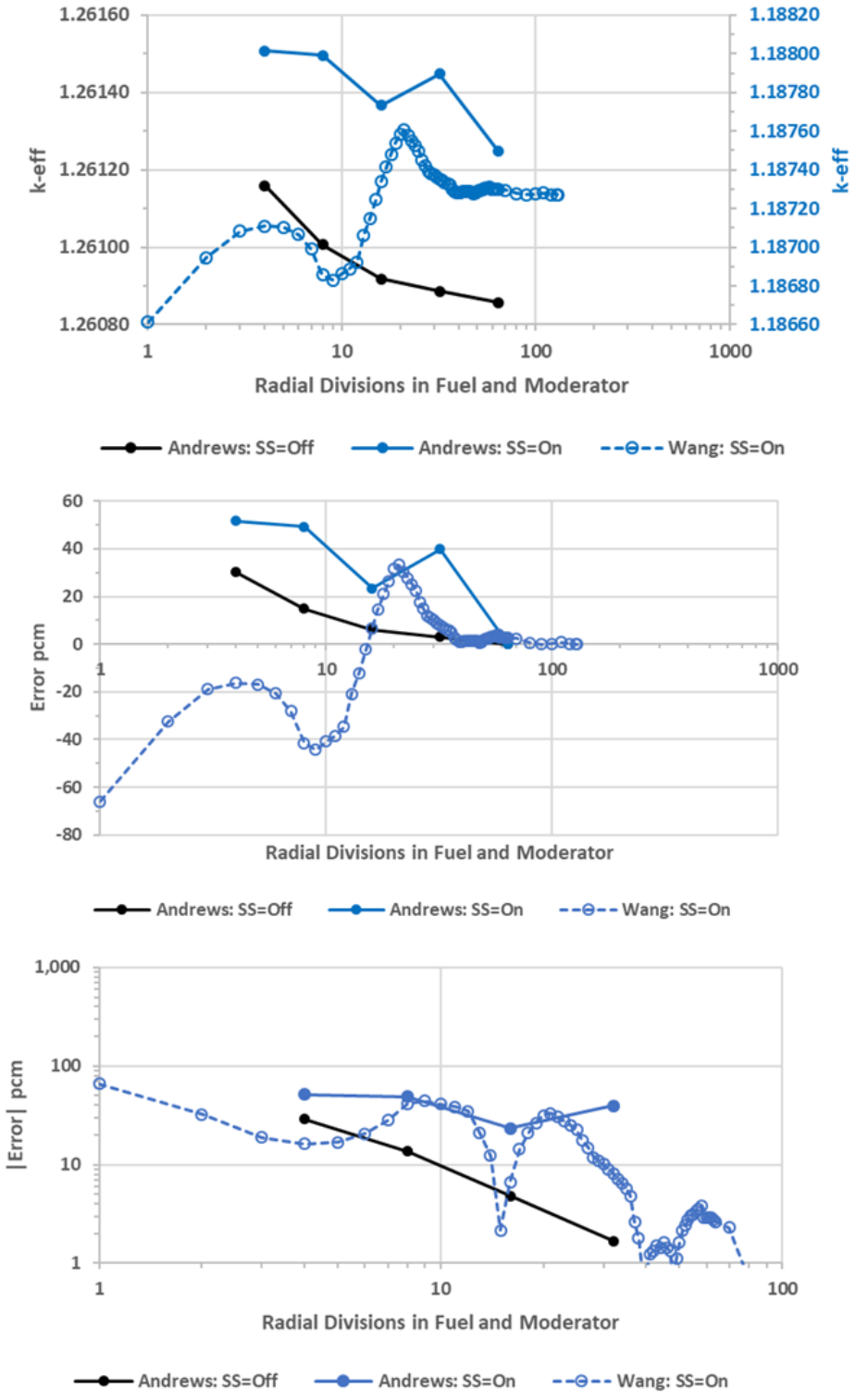

Figure 2.22. Isolation of radial division term in the fuel and moderator, 2D pin geometry.

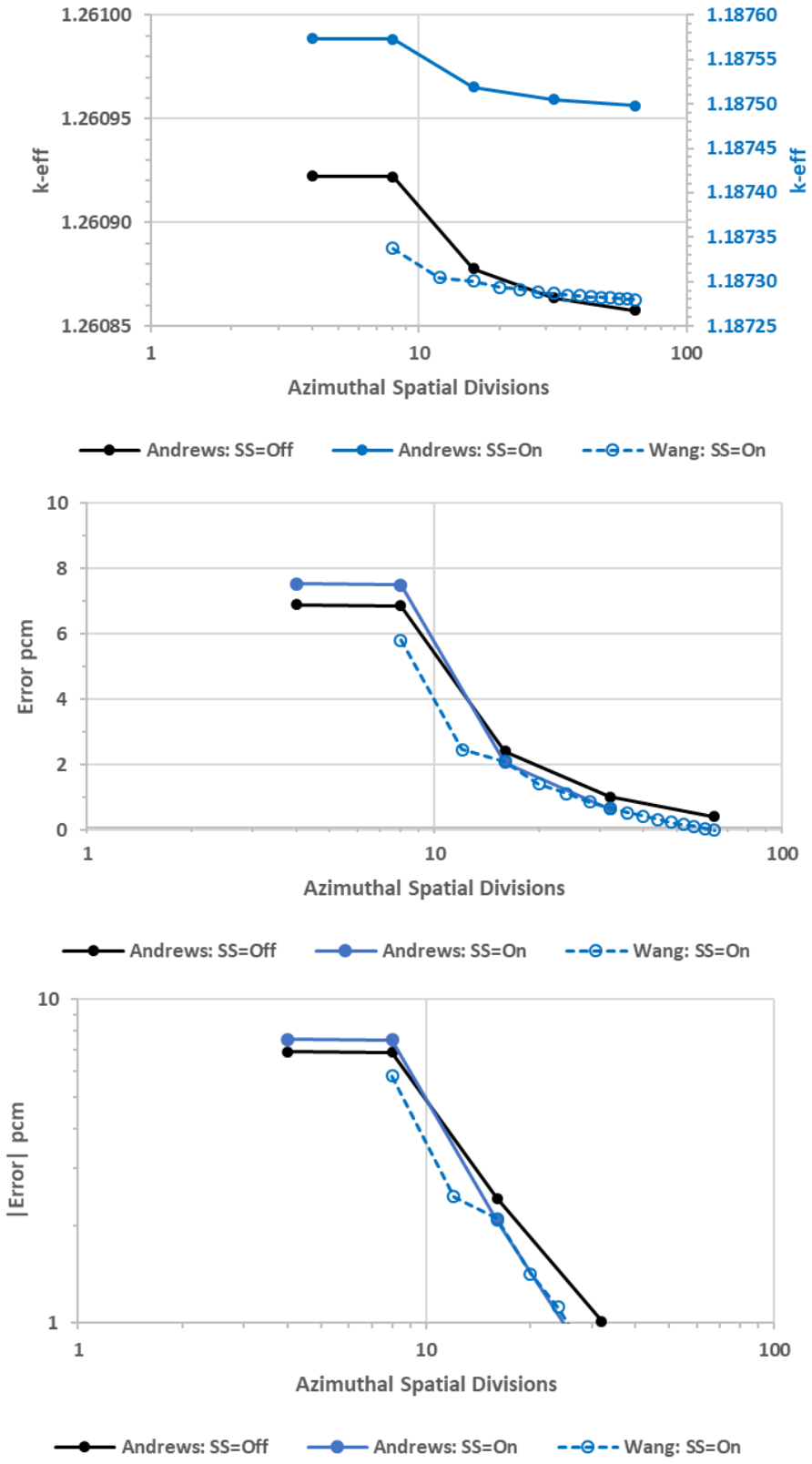

Figure 2.23. Isolation of the azimuthal spatial division term, 2D pin geometry.

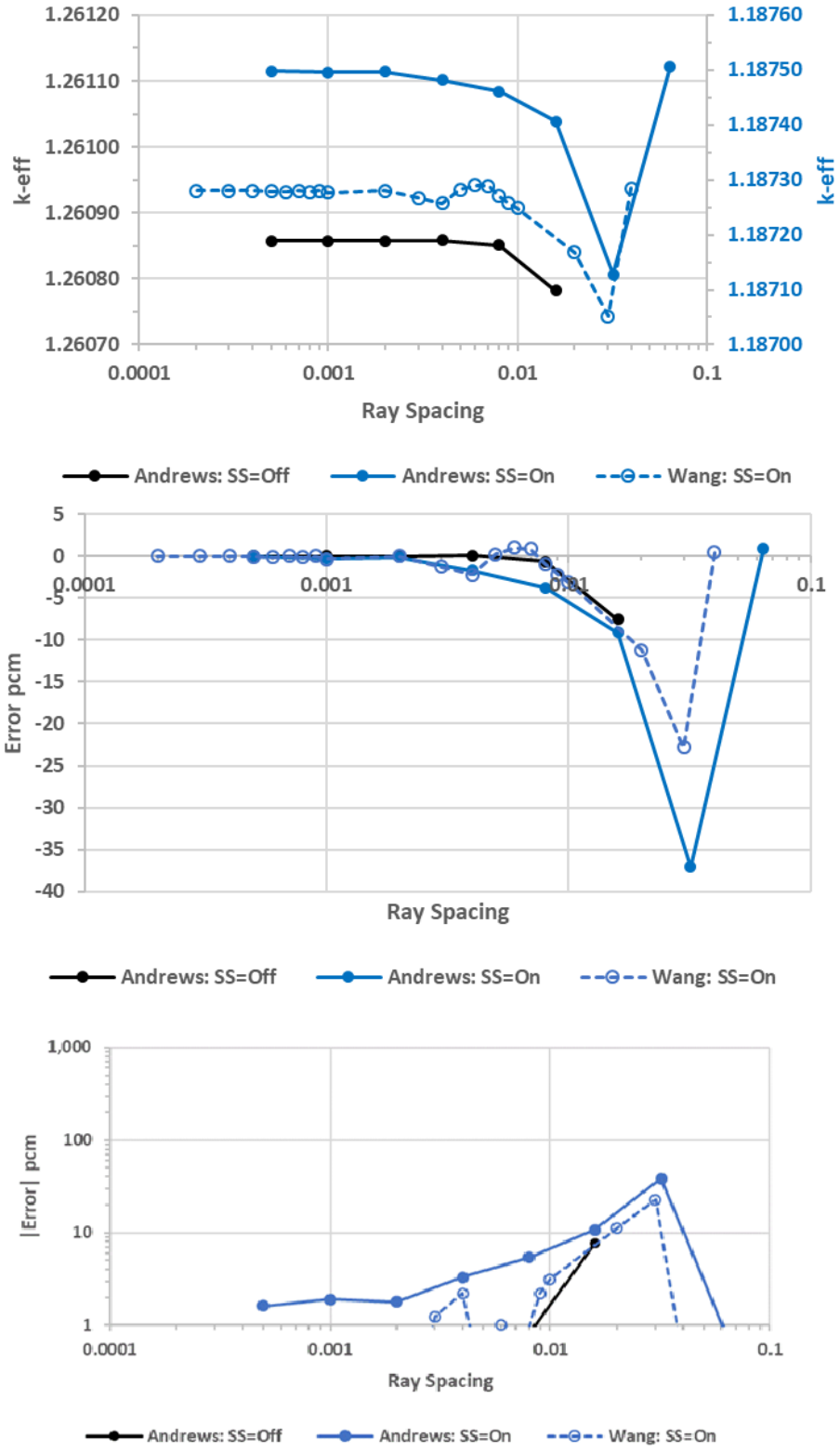

Figure 2.24. Isolation of the ray spacing term, 2D pin geometry.

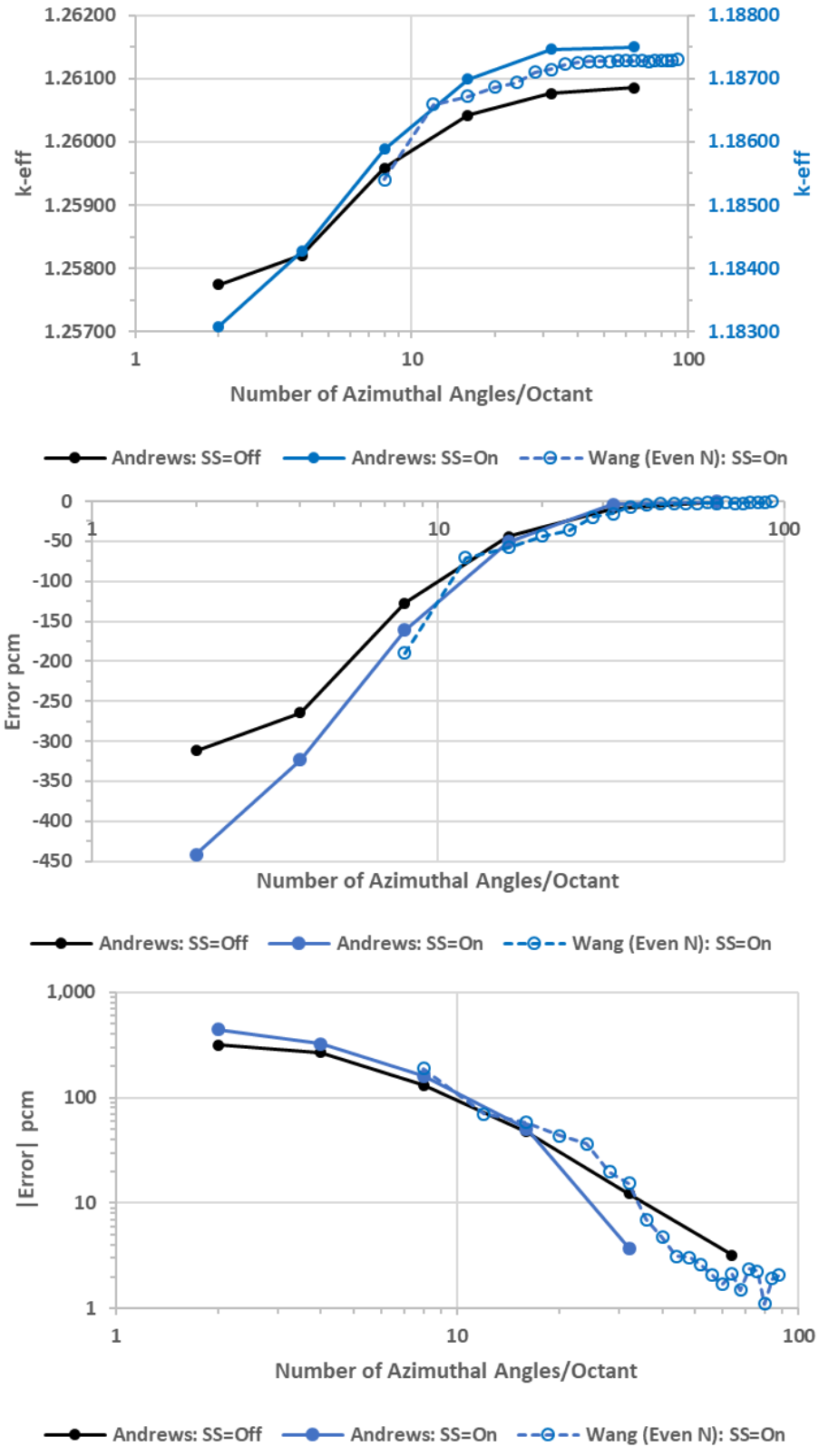

Figure 2.25. Isolation of the azimuthal angle term for even numbers only, 2D pin geometry.

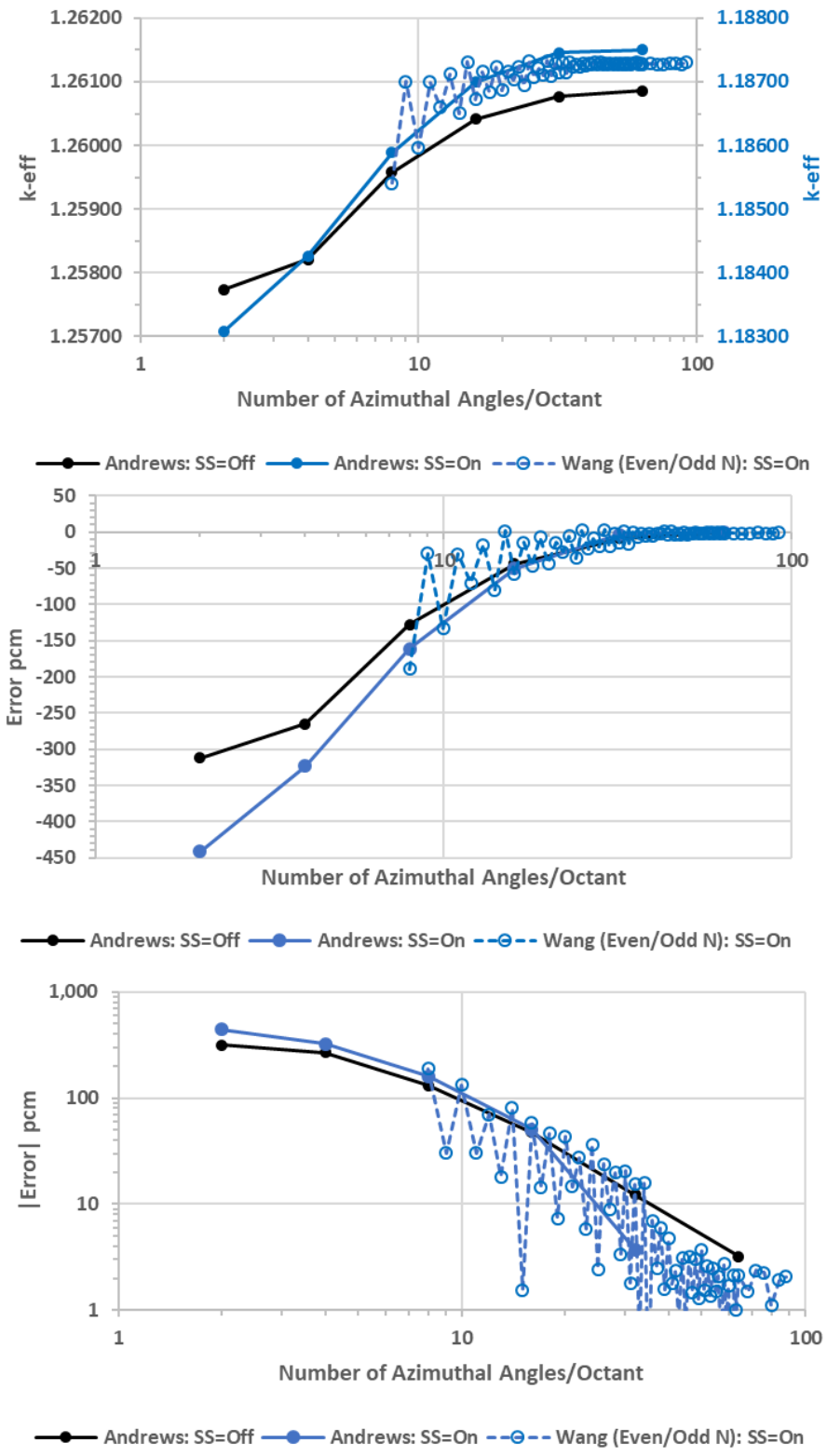

Figure 2.26. Isolation of the azimuthal angle terms for all angles, 2D pin geometry.

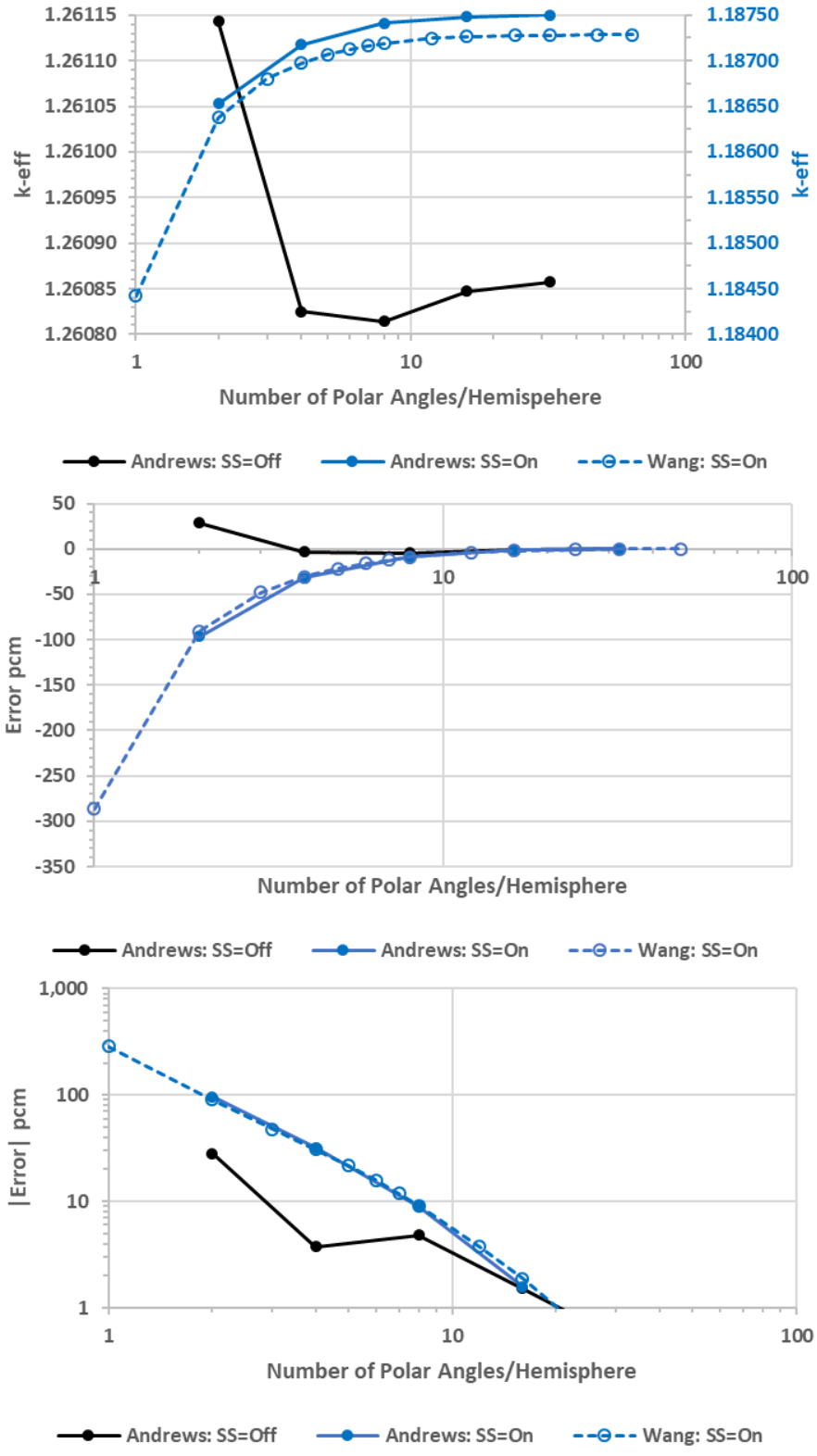

Figure 2.27. Isolation of the polar angle terms, 2D pin geometry.

2.5 SOLUTION VERIFICATION IN 3D ASSEMBLY GEOMETRY

To assess the convergence rates within MPACT, two separate analyses were performed. The first, which is addressed here, is a solution verification exercise of a 3D assembly, which was performed by Walker [17] in a companion milestone. The quantity of interest is the multiplication constant (k-eff). For these analyses, the self-shielding correction algorithm is turned on within the code. A 3D uniform refinement assessment is performed, varying the six terms noted above. Note that the default for the polar angle uses the Yamamoto quadrature, which is considered fully refined for N=3, which is the maximum allowed. Consequently, the polar angle was not refined as part of this study. Five separate refinements are examined, with the medium grid representing the defaults offered by the code. These refinement cases can be seen in Table 2.9, with the total variation in refinement parameters spanning five orders of magnitude.

Table 2.9. Grids for 3D uniform refinement in 3D assembly geometry

Walker	**Uniform refinement in 3D assembly geometry**				
	Number of elements				
	xcoarse	**coarse**	**medium**	**fine**	**xfine**
Reflector	**4**	**16**	**64**	**256**	
Reflector	2×2	4×4	8×8	16×16	
Axial Divisions	**25**	**50**	**100**	**200**	**400**
Axial Division (cm)	16	8	4	2	1
Radial Division	**3**	**6**	**12**	**24**	**48**
Fuel	2	4	8	16	32
Gap	1	1	1	1	1
Clad	1	1	1	1	1
Moderator	1	2	4	8	16
Azimuthal Division	**4**	**8**	**16**	**32**	**64**
Ray Spacing N	6	12	24	48	96
Ray Spacing h	0.1	0.05	0.025	0.0125	0.00625
Polar Angle	**3**	**3**	**3**	**3**	**3**
Azimuthal Angle	**8**	**16**	**32**	**64**	**128**
NTotal	5.76×10^2	9.22×10^3	1.47×10^5	2.36×10^6	3.77×10^7

The results of the uniform grid refinement are shown in Figure 2.28. The extrapolated converged solution, k-extrap, is taken to be 1.17694 by applying the Richardson extrapolation to the three finest grids. The error on any specified grid references k-eff on that grid to the k-extrap. With self-shielding activated (SS=On in the chart), the code is monotonically convergent on the four finest grids. After applying the Richardson extrapolation, the order of convergence was calculated to be 2.75.

Walker's milestone was primarily focused on the sensitivity of k-eff to axial refinement. The scope of Walker's work did not include coarsening of all the six terms individually as recommended by Pilch [18], which is necessary to understand the individual convergence behavior of each term in isolation of the others. The exception was axial refinement, because that was the focus of his milestone. Walker [17] found that the sensitivity of k-eff to axial refinement was so small that convergence behavior could not be distinguished from other sources of numerical error.

If the "exact" solution is estimated from either super-refinement of the grid or from the Richardson extrapolation, then the solution error on any other grid can be obtained by referencing the solution on the new grid

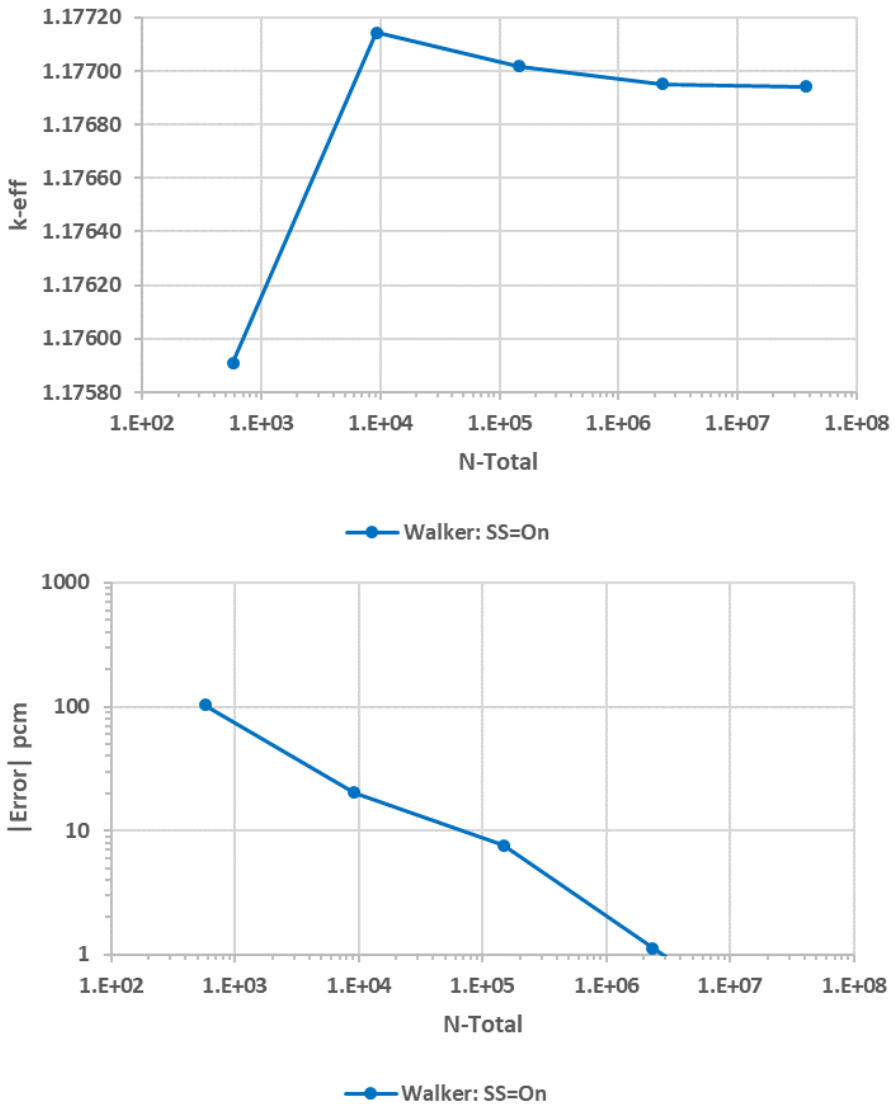

Figure 2.28. Uniform grid refinement in 3D assembly geometry.

to the exact solution. The solution error on the medium refinement grid above is thus 20 pcm, which is less than the accepted threshold of 50 pcm that might trigger concern. This is significant, because the medium grid corresponds closely to code defaults. On the assembly scale, monotonic convergence can be seen, with error decreasing from the medium grid case all the way through the xxfine grid case. This is a significant result because the MPACT software is intended to be used for assembly-size problems or larger.

3. CODE VALIDATION

As discussed in the paper by Oberkampf [19], the process of determining the degree to which a computational model provides an accurate representation of the real world from the perspective of the intended uses of the code is generally referred to as *validation*. This is depicted in the schematic shown in Figure 3.1 which was from the Guide for Verification and Validation of Computational Fluid Dynamics Simulations [3].

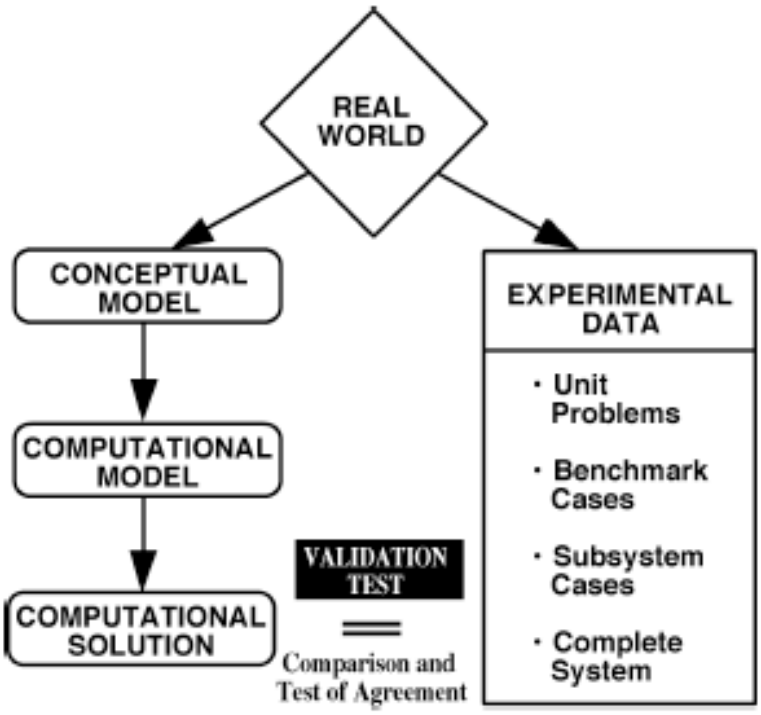

Figure 3.1. Schematic of code validation [3].

The goal of MPACT validation has been to identify those validation tests which will increase confidence in the quantitative predictive capability of the code for practical reactor applications. This section summarizes the roadmap developed for MPACT validation, and subsequent sections review some of the preliminary work performed on each of the validation areas.

3.1 INTRODUCTION

A comprehensive validation plan was developed for VERA-CS [4]; this section briefly summarizes some aspects of the plan that are relevant to MPACT, to include the validation matrix proposed for the VERA-CS reactor neutronics codes. The four principal validation components identified in the plan are shown in Figure 3.2 [4].

As shown in Figure 3.2, MPACT results are assessed using the following four sources of benchmark data:

1. Measured data from experiments with *small critical nuclear reactors*, including critical conditions, fuel rod fission rate distributions, control rod or burnable poison worths, and isothermal temperature coefficients.

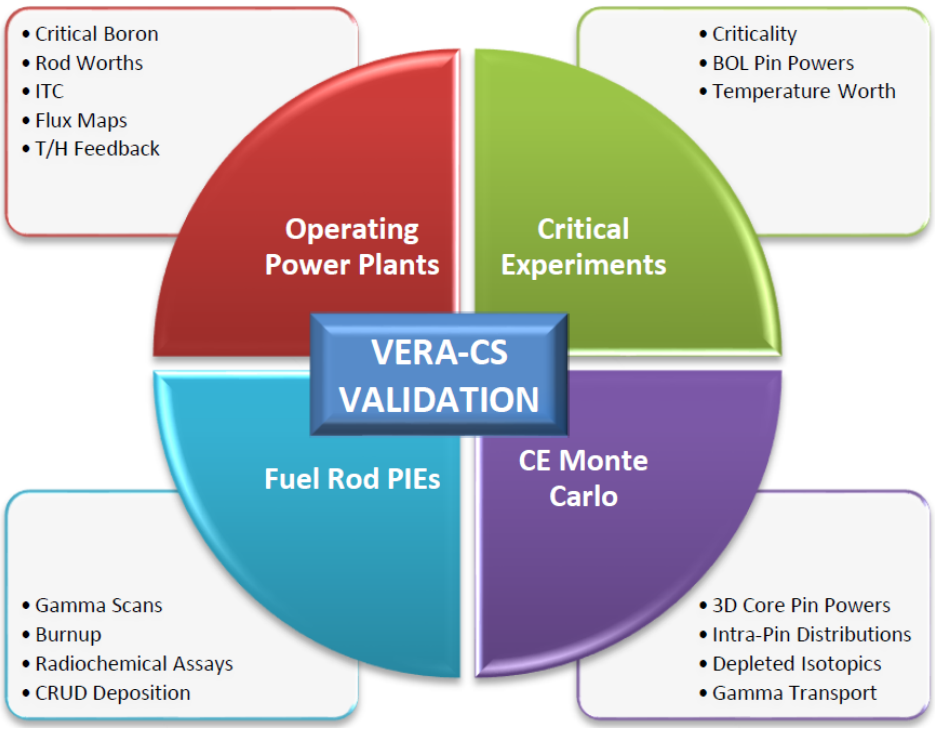

Figure 3.2. Components of VERA-CS validation [4].

2. Measured data from *operating nuclear power plants*, including critical soluble boron concentrations, beginning-of-cycle (BOC) physics parameters such as control rod worths and temperature coefficients, and measured fission rate responses from in-core instrumentation.

3. *Measured isotopics* in fuel after being irradiated in a nuclear power plant, including gamma scans of ^{137}Cs activity, burnup based on ^{148}Nd concentrations, and full radiochemical assays (RCAs) of the major actinides and fission products.

4. Calculated quantities on fine scales from *continuous energy (CE) Monte Carlo methods*, including 3D core pin-by-pin fission rates at operating conditions, intra-pin distributions of fission and capture rates, reactivity and pin power distributions of depleted fuel, and support for other capabilities such as gamma transport and thick radial core support structure effects, for which there are currently no known measurements to benchmark against.

During the past several years, progress has been made in each of these areas. The "neutronics-only" validation cases in item 1 included those which could be simulated with the VERA-CS input, as well as those which required the use of the native MPACT input. Furthermore, to the extent possible, the validation cases performed in item 2 were performed using the integrated core simulator MPACT / COBRA-TF. The comprehensive validation matrix constructed by Godfrey based on these four general areas is shown in Figure 3.3, which compares the required capabilities, features, and application range of VERA-CS neutronics codes to the proposed benchmarking activities. The purpose of this matrix was to provide guidance in prioritizing validation activities to ensure that sufficient effort is performed across the full range of capabilities and features required of a core simulator such as MPACT. In Figure 3.3, the capabilities desired for coverage are listed on the left, and the validation activities, described in the following sections are shown across the top. Coverage is indicated by an *X* in the corresponding row and column positions. The optional activities (mostly critical experiments) are shaded. In general, the priorities for the activities for each component are

decreasing from left to right, so the cases on the left side of each section should be performed first. Ideally, all capabilities should be covered by at least one activity; however, because of budget and time constraints, only selected activities listed in the matrix have been performed.

During the past several years, selected activities from the validation matrix have been included as part of the normal code development tasks in both the Physics Integration (PI) and Radiation Transport Methods (RTM) focus areas of the Consortium for Advanced Simulation of Light-Water Reactors (CASL). In FY16, the core follow results were included in the MPACT V&V manual, even though the calculations were performed with VERA-CS multiphysics involving neutronics, thermal-hydraulics, and fuel temperature modeling. In FY17, a plan was formulated to develop a VERA-CS Verification and Validation manual [20] to include the core follow results. Therefore, the validation results in versions 4–5 of the MPACT manual included only single physics validation data, which include primarily the critical experiments and Cycle 1 start-up testing. However, primarily because of the proprietary nature of most of the core follow data, the decision was made to resume including the publicly available coupled core follow results in the MPACT manual. This will be done beginning with Version 6 of the MPACT manual, which will be completed in the future. However, for current version 5, the core follow results are included as an Appendix.

	Validation activities																																	
	Operating power plants								Critical experiments																		Post-irradiation Exams					CE Monte Carlo			
Capabilities	Watts Bar	BEAVRS	Catawba	McGuire	Westinghouse 3-Loop	Krsko	B&W Type	CE Type	BW	Helstrand	KRITZ	DIMPLE	BENUS	IPEN/MB-01	RPI	SPERT III											Catawba MOC LTAs	Three Mile Island	MALIBU	Robinson	Calvert Cliffs	Pin-by-pin fission rates	Intra-pin distributions	Depleted isotopics	Misc. applications
PWR types																																		
Westinghouse 4-Loop	X	X	X	X																							X					X			
Westinghouse 3-Loop					X								X																X					
Westinghouse 2-Loop						X																										X			
Babcock & Wilcox (B&W)							X																					X							
Combustion Engineering (CE)								X							X															X					
Fuel assembly types																																			
17×17	X	X	X	X	X				X										X								X					X	X	X	
16×16						X																										X			
16×16 CE								X	X						X																				
15×15					X																								X	X					
15×15 B&W							X		X																			X							
14×14 CE								X							X																X				
Mixed Oxide Fuel (MOX)			X								X		X					X	X	X						X		X						
Burnable poison types																																			
Pyrex	X	X	X	X	X	X			X											X												X			
IFBA	X		X	X	X	X																					X					X			
WABA	X		X	X	X																						X					X			
Solid B_4C-AL_2O_3							X	X																			X	X			X				
Gadolinia							X		X				X							X	X		X				X	X							
Erbia								X							X																				
Control rod types																																			
AIC	X	X	X	X	X	X	X		X					X					X		X	X					X					X			
B_4C	X		X					X	X					X							X	X	X												
Hybrid	X		X																								X					X			
Gray							X															X						X				X			
Hafnium					X																														
Incore Instrument types																																			
Movable	X	X	X	X	X	X																					X					X			
Fixed	X						X	X	X																			X							
Radial Reflector types																																			
Thin baffle	X	X	X	X	X	X	X	X				X	X														X	X				X			
Thick (heavy) shroud																																			X
Physics components																																			
Neutron transport	X	X	X	X	X	X	X	X	X	X	X	X	X	X	X	X	X	X	X	X	X	X	X	X	X	X	X	X	X	X	X	X	X	X	X
Gamma transport																																			X
Coolant density feedback	X	X	X	X	X	X	X	X			X								X				X				X	X	X	X	X	X			
Fuel temperature feedback	X	X	X	X	X	X	X	X			X								X				X				X	X	X	X	X	X	X		
Isotopic depletion	X	X	X	X	X	X	X	X																			X	X	X	X	X		X	X	
Xenon concentration	X	X	X	X	X	X	X	X																										X	
Shutdown decay	X	X	X	X	X	X	X	X																			X	X	X	X	X				
Physics Results																																			
Reactivity	X	X	X	X	X	X	X	X	X		X	X	X	X	X	X	X	X	X	X	X	X	X	X	X	X	X					X	X	X	
Assembly power distribution	X	X	X	X	X	X	X	X																			X					X			
Pin power distribution									X		X	X	X	X	X				X	X	X	X										X	X	X	
Intra-pin power distribution																																	X		
Pin burnup distribution																											X	X	X	X	X		X		
Intra-pin burnup distribution																															X		X		
Incore instrumentation response	X	X	X	X	X	X	X	X	X				X							X							X	X							
Excore instrumentation response			X	X								X	X																						X
Control rod worth	X	X	X	X	X	X	X	X	X					X					X		X	X	X				X					X			
Temperature coefficient	X	X	X	X	X	X	X	X			X			X						X				X			X								

Figure 3.3. VERA-CS Validation Assessment Matrix [4].

3.2 VALIDATION TEST ACCEPTANCE CRITERIA

The acceptance criteria for MPACT for the validation benchmark problems were established based on an extensive review of the literature [21], as well as the opinion of stakeholders within and outside of CASL.

The following validation test acceptance criteria were adopted:

1. Single physics analysis test acceptance criteria were adopted:
   - k-eff: ±500 pcm
   - pin power RMS: < 2.0%
2. Reactor hot zero power conditions:
   - k-eff: ±300 pcm
   - 7.5% for rod bank worths
3. Core follow and depletion at hot full power conditions:
   - ±50 ppm boron (US NRC Standard)

A summary of the current performance of MPACT for several of the critical experiments and for Watts Bar units I and II is shown below, and as indicated, the MPACT results satisfy the acceptance criteria. The detailed results can be found in the following sections of this chapter.

3.3 CRITICAL EXPERIMENTS

Table 3.1. Summary of MPACT criticals

Critical	Max k-eff (pcm)	Pin RMS (%)	Max Bank Worth (%)	MPACT Version	Cross Section Library
B&W Core 1484	212	1.24	–	2.1.0 (SHA1:55125e2)	v4.2m5
B&W Core 1810	131	1.09	–	2.1.0 (SHA1:55125e2)	v4.2m5
DIMPLE	200	1.15	–	2.1.0 (SHA1: 6ba80c2)	v4.2m5
VENUS 2D	10	1.06	–	2.1.0 (SHA1:28322b7)	v4.3m2
VENUS 3D	216	1.09	–	2.1.0 (SHA1:28322b7)	v4.3m2
WB I Startup	121 pcm 11.8 ppm	–	5.8	–	v4.0
WB II Startup	21 pcm 2 ppm	–	3.0	–	v4.2m5

Critical experiments are small nuclear reactors typically designed to provide validation data for nuclear methods and software, particularly for materials and geometries similar to those found in operating nuclear power plants. These experiments are usually performed without power at isothermal conditions and without fuel depletion. During the past several years, work was performed on the B&W, DIMPLE, and VENUS critical experiments, which are among the most widely analyzed critical experiments in the light-water reactor (LWR) industry. Additionally, as part of work being performed in the development of transient methods in MPACT, work was performed on the critical condition of the Special Power Excursion Reactor Test (SPERT) reactor. New additions to the validation base of MPACT are the IPEN experiments, which provide the first validation of the "pin-resolved" capability of the code. The following section summarizes the work performed on these tests.

3.3.1 Babcock & Wilcox Critical Experiments

The B&W critical experiments most relevant to MPACT validation are the 1484 series fuel storage experiments and the 1810 series of beginning of life (BOL) reactor experiments. Initial results have been prepared on both experiments with MPACT and are reported in CASL-U-2015-0143-000 [22]. More recently, the 1484 and 1810 series experiments were recalculated with some changes to the model and an updated cross section library.

[23].

3.3.1.1 1484 – Fuel Storage Experiments

The Babcock & Wilcox 1484 critical experiments were designed to provide criticality data to support the long-term storage of LWR fuel in spent fuel pools. A total of 20 critical configurations were constructed to provide measured benchmark data for validation of nuclear codes. The report for the experiments, funded by what is now the US Department of Energy (DOE), was released in 1979 [24].

The 20 critical configurations were built in a core tank with low enriched (2.46%) UO_2 fuel rods and water as the neutron moderator. The rods were clustered into nine LWR-like assemblies in a 3×3 configuration, with variable spacing in between the assemblies, as shown in Figure 3.4. In some configurations, stainless steel or borated aluminum sheets are placed between the assemblies to simulate a spent fuel storage configuration. Therefore, only a subset of the experiments is consistent with power plant geometries for validation.

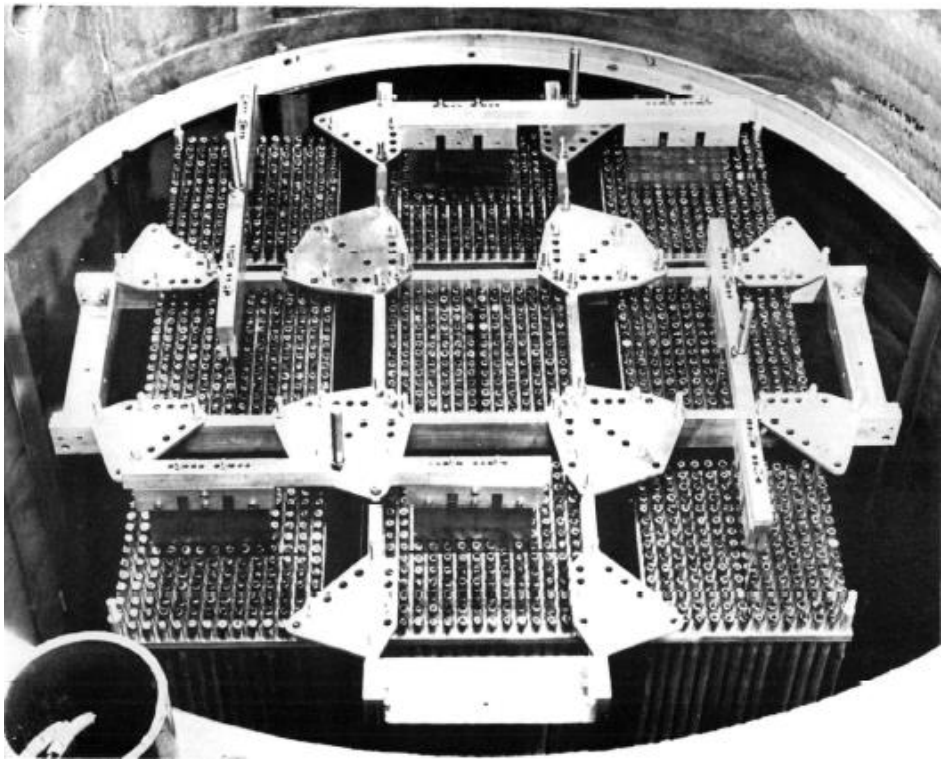

Figure 3.4. B&W Critical Experiment Facility.

The B&W-1484 experiment consisted of 21 critical configurations (listed here as 4:1–4:21) that simulated a variety of close-packed LWR fuel storage configurations. Criticality measurements were performed, and a series of Monte Carlo criticality calculations were also performed at the same time to create an analytical basis for comparison with the experimental data. Core 4:1 is a reference "core" containing 438 fuel rods

arranged in a roughly cylindrical configuration. All of the remaining cores consist of nine 17×17 fuel pin assemblies grouped into a 3×3 array spaced from 0 to 4 pin pitches apart. Based on the results from this set of experiments, cores 4:1 and 4.2 were determined to be the most appropriate for the initial phase of MPACT validation, and the results are summarized here. Most of the other cases represent configurations that are not appropriate for assessment of a core simulator, but rather are appropriate for assessing spent fuel pool calculation codes. However, Core 4:3 is also currently being analyzed and will be included in a future update to this document.

All calculations were performed with MPACT using the 2D MOC with an axial buckling to represent the axial leakage. In addition to MPACT, the 3D generalized geometry Monte Carlo computer code KENO was used to rerun the cases prepared as part of the original benchmarking effort for cores 4:1 and 4:2. The details of the MPACT and KENO models are provided in CASL-U-2015-0143-000 [22].

3.3.1.2 B&W Core 1484 Geometry/Materials

The geometry and material distribution plan views of cores 4:1 and 4:2 are shown in the top and bottom of Figure 3.5, respectively. In these figures, the fuel is shown in red, the cladding is green, and the moderator is blue. Taking advantage of geometric symmetry, core 4:1 is a half-core reflective model, and core 4:2 is a quarter-core reflective model.

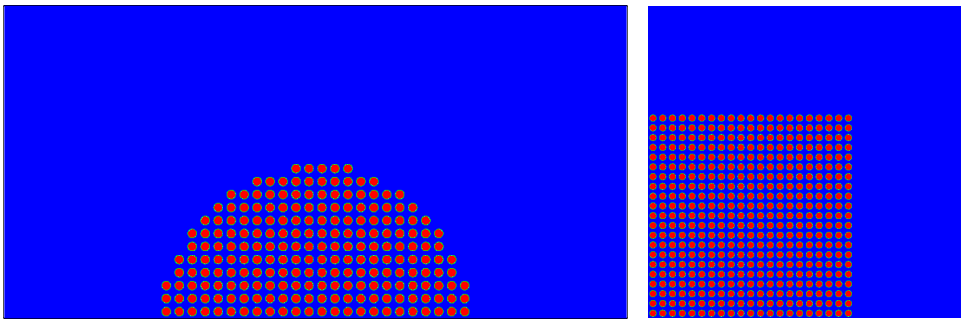

Figure 3.5. B&W-1484 core 4:1 (left) and core 4:2 (right).

3.3.1.3 MPACT Model

All MPACT results reported below [23] were obtained with MPACT version 2.1.0 built with the source on July 14, 2017 (rev: 60, SHA1: 55125e2). This source is a release candidate for the MPACT 3.7 release. Results are shown using the current 51-group ENDF/B-VII.1 cross section library recommended for MPACT (mpact51g 71 v4.2m5 12062016 sph.fmt). Results are also shown for an older 47-group library that is no longer used in production. The 47-group results are only included to show improvements in the library development process. The 47-group library version is mpact47g 70s v4.1m3 03192015.fmt. MPACT uses the subgroup method to calculate the resonance parameters, and unless otherwise stated, all cross sections are P0 transport corrected (TCP0). Results are also shown for P2 scattering, but this option is not the default in MPACT. Table 3.2 shows the mesh parameters used in this study, as well as typical parameters used for core calculations. In general, the smaller critical cores have higher neutron leakage and are more sensitive to the mesh parameters than standard sized cores.

Table 3.2. MPACT mesh parameters for B&W 1484

MPACT mesh parameters	Typical value Value	Small criticals Criticals
Ray spacing	0.05	0.01
Polars octant	2	3
Azimuthals octant	16	32
Number of FSR radial rings in fuel	3	10
Number of FSR azimuthal sections	8	16

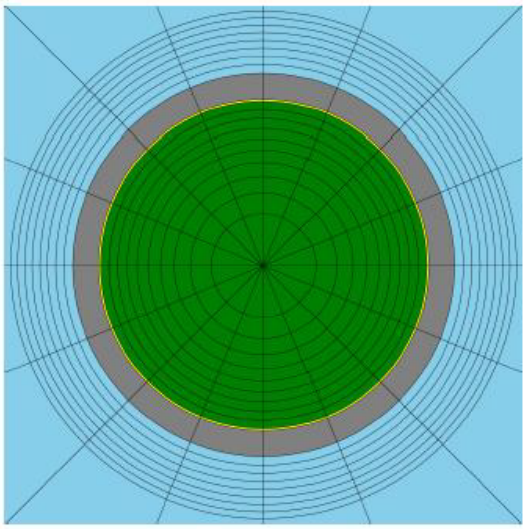

Figure 3.6. B&W 1484 pin cell mesh

3.3.1.4 Results: Core 1484

The MPACT results of the 1484 cores are shown in Table 3.3. From these results, it can be observed that the MPACT results with the most recent 51-group library are improved over the older 47-group library.

3.3.1.5 B&W-1810 Critical Experiments

The B&W 1810 series of critical experiments was developed by B&W, Duke Power, and DOE to provide beginning-of-life (BOL) benchmark data to support the development of an advanced pressurized water reactor (PWR) fuel assembly for extended fuel burnup [25]. Twenty-three core configurations were constructed, and the following measurements were taken:

a. Reactivity worths of gadolinia, control, and void rods

b. Core radial power distribution

c. Radial power profiles within a UO_2 pellet containing gadolinia

d. ^{238}U resonance integrals for solid and annual fuel pellets

e. Rhodium in-core detector signals

The experiments were performed at the B&W Lynchburg Research Center using UO_2 fuel rods with 2.46% and 4.02% ^{235}U enrichment. Both solid and annular rods containing 4.0% gadolinia were included in some

Table 3.3. MPACT results for B&W 1484

	NORUP	NORUP	RUP	RUP
	47g	51g NRUP	51g	51g P2
1	-270	-131	-212	-53
2	-420	-97	-182	-6
3a	-343	35	-36	160
3b	-310	67	-4	192
3c	-359	18	-53	143
3d	-374	1	-70	125
3e	-385	-11	-83	113
3f	-388	-17	-89	106
3g	-433	-66	-138	57

of the arrangements, and Ag-In-Cd (AIC) and B_4C control rods were also used. The rods were arranged inside a large core tank with variable moderator height. In some cases, multiple fuel rods were removed to simulate the large water rods similar to those in the Combustion Engineering (CE) lattice design. A core configuration is shown in Figure 3.7.

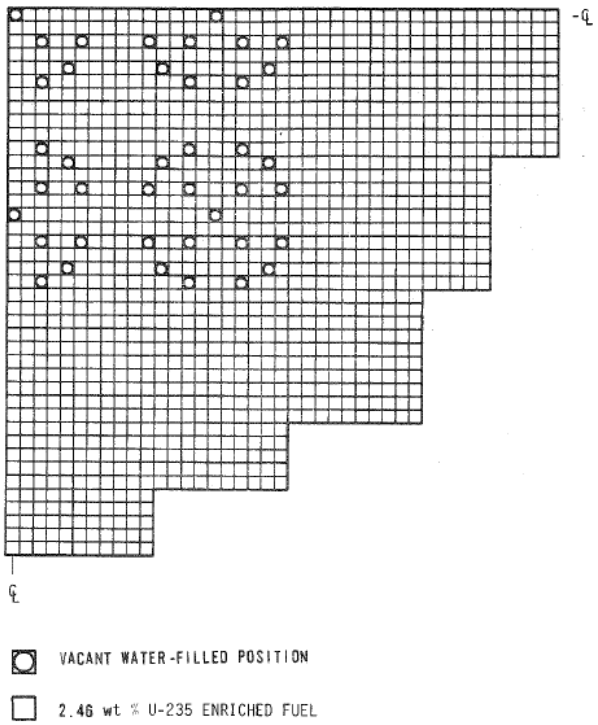

Figure 3.7. B&W-1810 Core 8:1 layout.

Table 3.4 shows a summary of 19 different core configurations assessed in CASL-U-2015-0143-0000 [22], all of which have varying layouts of fuel and burnable absorber rods. Additionally, select cases also have control rods inserted. There are two types of control rods: Ag-In-Cd, also commonly referred to as AIC, and B_4C. There was a variety of materials used in these cases, including three different fuel compositions, two burnable absorber materials, and a handful of different metals for fuel rod cladding and detector mod-

eling. The detailed VERA input for each of these cases is provided in the CASL report. Lastly, the boron concentration of the coolant was adjusted in the experiment until a critical configuration was obtained. All of these cases were simulated in 2D with a prescribed axial buckling value of $4.1 \times 10 - 4$ cm^2 to account for the 3D effect. All cases were run using the same 47-group ORNL library that was used in the 1484 cases.

Table 3.4. B&W-1810 benchmark configuration summary

Core	Short description	2.46% pins	4.02% pins	Gd pins	B_4C pins	AIC pins	Water holes	Boron (ppm)
1	**0 Gd**	4808	0	0	0	0	153	1337.9
2	**0 Gd, AIC rods**	4808	0	0	0	16	137	1250.0
3	**20 Gd**	4788	0	20	0	0	153	1329.3
4	**20 Gd, AIC rods**	4788	0	20	0	16	137	1171.7
5	**28 Gd**	4780	0	28	0	0	153	1208.0
5A	**32 Gd**	4776	0	28	0	0	153	1191.3
5B	**28 Gd**	4780	0	32	0	0	153	1207.1
6	**28 Gd, AIC rods**	4780	0	28	0	16	137	1135.6
6A	**32 Gd, AIC rods**	4776	0	32	0	16	137	1135.6
7	**28 Gd (annular)**	4780	0	28 (ann.)	0	0	153	1208.8
8	**36 Gd**	4772	0	36	0	0	153	1170.7
9	**36 Gd, AIC rods**	4772	0	36	0	16	137	1130.5
10	**36 Gd, void rods**	4772	0	36	0	0	137	1177.1
12	**0 Gd**	3920	0	0	0	0	153	1899.3
13	**0 Gd, B_4C rods**	3920	888	0	16	0	137	1635.4
14	**28 Gd**	3920	888	28	0	0	153	1653.8
15	**28 Gd, B_4C rods**	3920	860	28	16	0	137	1479.7
16	**36 Gd**	3920	852	36	0	0	153	1579.4
17	**36 Gd, B_4C rods**	3920	852	36	16	0	137	1432.1

The MPACT results for the B&W 1810 cores are shown in Table 3.5. The CASMO-5 results use an ENDF/B-VII.0 library with 95 energy groups and TCP0. As with the previous 1484 results, the MPACT results with the latest 51-group library are much improved compared to those from the older 47-group library.

The B&W 1810 experimental results include measured pin powers for every pin in the central assembly of cores 1, 5, 12, 14, 18, and 20. A summary of the pin power results for these cores is shown in Figure 3.8, and the results are summarized and compared to CASMO in Table 3.6. As indicated, there is consistency in the RMS accuracy achieved with CASMO.

In this study, a set of critical experiments was modeled with MPACT. The results agree well with other industry results and provide important validation of the MPACT cross section library and transport solutions.

Table 3.5. B&W-1810 benchmark results

Core	CASMO	47g	51g NOR	51g RUP	51g P2
1	83	-358	39	-38	130
2	27	-340	39	-39	116
3	47	-378	-7	-85	66
4	106	-265	94	15	161
5	18	-402	-41	-119	26
05A	8	-410	-53	-131	13
05B	25	-397	-35	-113	33
6	37	-340	13	-66	78
06A	31	-342	7	-72	69
7	19	-399	-38	-116	30
8	28	-385	-34	-112	31
9	15	-363	-16	-95	47
10	10	-404	-53	-131	10
12	114	-313	51	-27	177
13	156	-273	81	3	152
14	84	-325	12	-65	103
15	140	-276	59	-19	118
16	81	-322	8	-69	92
17	98	-312	19	-59	77
18	268	-170	182	104	295
19	235	-188	149	72	243
20	214	-198	128	51	208
Avg	84	-326	27	-50	103
Std dev	77	72	66	66	77
Min	8	-410	-53	-131	10
Max	268	-170	182	104	295

Table 3.6. B&W 1810 pin power RMS summary

Core	MPACT (%)	CASMO (%)
1	0.48	0.51
5	0.49	0.57
12	0.69	0.69
14	0.80	0.79
18	0.87	0.86
20	1.00	N/A

Core 1

	0	1	2	3	4	5	6	7
0		0.49	-0.40	0.44	0.60	-0.84	-0.16	-0.22
1	0.49	0.49	-0.30	0.62	0.58	-0.97	-1.32	0.25
2	-0.40	-0.30		0.33	-0.36		0.45	0.20
3	0.44	0.62	0.33	0.94	-0.07	-0.25	0.27	0.09
4	0.60	0.58	-0.36	-0.07		-0.31	-0.01	0.04
5	-0.84	-0.97		-0.25	-0.31	-0.34	0.42	-0.01
6	-0.16	-1.32	0.45	0.27	-0.01	0.42	-0.03	-0.15
7	-0.22	0.25	0.20	0.09	0.04	-0.01	-0.15	0.00

Average	0.00
Stdev	0.48
Min	-1.32
Max	0.94

Core 5

	0	1	2	3	4	5	6	7
0		0.30	0.37	0.65	0.20	1.32	1.01	1.16
1	0.30	0.97	0.32	-0.57	0.31	-0.44	0.41	0.03
2	0.37	0.32		-0.19	-0.35		-0.42	-0.23
3	0.65	-0.57	-0.19	-0.06	-0.23	0.42	0.54	-0.13
4	0.20	0.31	-0.35	-0.23		-1.16	-0.16	-0.35
5	1.32	-0.44		0.42	-1.16	0.15	-0.26	-0.29
6	1.01	0.41	-0.42	0.54	-0.16	-0.26	-0.16	-0.13
7	1.16	0.03	-0.23	-0.13	-0.35	-0.29	-0.13	-0.12

Average	0.00
Stdev	0.50
Min	-1.16
Max	1.32

Core 12

	0	1	2	3	4	5	6	7
0		0.41	-0.33	0.57	-2.01	-0.78	-0.43	-0.38
1	0.41	0.31	-0.79	0.09	-0.14	-0.13	-0.42	-0.39
2	-0.33	-0.79		1.28	0.16		1.33	-1.41
3	0.57	0.09	1.28	0.54	-0.01	0.56	0.18	0.56
4	-2.01	-0.14	0.16	-0.01		-0.45	0.18	0.07
5	-0.78	-0.13		0.56	-0.45	1.06	0.91	-0.62
6	-0.43	-0.42	1.33	0.18	0.18	0.91	-0.24	0.12
7	-0.38	-0.39	-1.41	0.56	0.07	-0.62	0.12	-0.89

Average	0.00
Stdev	0.70
Min	-2.01
Max	1.33

Core 14

	0	1	2	3	4	5	6	7
0		-0.52	-0.26	-0.43	0.03	-0.63	0.63	0.03
1	-0.52	-0.29	-1.13	-0.21	-0.52	-1.35	-1.57	0.51
2	-0.26	-1.13		0.75	0.49		0.73	0.11
3	-0.43	-0.21	0.75	-0.44	0.78	2.01	1.06	0.99
4	0.03	-0.52	0.49	0.78		-0.16	-0.42	-0.17
5	-0.63	-1.35		2.01	-0.16	-0.41	-0.33	0.43
6	0.63	-1.57	0.73	1.06	-0.42	-0.33	-0.43	-0.71
7	0.03	0.51	0.11	0.99	-0.17	0.43	-0.71	0.17

Average	0.00
Stdev	0.79
Min	-1.57
Max	2.01

Core 18

	1	2	3	4	5	6	7	8
1		3.55	0.81	0.27	0.46	0.33	0.00	0.87
2	3.55	1.72	1.34	1.70	0.38	-0.45	-0.17	0.46
3	0.81	1.34	1.56	-1.56	-0.41	-0.43	-0.27	-1.34
4	0.27	1.70	-1.56			-0.84	-0.68	-1.38
5	0.46	0.38	-0.41			-0.77	-1.42	-1.00
6	0.33	-0.45	-0.43	-0.84	-0.77	0.89	-0.39	-0.51
7	0.00	-0.17	-0.27	-0.68	-1.42	-0.39	-0.59	-0.58
8	0.87	0.46	-1.34	-1.38	-1.00	-0.51	-0.58	0.53

Average	0.00
Stdev	1.09
Min	-1.56
Max	3.55

Core 20

	1	2	3	4	5	6	7	8
1		3.88	0.79	-0.34	0.51	-0.80	0.34	0.80
2	3.88	1.59	0.65	0.42	0.08	-0.50	-0.69	1.44
3	0.79	0.65	-0.53	-1.27	0.78	-1.36	-0.48	-0.31
4	-0.34	0.42	-1.27			-2.62	2.37	-1.05
5	0.51	0.08	0.78			-1.04	-0.79	-0.14
6	-0.80	-0.50	-1.36	-2.62	-1.04	0.32	-0.51	-1.35
7	0.34	-0.69	-0.48	2.37	-0.79	-0.51	-0.46	0.86
8	0.80	1.44	-0.31	-1.05	-0.14	-1.35	0.86	-0.28

Average	0.00
Stdev	1.24
Min	-2.62
Max	3.88

Figure 3.8. B&W-1810 results: pin power distributions.

3.3.2 DIMPLE Experiments

The DIMPLE experimental program considered critical experiments with low enriched uranium dioxide fuel rods containing 3.0 wt.% ^{235}U with light water moderation and reflection. These experiments were performed in the DIMPLE low power reactor at U.K.A.E.A's Winfrith site in 1983. A general view of the DIMPLE reactor is shown in Figure 3.9.

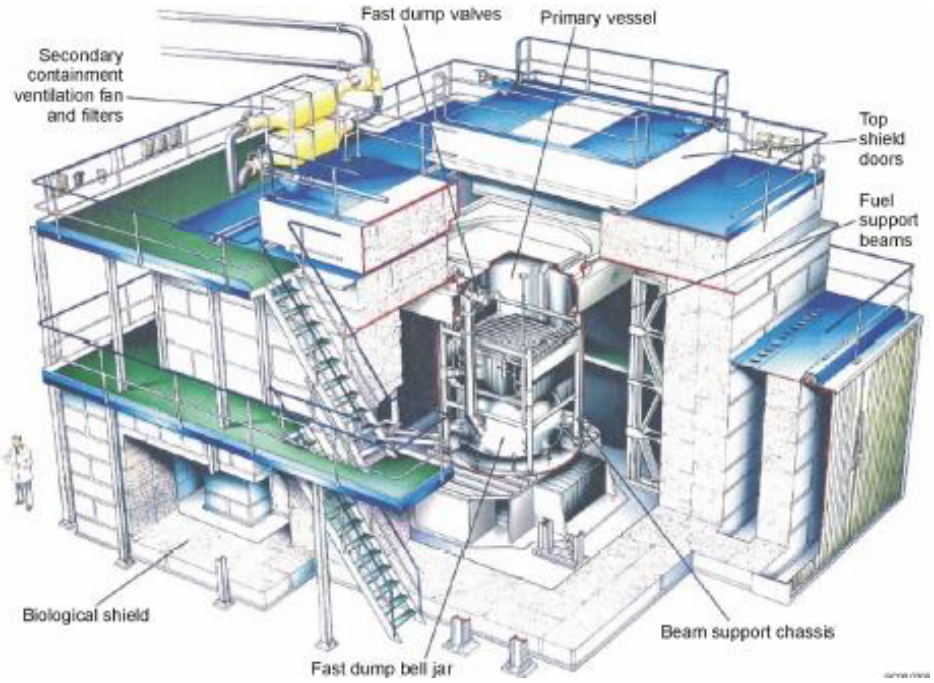

Figure 3.9. Schematic view of the DIMPLE Reactor.

The experimental configuration comprised a cylindrical array of fuel rods centrally located within a large aluminum vessel (2.6 m diameter and 4 m high) containing water. The array of rods was light-water moderated and fully reflected to a critical height of around 50 cm above the base of the fuel stack in the rods. The fuel rods were located on a square pitch of 1.32 cm and were supported by an upper and lower lattice plate. The lower lattice plate was situated on an aluminum fuel support assembly. The experimental program is described in detail in the report by Knipe [26].

The S01 series of measurements was built as part of commissioning tests following the 1983 refurbishment of the DIMPLE reactor at AEA Technology's Winfrith site. The initial fuel loading of 1,565 3% enriched uranium dioxide fuel rods (S01A) was a rebuild of an earlier benchmark, R1/100H/20, which was originally studied in DIMPLE during 1967. A further four configurations with different water levels using 1,441, 1,549, 1,585, and 1,597 3% fuel rods were assembled to assess the reactivity worth of core edge rods. The cylindrical fuel-rod arrays were loaded within the large aluminum primary vessel of the DIMPLE reactor. The primary vessel had an inner diameter of 2.591 m and was 4 m high, with a side-wall thickness of 0.65 cm and a base thickness of 0.9 cm.

In support of the MPACT validation, an analysis was initially performed in 2015 and reported in CASL-U-2016-1045-000 [27] on two of the DIMPLE experiments, the S01A and SO6 core configurations, as shown in Figure 3.10. The purpose of this analysis was to use KENO Monte Carlo models to assess the impact of limitations in the MPACT geometry and library for modeling the DIMPLE experiments.

An update to that work was performed CASL-I-2017-1359-000 [28] focusing primarily on S06A and S06B. The same basic approximations described in the previous work of CASL-U-2016-1045-000 were used in

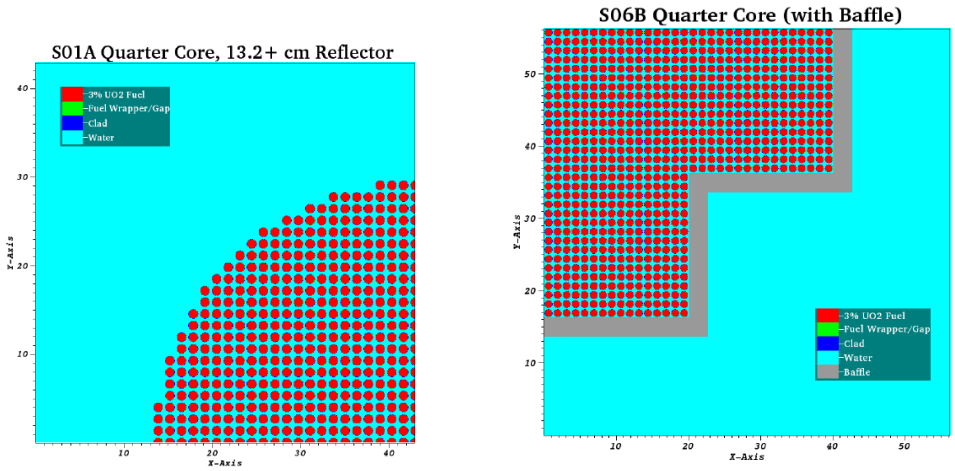

Figure 3.10. MPACT models of the S01A (left) and S06 (right) cores.

the updated work, with the principal difference being the use of an updated 51-group cross section library. The version of MPACT used for the analysis in this report is v2.1.0 with sha1 6ba80c2. This version was built on 02/22/17. Additionally, the 51g cross section library version used is v4.2m5 and was released on 12/06/16. The 51-group MPACT cross section library contains more groups in the resonance energy range compared to the 47-group library. Specifically, group 11 in the 47-group library ranging from 1.30E-4 to 2.03E-03 MeV was split into two groups ranging from 1.43E-04 to 3.05E-04 MeV and 9.50E-04 to 2.25E-03 MeV. The same is true for group 9, which ranged from 9.12E-03 to 6.74E-02 MeV, which was split into two groups ranging from 9.50E-03 to 2.00E-02 MeV and 5.00E-02 to 7.30E-02 MeV. Figure 3.11 shows the new group structure for these energy ranges.

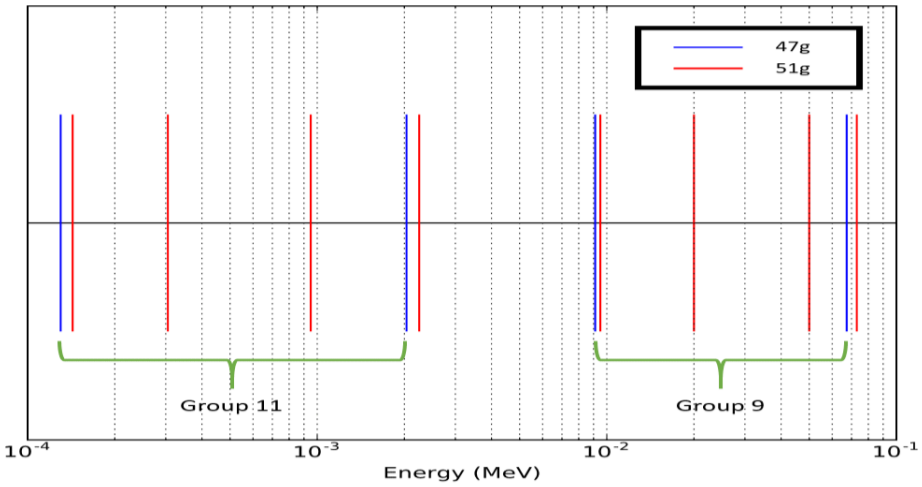

Figure 3.11. Comparison of energy groups for 47- and 51-group cross section libraries.

The set of discretization parameters that were used in the original and updated work are shown in the tables below.

In the previous study reported in CASL-U-2016-1045-000, a pin power bias was observed at the fuel-bulk moderator boundary for S06A which lacks the stainless-steel baffle present in S06B. An investigation was performed to determine the cause of this bias. Mesh discretization studies were performed in which MOC

Table 3.7. Coarse discretization parameters

Parameter	Location	Value
Radial mesh sectors	Moderator (assembly)	3
	Fuel	3
Azimuthal mesh sectors	Moderator (assembly)	8
	Fuel	8
Rectangular mesh divisions	Moderator (reflector)	5×5
Ray spacing (cm)	N/A	0.05
Azimuthal quadrature angles	N/A	8
Polar quadrature angles	N/A	2

Table 3.8. Fine discretization parameters

Parameter	Location	Value
Radial mesh sectors	Moderator (assembly)	10
	Fuel	10
Azimuthal mesh sectors	Moderator (assembly)	36
	Fuel	36
Rectangular mesh divisions	Moderator (reflector)	30×30
Ray spacing (cm)	N/A	0.01
Azimuthal quadrature angles	N/A	16
Polar quadrature angles	N/A	3

parameters and the spatial mesh were refined to observe the effect on the eigenvalue error and pin power error between MPACT and KENO. The results of this analysis are reported in Dodson et al. [28]. Table 3.9 summarizes the pin power comparison between MPACT and KENO for both the coarse and fine MOC discretizations and P2 and TCP0 scattering treatment. For the mesh converged case (fine), the maximum difference in the RMS fission rate is <0.44%, and the pcm difference is <170 pcm. This is compared to the results for the default cases, which show larger fission rate and pcm errors.

The MPACT model was also run with the experimentally derived critical axial buckling values provided by the DIMPLE benchmark documentation. The resulting keff values were assessed based on their deviation from criticality (i.e., keff = 1). The results are summarized in the tables below, which provide the coarse and fine discretizations in MPACT using P2 and TCP0 scattering treatment, respectively. Results are included from CASL-U-2016-1045-000 for comparison with the updated values in Tables 3.11 and 3.12. As indicated, there is significant improvement in the accuracy of the MPACT code compared to the previous results, likely the result of improvements in the cross section library and modeling methodology. The uncertainty in each buckling value is ±0.2 $m^{-}2$, so the upper and lower value cases are also presented for comparison.

Table 3.9. Results for unbuckled MPACT criticality calculations in comparison to KENO results

Experiment	Disc.	Scat. Type	% RMS	Max. % Abs. Diff.	MPACT k_{eff}	KENO k_{eff}	pcm error
S01A	Coarse	P_2	1.030	2.325	1.091030	1.089035	168
		TCP_0	0.921	1.735	1.090110		91
	Fine	P_2	0.372	0.862	1.090769		146
		TCP_0	0.418	0.922	1.089430		33
S06A	Coarse	P_2	1.257	3.904	1.098447	1.096431	167
		TCP_0	1.150	3.580	1.098090		138
	Fine	P_2	0.345	1.010	1.098171		145
		TCP_0	0.434	1.207	1.097443		84
S01A	Coarse	P_2	0.285	0.700	1.084490	1.083565	79
		TCP_0	0.319	0.809	1.084773		103
	Fine	P_2	0.208	0.519	1.085303		148
		TCP_0	0.290	0.769	1.085066		128

Table 3.10. Previous results for MPACT criticality calculations with P2 scattering

Configuration	B^2 [m^{-2}]	Discret.	Code	k_{eff}	Δk_{eff} (pcm)
S01A-Sq	24.2	–	WIMS	1.00007	+7
		Coarse	MPACT	1.00267	+267
		Fine	MPACT	1.00297	+297
S06A-Sq	24.7	–	WIMS	1.00039	+39
		Coarse	MPACT	0.99990	-10
		Fine	MPACT	1.00137	+137
S06B-Sq	21.1	–	WIMS	0.99952	-48
		Coarse	MPACT	1.00019	+19
		Fine	MPACT	1.00171	+171

Table 3.11. Updated results for MPACT criticality calculations with P_2 scattering

Configuration	B^2 [m^{-2}]	Discret.	Code	k_{eff}	Δk_{eff} (pcm)
S01A-Sq-Nominal	24.2	–	WIMS	1.00007	+7
		Coarse	MPACT	1.00229	+229
		Fine	MPACT	1.00248	+248
S01A-Sq-Lower	24.0	Fine	MPACT	1.00317	+317
S01A-Sq-Upper	24.4	Fine	MPACT	1.00179	+179
S06A-Sq-Nominal	24.7	–	WIMS	1.00039	+39
		Coarse	MPACT	0.99968	-32
		Fine	MPACT	1.00030	+30
S06A-Sq-Lower	24.5	Fine	MPACT	1.00104	+104
S06A-Sq-Upper	24.9	Fine	MPACT	0.99956	-44
S06B-Sq-Nominal	21.1	–	WIMS	0.99952	-48
		Coarse	MPACT	0.99953	-47
		Fine	MPACT	1.00101	+101
S06B-Sq-Lower	20.9	Fine	MPACT	1.00176	+176
S06B-Sq-Upper	21.3	Fine	MPACT	1.00026	+26

Table 3.12. Updated results for MPACT criticality calculations with TCP_0 scattering

Configuration	B^2 [m^{-2}]	Discret.	Code	k_{eff}	Δk_{eff} (pcm)
S01A-Sq-Nominal	24.2	–	WIMS	1.00007	+7
		Coarse	MPACT	1.00110	+110
		Fine	MPACT	1.00131	+131
S01A-Sq-Lower	24.0	Fine	MPACT	1.00199	+199
S01A-Sq-Upper	24.4	Fine	MPACT	1.00062	+62
S06A-Sq-Nominal	24.7	–	WIMS	1.00039	+39
		Coarse	MPACT	0.99872	-128
		Fine	MPACT	0.99972	-28
S06A-Sq-Lower	24.5	Fine	MPACT	1.00046	+46
S06A-Sq-Upper	24.9	Fine	MPACT	0.99898	-102
S06B-Sq-Nominal	21.1	–	WIMS	0.99952	-48
		Coarse	MPACT	0.99908	-92
		Fine	MPACT	1.00084	+84
S06B-Sq-Lower	20.9	Fine	MPACT	1.00160	+160
S06B-Sq-Upper	21.3	Fine	MPACT	1.00009	+9

3.3.3 VENUS-2 Critical Experiment

VENUS-2 is an international benchmark with 2D and 3D exercises [29]. The VENUS facility is a zero-power critical reactor located at SCK-CEN in Belgium. As shown in Figure 3.12, the core consists of 12 15×15 assemblies with the typical pitch of a 17×17 assembly, 1.26 cm. The four central assemblies consist of the 3.3 wt.% UO_2 fuel pins with 10 Pyrex pins each. The 8 assemblies on the periphery of the core consist of UO_2 and MOX fuel: 7 internal rows contain 4.0 wt.% UO_2 fuel pins, and 8 external rows contain MOX fuel with 2.0/2.7 wt.% high-grade plutonium. The core is 50 cm in height.

Figure 2.3. Horizontal reactor description

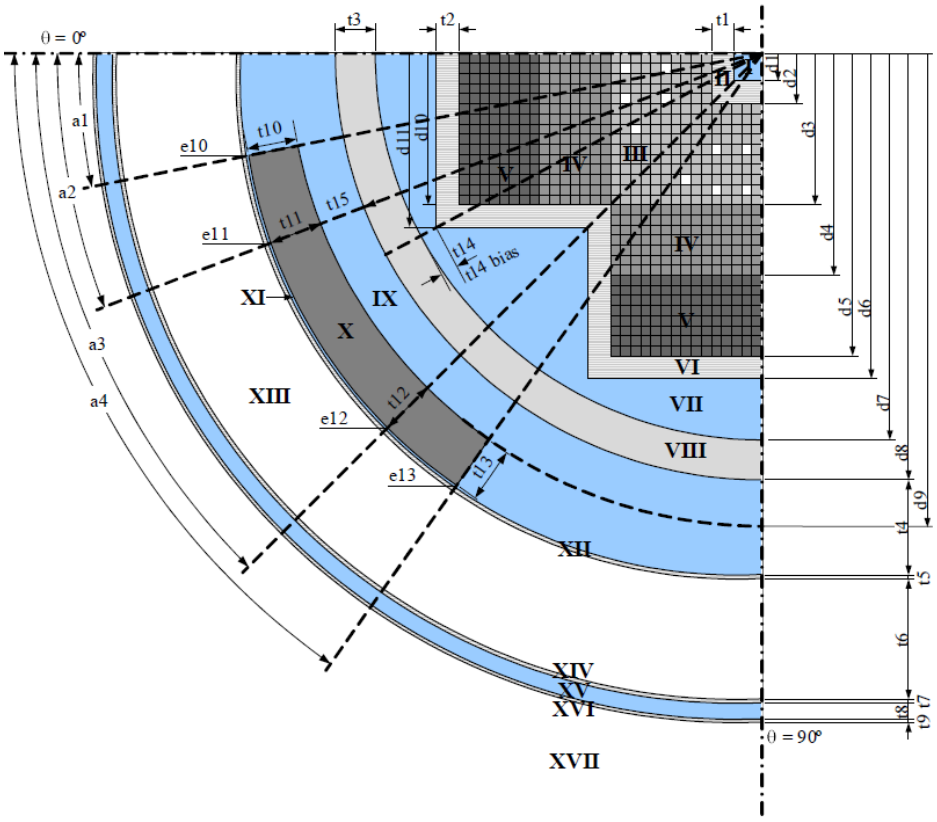

I	Central Hole	IX	Water Gap
II	Inner Baffle	X	Neutron Pad
III	3.3/0 Fuel Region	XI	Space between Neutron Pad and Jacket
	(White Color: Pyrex)	XII	Jacket Inner Wall
IV	4.0/0 Fuel Region	XIII	Jacket Volume
V	2.0/2.7 Fuel Region	XIV	Jacket Outer Wall
VI	Outer Baffle	XV	Space between Jacket and Reactor Vessel
VII	Reflector	XVI	Reactor Vessel Wall
VIII	Barrel	XVII	Reactor Room

Figure 3.12. VENUS-2 core configuration

The 2D VENUS-2 experimental data consist of fission rate measurements in 121 of the 325 fuel rods in 1/8 of the core: 41 with 3.3% UO_2, 35 with 4.0% UO_2, and 45 with 2.0/2.7% MOX. A complete description of the facility is given in the benchmark specifications, including all geometry and material composition data required to create a detailed computational model of the VENUS-2 core. The objective of the benchmark was to validate and compare the nuclear data sets and production codes used for MOX-fueled system cal-

culations, especially for systems with MOX and UO_2. The results in this section contain analyses of the 2D and 3D versions of the VENUS-2 core model. Future work will focus on improving the modeling of the barrel and pad and performing comparisons to the dosimetry measurements in the pad and barrel to assess MPACT's to predict the ex-core flux directly.

3.3.3.1 2D results

The current 2D model of the VENUS-2 facility is shown in Figure 3.13, and the MPACT flat source region meshing in this model is shown in Figure 3.14. The benchmark specifications give the material descriptions in terms of number densities and nuclides; the measured critical axial buckling is also applied to this 2D model. The comparison of the predicted criticality is given in Table 3.13. This shows the MPACT results alongside the benchmark participant results reproduced here from [29]. From the criticality comparison, MPACT results compare very well to those from the experiment for TCP0 and P2 scattering, with differences of 10 and -27 pcm, respectively. This comparison is better than any of the benchmark participant results reported in the benchmark final report. The maximum, minimum, and average calculated vs. experimental (C/E) results for comparing the core midplane radial fission rates of MPACT show trends similar to the other benchmark participants. The average C/E is high by 1.2%, which is consistent with many of the other deterministic results. The Monte Carlo results from the benchmark participants are slightly better, typically being <1%. The minimum C/E for most participants is approximately -4 to -6%, and the MPACT results are -5.6 and -5% for the two scattering methods, respectively. Similarly, for the maximum C/E, the difference observed for the benchmark participants is around +10%. The MPACT results for maximum C/E are +9.5 and +9.9%, again exhibiting the same trend as the other benchmark participants. The other results shown here include the average and standard deviations of the C/Es of the fission rate by fuel region, and the differences in the fission rate C/E along the core centerline. With MPACT, the average C/E in the UO_2 3.3% is a bit lower than the average of the benchmark participants. The comparison for the UO_2 4.0% and MOX regions are about the same and slightly better, respectively, when compared to the average of the benchmark participants.

This trend of underpredicting the 3.3% UO_2 region and having better comparison for the other fuel regions is also apparent in Figure 3.15 and Table 3.13. In this figure, the MPACT results are clearly bounded by the benchmark participants, and the in-out tilt of the fuel regions is slightly less than in some of the other participants. Because the same trends are observed in MPACT as the benchmark participants, it is reasonable to conclude that MPACT is adequately modeling the VENUS-2 facility, and it is more likely that the observed differences are from uncertainties in the benchmark specification rather than a systemic issue specific to MPACT.

A direct comparison was also made between MPACT and MCNP6 with ENDF/B-VII.1 cross sections. Computed k-eff values were 1.08914 ± 0.00007 for MCNP6 and 1.088868/1.088449 for MPACT with TCP0/P2 scattering treatment. The MPACT/MCNP ratio results are shown in Table 3.15, and show the same trend in the region-wise fission rate: slight underestimation in the 3.3 wt.% UO_2 fuel region and slight overestimation in the MOX fuel region. It should be noted that the magnitude of the discrepancies in this comparison is much smaller relative to the comparison between MPACT and the experimental results.

The 2D MPACT model was extruded to the full core height (50 cm) to create the 3D model. Some additional details were also added to complete the model, including the Plexiglass axial reflectors for each of the fuel and Pyrex pins, an AISI 304 stainless steel/aluminum blanket for the 3.3% UO_2 fuel/Pyrex region, and the Plexiglass intermediate grid above the core. The MOC parameters used for this analysis are shown in Table 3.16, and the axial plane thickness in the fuel was 5 cm, resulting in 10 axial fuel planes. SP3 nodal treatment was also used. Results using both P2 and TCP0 scattering treatment are presented in comparison to the other benchmark participants, as for the 2D results.

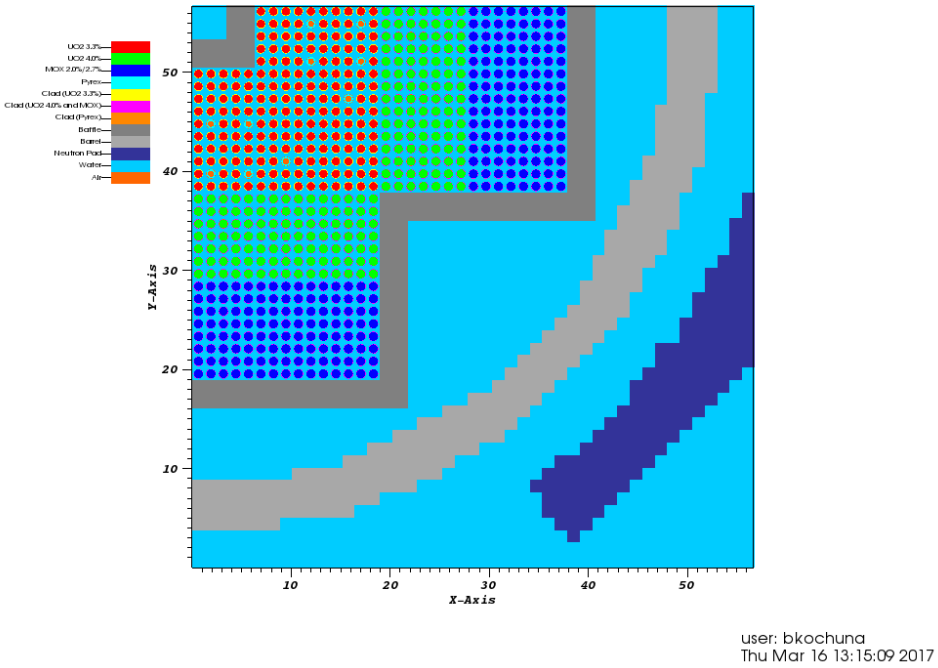

Figure 3.13. MPACT VENUS model.

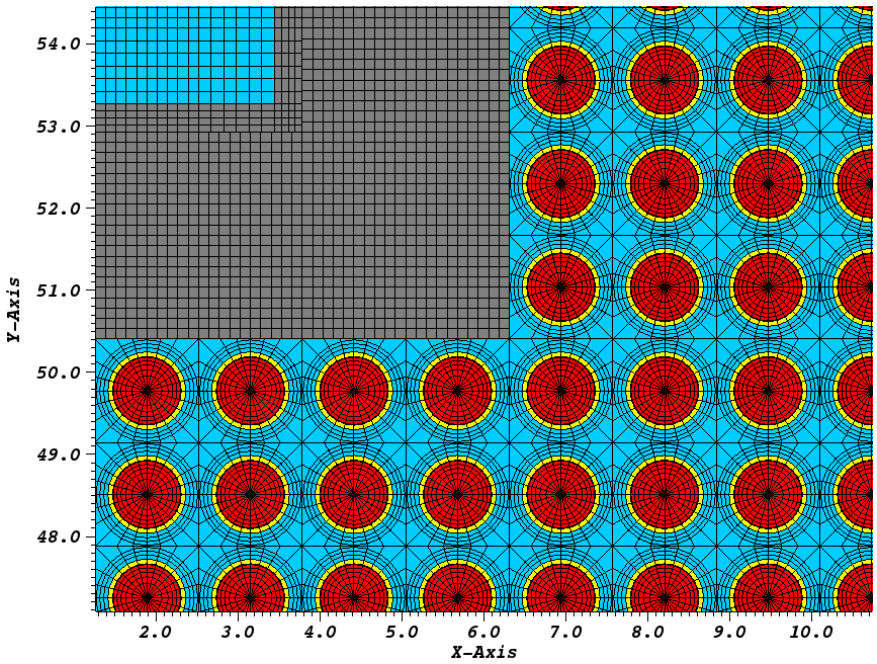

Figure 3.14. MPACT model: close-up of mesh.

Table 3.13. Comparison of 2D MPACT VENUS-2 results: k-eff

Institution	Code		keff	Deviation (%)	Deviation (pcm)	Min C/E	Max C/E	Avg. C/E
NEA	DORT		0.994520	-0.55	-548	0.941	1.102	1.013
KAERI	HELIOS-1.5		0.998170	-0.18	-183	0.944	1.091	1.010
ORNL	HELIOS-1.4		0.998700	-0.13	-130	0.939	1.082	1.002
PSI	BOXER		1.003780	0.38	378	0.934	1.124	1.016
SCK-CEN	DORT		0.992330	-0.77	-767	0.941	1.100	1.012
NEA+KAERI	MCNP-4B		1.002130	0.21	213	0.963	1.084	1.004
JAERI	MVP		none	none	none	0.952	1.071	1.007
KI	MCU-B		0.996500	-0.35	-350	0.944	1.069	1.003
KFKI	MCNP-4B		1.000500	0.05	50	0.941	1.119	1.016
GRS	MCNP-4B		1.004300	0.43	430	0.946	1.086	1.007
IJS-Jeraj	MCNP-4B		0.995700	-0.43	-430	0.939	1.113	1.015
UM	MPACT	TCP0	1.000101	0.01	10	0.946	1.099	1.012
		P2	0.999729	-0.03	-27	0.950	1.095	1.012

In this analysis, the multiplication factor and core midplane fission rates are compared to the experimental values. Table 3.17 shows the comparison of MPACT multiplication factor and fission rate distribution results to the other benchmark participants. For the two scattering methods, TCP0 and P2, the error in the multiplication factor was 216 and 166 pcm, respectively. Additionally, the fission rate minimum C/E was -5.0% and -5.0%, maximum C/E was +9.8% and +9.5%, and the average C/E was +1.2% and +1.2% for TCP0 and P2 scattering treatment, respectively. While the error in the multiplication factor is larger for the 3-D case compared to the 2-D, the error in the fission rates is similar.

The observed regional power bias in the 2D results is also present in the 3D results. Table 3.18 shows the region-wise fission rate results, with an underestimation in the 3.3% UO2 region and overestimation in the MOX fuel region. This bias is better visualized in Figure 3.16 and 3.17, which show the spatial fission rate error for the experimentally measured pins for TCP0 and P2 scattering treatment, respectively. The error distribution is very similar for the two scattering types, with P2 scattering having a slightly lower maximum error (+9.5% compared to +9.8% with TCP0).

Overall, the results of the radial analysis are very similar to the 2D results. The bias in the fission rate distribution is present in the 2D and 3D MPACT cases, as well as the results from the other benchmark participants. There is also an overestimation of the multiplication factor for the 3D MPACT case, although it is not as large as some of the other codes in the comparison.

The VENUS-2 benchmark contains axial fission rate data for 6 pins, as shown in Figure 3.18, reproduced from the benchmark report [29]. A comparison was also made for these pins, with the results listed in Table 3.19 and Figures 3.19 and 3.20.

Overall, the comparison shows close agreement between MPACT and the experimental fission rate distribution. The average deviation from unity C/E for all of the axial pin regions is 0.02% and 0.01% for TCP0 and P2 scattering treatment, respectively. Pin 240 in the MOX region saw the largest error of 4.25%. This pin is located in the MOX fuel region, where the largest radial error was also observed. In the axial plots, there does not appear to be a spatial bias in the fission rate, which was seen in the radial fission rate comparison.

Table 3.14. Comparison of 2D MPACT VENUS-2 results: fission rate distribution (% deviation from unity C/E)

Institution		UO_2 3.3% pins		UO_2 4.0% pins		MOX pins		All fuel pins	
		Avg. %	% Std. Dev.	Avg. %	% Std. Dev.	Avg. %	% Std. Dev.	Avg. %	% Std. Dev.
NEA		-2.58	1.52	-0.36	1.59	5.65	2.01	1.18	4.02
KAERI		-2.16	1.36	-0.34	1.52	4.74	2.05	0.90	3.39
ORNL		-0.49	1.52	-0.83	1.93	1.36	2.86	-0.13	2.46
PSI		-2.82	1.51	-0.80	1.85	6.76	2.66	1.33	4.69
SCK-CEN		-2.55	1.50	-0.36	1.50	5.39	2.01	1.07	3.86
NEA+KAERI		-0.46	1.41	0.01	1.74	1.17	1.94	0.34	1.84
JAERI		-0.37	1.46	-0.88	1.47	2.93	2.01	0.76	2.42
KI		-0.74	1.66	-1.30	1.53	1.86	2.36	0.03	2.31
KFKI		-1.59	1.63	-0.81	2.11	6.54	2.27	1.66	4.26
GRS		-0.68	1.25	-0.95	1.43	3.19	1.94	0.67	2.46
IJS-Jeraj		-2.26	1.35	-1.17	1.79	6.84	2.01	1.46	4.51
Average		-1.52	1.47	-0.71	1.68	4.22	2.19	0.84	3.29
MPACT	TCP_0	-2.29	1.28	-0.43	1.63	5.23	2.06	1.05	3.68
	P_2	-2.12	1.25	-0.38	1.65	4.99	2.02	1.06	3.53

Table 3.15. MPACT/MCNP comparison

Scat. Type	MPACT/MCNP fission rate ratio deviation from unity								pcm Diff.
	UO_2 3.3%		UO_2 4.0%		MOC		All pins		
	Avg. %	% Std. Dev.	Avg. %	% Std. Dev.	Avg. %	% Std. Dev.	Avg. (Min. %/Max. %)	% Std. Dev.	
TCP_0	-0.95	0.42	0.15	0.36	1.35	0.46	0.22 (-1.76/2.27)	1.06	-23
P_2	-0.77	0.36	0.20	0.39	1.17	0.49	0.23 (-1.44/2.41)	0.92	-58

Table 3.16. MOC discretization parameters

Parameter	Location	Value
Radial mesh sectors	Moderator (assembly)	3
	Fuel/Pyrex	5
Azimuthal mesh sectors	Moderator (assembly)	16
	Fuel/Pyrex	16
Rectangular mesh divisions	Moderator/barrel/pad	10×10
Ray spacing (cm)	N/A	0.01
Azimuthal quadrature angles	N/A	16
Polar quadrature angles	N/A	3

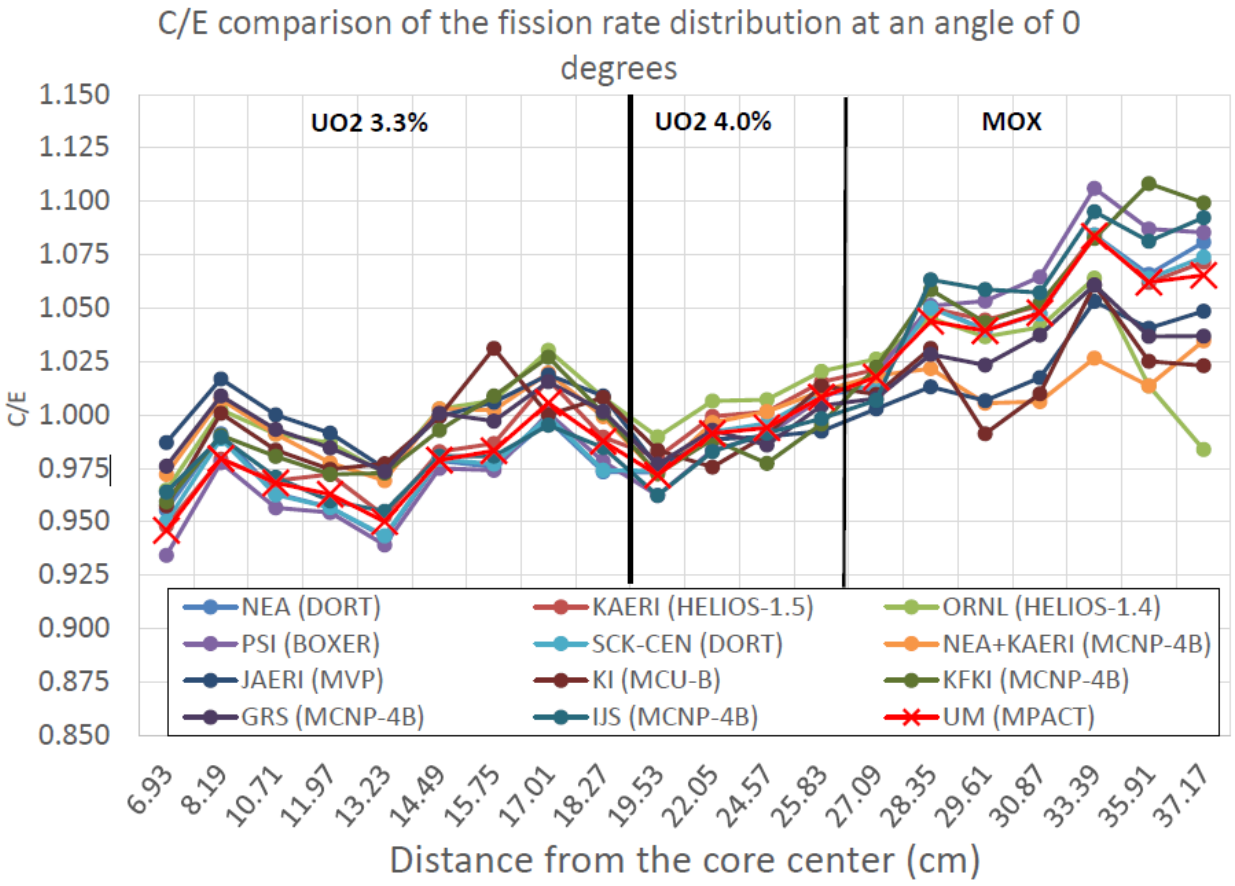

Figure 3.15. MPACT fission rate distribution at 0 degrees of VENUS core.

Table 3.17. Comparison of 3D MPACT Venus-2 results: k-eff

Institution	Code		k_{eff}	Deviation (%)	Deviation (pcm)	Min C/E	Max C/E	Avg. C/E
NEA	DORT		0.994520	-0.55	-548	0.941	1.102	1.013
KAERI	HELIOS-1.5		0.998170	-0.18	-183	0.944	1.091	1.010
ORNL	HELIOS-1.4		0.998700	-0.13	-130	0.939	1.082	1.002
PSI	BOXER		1.003780	0.38	378	0.934	1.124	1.016
SCK-CEN	DORT		0.992330	-0.77	-767	0.941	1.100	1.012
NEA+KAERI	MCNP-4B		1.002130	0.21	213	0.963	1.084	1.004
JAERI	MVP		none	none	none	0.952	1.071	1.007
KI	MCU-B		0.996500	-0.35	-350	0.944	1.069	1.003
KFKI	MCNP-4B		1.000500	0.05	50	0.941	1.119	1.016
GRS	MCNP-4B		1.004300	0.43	430	0.946	1.086	1.007
IJS-Jeraj	MCNP-4B		0.995700	-0.43	-430	0.939	1.113	1.015
UM	MPACT	TCP0	1.002161	0.22	216	0.950	1.098	1.012
		P2	1.001668	0.17	166	0.950	1.095	1.012

Table 3.18. Comparison of 3D MPACT Venus-2 results: fission rate distribution (% deviation from unity C/E)

Institution		UO_2 3.3% pins		UO_2 4.0% pins		MOX pins		All fuel pins	
		Avg. %	% Std. Dev.	Avg. %	% Std. Dev.	Avg. %	% Std. Dev.	Avg. %	% Std. Dev.
NEA		-2.58	1.52	-0.36	1.59	5.65	2.01	1.18	4.02
KAERI		-2.16	1.36	-0.34	1.52	4.74	2.05	0.90	3.39
ORNL		-0.49	1.52	-0.83	1.93	1.36	2.86	-0.13	2.46
PSI		-2.82	1.51	-0.80	1.85	6.76	2.66	1.33	4.69
SCK-CEN		-2.55	1.50	-0.36	1.50	5.39	2.01	1.07	3.86
NEA+KAERI		-0.46	1.41	0.01	1.74	1.17	1.94	0.34	1.84
JAERI		-0.37	1.46	-0.88	1.47	2.93	2.01	0.76	2.42
KI		-0.74	1.66	-1.30	1.53	1.86	2.36	0.03	2.31
KFKI		-1.59	1.63	-0.81	2.11	6.54	2.27	1.66	4.26
GRS		-0.68	1.25	-0.95	1.43	3.19	1.94	0.67	2.46
IJS-Jeraj		-2.26	1.35	-1.17	1.79	6.84	2.01	1.46	4.51
Average		-1.52	1.47	-0.71	1.68	4.22	2.19	0.84	3.29
MPACT	TCP_0	-2.07	1.27	-0.47	1.67	5.15	2.08	1.09	3.60
	P_2	-2.05	1.24	-0.39	1.70	4.93	2.05	1.06	3.50

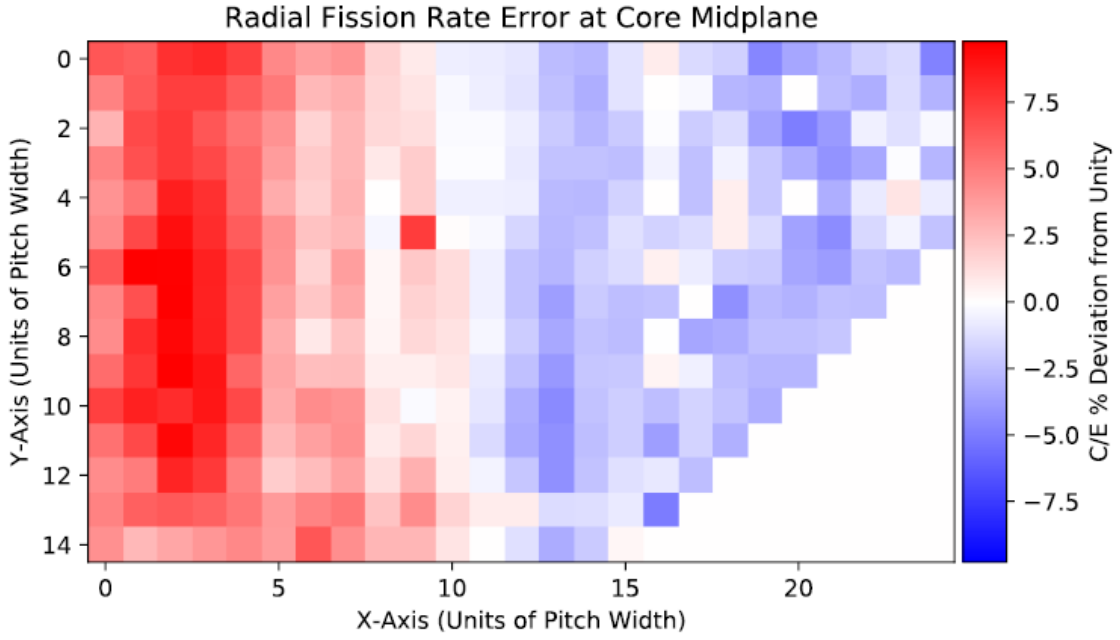

Figure 3.16. MPACT radial fission rate error with TCP_0 scattering treatment.

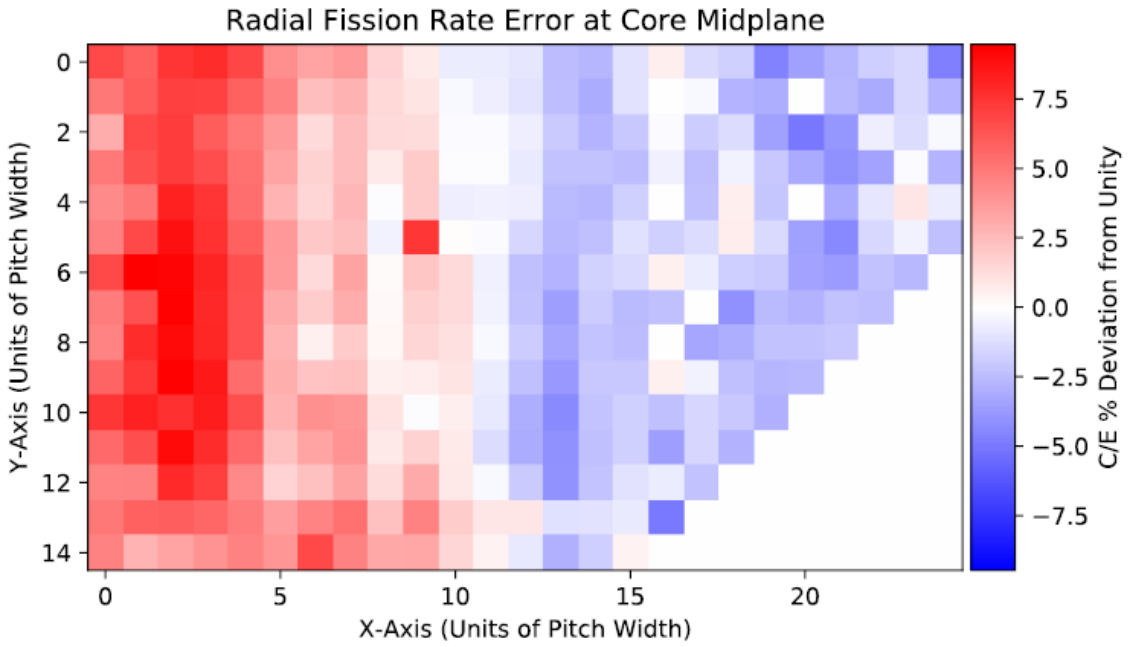

Figure 3.17. MPACT radial fission rate error with P_2 scattering treatment.

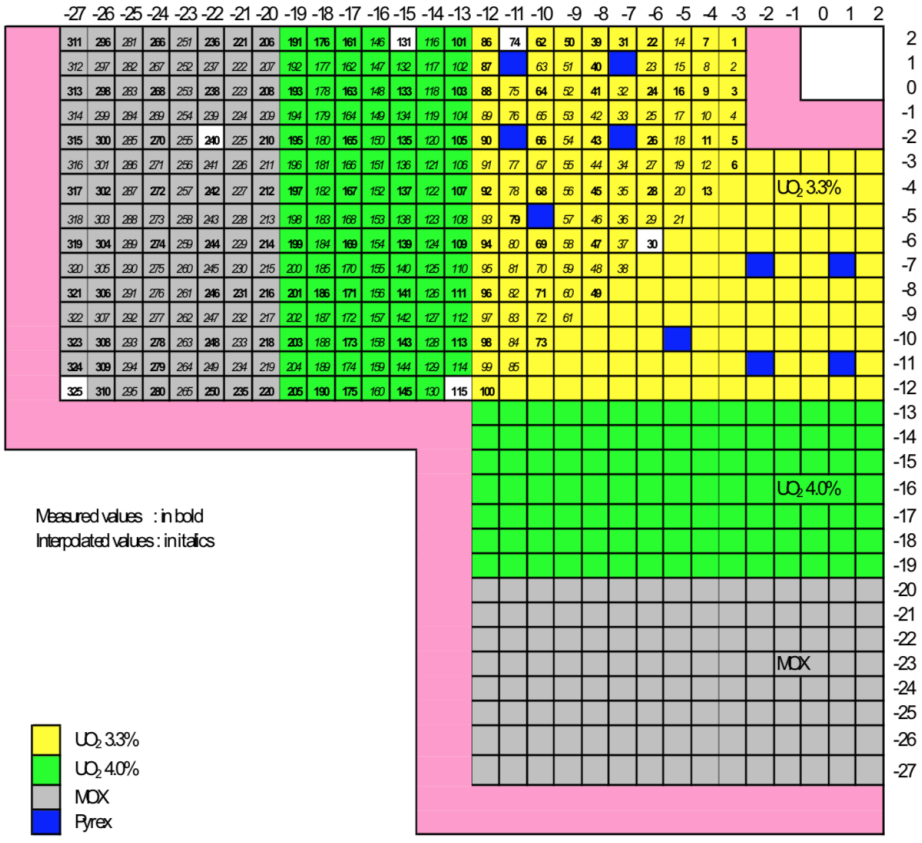

Figure 3.18. VENUS-2 measured pins (axial data are provided for the 6 pins in white cells).

Table 3.19. Comparison of 3D MPACT VENUS-2 results: axial fission rate distribution (% deviation from unity C/E) for 6 measured pins

Pin # (Type)	Scat. Meth.	Avg. %	% Std. Dev.	Min. %	Max. %
30 (3.0% UO2)	TCP_0	-0.12	0.97	-3.56	1.42
	P_2	-0.11	0.97	-3.56	1.42
74 (3.0% UO2)	TCP_0	0.00	0.63	-1.46	1.25
	P_2	-0.01	0.62	-1.46	1.25
115 (4.0% UO2)	TCP_0	0.04	0.81	-1.62	1.56
	P_2	0.04	0.84	-1.69	1.56
131 (4.0% UO2)	TCP_0	0.09	0.73	-1.06	1.87
	P_2	0.10	0.74	-1.06	1.87
240 (MOX))	TCP_0	0.11	1.59	-2.68	4.25
	P_2	0.13	1.59	-2.68	4.25
325 (MOX)	TCP_0	-0.03	1.26	-2.40	2.25
	P_2	-0.06	1.22	-2.40	2.25
All	TCP_0	0.02	1.03	-3.56	4.25
	P_2	0.01	1.03	-3.56	4.25

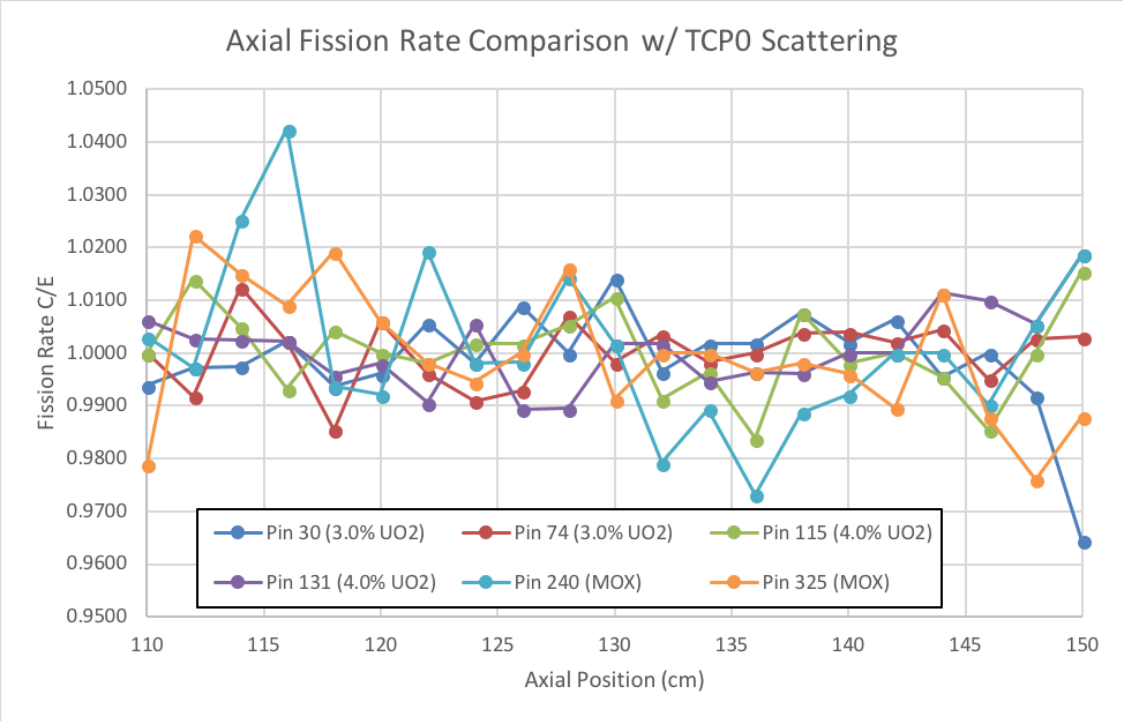

Figure 3.19. VENUS-2 axial fission rate C/E with TCP_0 scattering treatment.

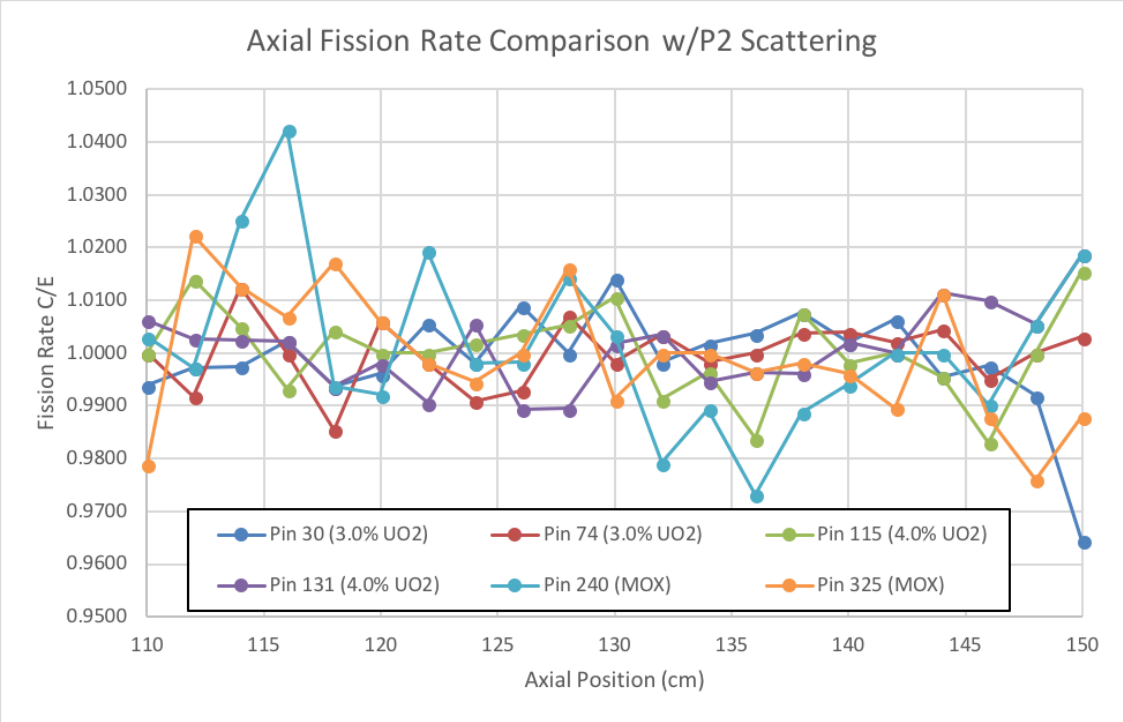

Figure 3.20. VENUS-2 axial fission rate C/E with P_2 scattering treatment.

3.3.4 Resonance Integral Validation with Hellstrand's Experiments

Validations of the MPACT code have been conducted against various critical experiments such as B&W, DIMPLE, and VENUS. These benchmarks are usually small reactors designed to validate the neutronics code in terms of critical conditions or fission rate distributions. They are often performed at room temperature and at zero power. In the last couple years of the CASL program, CASL researchers observed negative reactivity bias at hot full power (HFP) in the core follow calculations. Efforts are ongoing to identify the source of the reactivity bias. Multiple aspects are being analyzed, ranging from cross section library data to various physical models.

To evaluate the quality of cross section data and methods at elevated fuel temperatures, validations of Hellstrand's experiments are performed to enhance the credibility of MPACT in terms of the resonance self-shielding and multigroup cross section calculation. The unique design of Hellstrand's experiments leads to a single physics benchmark that is similar to most critical experiments. This was realized by introducing external heating for isothermal temperature elevations of the fuel sample. The present report focuses on validating the temperature coefficient of ^{238}U resonance integral (RI), which dominates the Doppler temperature coefficient in LWRs.

3.3.4.1 Hellstrand's RI experiments

Hellstrand's experiment for measuring ^{238}U RI was performed in a Swedish heavy water reactor. Fuel rods of uranium metal or uranium oxide were placed in a cadmium-covered oven and irradiated in the central channel of the reactor, as shown in Figure 3.21 [30]. The capture of neutrons in ^{238}U gives rise to ^{239}Np, the gamma decay of which can be measured to deduce the capture rate of ^{238}U.

The samples from the original experiments included uranium metal and oxide (UO_2). They were mounted between end pieces of the same material, forming a rod of uniform diameter approximately 90 mm long. Because the MPACT library is tailored to model UO_2 fuel in a typical range of fuel radii, only the UO_2 samples are compared in this work.

The RI (^{238}U capture rate) must be normalized for comparison with different sample temperatures; however, it would be practically difficult to measure the flux inside the sample. Therefore, epithermal flux outside the sample was measured with gold foils (see Figure 3.21), and the RI was normalized to the unit epithermal flux. The apparatus also includes a cadmium-covered holder that shields the thermal neutrons from being absorbed by the sample, given that the experiment is targeted on the epithermal range of ^{238}U resonances.

This report does not include details such as reactor geometry or assembly layout. It was determined that this information is not important to the evaluation of RI, because the objective of the experiment was to create a 1/E spectrum (measured by the gold foils) outside the sample. The amplitude of the flux that relates to the core configuration is not important, because RI is normalized to the unit 1/E epithermal flux.

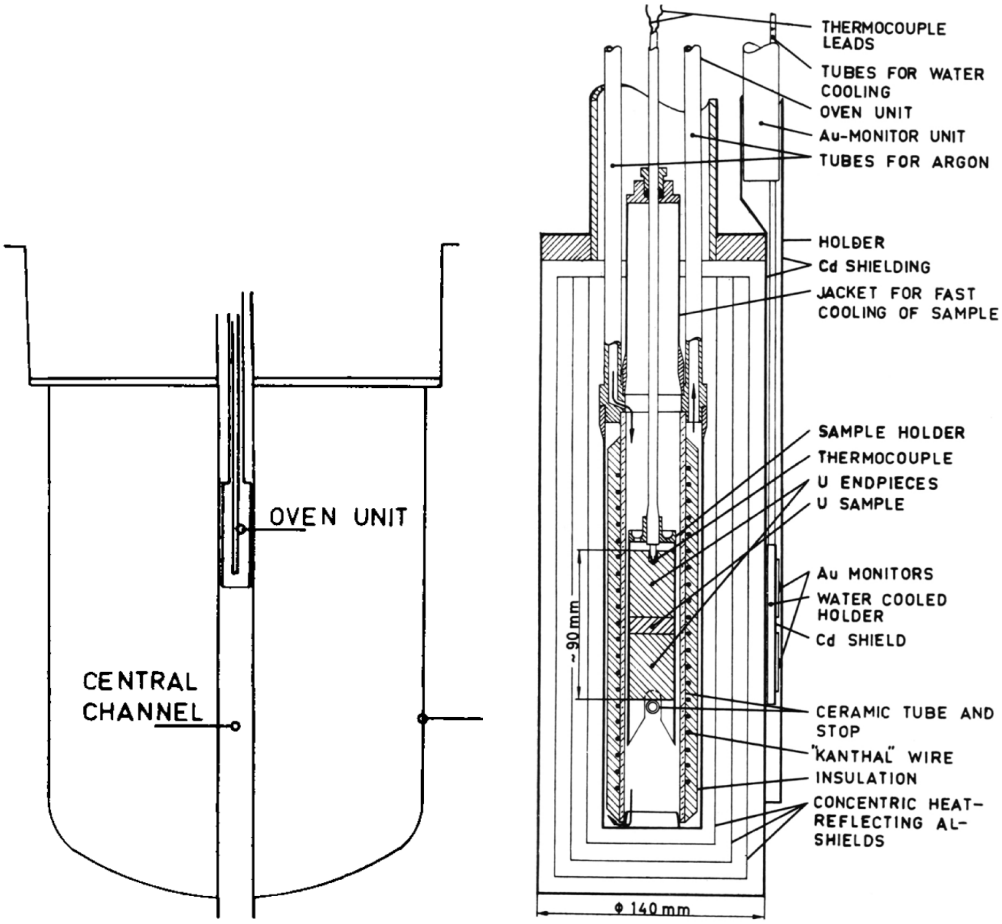

Figure 3.21. Position of the oven in the core and the cross section of the oven unit.

3.3.4.2 MPACT simplified model

The objective of a simplified model in MPACT is to resemble the 1/E flux surrounding the fuel sample without modeling the details of the original core geometry. A 2D 3×3 assembly block (7×7 pins in each assembly) is modeled in MPACT, as shown in Figure 3.22.

To be consistent with the experiment, natural UO_2 fuel and heavy water moderator are used in this problem. The pin pitch is set to 3.5 cm with a fuel radius of 0.61 cm (fuels other than the sample). All the six boundaries are reflective. The system is close to criticality, leading to a neutron spectrum similar to that in the central channel of the heavy water reactor.

In the central assembly of the 3×3 block, a large amount of moderator is used to achieve a 1/E incoming flux as seen by the fuel sample. The MPACT reaction rate edits were used to obtain the ^{238}U group-wise capture rates of the sample. To consider the cadmium shielding effect for thermal neutrons in the original experiment, the ^{238}U capture rates are integrated above 0.625eV, corresponding to 1–39 groups of the 51-group MPACT library.

To normalize the RIs for different sample sizes and fuel temperatures, the epithermal 1/E flux was monitored using the gold foils outside the sample. The normalized RI was calculated as

$$RI = \frac{\int_V \int_u \sigma_{\gamma,28}(u,r)\,\phi(u,r)\,dudr}{\overline{\phi}}, \tag{3.1}$$

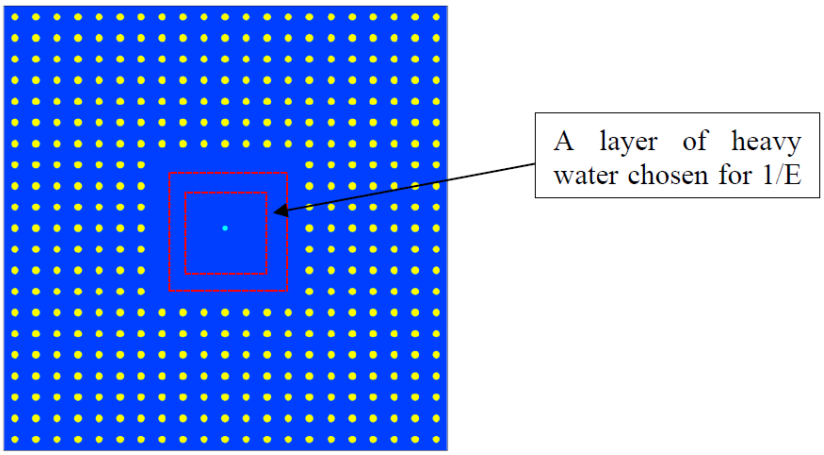

Figure 3.22. Simplified MPACT mode for RI calculation.

where $\overline{\phi} = \frac{\int_V \int_u \phi(u,r)dudr}{\Delta u V}$ is the average epithermal flux. In MPACT calculation, this asymptotic flux is calculated at a layer of heavy water, as marked in Figure 3.22.

3.3.4.3 Results and discussion

Hellstrand's experimental results were fitted into a linear correlation of $\sqrt{T} - \sqrt{T_0}$,

$$RI = RI_0 \left[1 + 0.01\,(0.58 + 0.5S/M)\left(\sqrt{T} - \sqrt{T_0}\right)\right] \quad \text{UO}_2 \text{ sample for 293 to 1,000 K .} \tag{3.2}$$

In this equation, S/M is the surface-to-mass ratio of the sample in cm^2/g. The problem described in Section 2 was run with a sample radius of 0.4 cm, a typical LWR fuel rod size. The temperatures were varied from 300 to 1,000 K in 100 K increments. Figures 3.23 and 3.24 show the comparison of RI/RI_0 between the MPACT calculation and Hellstrand's correlation. For this rod size, the reported uncertainty of Hellstrand's correlation is ±0.0006 [30]. With resonance upscattering (Figure 3.23), the MPACT coefficient 0.0079 has a good agreement with Hellstrand's 0.0082±0.0006. Without resonance upscattering (Figure 3.24), the temperature coefficient of RI is reduced by about 10%. This is comparable to the amount of reactivity change for the resonance upscattering model reported by Lee et al. [31].

In addition to documenting RI/RI_0, Hellstrand also documented the correlation of absolute RI in cold conditions [32],

$$RI\,(barns) = 11.6 + 22.8\frac{S}{M}\,,\ 0.2 \le \frac{S}{M} \le 0.7\,. \tag{3.3}$$

According to Eq. (3.3), the absolute RI is dependent on the normalization flux. Figure 3.25 shows the neutron spectrum of the moderator layer that was used for RI normalization. Between 0.625eV and 10^5eV, a well-developed 1/E spectrum is observed. If the flux in this energy range is used to compute $\overline{\phi}$ and to normalize RI, then good comparison of RI_0 can be found in Table 3.20. Note that for the cold condition, the resonance upscattering effect is small.

Table 3.20. RI_0 of the 300 K sample

	Hellstrand	MPACT w/ res. upscat.	MPACT w/o res. upscat.
RI_0 (barns)	22.72	22.98	22.94

From these results, it can be concluded that

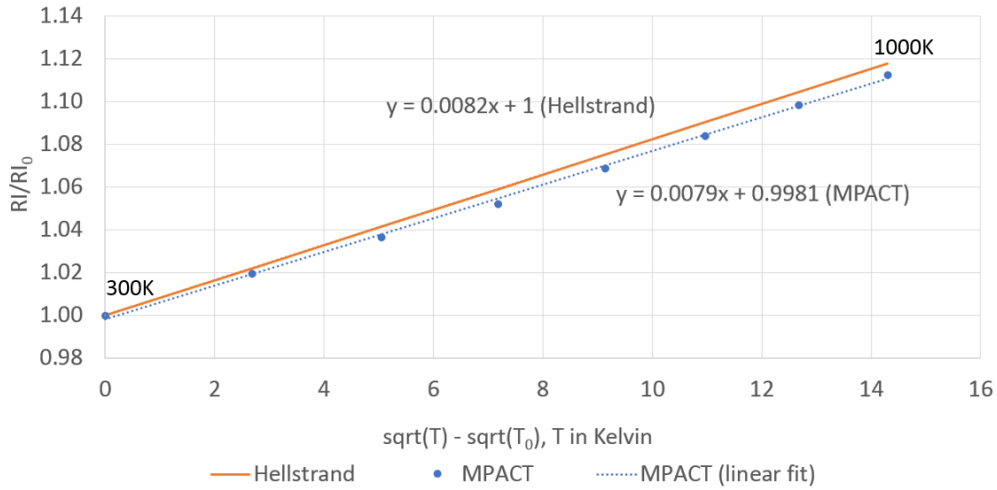

Figure 3.23. Temperature coefficient of MPACT *with resonance upscattering*.

1. The temperature coefficient of ^{238}U RI calculated by MPACT with resonance upscattering agrees within 1 σ error of the Hellstrand's correlation;
2. The difference of temperature coefficients with and without resonance upscattering are consistent with the reported value from the other source;and
3. By using the well-developed 1/E flux for normalization, the absolute RI of the MPACT calculation also agrees with Hellstrand's result.

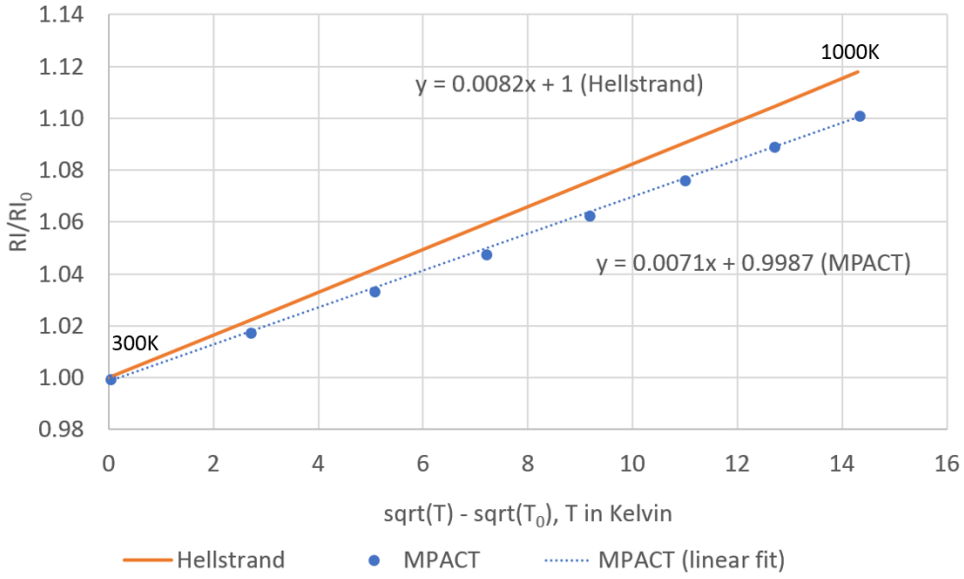

Figure 3.24. Temperature coefficient of MPACT *without resonance upscattering*.

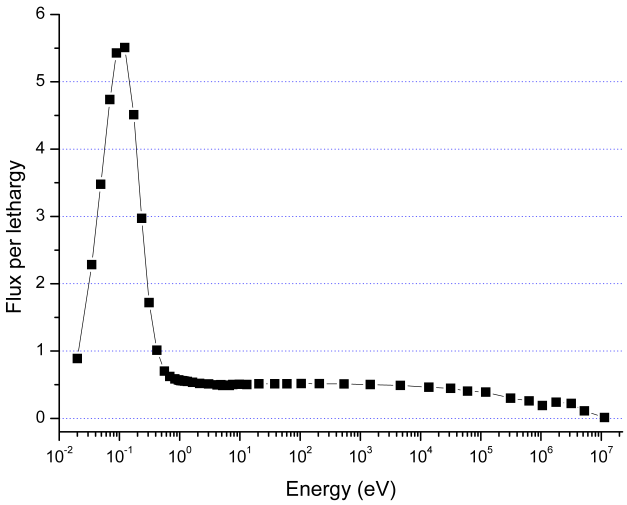

Figure 3.25. Neutron spectrum of the moderator layer for 300 K sample.

3.4 POWER PLANT START-UP PHYSICS TESTING: WATTS BAR NUCLEAR PLANT

Measurement data from operating nuclear power plants provide the broadest range of core simulator validation data. CASL collaborated with several stakeholders that own and/or operate PWR power plants, and some of the data are now available for validation of MPACT. As shown in Figure 3.26, the Watts Bar Nuclear Plant in Spring City, Tennessee, is owned and operated by the Tennessee Valley Authority (TVA), which was a CASL core partner. Watts Bar was selected as CASL's "physical reactor" for initial benchmarking activities. Unit 1 was the last commercial nuclear unit to come online in the 20th century, and Unit 2 was the first to come online in the 21st century.

Figure 3.26. TVA's Watts Bar Nuclear Plant

Watts Bar Nuclear Unit 1 (WBN1) is a traditional Westinghouse 4-loop PWR with an ice condenser containment design, one of the most common reactor designs in the United States today. It is currently licensed to 3,459 MWth power. WBN1 has 193 fuel 17×17 assemblies, has used Pyrex, integral fuel burnable absorber (IFBA), and wet annular burnable absorber (WABA) burnable poisons, and it has 57 AIC/B_4C hybrid rod cluster control assemblies (RCCAs). A schematic of the core loading is shown in Figure 3.27.

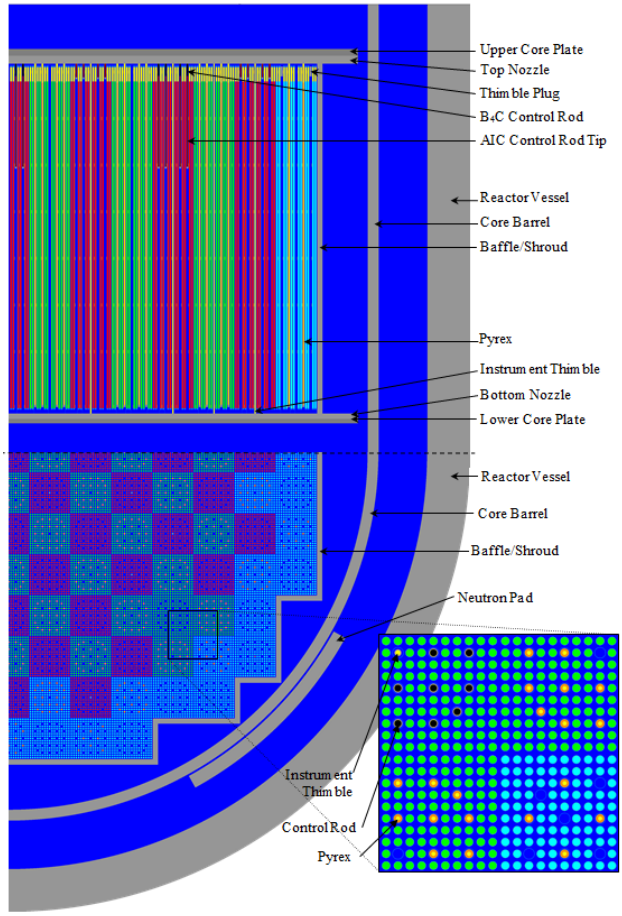

Figure 3.27. Problem 5 core geometry for initial criticality (quarter symmetry).

3.4.1 Watts Bar Nuclear Unit 1: Cycle 1 Hot Zero Power Reactor Zero Power Physics Tests

The hot zero power (HZP) power physics tests from WBN1 were the basis for the specifications of problem 5 of the VERA Benchmark Test Suite. The MPACT solution to problem 5 was first reported in the paper by Godfrey [33], and the results are briefly described here. These tests represent the HZP startup physics testing for WBN1, including measurement of BOC initial criticality, control bank worths, isothermal temperature coefficient, and the differential soluble boron worth. The cases are calculated without thermal-hydraulic feedback. The KENO-VI geometry for this calculation is shown in Figure 3.27, and Figure 3.28 provides the core loading pattern. The results of the measured startup tests, along with the KENO-VI reference solution, are shown in Table 3.21.

For comparison to CE KENO-VI, the same cases were calculated with MPACT. These cases include a variety of rod positions and soluble boron concentration. For these cases, the average eigenvalue difference is -48 pcm with a standard deviation of 5 pcm. The results for the ten critical configurations selected from the rod swap measurements are shown in Figure 3.29. The average of these cases (compared to measurements) is -177 ± 45 pcm.

The integral and differential rod worth of Bank D was calculated by both KENO-VI and VERA-CS, and the results were compared in Figure 3.30. The measured values have not been released publicly, other than the total Bank D worth (VERA-CS over-predicts by 2.6%). The integral rod worth curve is very nearly identical between the two codes, within 0.6%, other than at the very shallow insertion points. Similarly, the

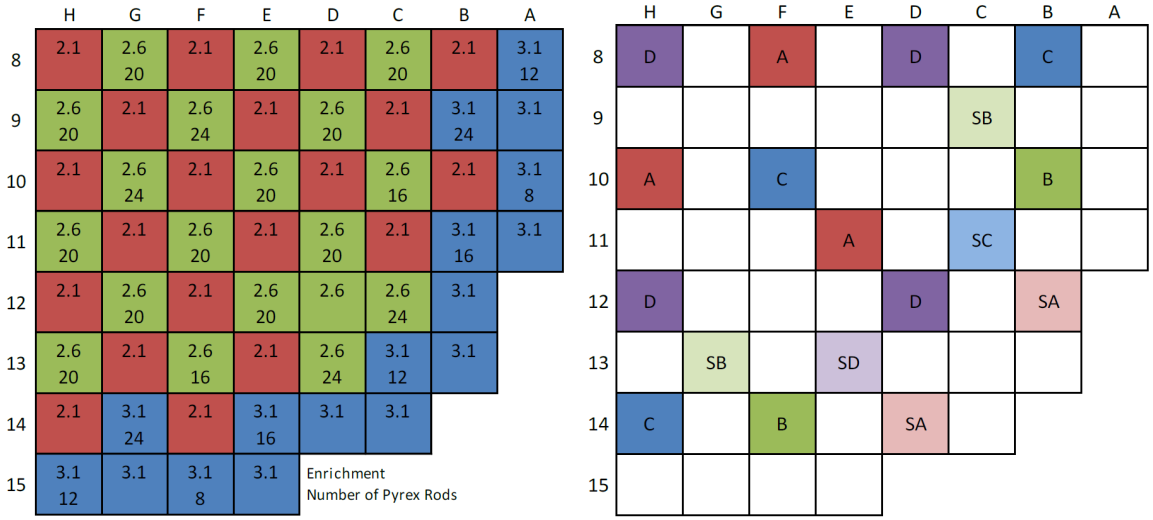

Figure 3.28. Problem 5 core loading pattern and control bank locations (quarter symmetry).

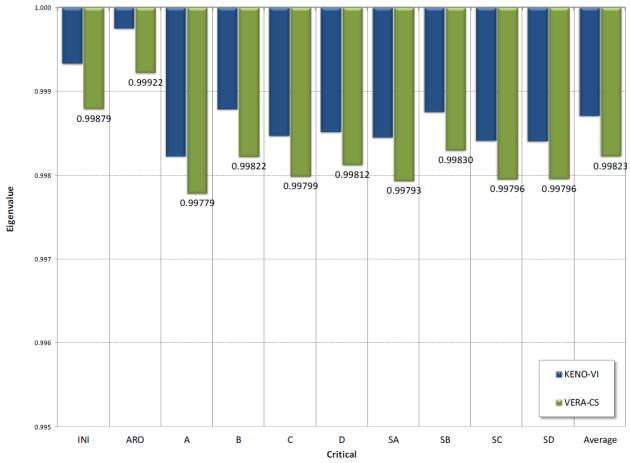

Figure 3.29. Problem 5 critical configurations.

differential worth of Bank D is compared in Figure 3.31 and demonstrates excellent agreement with the CE KENO-VI reference.

Finally, power distribution statistics are provided in Table 3.22 for the initial criticality case, with Bank D at 167 steps withdrawn. The pin power distributions compare very well, especially considering the larger uncertainty in the reference solution. The axial distribution is within 0.3%, resulting in an axial offset difference of only 0.14%, and the radial distribution is within 1.1% everywhere in the core. The 3D pin power RMS is also impressive at less than 0.5%, with a maximum pin power difference of 2.8% anywhere.

Table 3.21. Watts Bar Cycle 1 startup physics test results

Physics test results	Measured*	CE KENO-VI results	VERA-CS results	CE KENO-VI difference	VERA-CS difference
Initial criticality†	1.00000‡	0.99933	0.99879	-67 ± 1 pcm	-121 pcm
Bank A worth (pcm)	843	898 ± 2	893	6.4% ± 0.2%	5.8%
Bank B worth	879	875 ± 2	877	-0.5% ± 0.2%	-0.2%
Bank C worth	951	984 ± 2	982	3.5% ± 0.2%	3.1%
Bank D worth	1,342	1,386 ± 2	1,376	3.3% ± 0.1%	2.6%
Bank SA worth	435	447 ± 2	448	2.6% ± 0.4%	3.3%
Bank SB worth	1,056	1,066 ± 2	1,064	1.0% ± 0.2%	0.6%
Bank SC worth	480	499 ± 2	497	3.9% ± 0.4%	2.9%
Bank SD worth	480	499 ± 2	497	4.0% ± 0.4%	2.7%
Total bank worth	6,467	6,654 ± 4	6,634	2.9% ± 0.1%	2.4%
DBW (pcm/ppm)	-10.77	-10.21 ± 0.02	-10.25	0.56	0.52
ITC (pcm/F)	-2.17	-3.18 ± 0.04	-2.41	-1.01	-0.24

†Critical conditions are 1,285 ppm and Bank D at 167 steps withdrawn. KENO uncertainty is 1 pcm
‡The initial criticality includes an allowance to account for thermal expansion (-57 pcm)
*The "measured" control bank worths are inferred from the critical position of Bank D based on constants calculated by KENO-VI. For the VERA-CS results, the measured values were recalculated based on constants from VERA-CS, resulting in a maximum change in measured bank worth of 4 pcm.

Table 3.22. WBN1 startup physics tests power distribution results

VERA k_{eff}	k_{eff} Diff (pcm)	ΔAO (%) RMS	Axial ΔP MAX (%)	Axial ΔP RMS (%)	Radial ΔP MAX (%)	Radial ΔP RMS (%)	ΔP MAX (%)‡	ΔP (min) (%)	Exec† Time
0.99962	-40	0.14	0.16	0.30	0.35	1.09	0.48	2.81	13.1

†Each case utilized 4,234 parallel processors on EOS and utilized quarter-core symmetry
‡Total pin power uncertainty in KENO-VI reference results in 0.2%

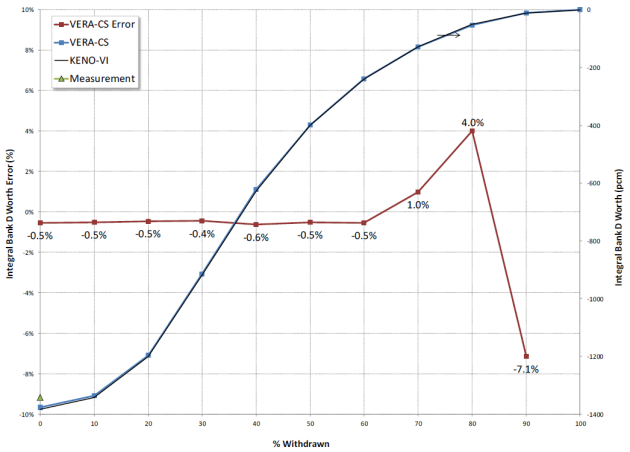

Figure 3.30. WBN1 startup test integral bank D worth.

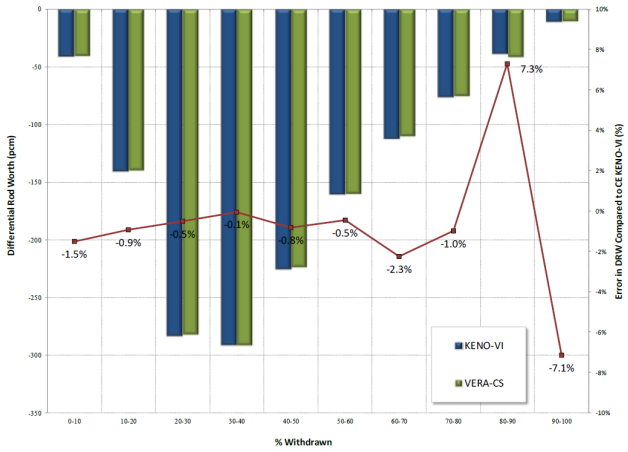

Figure 3.31. WBN1 startup test differential bank D worth.

3.4.2 Watts Bar Unit II: Cycle 1 HZP Reactor Zero Power Physics Tests

In FY17, the startup physics tests were performed on WBN2 and were simulated using MPACT. The modern core design of WBN2 and the availability of data provide an excellent validation benchmark for MPACT. The core loading pattern is shown in Figure 3.32. As reported in Godfrey [34], calculations were performed three months prior to the startup, and in the first blind application of VERA to a new reactor, predicted criticality and physics parameters were very close to those later measured by TVA.

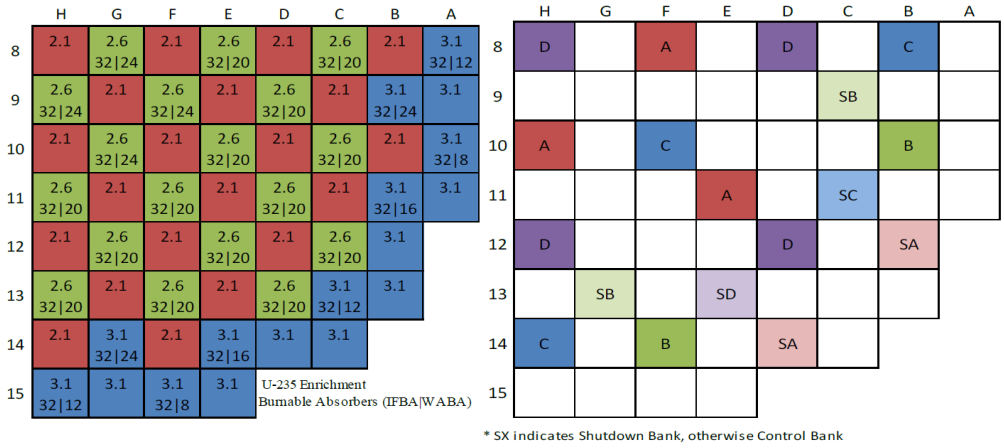

Figure 3.32. Core loading pattern for cycle 1 of WBN2.

The escalation to full power took approximately five months, including several intermediate testing power plateaus. The entire power, temperature, and control rod history was simulated with VERA by the hour, requiring 4,130 time steps, and it included isotopic depletion and decay through ten additional shutdown intervals. TVA provided the startup data, as well as the measured boron concentrations, reactor temperatures, ex-core axial flux difference (AFD), and twelve measured incore neutron flux distributions. The entire simulation required 892,837 core hours, or 13.5 days on 2,784 cores.

The VERA simulation was performed twice. At first the recommended BISON fuel temperature table was used, but large diverging axial power oscillations occurred at many of the power plateaus. To dampen these oscillations, a modified temperature set was generated with an increased fuel temperature response to power. This was effective in dampening the axial power oscillations, significantly improving the axial results, but the error in the critical boron predictions and radial power distributions increased. Research into the source of the oscillations is ongoing.

A summary of the final comparisons with VERA 3.6 is included in Table 3.23. All results are good except for the operating critical boron concentrations. Furthermore, the in-core power distribution comparisons were not very good initially at low power, but the recent results are very good and are consistent with the performance of VERA for WBN1 Cycle 1. It should be noted that the Watts Bar Nuclear Units 1 and 2 have significantly different detector types in their cores. The core in WBN2 has a state-of-the-art self-powered vanadium detector, whereas there standard movable detectors are used in WBN1.

Table 3.23. Summary of VERA performance for WBN2 startup

Parameter	Difference from measurement
Initial critical boron	-2 ppm B
Total / Max bank worth	0.7 ± 1.4% / 3.0%
Isothermal temperature coefficient	-0.8 pcm/°F
HZP critical boron concentrations	-7 ± 3.3 ppm B
At-power critical boron concentrations	-37 ± 11.1 ppm B
In-core detector segments: total / radial / axial RMS	4.4% / 2.6% / 2.5%
In-core detector currents: all wires / long wires RMS	3.3% / 2.7%

3.4.2.1 Initial criticality

WBN2 first achieved criticality at 2:14 AM on May 23, 2016 by dilution of the primary coolant system (reducing the soluble boron concentration) and withdrawal of the regulating control rod bank, Bank D. The measured boron "endpoint" following complete Bank D withdrawal was 1,089 ppmB, with a measured 10B abundance of 19.76 at%. Comparisons to results from VERA, including the values predicted on March 1, 2016, but adjusted to the measured 10B content, are included in Table 3.24. The original predicted values were from with a previous cross section library, but they are included here as evidence of the predictive capability of VERA when used in a blind test. The Monte Carlo Shift result is calculated by eigenvalue calculation but converted to a boron difference using the MPACT calculated boron worth. The results are very good, but recent enhancements in the MPACT 1-group cross section library have improved consistency with continuous-energy Monte Carlo results, resulting in excellent agreement with the initial plant measurement of criticality conditions.

Table 3.24. Initial all-rods-out critical boron results

	Critical boron concentration (ppm B)	**Difference (ppm B)**
Measured	1,089	–
Original prediction	1,072	**-17**
Latest MPACT	1,087	**-2**
Shift	1,087	**-1**

3.4.2.2 Control bank worth measurements

Following initial criticality, WBN2 commenced with typical startup physics testing in which control bank worth and the temperature coefficient of reactivity were measured. Bank worth measurements were performed using the dynamic rod worth measurement (DRWM) technique, in which the control banks are moved quickly in and out of the reactor core individually, and a reactivity computer estimates the reactivity worth from the ex-core detector response and the time-dependent kinetics data provided by licensed core design methods. The VERA bank worths were performed by calculation of steady-state eigenvalues with each bank fully inserted and fully withdrawn. The measured data, the original predictions, and the latest VERA bank worths and their relative errors compared to measurements are shown in Table 3.25 and Figure 3.33. Acceptance criteria are typically 15% for a single bank and 10% for the total worth, and the criteria for low worth banks can be even greater. Therefore, these results are considered to be excellent for this type

of benchmark. It should be noted that the Shift Monte Carlo calculations were performed with 10 billion particle histories using 2,000 cycles and 500 inactive cycles.

Table 3.25. Control bank worth results

Control bank	Measured (pcm)	Original prediction (pcm)	Latest MPACT (pcm)	Shift (pcm)	Original prediction error	Latest VERA error	Shift error
Bank D	1,304	1,320	1,311	1,322	1.2%	0.5%	1.4%
Bank C	1,061	1,078	1,065	1,076	1.6%	0.4%	1.4%
Bank B	794	821	815	816	3.4%	2.6%	2.7%
Bank A	910	912	904	913	0.2%	-0.6%	0.3%
Bank SD	438	452	451	449	3.3%	3.0%	2.6%
Bank SC	447	452	450	450	1.0%	0.7%	0.6%
Bank SB	1,056	1,072	1,063	1,070	1.5%	0.7%	1.4%
Bank SA	424	420	420	415	-1.0%	-1.1%	-2.1%
Total	**6,435**	**5,426**	**6,478**	**6,512**	**1.4%**	**0.7%**	**1.5%**
St. Dev.					**1.4%**	**1.4%**	**1.5%**

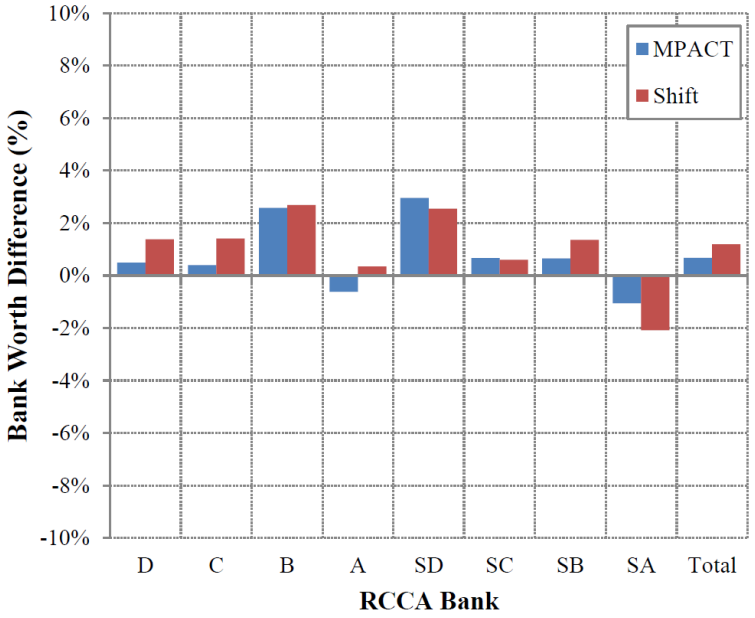

Figure 3.33. Control rod bank worth errors (%).

3.4.2.3 Isothermal temperature coefficient

The WBN2 isothermal temperature coefficient (ITC) was also calculated by reactivity measurement during small perturbations in primary coolant temperature. The amount of temperature change (one heat-up and one cooldown) was approximately ±1 °F. The original prediction with VERA was based on ±5 °F perturbations, whereas the most recent result is based on the actual temperature variations. These results show good agreement with plant data and are well within the typical acceptance criteria of 2 pcm/°F.

Table 3.26. Isothermal temperature coefficient results

	Coefficient (pcm/°F)	**Difference (pcm/°F)**
Measured	-5.3	–
Original prediction	-6.1	**-0.8**
Latest MPACT	-6.1	**-0.8**

3.4.2.4 Power distribution comparisons

Neutron flux measurements are taken inside the WBN2 reactor core using a fixed self-powered in-core detector system. Unlike WBN1, in-core detectors are not movable. They are installed at fixed positions in the core for the entirety of the fuel cycle. In MPACT, the 3D detector response distributions were calculated from the neutron absorption reaction rate of vanadium at the pin-wise local conditions and 51-group neutron flux levels at any user-specified core location. As discussed in Godfrey et al. [34], several subtleties limited the consistency of the detector modeling: for example, MPACT does not explicitly model the five vanadium wires and their currents; nor does it account for the time-dependence in the instrument response from the delayed beta decay. Nonetheless, modeling was performed as physically consistent as possible, and the relative vanadium emitter currents were reconstructed from VERA output by post-processing the detailed 3D detector response edits from MPACT. Figure 3.34 shows a VERAView screenshot of the default detector response distribution from MPACT. The 3D distribution is represented by a 1D axial plot of the response in each core location containing an instrument.

To estimate the relative current of the vanadium wires, which have different lengths and axial positions than the MPACT axial mesh, a cubic spline (piece-wise third order polynomial) is used to fit the 50 level detector response and to extend the calculated distribution above and below the active fuel column. For reliability, the highest and lowest extents of the spline are replaced with linear extrapolation. An example of this calculation is shown below in Figure 3.35 using core location F-7 (shown in Figure 3.34) for demonstration. The blue circles are the mesh-centered volume-average vanadium detector response values from MPACT, and the red curve is the cubic spline representation with extrapolation. Agreement between the two is very good, with only 0.25% error in the total integrated response within the active fuel region.

Overall, the WBN2 startup simulations and subsequent analyses showed very good agreement between the measured and predicted results and provided an important contribution to the validation database for MPACT.

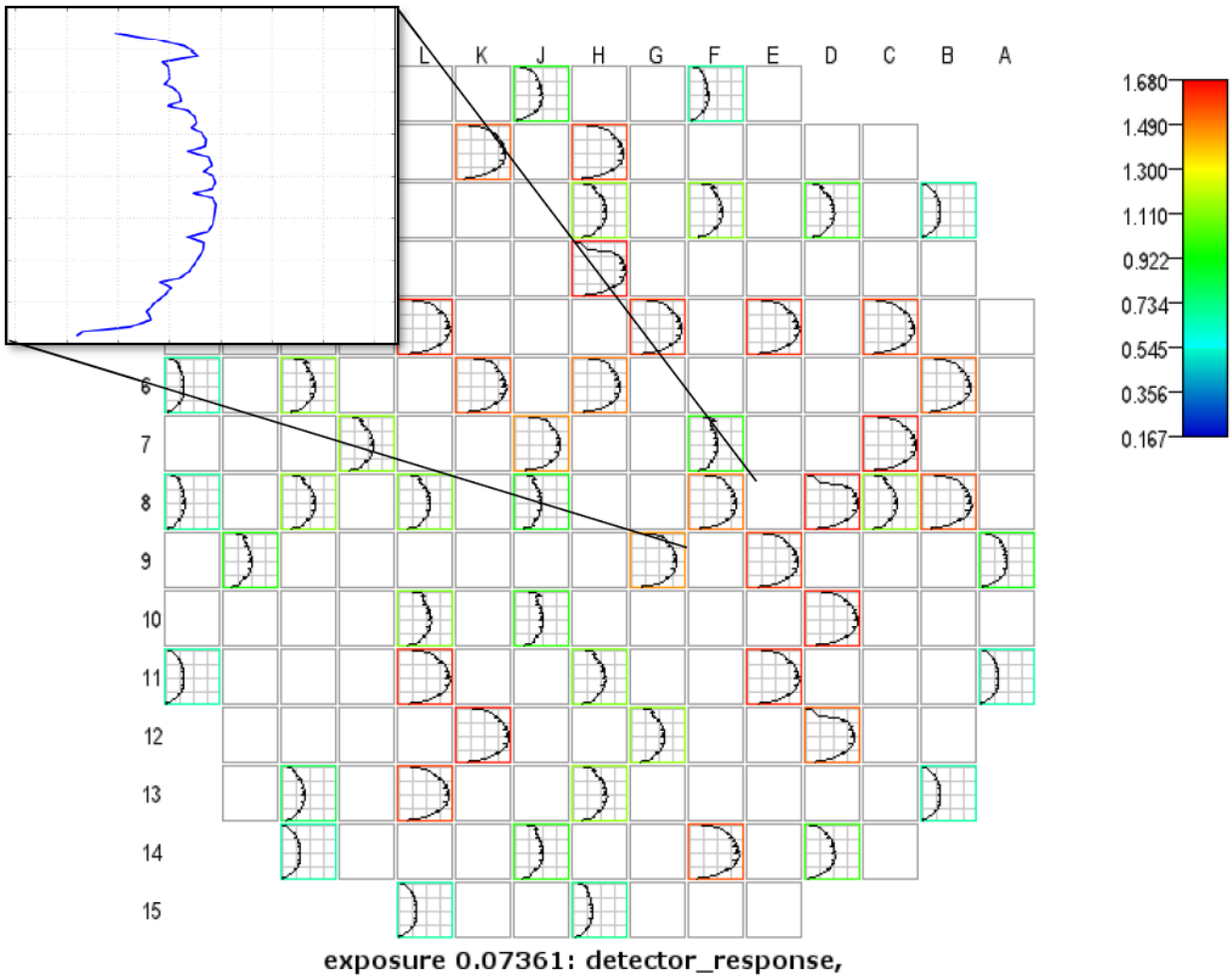

Figure 3.34. Raw detector response output from VERA for the first WBN2 flux map.

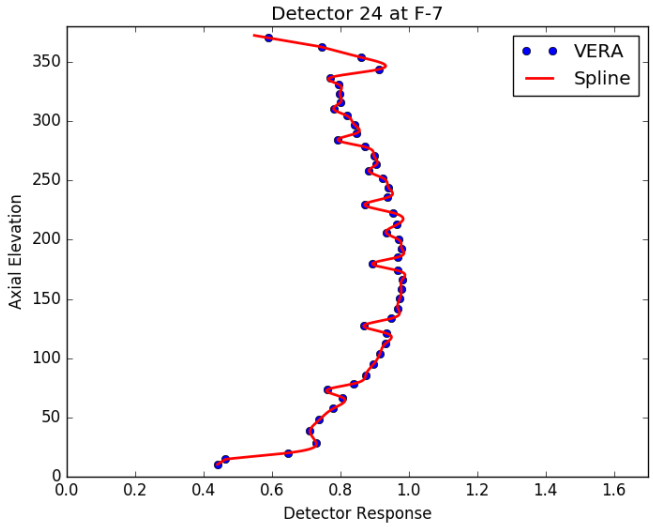

Figure 3.35. Example cubic spline fit of raw detector response output from VERA.

3.5 POST-IRRADIATION EXAMINATION (PIE) / PIN RESOLVED

The purpose of the PIE portion of the validation plan proposed by Godfrey [4] is to demonstrate the accuracy of the isotopic depletion and decay calculations in VERA-CS. This is important in MPACT, because it is possible to perform a more detailed comparison to measured data than that typically performed through the capability to explicitly model 3D pin-wise powers, isotopic depletion, and decay. The objectives are (1) to perform comparisons with data that include radiochemical assay characterizations used to benchmark pin cell depletions or lattice physics codes, and (2) to include axial gamma scans, radial pellet gamma scans, and inferred burnup distributions. The work performed in FY16 focused on a publicly available set of PWR PIE measurements [35].

3.5.1 PWR PIE Data

As shown in Table 3.27, three sets of RCA measurements were selected for this task. The modeled assemblies include 17×17 Westinghouse (WEC), 15×15 WEC and 14×14 Combustion Engineering (CE) designs. Fuel samples were taken from UO_2 and UO_2-Gd_2O_3 (gadolinia) -loaded fuel rods with enrichments varying from 2.63 to 4.3% ^{235}U. Selected samples covered fuel burnups ranging from low (16.44 GWd/MTU) to high (67.9 GWd/MTU).

Table 3.27. PWR fuel samples

Reactor	Assembly type	Number of samples	Enrichment (^{235}U %)	Fuel type	Burnup (GWd/MTU)
Takahama-3[a]	17×17 WE	3	4.11–2.63(Gd_2O_3)	UO_2, UO_2-Gd_2O_3	16.44–47.5
Calvert Cliffs-1[b]	14×14 CD	2	3.04	UO_2	27.35–44.34
Göesgen[c]	15×15 WE	3	4.3	UO_2	46-67.9

[a]Nakahara, 2002 [36], [b]Guenther, 1988 [37], [c]Alejano, 2011 [38]

Each assembly was modeled based on the assembly description specified by the experiment. A reflective boundary condition was used in all models, which implies that the neighboring assemblies are identical in burnup and enrichment. However, it should be noted that the effect of neighboring assemblies on isotopic distributions is non-negligible for corner fuel pins in uranium oxide (UOX)-loaded lattices and all peripheral fuel pins in MOX-loaded lattices.

Only lattice average state parameters were provided, so the fuel and moderator temperatures, boron concentration, and moderator density were assumed to be uniform across all fuel rods. This assumption generally has a negligible effect on isotopic distributions, but a detailed uncertainty analysis was not performed. The power history of each sample was provided based on core simulator data, and the reported sample burnups were calculated based on the measured 148Nd concentrations. Because MPACT only accepts the assembly power history for depletion calculations, the specified fuel pin power history was used as an initial guess, and the assembly power level was increased/decreased iteratively until the calculated and measured burnups were in agreement within 1% for the fuel sample. The MPACT solution/discretization parameters used in the modeling are shown in Table 3.28.

Table 3.28. MPACT solution/discretization parameters for PIE validation

Solution parameter	PWR
Guide tube/water rod mesh	3
Fuel mesh	3
Number of inner iterations	1
Up-scatter iterations	1
Max. number of outer iterations	500
Cross section library	mpact47_70s_v4.0_11032014.fmt

3.5.1.1 Takahama-3

The Takahama-3 data [36] were taken from three fuel rods—SF95, SF96, and SF97—which were removed from two 17 × 17 WE fuel assemblies. Sixteen samples were measured from the three fuel rods, but only three samples were modeled for this initial validation. Two of the modeled fuel samples were taken from a gadolinia-bearing fuel rod (SF96). Because of their burnable absorber content, these two samples offer a useful validation opportunity for PWR fuel depletion. Modeled lattice segments and locations of the measured rods are shown in Figure 3.36. Sample specifications are provided in Table 3.29.

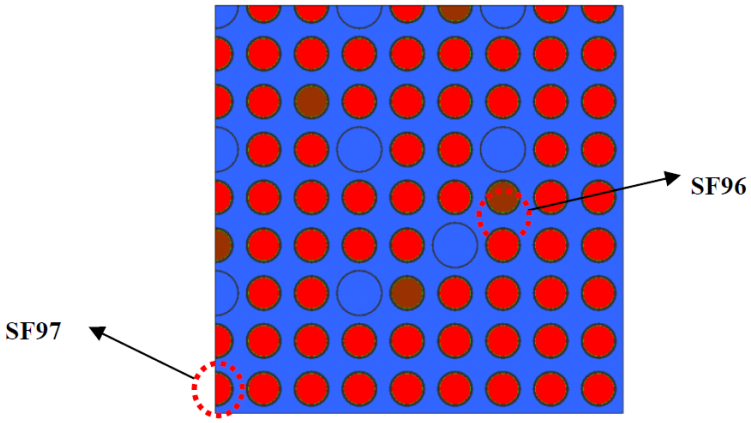

Figure 3.36. Takahama-3 measured rod locations.

Table 3.29. Takahama-3 fuel samples

Sample name	Enrichment %	Fuel type	Burnup (GWd/MTU)	Sample location (cm from the bottom)
SF96-2	2.63 (^{235}U)-5 (Gd_2O_3)	UO_2-Gd_2O_3	16.44	347
SF96-4	2.63 (^{235}U)-5 (Gd_2O_3)	UO_2-Gd_2O_3	28.91	167
SF97-5	4.11	UO_2	47.5	88.1

Relative percent differences between calculated (C) and measured (M) isotope contents are shown in Figures 3.37 through 3.39; SCALE 6.1 TRITON/NEWT depletion results are also shown in the same figures for comparison. MPACT results show good agreement with the measurements for important actinides. ^{235}U, ^{239}Pu, ^{241}Pu, and ^{240}Pu all show less than 5% difference for SF96 samples. Although relative differences for SF97 sample isotopics are relatively higher, the only significant difference is in ^{241}Pu (7%).

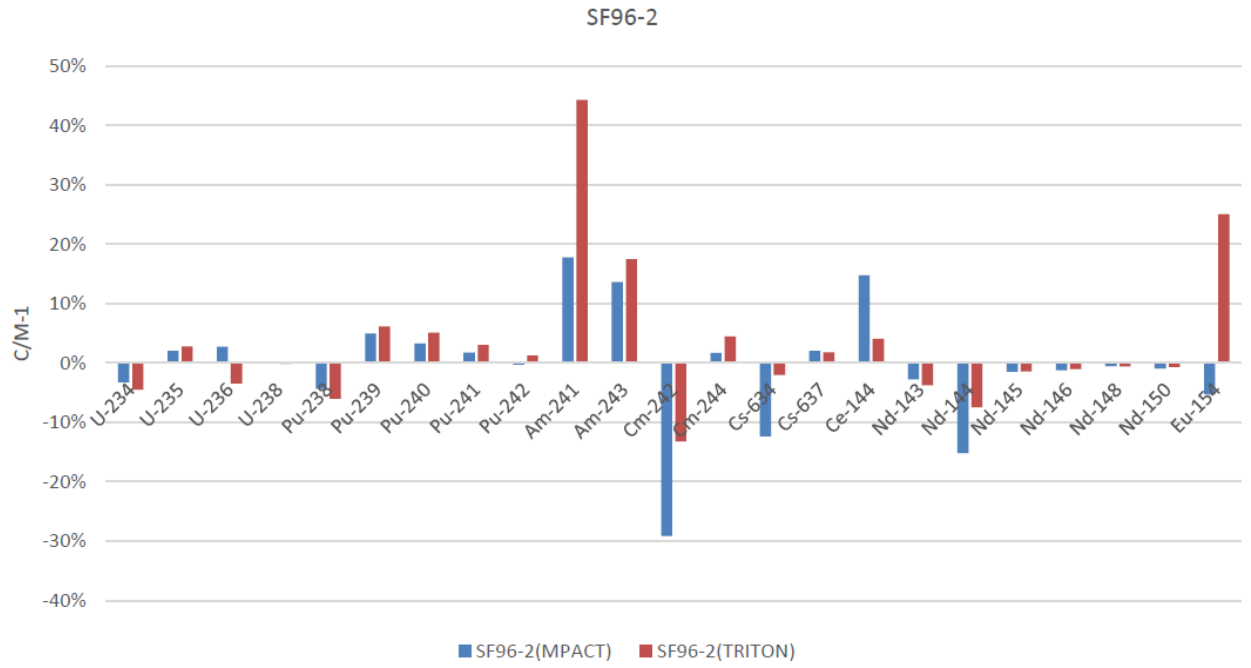

Figure 3.37. Takahama-3 SF96-2 sample isotopic comparison.

Figure 3.38. Takahama-3 SF96-4 sample isotopic comparison.

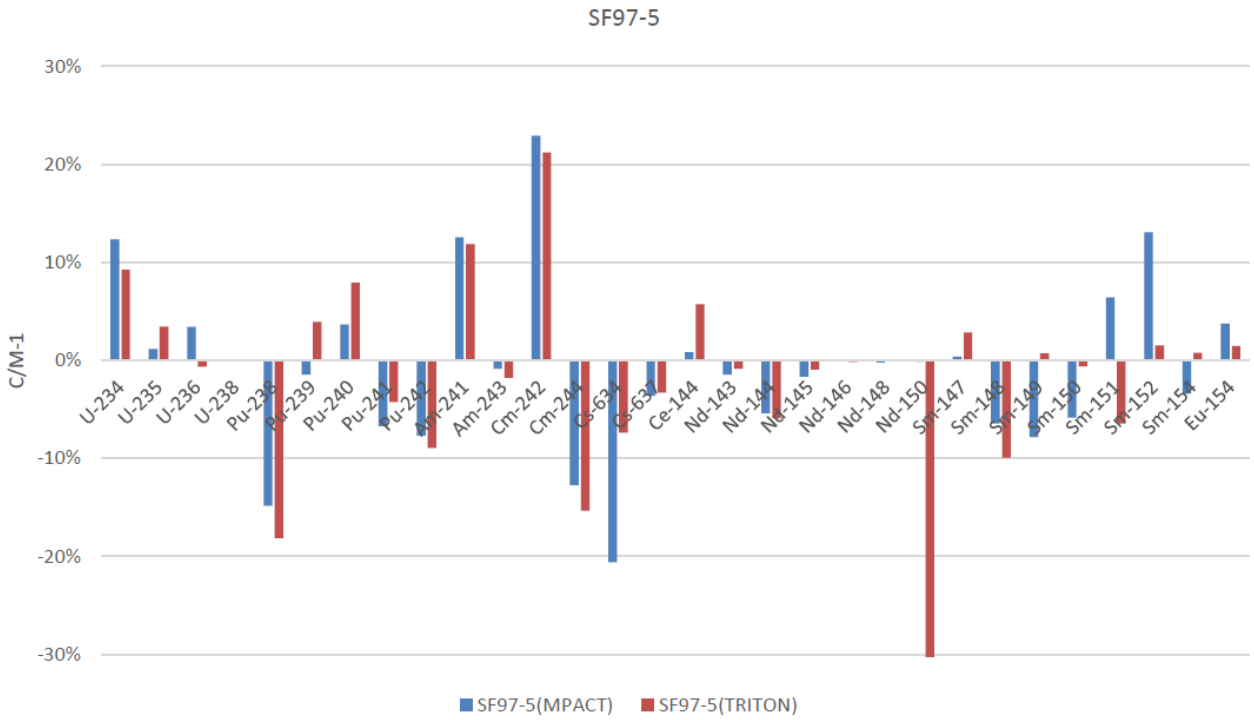

Figure 3.39. Takahama-3 SF97-5 sample isotopic comparison.

3.5.1.2 Calvert Cliffs-1

The Calvert Cliffs-1 core consisted of 14 × 14 CE fuel assemblies which contained large guide tubes occupying four rod locations in each assembly. One fuel rod was selected from three fuel assemblies, and three samples were taken from each rod and measured at the Material Characterization Center (MCC) of Pacific Northwest Laboratory (PNL) [37]. The two samples with the highest enrichments were selected for analysis in this report. The modeled lattice segments and measured rod locations are shown in Figure 3.40, and the specifications of the samples are listed in Table 3.30. Relative isotopic differences are shown in Figures 3.41 and 3.42, and SCALE 6.1 TRITON/NEWT, SCALE 6.2 TRITON/ NEWT, and SCALE 6.2 CE KENO depletion results are included for comparison. Again, MPACT isotopic predictions are in good agreement with measurements for all U and Pu vectors except ^{238}Pu, for which the difference was as large as 10% but is similar to SCALE 6.1 TRITON results.

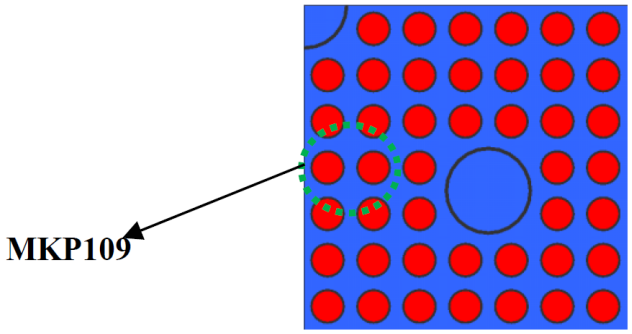

Figure 3.40. Calvert Cliffs-1 measured rod locations.

Table 3.30. Calvert Cliffs-1 fuel samples

Sample name	Enrichment %	Fuel type	Burnup (GWd/MTU)	Sample location (cm from the bottom)
MKP109-2	3.038	UO_2	37.12	280
MKP109-3	3.038	UO_2	44.32	164

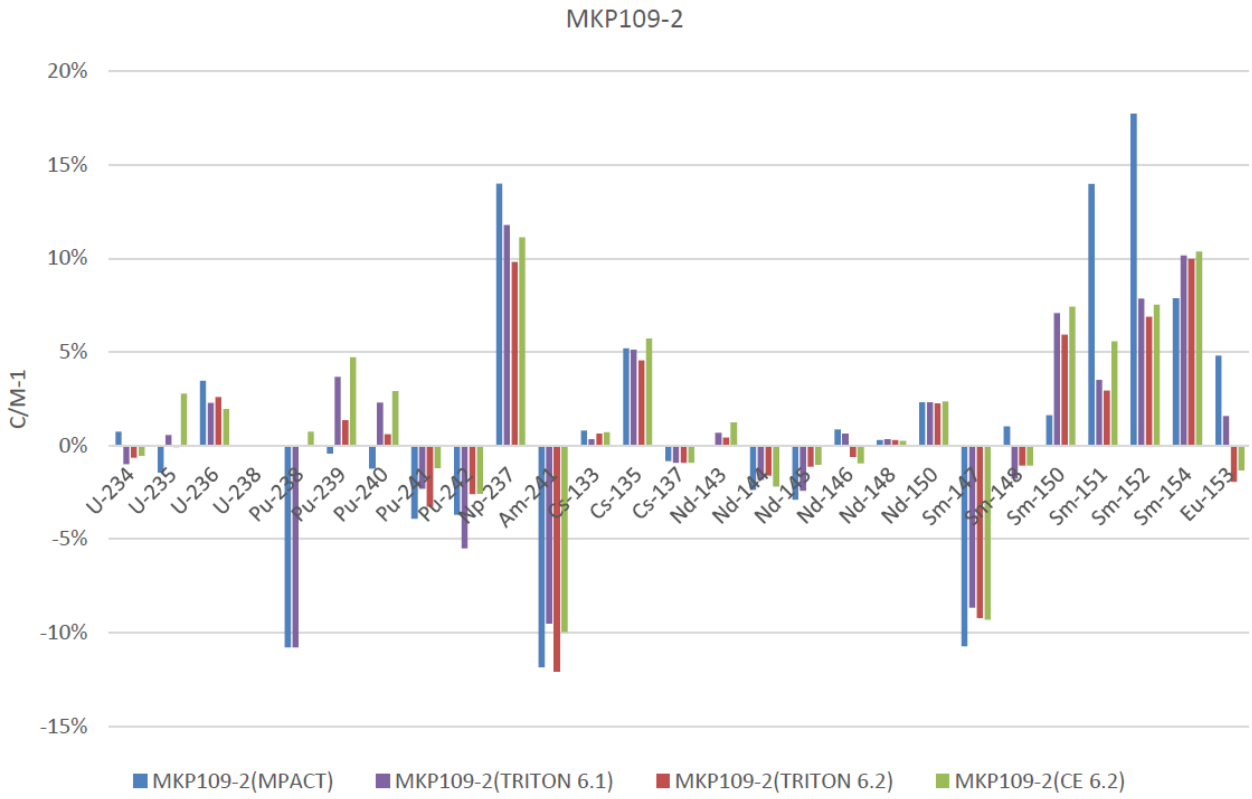

Figure 3.41. Calvert Cliffs-1 MKP109-2 sample isotopic comparison.

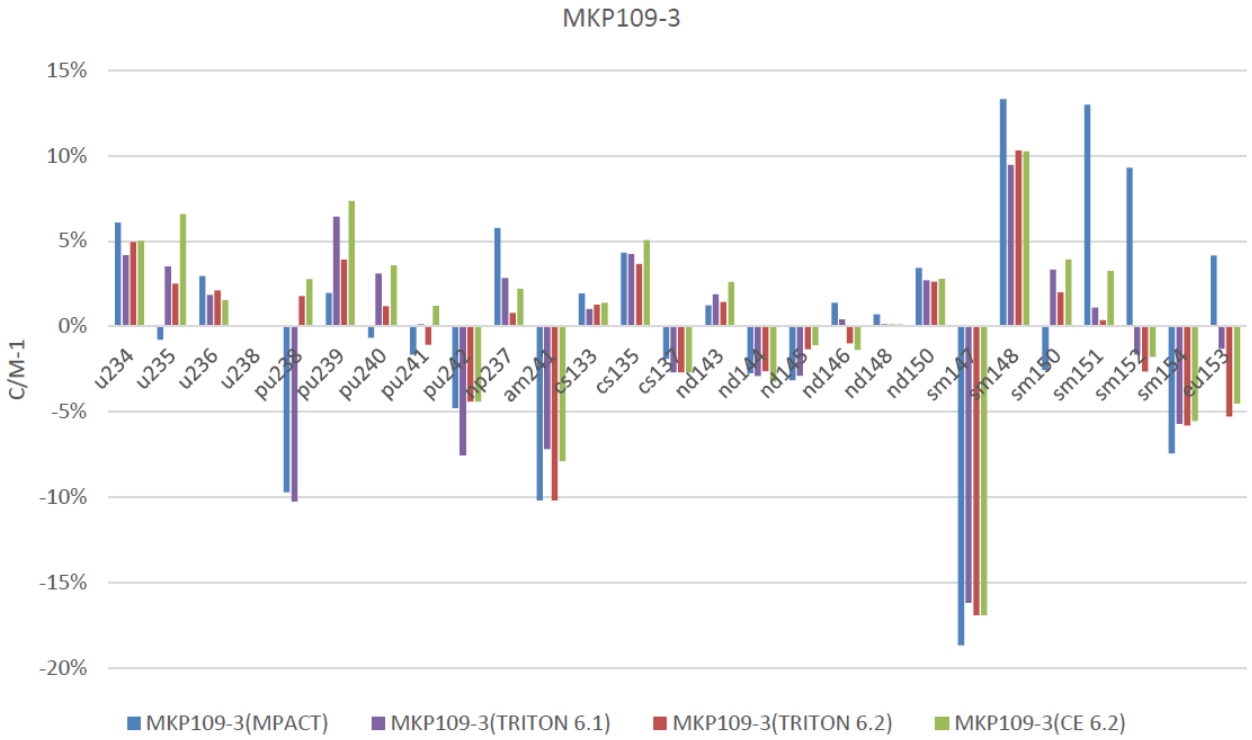

Figure 3.42. Calvert Cliffs-1 MKP109-3 sample isotopic comparison.

3.5.1.3 Göesgen

The Göesgen measurements were performed as part of the MALIBU program [38] and are some of the most recent and detailed PIE measurements available. Samples were taken from UOX and MOX assemblies, and each sample was sent to two of the three participating labs (SCCA, PSI, and CEA). Based on the comparison of the reported results, a recommended set of results was provided. The modeled 15×15 UOX lattice and the measured fuel rod location are shown in Figure 3.43, and the specifications of the samples are listed in Table 3.31. Because the results of the GGU2 samples from two labs (PSI, and CEA) differ significantly, they are not as reliable as the GGU1 sample results, and they are considered as two different samples (GGU2-1, GGU2-2).

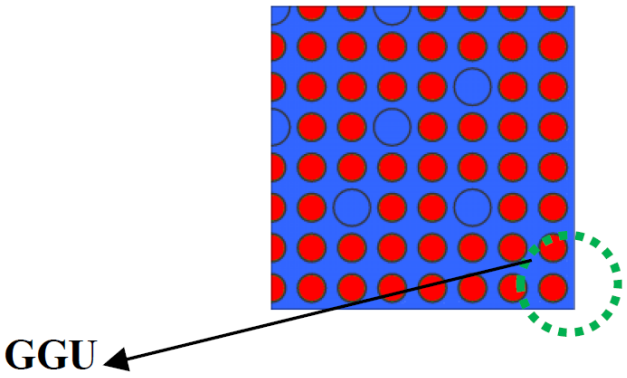

Figure 3.43. Göesgen measured rod locations.

Table 3.31. Göesgen fuel samples

Sample name	Enrichment %	Fuel type	Burnup (GWd/MTU)	Sample location (cm from the bottom)
GGU1	4.3(^{235}U)	UO_2	67.9	237
GGU2-1	4.3(^{235}U)	UO_2	49	26.6
GGU2-2	4.3(^{235}U)	UO_2	46	26.6

Relative differences between MPACT results and measurements are show in Figures 3.44–3.46, which also include SCALE 6.1 TRITON/NEWT results. The GGU1 and GGU2-2 results are consistent with Takahama-3 and Calvert Cliffs-1 results. Except for ^{238}Pu, U, and Pu vectors show less than 5% difference with measurements. GGU2-1 results show elevated differences for ^{235}U (-8%) and ^{239}Pu (-13%) isotopes. These are the only measurements in which the SCALE 6.1 TRITON/NEWT isotope predictions are better than those from MPACT. Future work will include a detailed assessment of the MPACT model for this case.

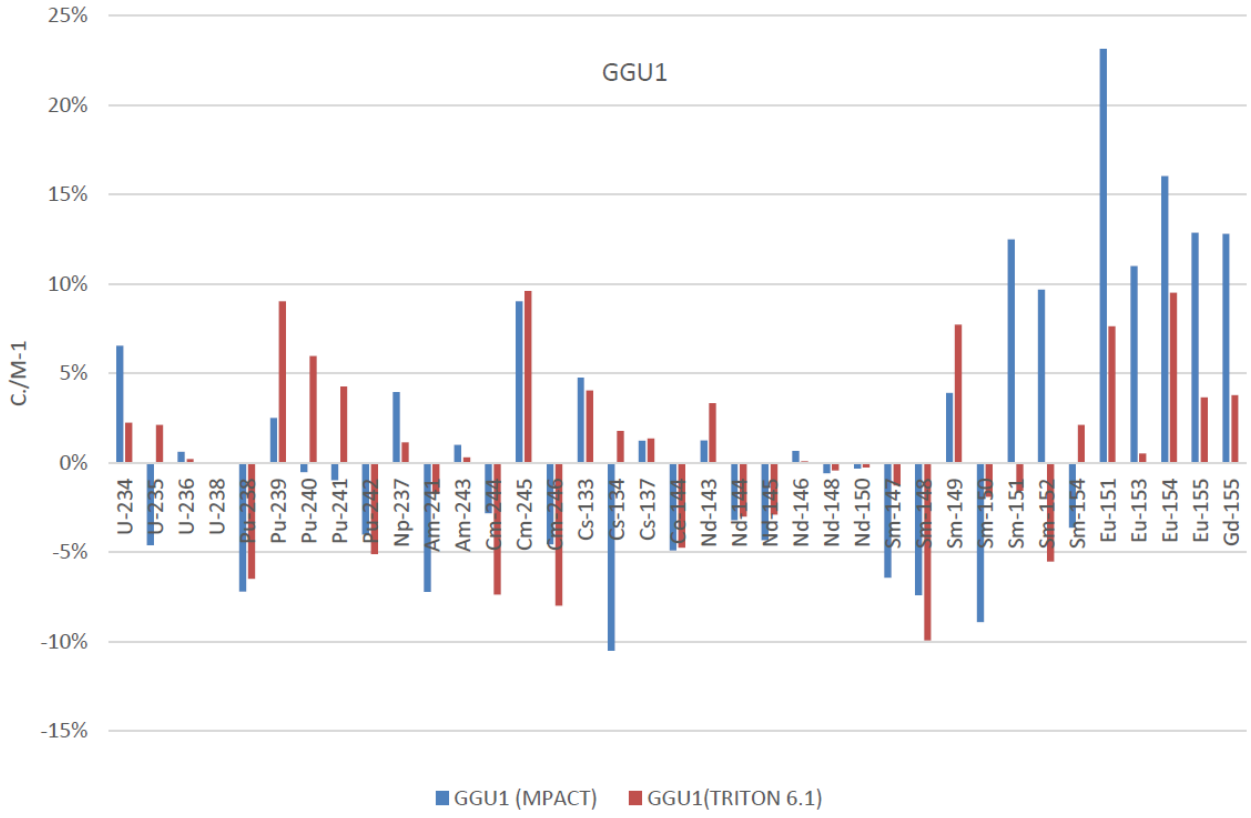

Figure 3.44. Göesgen GGU1 sample isotopic comparison.

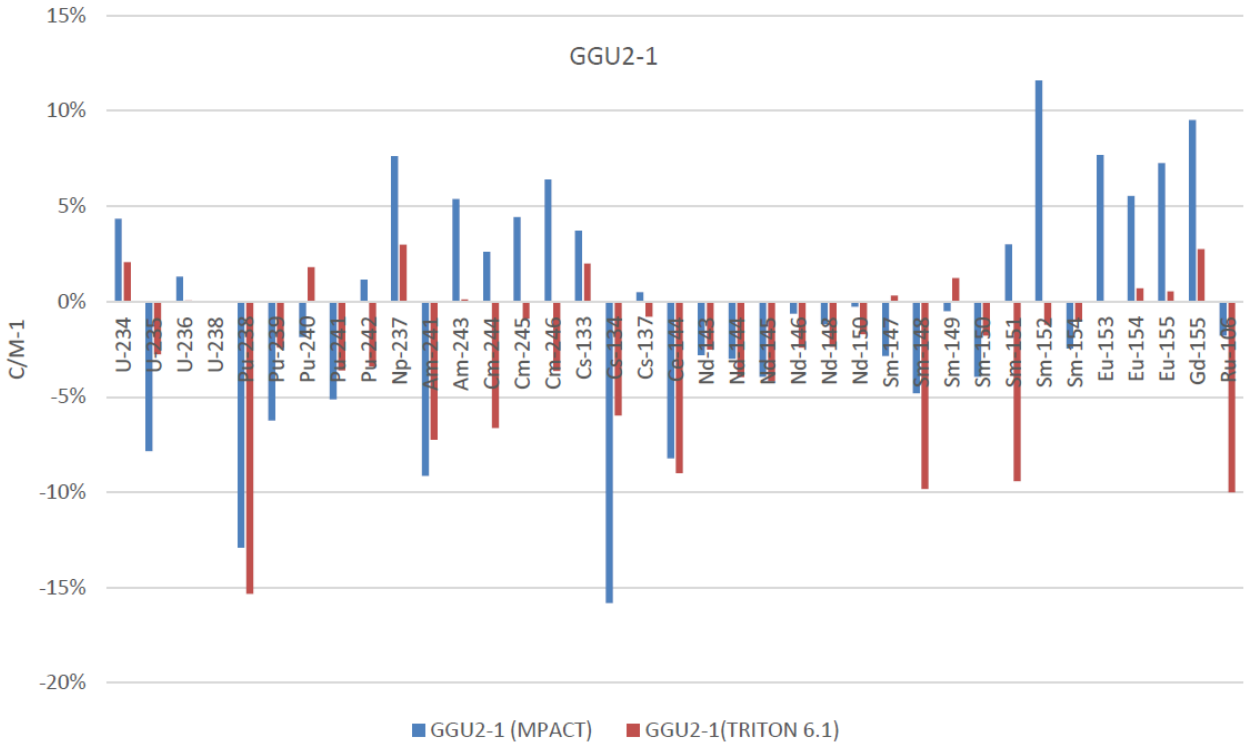

Figure 3.45. Göesgen GGU2-1 sample isotopic comparison.

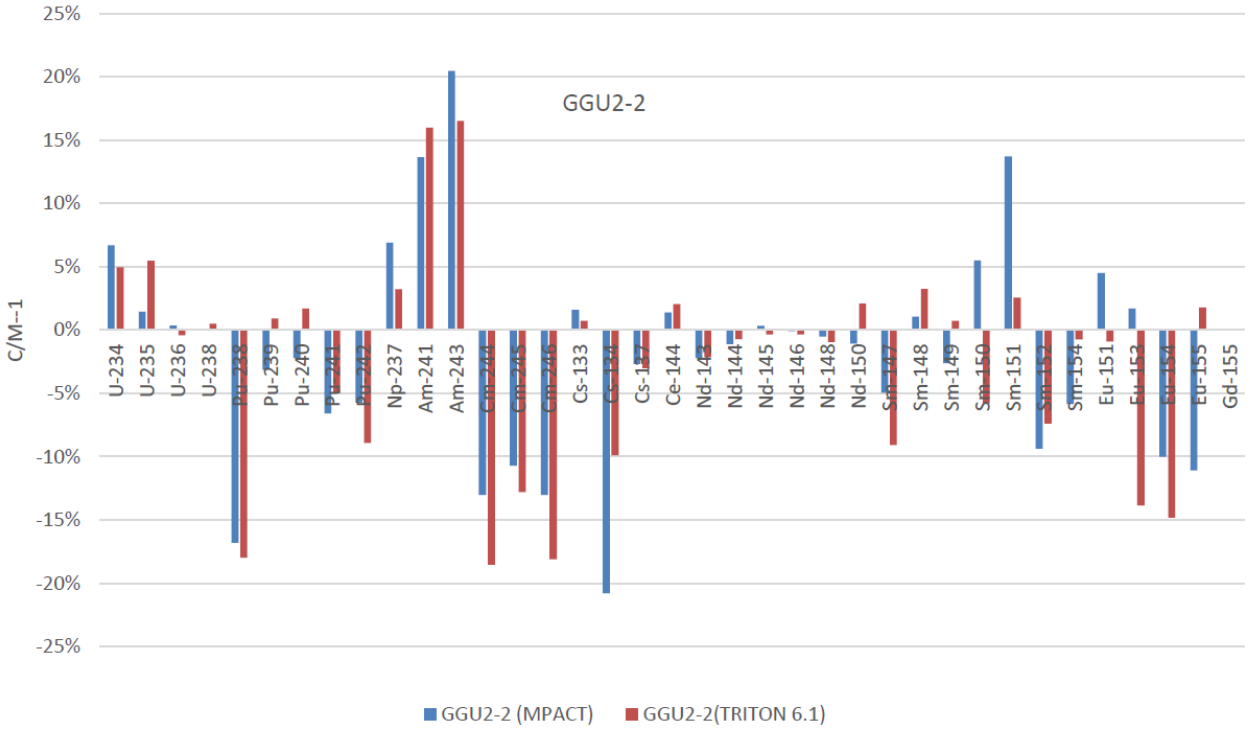

Figure 3.46. Göesgen GGU2-2 sample isotopic comparison.

3.5.2 Pin-Resolved Validation

The validation of the pin-resolved capability in MPACT has been limited by the availability of experiments and measurement techniques that provide such detailed data. There have been several efforts over the years, including the work performed by Macku et al. [39,40], in which direct and indirect measurements of nuclear reaction rates were made along the radial direction of fuel pellets using the SVEA-96 reactor Optima2, a boiling water reactor (BWR) critical unit type in the PROTEUS complex [41]. In this work, direct measurements of capture reaction rate were made in the ^{238}U foils (C8) and fission measurements in ^{235}U foils (F5) that had been irradiated between the fuel rod pellets. After irradiation, the foils were "cut"into rings and measured separately, enabling sampling of four different radial regions of the fuel. The results of these measurements were compared to those calculated by the MCNP-4C [42] code and the Casmo-4 code [43]. This type of measurement induced high uncertainty, because part of the irradiated material was lost during the cutting process. In the second study, copper foils were used within the fuel rods to determine the spatial distribution of ^{63}Cu(n,c)^{64}Cu reaction. This reaction is of interest because the 1/v cross section region is similar to the ^{235}U fission reaction. The results were compared to those calculated with the MCNP-4C code. Although the shape of the cross section of ^{63}Cu(n,c) and ^{235}U(n,f) is similar below 0.3 eV, the radial fission profile was not fully determined. However, the initial focus of MPACT development has been on the PWR, so the PROTEUS BWR experiments were not of primary interest for validation of the pin resolution in MPACT. Instead, a series of experiments and measurements performed at the IPEN/MB-01 research reactor facility, which simulates a PWR lattice, were reviewed, and work has been performed on these experiments to validate the pin-resolved capability in MPACT. The following section describes the IPEN experiments and summarizes the results of measurements as reported in Mura et al. [44] The modeling of these experiments with MPACT will then be discussed.

3.5.2.1 IPEN

The IPEN/MB-01 research reactor facility is part of the Center for Nuclear Engineering, which provided research and technological development support for the Brazilian Nuclear Program. A complete description of the IPEN/MB-01 reactor can be found in the handbook by Briggs [45]. A new experimental approach at IPEN is of interest for the validation of MPACT to experimentally determine the reaction rate along the pellet's radius. The methodology employs concentric hollow cylindrical lead collimators, together with gamma-ray spectrometry, using a special high purity germanium (HPGe) detector for the discrimination of very low gamma energy emitted by ^{239}Np and ^{99}Mo. The ^{238}U neutron capture and total fission rates were inferred, respectively, from the 106.2 keV gamma emitted by ^{239}Np and from the 140.51 keV gamma-ray emitted by ^{99}Mo. These lower gamma-ray energies allowed the thickness of the lead collimator to be small enough so that the correction factors applied to the procedure were minimized. However, the initial focus of MPACT development has been on the PWR instead of the BWR. Therefore, the PROTEUS experiments were not of primary interest for validation of the pin resolution in MPACT. Instead, a series of experiments and measurements performed at the IPEN/MB-01 research reactor facility, which simulates a PWR lattice, were reviewed and simulated to validate MPACT. The following section describes the IPEN intra-pin reaction rate experiments and summarizes the results of measurements as reported in the literature [44, 46]. The intra-pin reaction rate experiments performed at IPEN were assessed to be well defined for a benchmark and are published in the 2018 International Reactor Physics Experiment Project (IRPhEP) handbook as the IPEN(MB01)-LWR-RESR-019 benchmark.

The measured values of the total fission rates are mainly from the thermal fissions in ^{235}U, because in the IPEN/MB-01 reactor, nearly 85% of the total fissions occur in the thermal neutron energy region. The nuclear reaction rates along the radius of the fuel pellets are obtained using the activation analysis technique, employing a very thin UO_2 disk (about 0.9 mm thickness and 4.3% enrichment obtained from the UO_2 pellets of the facility). The UO_2 disk was inserted between the tenth and eleventh pellets of the rod, which is

nearly 105.5 mm from the bottom of the active region of the core. This position is in the asymptotic region of the core and far enough from the control banks to prevent undesirable flux perturbation. The experimental fuel rod is irradiated at the central position of the core (position M-14 in Figure 3.47) for 1 hr at 100 W power level (maximum power of the IPEN/MB-01 reactor). The core configuration in this experiment consists of an array of 28 × 26 with 680 fuel rods with 24 Ag–In–Cd control rods, which control the reactivity, and 24 B_4C safety rods kept at a position 19.20 cm above the active region of the core during the experiment. Figure 3.47 shows the radial configuration in the experiments. The measurements of the radiative capture rate in ^{238}U and fission rates in both ^{238}U and ^{235}U required that the UO_2 disk be inserted between the fuel pellets of the fuel rod, as also shown in Figure 3.47.

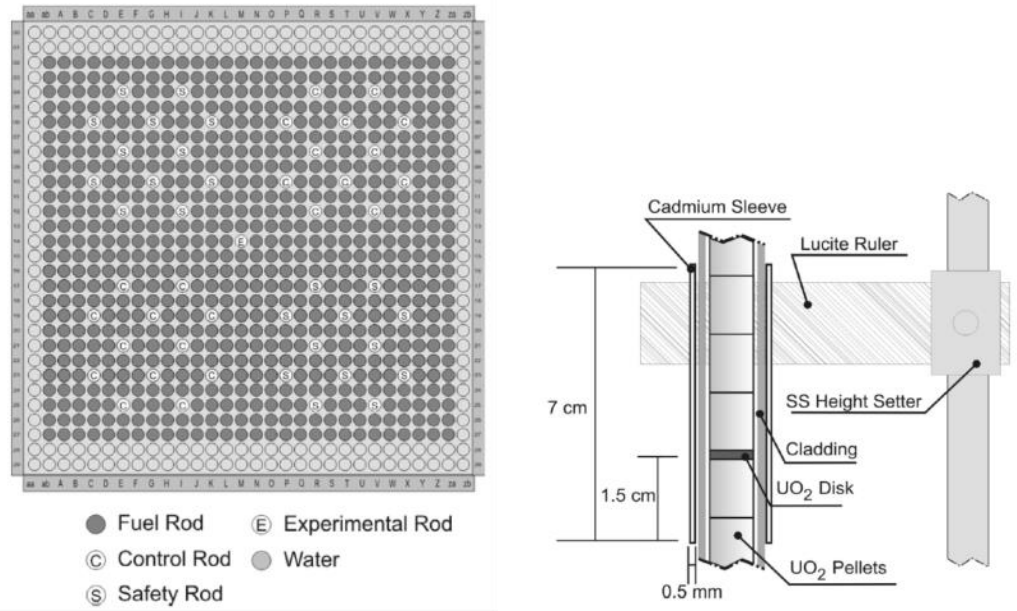

Figure 3.47. IPEN/MB-01 core configuration (left) and UO_2 disk configuration (right).

The experiments consisted of two core configurations, each with a different UO_2 disk in the experimental rod. In configuration A, the experimental rod was bare, and in configuration B, the experimental rod was wrapped in a cadmium sleeve which was held in place by a lucite ruler, as seen in Figure 3.48. Gamma spectrometry of each disk was performed by the gamma detection system (GDS), as shown in Figure 3.48. The GDS is composed of a very thin set of Pb collimators and a special HPGe detector. Measurements were performed at six radial locations, as shown in Figure 3.47. The results of these measurements may be seen in Tables 3.32 and 3.33.

Theoretical analyses were also performed using MCNP-5 and the ENDF/B-VII.0 library. The geometric model (both axial and radial) and the material and geometric data applied in the theoretical analysis were based on work by Dos Santos et al. [47], which is a full 3D core modeling of the IPEN/MB-01 reactor. The KCODE option was used to calculate reaction rates and to simulate the irradiation of the target over several fission cycles. The tally F4 was used to calculate the reaction rates. Six tallies were created to represent the regions measured within the collimators. The results are the reaction rates of a given type occurring in a cell in relative units. The results from the theoretical approach based on the MCNP-5 code using the ENDF/B-VII.0 library are shown for the normalized $^{238}U(n,c)$ reaction in Tables 3.34 and 3.35. Similarly, the results for the normalized fission reaction are shown in Tables 3.36 and 3.37.

The experimentally and theoretically determined $^{238}U(n,c)$ reaction rate in each disk region is shown in

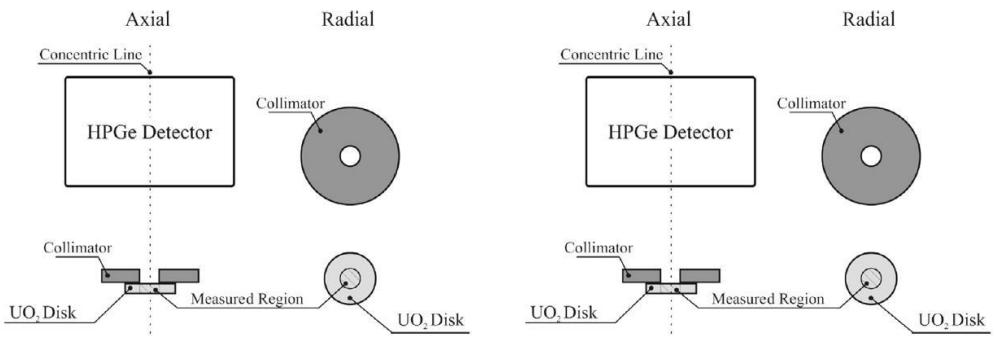

Figure 3.48. The gamma detection system (left) and pin measurement locations (right).

Table 3.32. The experimentally determined relative ^{238}U capture reaction rate and uncertainty for each configuration and disk region

UO_2 disk region	Relative reaction rates		
	Configuration A	Configuration B	Thermal capture
1	0.124 ± 0.007 (5.6%)*	0.126 ± 0.004 (3.2%)	0.115 ± 0.012 (10.4%)
2	0.137 ± 0.006 (4.4%)	0.131 ± 0.004 (3.1%)	0.159 ± 0.010 (6.3%)
3	0.145 ± 0.006 (4.1%)	0.139 ± 0.003 (2.2%)	0.171 ± 0.010 (5.8%)
4	0.155 ± 0.005 (3.2%)	0.149 ± 0.004 (2.7%)	0.178 ± 0.011 (6.2%)
5	0.173 ± 0.005 (2.9%)	0.169 ± 0.006 (3.6%)	0.187 ± 0.010 (5.3%)
6	0.265 ± 0.009 (3.4%)	0.285 ± 0.009 (3.2%)	0.190 ± 0.017 (8.9%)

*Uncertainties are 1-σ

Figures 3.49 and 3.50, with the (C-E)/E values in Table 3.38. Likewise, experimentally and theoretically determined fission rates are shown in Figures 3.51 and 3.52, with (C-E)/E values in Table 3.39.

Table 3.38 shows that the MCNP-5 calculated relative values for the ^{238}U(n,c) are in good agreement with the experimental values, with the exception of region 1 for configuration A. The (C-E)/E values for all regions fall inside of 3 standard deviations, and most values fall within 1 or 2 standard deviations. The IPEN/MB-01 reactor is an experimental facility in which the majority of the reaction rate events occur in the thermal energy region. In this context, ^{235}U plays an important role, because around 86% of the fissions in this nuclide occur in the thermal neutron energy region. Moreover, around 70% of the total neutron absorptions in the thermal neutron energy range are caused by ^{235}U. Consequently, the thermal ^{235}U cross sections play an important role in the spatial and energetic neutron flux in this neutron energy region of the IPEN/MB-01 core. For this reason it is suggested in the literature ([44], [46]) that the source of the discrepancies in the thermal neutron capture in ^{238}U may be credited mostly to the ENDF/B-VII.0 ^{235}U thermal data. Because the cadmium sleeve in configuration B should absorb most thermal neutrons, the configuration B result is less contaminated by errors in ^{235}U thermal data, yielding better agreement with experimental results and radial shape.

Table 3.39 shows that the MCNP-5 results are not consistently in agreement with the experiments. ^{235}U is responsible for more than 97% of the total fissions, with nearly 86% of fissions occurring from thermal neutrons. Therefore, comparison of experimental and theoretical results for the IPEN facility is essentially a comparison of thermal events. Table 3.39 shows that for configuration A, results are mostly within 1 standard deviation, but Figure 3.52 indicates that the radial shape of the theoretical and experimental results differ, particularly in region 5, where there is a peak that was not predicted. As suggested by Mura et al. [44] and in the IRPhEP [46], this unpredicted peak is the result of an error in the ENDF/B-VII.0 ^{235}U

Table 3.33. The experimentally determined relative fission rate and uncertainty for each configuration and disk region

UO_2 Disk Region	Relative reaction rates	
	Configuration A	Configuration B
1	0.143 ± 0.009 (6.3%)*	0.151±0.005 (3.3%)
2	0.159 ± 0.009 (5.7%)	0.154 ± 0.003 (1.9%)
3	0.166 ± 0.010 (6.0%)	0.166 ± 0.003 (1.8%)
4	0.176 ± 0.009 (5.1%)	0.167 ± 0.003 (1.8%)
5	0.182 ± 0.010 (5.5%)	0.196 ± 0.005 (2.6%)
6	0.174 ± 0.010 (5.7%)	0.166 ± 0.003 (1.8%)

*Uncertainties are 1-σ

Table 3.34. The MCNP-5 computed relative ^{238}U capture rate and uncertainty for each disk region in configuration A

Disk region	**Averaged radius (cm)**	**Volume (cm^3)**	**Tally**	**Relative uncertainty**	**Relative reaction rate**	**Uncertainty**
1	0.1733	9.43511E-02	3.69121E-04	0.0046	0.135	0.001
2	0.2450	9.42230E-02	3.84340E-04	0.0041	0.140	0.001
3	0.3000	9.41692E-02	3.99346E-04	0.0040	0.146	0.001
4	0.3470	9.55327E-02	4.20154E-04	0.0038	0.155	0.001
5	0.3869	9.19940E-02	4.60229E-04	0.0042	0.164	0.001
6	0.4243	9.53124E-02	7.03553E-04	0.0062	0.260	0.002
Total		5.65582E-01	4.56487E-04	0.0028		

thermal data. The disagreement between theory and experiment is much larger in the case of configuration B. Mura et al. [44] and [46] the IRPhEP also suggest that the discrepancy results from ENDF/B-VII.0 ^{235}U thermal data. Although cadmium is a very good thermal neutron absorber, the MCNP-5 analysis suggests that epithermal fissions are still contaminated by a small portion of thermal fissions. Approximately 1% of the thermal neutron flux penetrates the cadmium sleeve and induces fissions, but this 1% thermal fission contribution is about 10% of the epithermal fission rates in the 6 disk regions. Therefore, it is suggested that thermal fission contamination and the ENDF/B-VII.0 ^{235}U thermal data are the source of error.

Table 3.35. The MCNP-5 computed relative ^{238}U capture rate and uncertainty for each disk region in configuration B

Disk region	Averaged radius (cm)	Volume (cm^3)	Tally	Relative uncertainty	Relative reaction rate	Uncertainty
1	0.1733	9.43511E-02	2.34288E-04	0.0046	0.127	0.001
2	0.2450	9.42230E-02	2.42130E-04	0.0039	0.131	0.001
3	0.3000	9.41692E-02	2.53312E-04	0.0037	0.137	0.001
4	0.3470	9.55327E-02	2.72142E-04	0.0037	0.150	0.001
5	0.3869	9.19940E-02	3.05619E-04	0.0038	0.162	0.001
6	0.4243	9.53124E-02	5.32180E-04	0.0051	0.292	0.002
Total		5.65582E-01	3.06959E-04	0.0026		

Table 3.36. The MCNP-5 computed relative fission rate and uncertainty for each disk region in configuration A

Disk region	Averaged radius (cm)	Volume (cm^3)	Tally	Relative uncertainty	Relative reaction rate	Uncertainty
1	0.1733	1.34833E-04	4.36715E-04	0.0022	0.157	0.0004
2	0.2450	1.42210E-04	4.45898E-04	0.0018	0.160	0.0004
3	0.3000	1.46034E-04	4.55785E-04	0.0017	0.164	0.0004
4	0.3470	1.48012E-04	4.67219E-04	0.0016	0.170	0.0004
5	0.3869	1.54610E-04	4.79628E-04	0.0016	0.168	0.0003
6	0.4243	1.71373E-04	4.95430E-04	0.0015	0.180	0.0004
Total		1.49528E-04	4.63447E-04	0.0013		

Table 3.37. The MCNP-5 computed relative fission rate and uncertainty for each disk region in configuration B

Disk region	Averaged radius (cm)	Volume (cm^3)	Tally	Relative uncertainty	Relative reaction rate	Uncertainty
1	0.1733	1.34833E-04	6.73416E-05	0.0017	0.166	0.0003
2	0.2450	1.42210E-04	6.73842E-05	0.0014	0.166	0.0003
3	0.3000	1.46034E-04	6.76068E-05	0.0013	0.166	0.0003
4	0.3470	1.48012E-04	6.78549E-05	0.0012	0.169	0.0003
5	0.3869	1.54610E-04	6.80195E-05	0.0012	0.163	0.0003
6	0.4243	1.71373E-04	6.86665E-05	0.0012	0.171	0.0003
Total		1.49528E-04	6.78131E-05	0.0010		

Table 3.38. (C-E)/E values for the ^{238}U(n,c) reaction rate in each disk region

Disk region	Configuration A total (%)	Configuration B cadmium covered (%)	Thermal (%)
1	9.0±5.9	0.9±3.2	30.8±15.2
2	2.3±4.3	0.1±3.1	-0.4±6.3
3	0.2±4.1	-1.0±2.7	-4.9±5.7
4	0.0±3.5	0.3±2.8	-6.1±5.8
5	-5.2±2.6	-4.3±3.4	-10.1±5.4
6	-21.±3.2	2.5±3.5	1.7±10.0

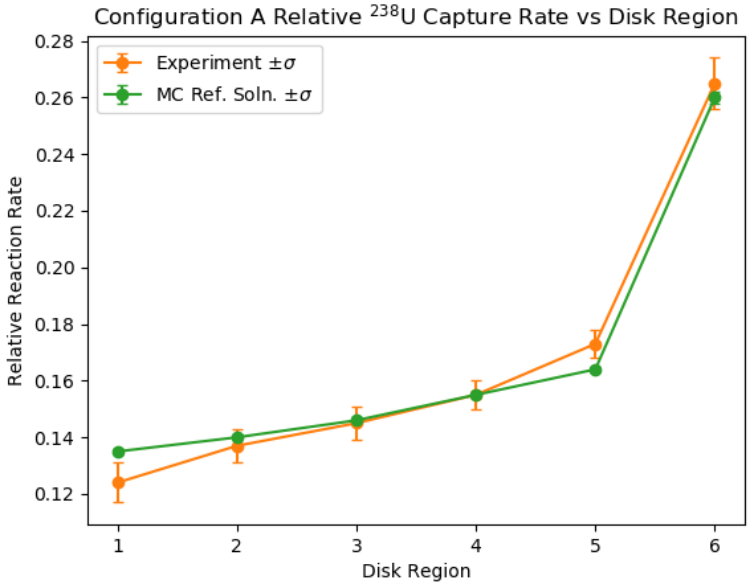

Figure 3.49. Experimental and MCNP-5 computed values for the relative ^{238}U(n,c) reaction rate in each disk region in configuration A

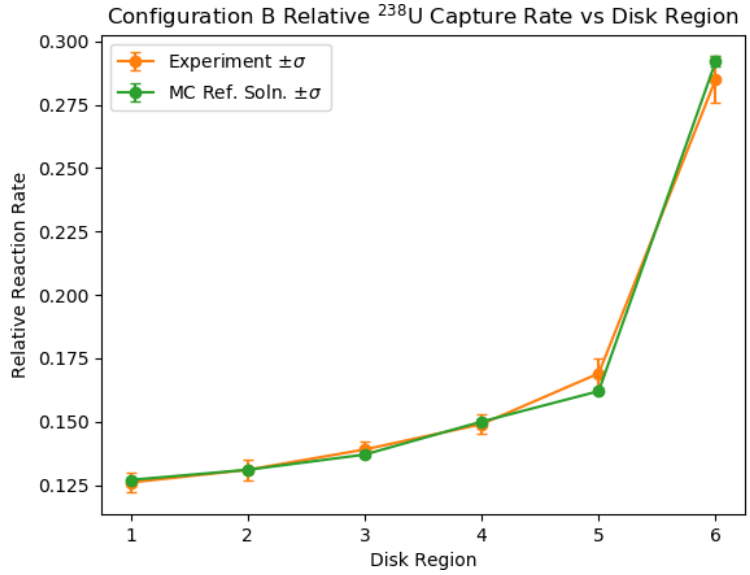

Figure 3.50. Experimental and MCNP-5 computed values for the relative ^{238}U(n,c) reaction rate in each disk region in configuration V

Table 3.39. (C-E)/E values for the total fission rate in each disk region

Disk Region	Total (%)	Cadmium Covered (%)
1	9.6±6.6	9.8±3.8
2	0.9±5.5	7.3±2.0
3	-1.1±5.9	0.1±2.0
4	-3.1±5.2	1.4±1.9
5	-7.7±5.0	-16.9±2.2
6	3.5±5.8	2.8±2.0

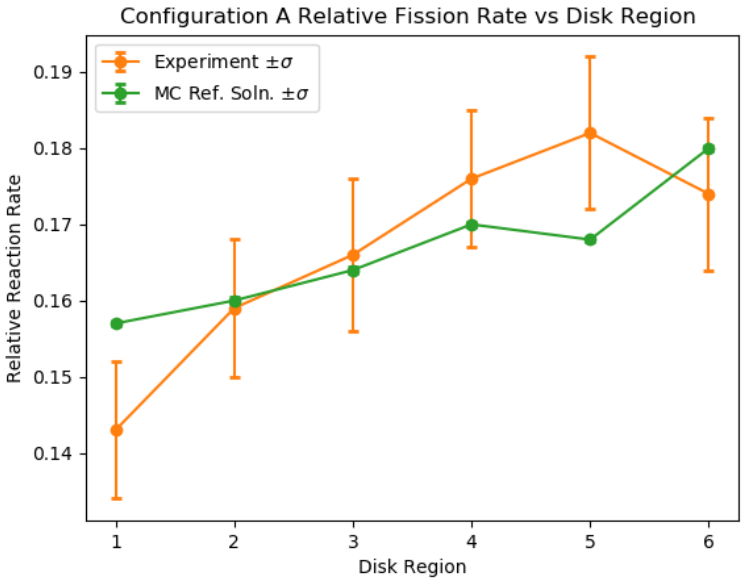

Figure 3.51. Experimental and MCNP-5 computed values for the relative fission rate in each disk region in configuration A.

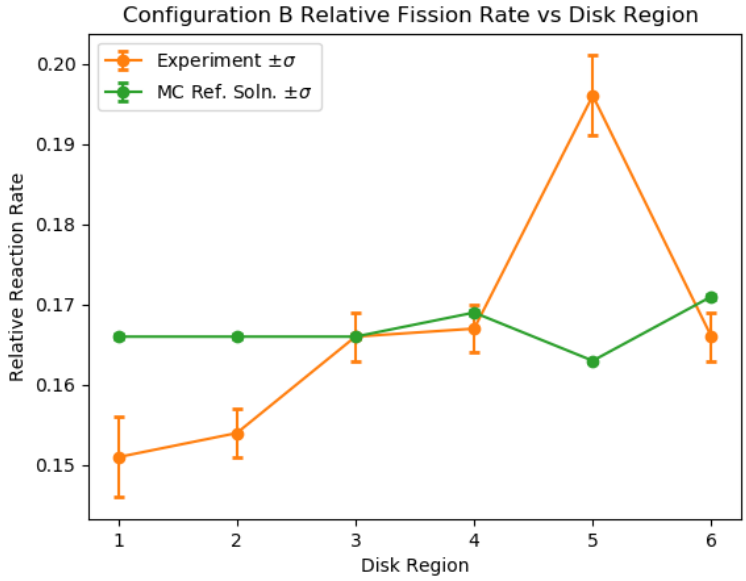

Figure 3.52. Experimental and MCNP-5 computed values for the relative fission rate in each disk region in configuration B.

3.5.2.2 Modeling of IPEN with MPACT

A 3D model of the IPEN facility was developed with the MPACT code. The radial and axial configuration of the facility is shown in Figure 3.53. The fast and thermal flux distribution is shown in Figure 3.54, and the power distribution is presented in Figure 3.55 from the MPACT calculation.

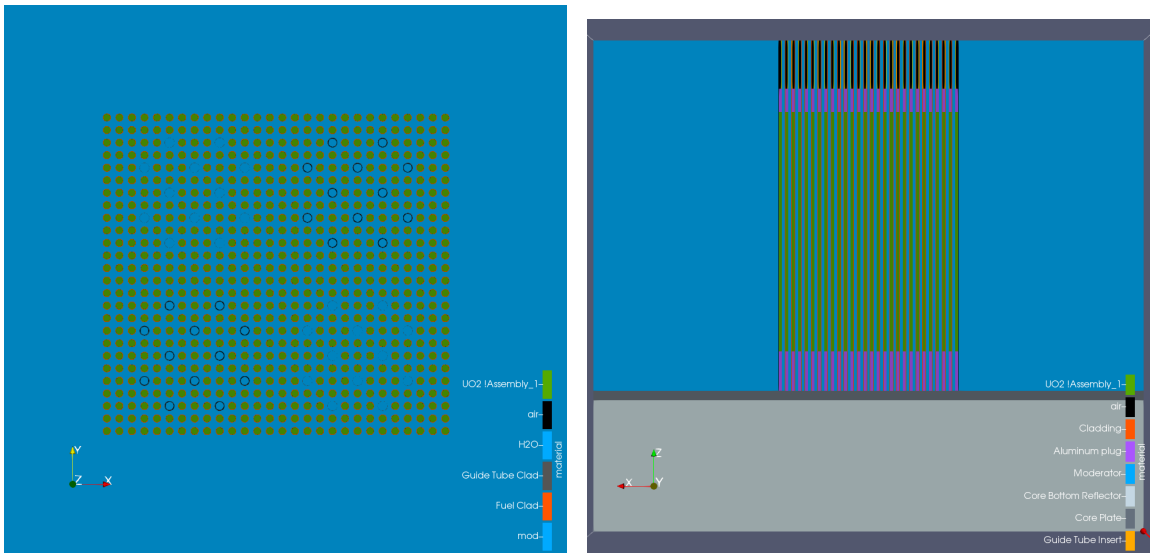

Figure 3.53. MPACT model of IPEN radial (left) and axial (right).

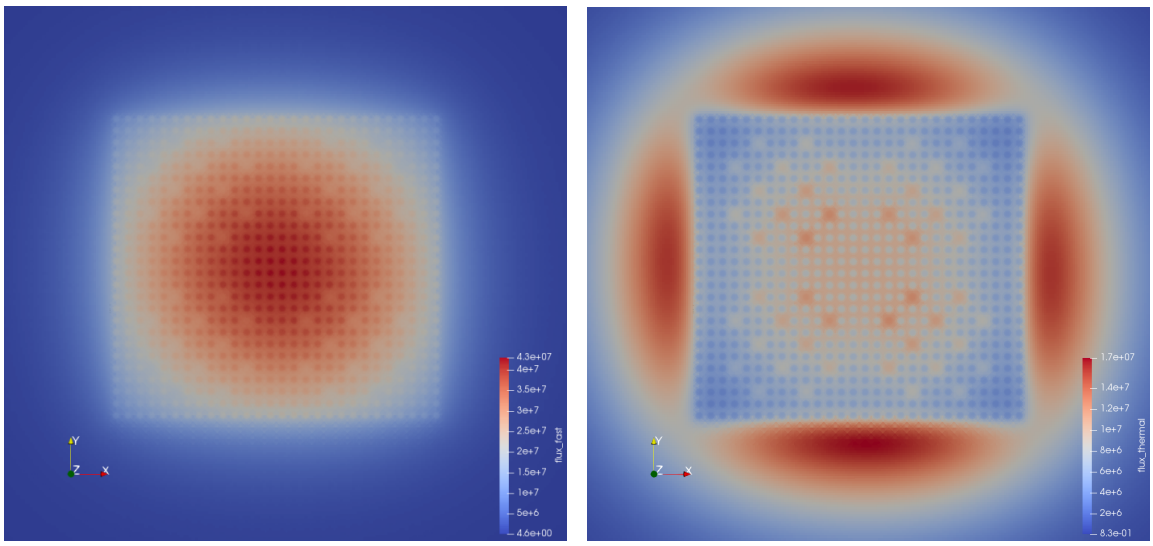

Figure 3.54. MPACT calculation of fast flux (left) and thermal flux (right).

The IPEN(MB01)-LWR-RESR-019 pin resolved benchmark experiments were simulated using the mpact51g_71_4.3m2_03262018 cross section library, and default meshing parameters were used unless specified otherwise for a particular case. In the default flat source discretization, there are 3 equal-volume rings in the fuel, an additional ring in the moderator, and 8 azimuthal divisions. For the reflector cells, a 5×5 mesh was used. The only pin cell without the default discretization is the pin containing the measured fuel disk in the IPEN(MB01)-LWR-RESR-019 benchmark model, which instead used the necessary 6 equal-volume rings in the measured fuel location. For the MOC discretization, the ray spacing was 0.04 cm,

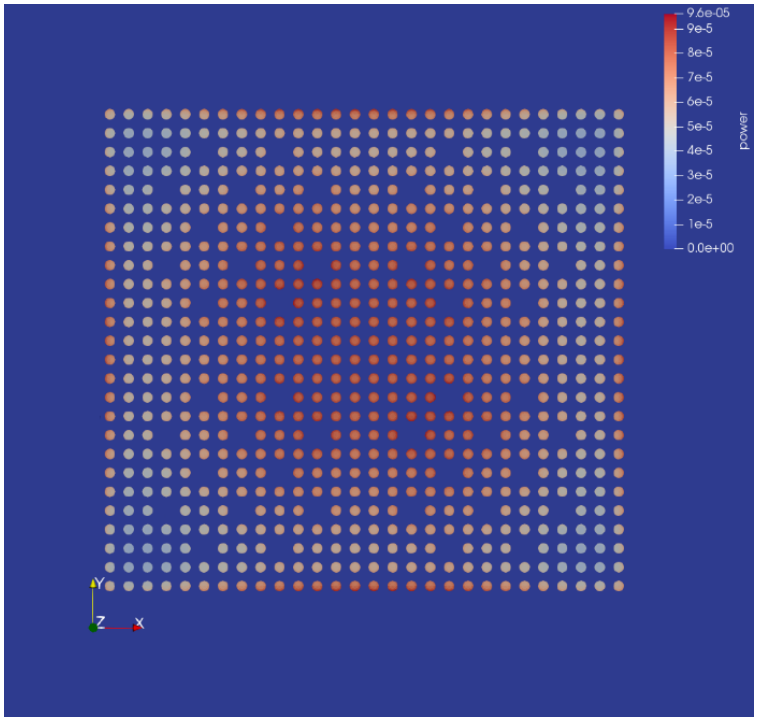

Figure 3.55. MPACT calculation of power distribution

.

the azimuthal angle quadrature was 32 equally spaced angles per quadrant, and the Tabuchi-Yamamoto quadrature was used for the polar direction with 3 directions in the half space.

The experimental, MCNP-5, and MPACT normalized ^{238U}(n,c) reaction rate in each disk region is shown in Figures 3.56 and 3.57, and the (C-E)/E values are given in Table 3.40. Likewise, the experimental, MCNP-5, and MPACT normalized fission rates in each disk region are shown in Figures 3.58 and 3.59, with the (C-E)/E values presented in Table 3.41.

Table 3.40. MPACT (C-E)/E values for the ^{238}U capture rate in each disk region compared to experimental and Monte Carlo reference solution values

Disk region	Configuration A		Configuration B	
	Experiment (%)	Monte Carlo (%)	Experiment (%)	Monte Carlo (%)
1	10.32	1.33	3.59	2.78
2	2.62	0.42	2.40	2.40
3	0.91	0.22	1.06	2.54
4	0.19	0.19	1.05	0.38
5	-1.01	4.42	0.70	5.05
6	-5.76	-3.94	3.82	-6.12
∞-norm	10.32	4.42	3.82	6.12
RMS	5.0	2.4	2.5	3.7

Table 3.40 and Figure 3.56 show that for configuration A, the shape of the experimental data, the Monte Carlo result, and the MPACT results are all similar, with some differences in the innermost and outermost disk regions. The MPACT result is within two standard deviations for all experimental data points and within

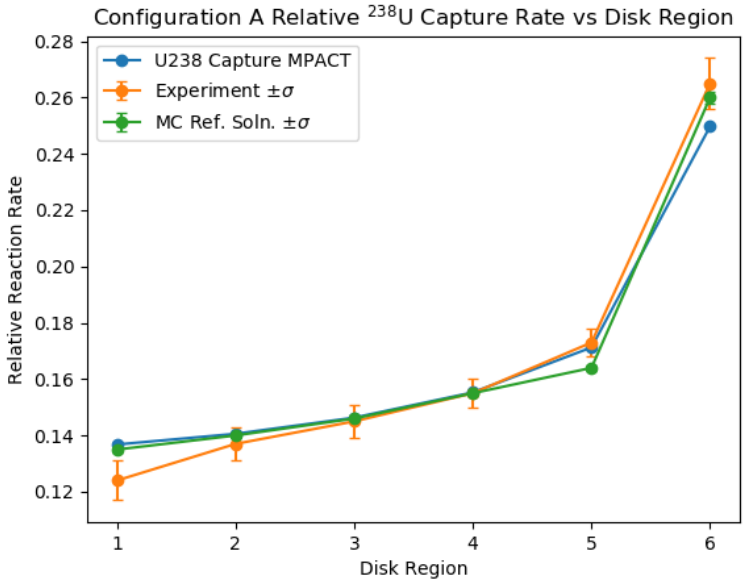

Figure 3.56. Experimental, MCNP-5, and MPACT values for the relative ^{238}U(n,c) reaction rate in each disk region for configuration A

.

one standard deviation for three regions. However, there is some disagreement in the computed and experimental results, specifically at the center and edge of the fuel pellet. In Mura et al. [44] and the IRPhEP [46], it is suggested that the difference between the Monte Carlo result and experimental data results from deficiencies in the thermal cross sections in the ENDF/B-VII.0 library. Considering the similarity of the MPACT and Monte Carlo result, it is likely that the same can be said for the mpact51g_71_4.3m2_03262018 cross section library. Table 3.40 and Figure 3.57 show the configuration B MPACT results. With approximately 99% of the thermal neutrons attenuated by the cadmium shield in configuration B, the large error in region 1 is mostly eliminated. This supports the conclusion from Mura et al. [44] and and the IRPhEP [46] that the error in region 1 is caused by an error in the ^{235}U thermal cross section.

In both configurations, MPACT underpredicts the capture rate in outer disk region 6 compared to both experiment and MCNP. Considering that the error suggested by Mura et al. [44] and the IRPhEP [46] is introduced almost solely by misrepresentation of the 0.3 eV ^{235}U resonance in the continuous energy ENDF/B-VII.0 library, it is possible that the MPACT capture rate underprediction may be the result of additional error in representing this resonance introduced by the multigroup approximation. This would also explain why capture rate results tend to agree with MCNP in the interior regions of the disk, despite misprediction at the outer disk region caused by spectral hardening as neutrons progress towards the interior of the disk, making the error in the thermal cross sections less significant towards the disk's interior. Although the cadmium sleeve in configuration B attenuates 99% of thermal neutrons, the 1% that penetrate the sleeve account for 10% of fissions in the disk; therefore, this effect would also be significant in configuration B.

Table 3.41 and Figure 3.58 show agreement between MPACT and both the experimental and MCNP results for fission rate in configuration A. Although the shape of the experimental results differ from that of MCNP and MPACT, the MPACT result is within two standard deviations of all experimental data and within one standard deviation for 5 of the 6 disk regions. Table 3.41 and Figure 3.59 show significant disagreement between the experimental data and the MPACT results, with 3 of the 6 MPACT fission rates outside of 3 standard deviations from the experiment. However, MPACT and MCNP results agree with a 2% RMS and 3.88% ∞-norm. If Mura et al. [44] and the IRPhEP [46] are correct about the misrepresentation of the 0.3

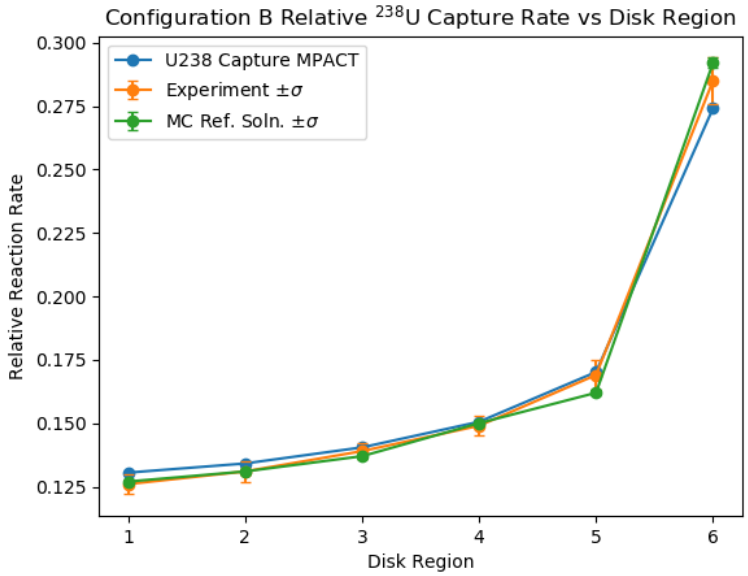

Figure 3.57. Experimental, MCNP-5, and MPACT values for the relative ^{238}U(n,c) reaction rate in each disk region for configuration b

.

eV resonance in the ^{235}U cross section data, then no matter how high fidelity a calculation is performed, the theoretical result will not agree with the experimental data. As a result, Monte Carlo methods provide the most numerically accurate answers given the available cross section data. For this reason, MPACT's close agreement with MCNP is the best that can be hoped for at this time.

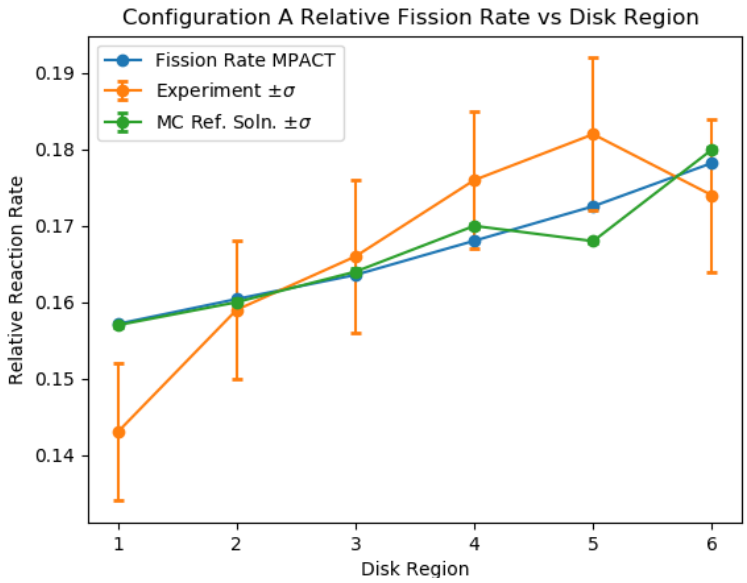

Figure 3.58. Experimental, MCNP-5, and MPACT values for the relative fission rate in each disk region for configuration A

.

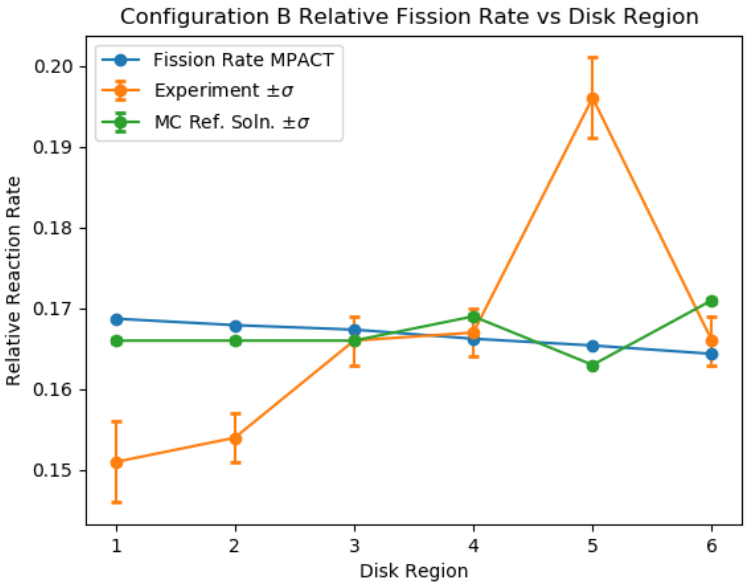

Figure 3.59. Experimental, MCNP-5, and MPACT values for the relative fission rate in each disk region for configuration b

.

Table 3.41. MPACT (C-E)/E values for the fission rate in each disk region compared to experiment and Monte Carlo reference solution

Disk region	Configuration A		Configuration B	
	Experiment (%)	Monte Carlo (%)	Experiment (%)	Monte Carlo (%)
1	9.90	0.10	11.73	1.64
2	0.89	0.26	9.04	1.15
3	-1.46	-0.26	0.82	0.82
4	-4.52	-1.15	-0.46	-1.64
5	-5.18	2.72	15.61	1.47
6	2.43	0.98	-0.98	-3.88
∞-norm	9.90	2.72	15.61	3.88
RMS	5.1	1.3	8.8	2.0

3.5.2.3 Summary and Conclusions

MPACT results for capture in both configurations and fission in configuration A agree with the experimental results, with all disk region reaction rates within 2 standard deviations of experimental data, and most reaction rates within 1 standard deviation. There is substantial disagreement between MPACT and experimental data for fission rates in configuration B. It is suggested by Mura et al. [44] and the IRPhEP [46] that the 0.3 eV resonance data of ^{235}U in the ENDF/B-VII.0 library is incorrect, resulting in discrepancies between the theoretical results predicted by MCNP-5 and the experimental data. Similarly, it is hypothesized that the differences between MPACT and experiment are from the thermal cross sections for ^{235}U in the mpact51g_71_4.3m2_03262018 cross section library.

Although MPACT and experimental results show disagreement in some areas, the MPACT results align with those of MCNP, with an RMS between 1.3 and 3.7% for all reaction rates and core configurations. If Mura et al. [44] and the IRPhEP [46] are correct about inaccurate cross section data, then the most accurate answer achievable is through the use of Monte Carlo with continuous energy cross sections, similar to MCNP-5. For this reason, MPACT's close agreement with MCNP is the best that can be hoped for at this time. Not shown here are the numerous sensitivity calculations performed with MPACT employing different discretizations and physics options, which resulted in only small differences in reaction rates on the order of 0.1% RMS and 0.1% ∞-norm from the results above. It is likely that these differences were caused by the disk's placement in the asymptotic region of the core, where changes in options such as scattering order would have little effect.

3.6 TRANSIENT VERIFICATION AND VALIDATION

This section presents the verification and validation of the MPACT transient capability. The first section describes the verification work performed using the OECD C5G7 Transport Transient Benchmark. The second section describes the assessment of the kinetics data used in the MPACT transient solution. The final section discusses the validation of MPACT transient capability using the SPERT Experiments.

3.6.1 C5G7 Transient Benchmark

The C5G7 is a numerical benchmark problem [48,49] developed to assess the accuracy of neutron transport codes. The C5G7 problem is based on a small reactor core with sixteen fuel assemblies: eight UO_2 assemblies and eight MOX assemblies. The assemblies are 21.42 cm square. The reactor is surrounded by a water reflector that is 21.42 cm thick. The OECD C5G7 transient benchmark is based on the well-established C5G7 benchmark, and the purpose of performing it with MPACT was to provide a code-to-code comparison that would complement the validation data provided by SPERT. Both 2D and 3D models are available in the benchmark; this makes it possible to investigate some of the details in modeling a transport transient.

Because the C5G7 is a very small reactor, ejecting a control rod with realistic cross sections would result in a very large reactivity insertion. Therefore, the control rod cross sections were adjusted so that a single control rod drive (CRD) would have more than 1$ reactivity. In addition, to simplify the modeling of the rod movement, the ejection of the rod was modeled as a step change in material composition. The control rod cluster was placed in a central UO_2 assembly, and the C5G7 transient was performed by ejecting only this rod from a full core geometry, as illustrated in Figure 3.60.

The C5G7 transient begins from an assumed steady-state critical condition for which the eigenvalue was calculated to be 1.14802. The power distribution by fuel assembly for the C5G7 reactor at steady state is depicted in the figure, which is color-coded according to the magnitude of the power. Figure 3.61 shows the steady-state power distribution by fuel cell for the southeast quadrant of the reactor.

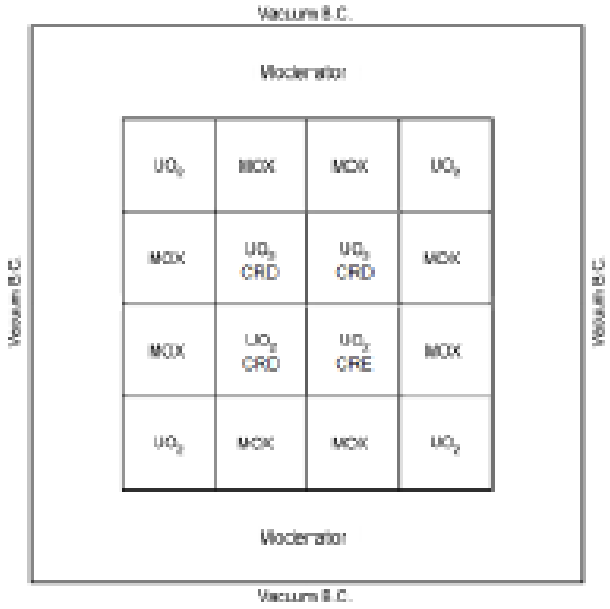

Figure 3.60. C5G7 with control rod drives (CRDs) and ejected CRDs (CREs).

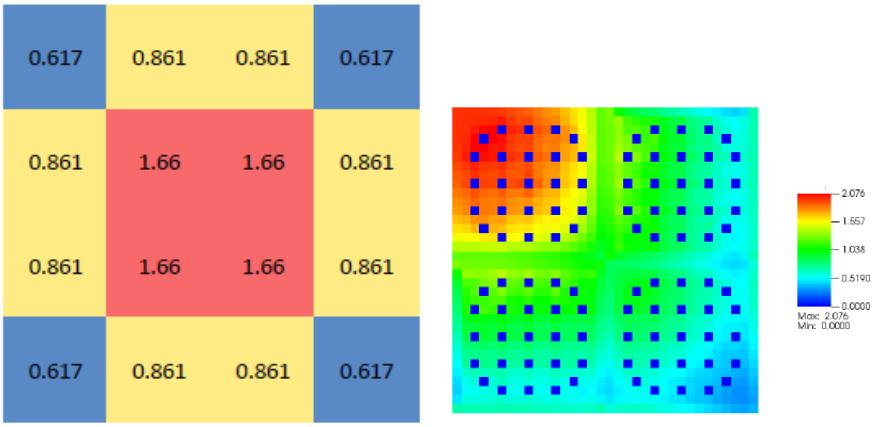

Figure 3.61. Steady-state relative power distribution.

3.6.1.1 C5G7-TD Benchmark

The C5G7 benchmark consists of 2D and 3D exercises. The total model is a miniature light water core with 8 UO_2 assemblies and 8 MOX assemblies. As of symmetry, the model can be simplified into a quarter of a core having 4 assemblies, as shown in Figure 3.62. For convenience, assemblies are numbered 1–4 respectively, as shown in Figure 3.62. The size of the 2D model is 64.26 cm×64.26 cm. The edge of the square shape assembly is 21.42 cm, and the thickness of the moderator is 21.42 cm. The west and the north boundaries use a vacuum boundary condition, whereas the north and the east boundaries use a reflected boundary condition. The 3D model shown in Figure 3.63 follows from the 2D model.

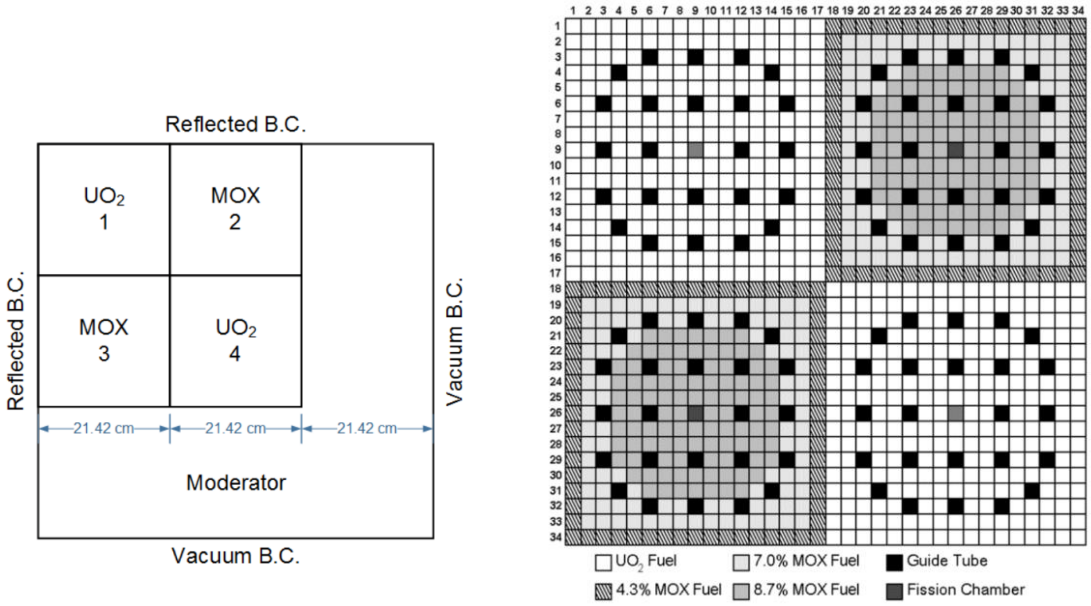

Figure 3.62. 2D model of C5G7-TD.

The benchmark material and cross section specifications are the same as the steady-state benchmark, except the kinetics data (e.g., delayed neutron fractions, delayed neutron precursor decay constants, delayed neutron group data, neutron energy structure and neutron velocities) are provided.

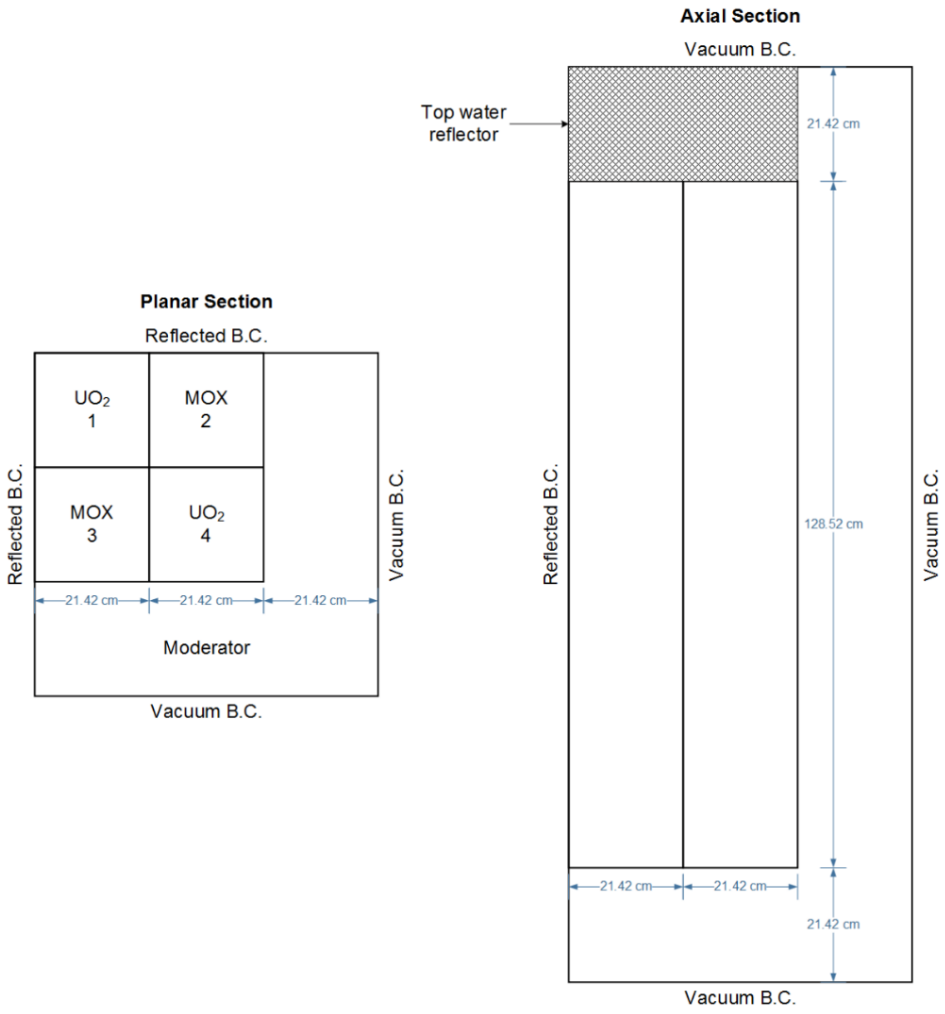

Figure 3.63. 3D model of C5G7-TD.

3.6.1.2 C5G7-TD transient description and results

As shown in Table 3.42, there are 6 exercises in C5G7 transient problems: TD0, TD1, TD2, TD3, TD4, and TD5. Each exercise contains a few exercises. These exercises are based on the stated 2D or 3D models, and the process of transient is either insertion/withdrawal of control rods or density change of moderator. Only results from one of the 2D and 3D exercises—TD-1 (2D) and TD-5 (3D)—are presented in this report; results for other problems will be provided in a separate report.

3.6.1.3 Exercise 1 (TD 1)

Exercise 1 is a 2D time-dependent benchmark with the process of insertion and withdrawal of control rods. In this exercise, control rods move at a constant speed. At 0 s, all control rods are out of the active core, and at the end of 1 s, the depth of rods in the active core is 1% of the height of the active core. The rods are then withdrawn with the same speed and are entirely out of the active core at the end of 2 s. The change of the cross section is used to simulate this process, as shown in the following equations, illustrated in Figure 3.64, and summarized for each of the 5 TD1 exercises in Table 3.43.

Table 3.42. Exercises in C5G7-TD benchmark

Dimension	Process	
	Insertion/withdrawal of control rods	Change of moderator density
2D	TD0 (TD 0-1~ TD 0-5)	TD3 (TD 3-1~ TD 3-4)
	TD1 (TD 1-1~ TD 1-5)	
	TD2 (TD 2-1~ TD 2-3)	
3D	TD4 (TD 4-1~ TD 4-5)	TD5 (TD5-1~ TD5-4)

$$\Sigma_x(t) = \Sigma_x^{GT} + 0.01\left(\Sigma_x^R - \Sigma_x^{GT}\right),\ 0 \le t < 1s$$
$$\Sigma_x(t) = \Sigma_x^{GT} + 0.01\left(\Sigma_x^R - \Sigma_x^{GT}\right)(2-t),\ 1 \le t < 2s$$
$$\Sigma_x(t) = \Sigma_x^{GT},\ t = 0,\ t \ge 2s$$

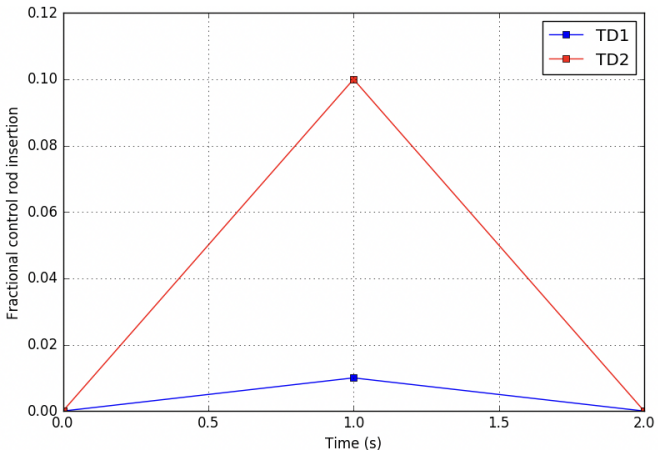

Figure 3.64. Insertion and withdrawal of control rods in TD 1 and TD 2.

Table 3.43. Control rod bank selections in TD 1

No.	Bank number
TD 1-1	1
TD 1-2	3
TD 1-3	4
TD 1-4	1, 3, and 4
TD 1-5	1, 2, 3, and 4

The MPACT reactivity and power results for TD 1 are summarized in Figure 3.65 and are compared to other participants in Figure 3.66 for TD1-5. As indicated, there is good agreement between the MPACT prediction and the results from other transport code solutions.

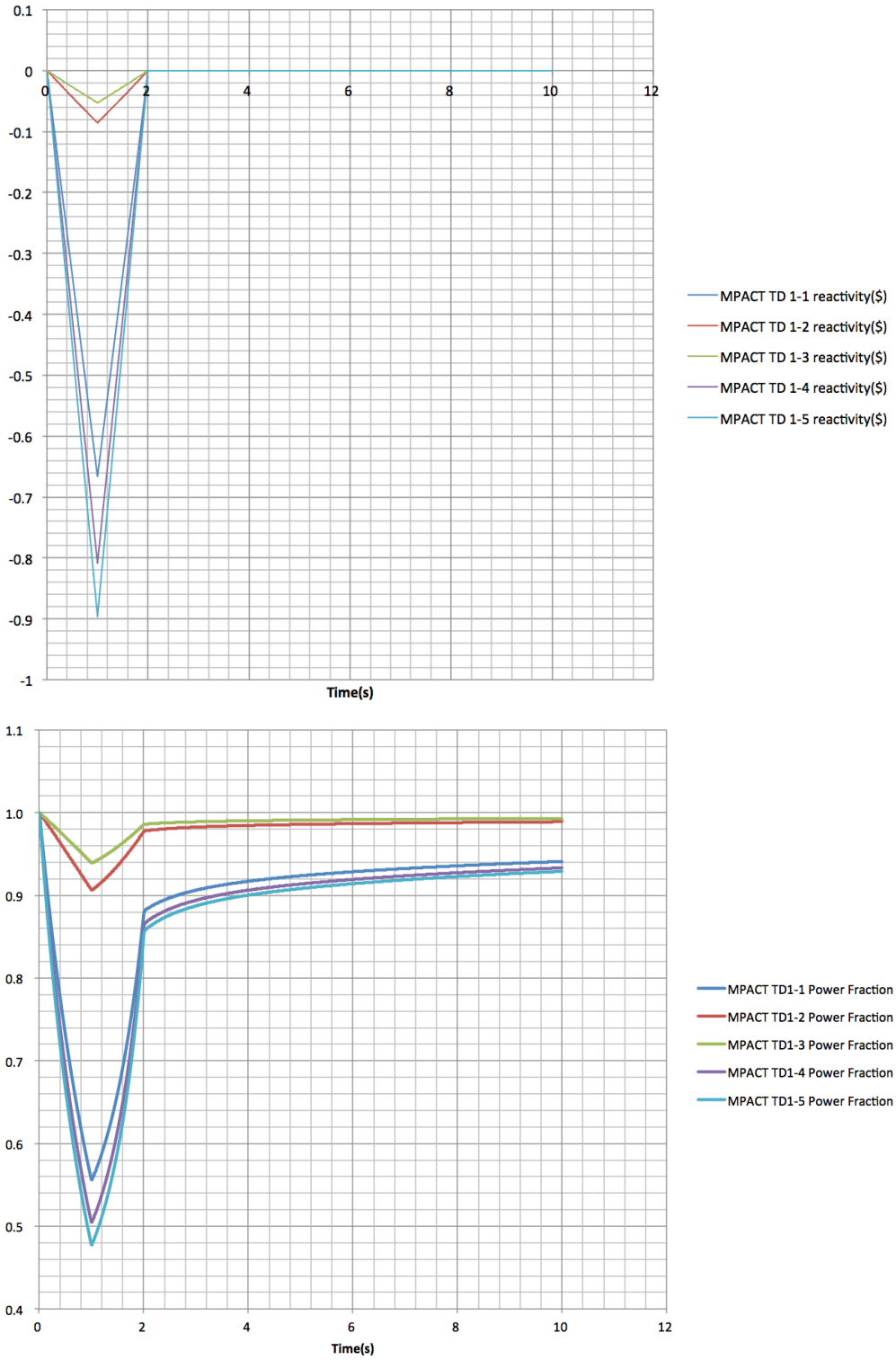

Figure 3.65. MPACT reactivity (top) and power fraction (bottom) for TD 1.

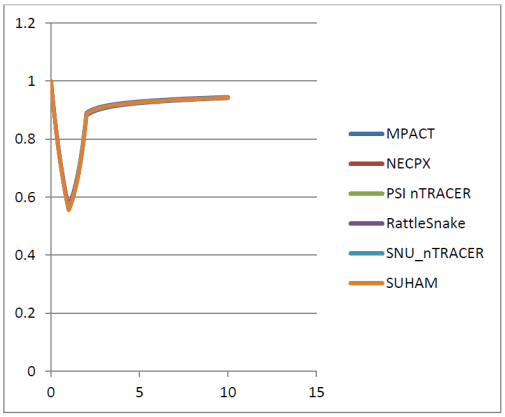

Figure 3.66. Comparison of results for TD1-5.

3.6.1.4 Exercise 5 (TD 5)

Exercise 5 is a 3D time-dependent benchmark with the process of density change of moderator. All control rods are in the fully withdrawn position at 0 s. Among the 4 cases, the moderators of the different assemblies change in density differently. This process is presented in Table 3.44 and is illustrated in Figure 3.67. Note that in the figure for TD 5-2, the moderators in assembly 2 and assembly 4 are always same in density.

Table 3.44. Assemblies with moderator density change in TD 5

No.	Bank number
TD 5-1	1 and 3
TD 5-2	1, 2 and 3
TD 5-3	1, 3 and 4
TD 5-4	2, 3 and 4

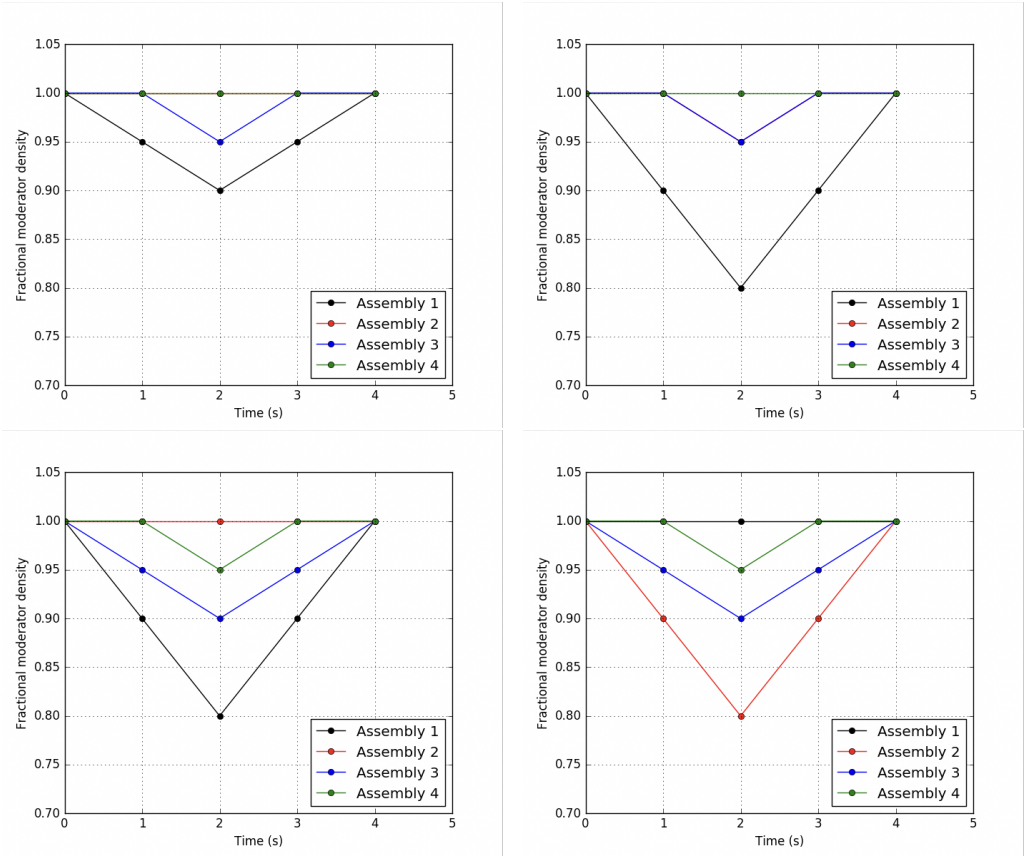

Figure 3.67. Moderator density change in TD 5.

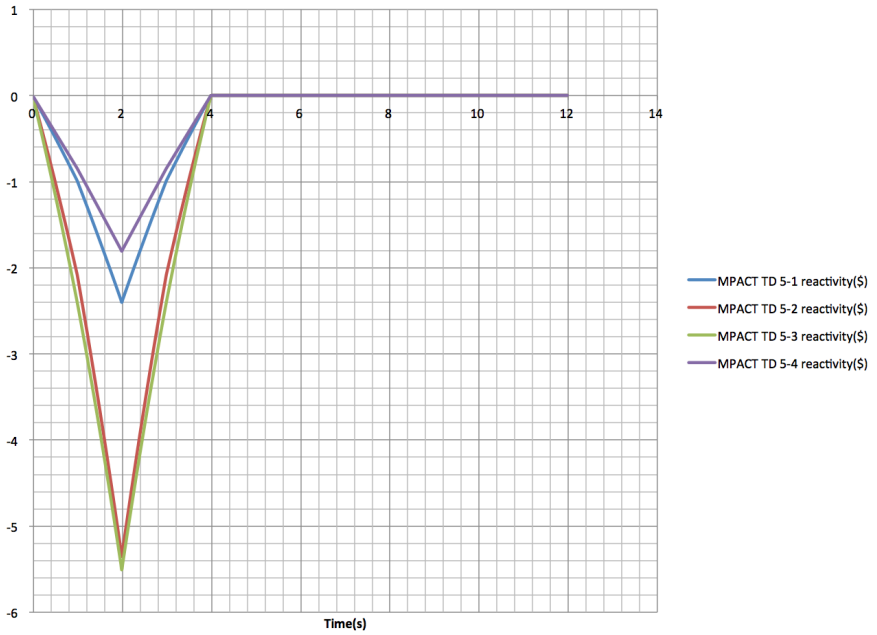

Figure 3.68. MPACT reactivity for TD 5.

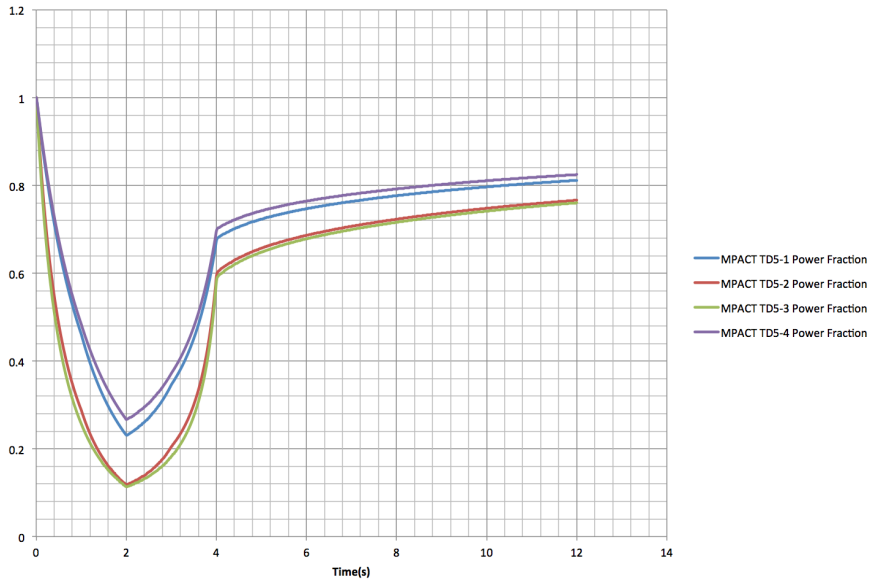

Figure 3.69. MPACT power fraction for TD 5.

3.6.2 Assessment of Kinetics Data

MPACT transient calculations presently use the kinetics data from ENDF/B-VII, which are embedded in the MPACT multigroup library [50]. A few recent validation studies [51,52] showed poor reactivity predictions between ENDF kinetics data (both VII.0 and VII.1) and experiments. Also, there have been discussions within the CASL team considering incorporation of the kinetics data from other sources for a sensitivity study. In addition to the data sources, approximations have been made in MPACT to collapse these data over isotope and neutron energy. These approximations must be improved or justified to minimize their effects in MPACT transient calculations.

To perform a thorough V&V of the kinetics data for MPACT transient calculation, progress has been made in the following aspects: (1) investigated various kinetics data sources, (2) justified the kinetics data calculation in MPACT, (3) developed a validation plan for kinetics data.

3.6.2.1 Kinetics data sources

A literature study has been performed to identify the available kinetics data sources, as shown in Table 3.45. For most of these data sets, the absolute delayed neutron yield per fission $\bar{\nu}_d$, the delayed group fractions β_k^f, and the decay constants λ_k are provided. These data are generally isotope dependent, except the SPERT data, for which uniform sets of data are provided based on the measurements of specific experiments.

For the first step, the data sets in Table 3.45 have been implemented in MPACT. The goal is to preserve the delayed neutron yield from a specific data source. When comparing the effects of using different data sets, all the other cross section data, including ν (total neutron yield per fission), are kept from the MPACT multigroup library. A rod ejection problem was tested involving 2D 3×3 assemblies. The control rods ($1.18 worth) in the center assembly were ejected in the first 5 ms. As shown in Figure 3.70, significant differences in peak power can be observed for different data sets. The results with SPERT data sets may be neglected, because they were tailored from SPERT experiments. For other data sets, $\beta-$ the total delayed neutron yield per emitted fission neutron results, are compared in Table 3.46, suggesting a strong correlation between the power peaks and β, indicating the importance of kinetics data V&V to potentially improve MPACT transient calculations.

Table 3.45. Kinetics data sources

Kinetics data set	Delayed groups	Brief description
KEEPIN	6	Keepin's data fitted by Godiva experiments at LANL [53]
TUTTLE	6	Tuttle's data based on a review and evaluation of experimental data and empirical correlations [54]
Library (ENDF)	6	ENDF data from MPACT multigroup libraries [50]
SPERT	6	SPERT measured data sets (three experiments) [55]
SCALE	6	A legacy SCALE data set (kept for backwards compatibility)
JEFF3	8	Kinetics data based on JEFF3.3 (processed by NJOY) [56]
SANTAMARINA	8	Two suggested changes to JEFF3.3 data by Santamarina [56]

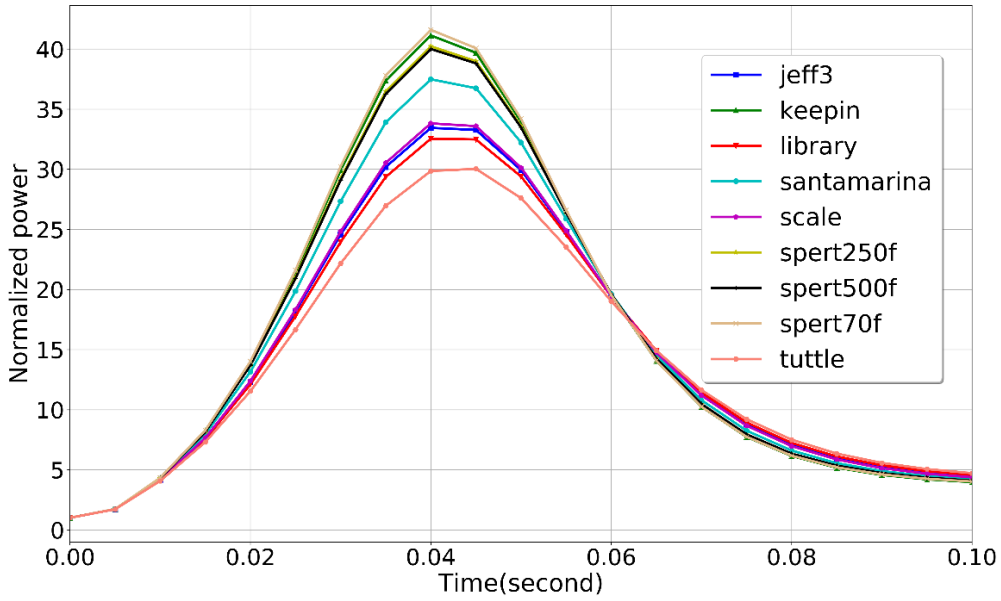

Figure 3.70. Comparison of kinetics data for the super-prompt rod ejection case.

For data sets with 6 delayed groups, each isotope has its own set of decay constants, although these values could be similar among isotopes. The 8-group data sets are fitted to a uniform set of half-lives for all isotopes, which simplifies the dynamic model when more than one fissionable isotope is present. To address the isotopic dependent lambda (6 group) and other subtleties of the kinetics data in MPACT transient calculation, more discussions are presented in Section 3.6.2.2.

Table 3.46. Total delayed neutron yield per emitted fission neutron

Data source	^{235}U	^{238}U
Tuttle	0.006958	0.016167
Library	0.006835	0.015780
Scale	0.006700	0.016400
Jeff3	0.006676	0.016898
Santamarina	0.006552	0.015923
Keepin	0.006478	0.014776

3.6.2.2 Justification of kinetics data calculation in MPACT

The kinetics data are dependent on isotope and incident neutron energy. Table 3.47 shows the decay constants λ_k of ^{235}U and ^{238}U from three data sources of six delayed groups. Although the decay constants between ^{235}U and ^{238}U are similar for many delayed groups, noticeable differences are seen in the short-lived groups, especially for Keepin's data. In addition, Figure 3.71 shows the energy dependence of ν and ν_d. Both are constant in most energy ranges of our interest, but they split from 1 MeV, indicating a potential problem if a typical thermal spectrum is used to pre-calculate β and use it for harder spectra, such as in the high void BWR regions.

Table 3.47. Six-group decay constants (1/s) for ^{235}U and ^{238}U

Delayed energy group	ENDF/B-VII.1		Tuttle		Keepin	
	^{235}U	^{238}U	^{235}U	^{238}U	^{235}U	^{238}U
1	0.0133	0.0136	0.0127	0.0132	0.0124	0.0132
2	0.0327	0.0313	0.0317	0.0321	0.0305	0.0321
3	0.1208	0.1233	0.1150	0.1390	0.1114	0.1386
4	0.3028	0.3237	0.3110	0.3580	0.3014	0.3591
5	0.8495	0.9060	1.4000	1.4100	**1.1363**	**1.4146**
6	2.8530	3.0487	3.8700	4.0200	**3.0137**	**4.0299**

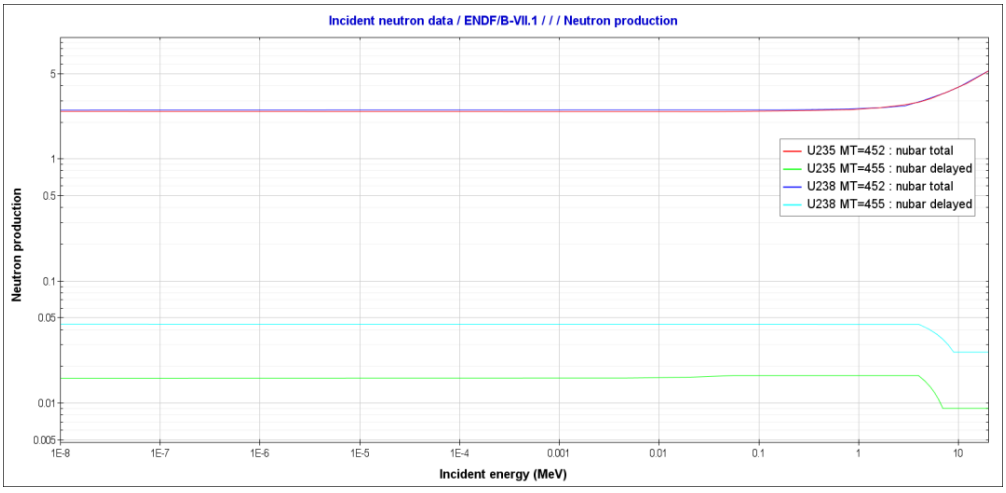

Figure 3.71. Energy dependence of total and delayed neutron yields.

Given the isotope and energy dependence of kinetics data, the rigorous way to evaluate the fission source

and delayed neutron precursors is written as

$$
\begin{aligned}
S_g &= \sum_i \chi_{p,g,i}\,(1-\beta_i)\,S_{F,i} + \sum_i \chi_{d,g,i} S_{d,i} \\
S_{F,i} &= \sum_{g'} \nu_{i,g'} \Sigma_{i,f,g'} \phi_{g'} \\
S_{d,i} &= \sum_k \lambda_{k,i} C_{k,i} \\
\frac{dC_{k,i}}{dt} &= \beta_{k,i} S_{F,i} - \lambda_{k,i} C_{k,i} \\
\beta_{k,i} &= \frac{\sum_{g'} \nu^k_{d,i,g'} \Sigma_{i,f,g'} \phi_{g'}}{\sum_{g'} \nu_{i,g'} \Sigma_{i,f,g'} \phi_{g'}} \,,
\end{aligned}
$$

where S_F and S_d are the overall and delayed fission sources, and i, g, and k denote the isotope, energy group, and delayed neutron group, respectively. To simplify the calculation, MPACT uses two approximations in the current implementation:

(a) Neglect the isotope dependence of precursor concentrations (this is not a problem for 8-group data sets). The 'effective' λ_k over all fissionable isotopes are weighted by isotopic total fission source.

(b) Use a typical PWR spectrum to pre-generate β_i and $\beta_{k,i}$ so that $\nu^k_{d,i,g'}$ does not need to be involved in the calculation.

The goal for the remainder of this section is to either remove the approximations or justify a more plausible approximation.

Improvement to the Approximation of Neglecting Isotope Dependence: Approximation (a)

Approximation (a) has been questioned as simply an intuitive scheme that does not preserve anything. Two additional options have been implemented in MPACT to investigate this approximation. One is the exact approach that allows isotope dependence of precursors. This is practically realized by multiplying the number of delayed energy groups by *nfiss*, or the number of fissionable isotopes in the system. The other is the HELIOS approach, which preserves the initial precursor concentrations at the beginning of a transient,

$$
\overline{\lambda}_k = \frac{\sum_i \beta_{k,i} S_{F,i}}{\sum_i \frac{\beta_{k,i} S_{F,i}}{\lambda_{k,i}}} \,. \tag{3.4}
$$

The same rod ejection problem was run by using the three lambda calculation schemes. The fresh fuel is replaced with depleted fuel composition at 60 GWd/tU to magnify the effect of isotopic lambda collapsing. Three data sets of six delayed groups were studied. Figures 3.72–3.74 show that the initial precursor weighting has very good agreement with the exact approach, whereas fission source weighting shows a difference up to 6% for Keepin's data. Because modeling the isotopic lambdas would significantly increase the memory in MPACT transient calculations (about 200 MB per 2D assembly), using the precursor weighting as default can be considered once more verifications have been made.

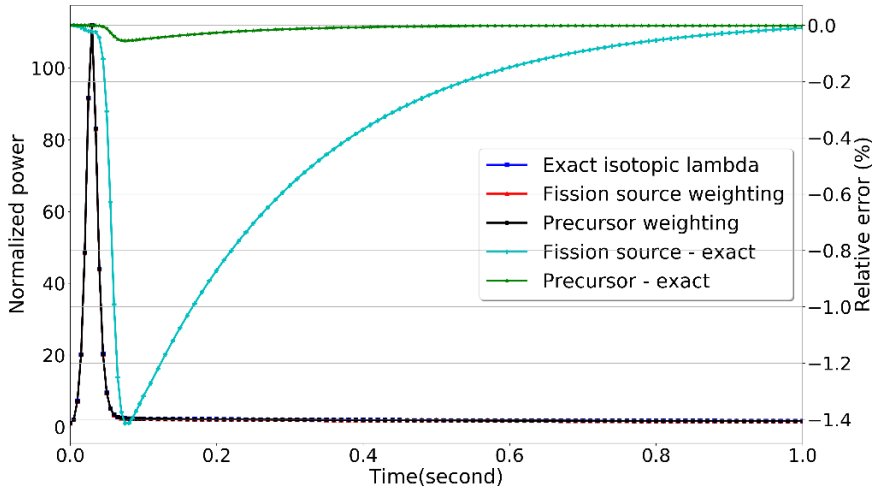

Figure 3.72. Comparison of weighting methods for isotopic decay constants of *ENDF/B-VII.1* data.

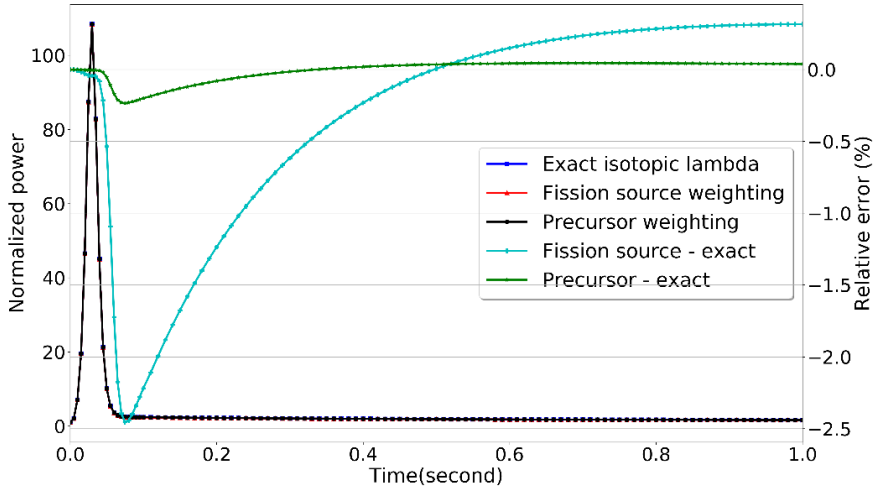

Figure 3.73. Comparison of weighting methods for isotopic decay constants of *Tuttle* data.

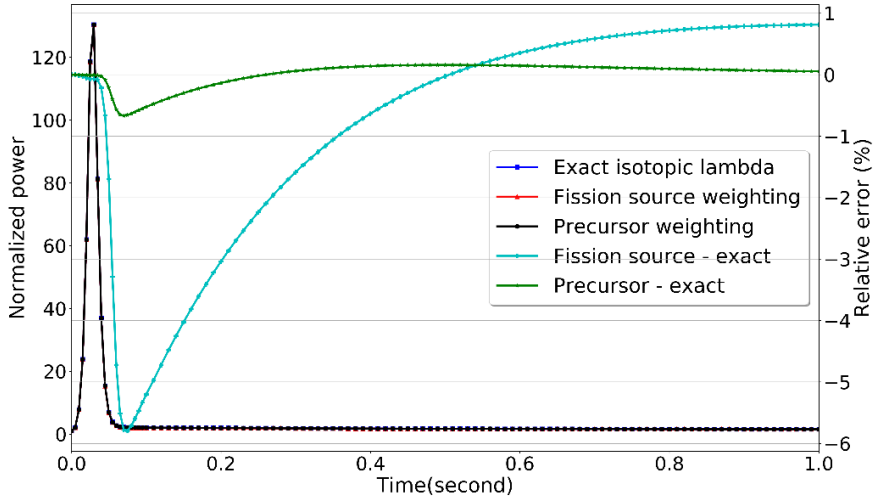

Figure 3.74. Comparison of weighting methods for isotopic decay constants of *Keepin* data.

Improvement to Approximation in Treatment of Delayed Neutron Fraction: Approximation (b)

In the generation of the kinetics data in the MPACT library based on ENDF/B-VII, a typical PWR spectrum has been used for pre-calculating $\beta_{k,i}$. In fact, on-the-fly evaluation of $\beta_{k,i}$ is straightforward if the energy-dependent ν and ν_d are provided. For Keepin, Tuttle, SCALE, and SPERT data sets, only the energy-independent ν_d is provided. For an MPACT library based on ENDF, it was decided to keep the data as is for backward compatibility. Therefore, the on-the-fly evaluation of $\beta_{k,i}$ is only implemented for Jeff3 and Santamarina data sets.

Figure 3.75 shows a comparison of power histories with the same rod ejection case. The energy-dependent beta calculation shows small differences, because the neutron spectrum in this case is very similar to the typical PWR spectrum that was used for typical $\beta_{k,i}$ generation. Even so, adding the option of energy-dependent beta verifies the default typical PWR betas, and it also allows potential transient calculations with harder neutron spectra.

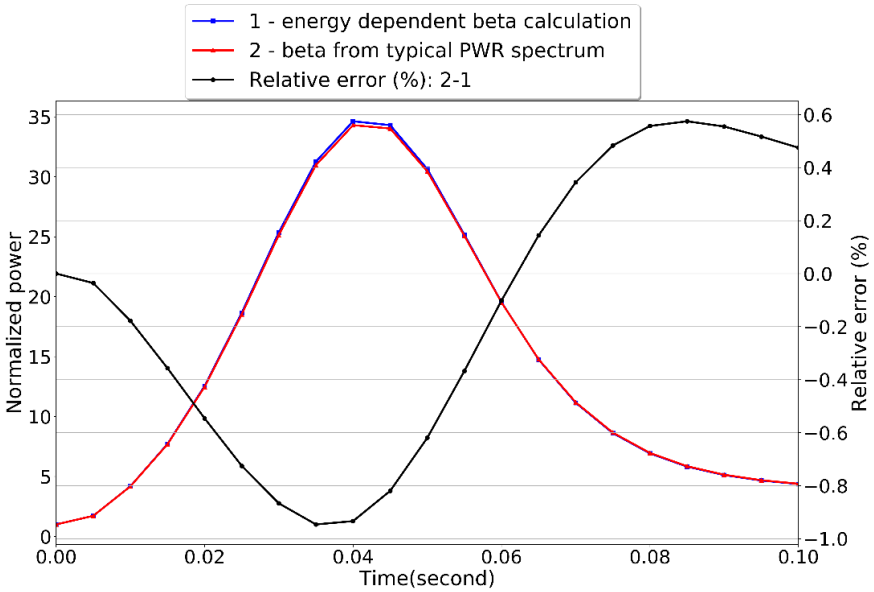

Figure 3.75. Comparison of beta calculations with JEFF3 kinetics data.

3.6.3 The Special Power Excursion Reactor Test (SPERT)

The SPERT Project was established as part of the US Atomic Energy Commission's reactor safety program in 1954, with the objective of providing experimental and theoretical investigations of the kinetic behavior and safety of nuclear reactors. The SPERT III pressurized water reactor [57] was constructed as a part of this safety program to fulfill the need for a facility where reactor kinetic behavior and safety investigations could be conducted under operating conditions. The facility was designed with incorporated essential features typical of pressurized water and boiling water reactors. Among several core designs, the E-Core, consisting of 60 assemblies, was employed to perform several reactivity insertion accident (RIA) experiments. The data measured during the experiments were made available to validate neutronics codes for both steady-state and transient core conditions. However, prior to performing any of the RIA experiments, a series of critical experiments at cold zero power (CZP) and hot zero power (HZP) were performed and were the focus of the validation work using SPERT during Phase I of CASL.

Models of SPERT were developed with both MPACT and KENO V.a, which is a 3D continuous energy Monte Carlo criticality transport program developed and maintained as part of the SCALE code package

[58]. The principal motivation for using KENO was to establish a steady-state Monte Carlo model for the SPERT III E-Core which could provide very detailed fission rates throughout the reactor to complement the experimental measurements.

3.6.3.1 SPERT core specifications

The SPERT III E-core is a small, low-enriched UO_2 fueled PWR core with the general neutronics characteristics of a commercial power reactor without a significant fission product inventory. The cross section of the core is illustrated in Figure 3.76 and consists of 60 fuel assemblies surrounded by different shapes of filler pieces and four rings of thermal shield, housed by the reactor vessel. There are 48 fuel assemblies, each containing 25 fuel rods in a 5×5 rectangular array with a square pitch of 1.4859 cm. There are 12 smaller fuel assembly cans 6.35 cm on a side, each containing 16 fuel rods arranged in a 4×4 rectangular array with the same pitch as the 25-rod assemblies. Four of the 16-rod assemblies surround the centrally located transient rod guide, and the remaining eight 16-rod assemblies form fuel followers of the eight E-core control rods. Four pairs of control rods and a cruciform-shaped transient rod are loaded in the core. The main design characteristics of the E-core are presented in Table 3.48. Other detailed core parameters can be found in the report by Durgone [57].

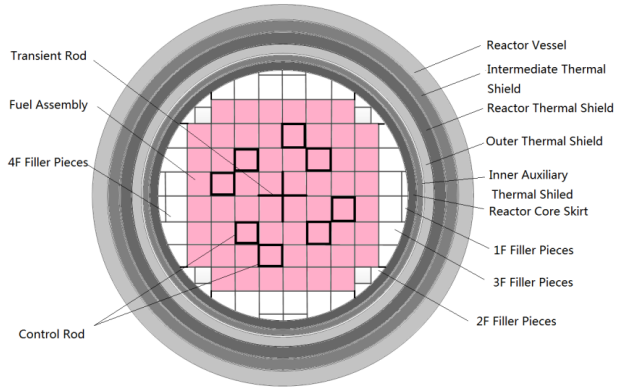

Figure 3.76. SPERT III E-Core cross-section.

The 25-rod assembly is modeled as shown in Figure 3.77. The inner part of the 25-rod assembly model consists of 10×10 quarter fuel pins. This array is surrounded by a 0.0635 cm thick can and 0.03175 cm of bypass water outside the can. The can and bypass water together form one layer of MPACT pins. Therefore, the 25-rod assembly is divided into a 12×12 array of pin mesh with the thicknesses of the inner pin mesh at 0.74295 cm, and the thicknesses of the outer pin mesh at 0.09525 cm. This meshing was also used for all other assembly models.

The core filler pieces are explicitly modeled in MPACT, as shown in Figure 3.78. The thickness of the filler box is 0.3175 cm, and the outer dimension is the same as the 25-rod fuel assembly. The curved portions of type 1F, 2F, and 3F are approximated on the rectangular grid.

The weight of the intermediate grids is not provided in the documentation and was estimated to be 300 grams. Because the structure of the grid is too complex to model explicitly, it is homogenized with the coolant at a height of approximately 6 cm (one axial mesh). The corresponding composition of the grid is 19% steel and 81% water. The positions of the two axial grids are in the 6th and the 12th nodes from the bottom of the active core, as shown in Figure 3.79.

The flux suppressors between the control rod absorbers and fuel followers were modeled explicitly. According to the documentation, the distance between the absorber and fuel follower is 11.938 cm, so the lower half

Table 3.48. Basic core / fuel data for SPERT III E-core

Parameters	Value
Reactor type	Experimental PWR
Moderator/coolant	H_2O/H_2O
Core rated power	20 MW
Core equivalent diameter	0.66 m
Active height	97.282 cm
Fuel rod outer diameter	1.1836 cm
Fuel rod inner diameter	1.0820 cm
Fuel pellet diameter	1.0668 cm
Fuel rod pitch	1.4859 cm
Fuel enrichment	4.8 wt% enriched UO_2 (10.5 g/cm^3)
Fuel tube	Stainless steel, type 348
Gas gap	Helium
Control rods composition	Absorber section 1.35 wt% 10B in Type 18-8 stainless steel; 0.4724 cm thick hollow square box
25-rod fuel assembly	7.5565×7.5565×130.175 cm
16-rod fuel assembly	6.3398×6.3398×130.175 cm
CR with fuel followers	6.2890×6.2890×112.673 cm
Fuel assembly pitch	7.62 cm
Filler pieces thickness	0.3175 cm
Assembly box thickness	0.3175 cm

of that height is filled with spring like the other fuel rods, whereas the upper half is filled with moderator and type 18-8 stainless steel containing 1.35 wt% ^{10}B. While the precise geometry of the flux suppressor was not available, the volume of steel containing ^{10}B was preserved with the data given in the documentation. The flux suppressors were modeled as shown in Figure 3.80. The MPACT model for the middle of the active core is shown in Figure 3.81.

3.6.3.2 KENO model of SPERT III E-core

The KENO model was developed to mimic the geometry of the MPACT model exactly. There are only three differences between the KENO and MPACT models: (1) the reactor containment vessel is explicitly modeled as a cylinder in KENO, rather than approximated on a rectangular grid as in the MPACT model; (2) the filler pieces do not closely contact the reactor skirt to avoid overlapping geometry; and (3) a small gap (10^{-5} cm) is introduced between assemblies in the KENO model to ensure that boundaries of "holes" (assemblies) do not overlap. These minor discrepancies had a negligible effect on the results of the simulations. The KENO simulations were run in continuous energy mode with 5,500 generations consisting of 5×106 neutrons per generation, of which 500 generations were skipped. To calculate pin powers throughout the core, a separate unit was created for each region of interest. KENO provides mesh tally capabilities, but only the flux can be tallied, and not reaction rates. KENO does not have the ability to explicitly calculate pin powers, so fission rates were calculated instead.

3.6.3.3 MPACT and KENO results and analysis

The eigenvalue and critical control rod positions for the CZP and HZP configurations of the SPERT III E-core were calculated with MPACT and KENO. The cases were performed in MPACT using P2 scattering with 0.05 cm ray spacing, and the Chebyshev-Gauss quadrature set and 16 azimuthal and 4 polar angles

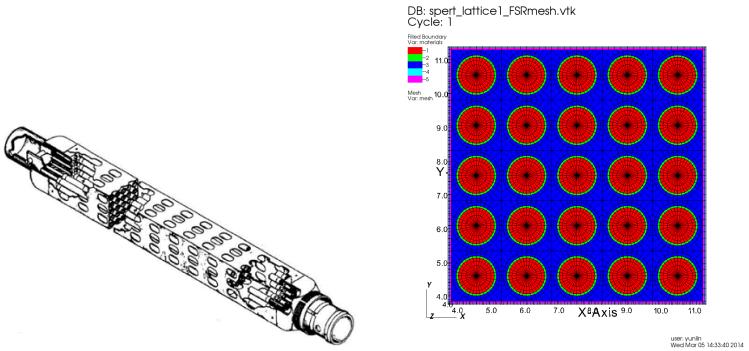

Figure 3.77. MPACT 25-rod fuel assembly model.

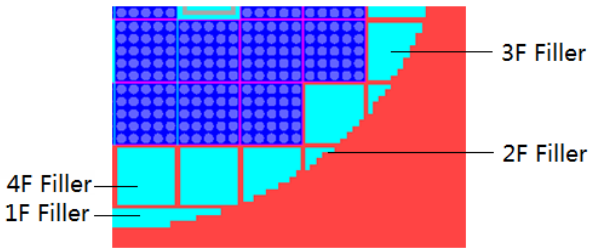

Figure 3.78. MPACT model for core filler.

per octant. The multigroup NEM kernel was used to perform the axial solution, and both CZP and HZP cases were run with 20 axial planes. Solutions were performed with the ORNL 47-group library based on ENDF-VII. The typical computational time for each case running with 720 cores is approximately 2 hours. The KENO cases were run with the continuous energy ENDF-VII library. The computational time of KENO with 240 cores for each case is approximately 150 hours. The eigenvalues for MPACT and KENO are compared in Table 3.49. The critical control rod positions are also compared with experimental results in Table 3.50. However, only the CZP critical control rod position was calculated with KENO.

Table 3.49. Comparison of eigenvalues

Case	Temp. (F)	CR position (cm)	MPACT	KENO-CE
CZP	70	37.0	0.99613	0.99857±0.00001
HZP	550	71.8	1.00023	1.00069±0.00001

As indicated, there is very good agreement for both eigenvalue and control rod positions, with the maximum difference in eigenvalue of less than 25 pcm for HZP and less than 400 pcm for CZP. The experimental data also include the control rod worth for CZP. The calculated results of MPACT and KENO are compared against the experimental results in Figure 3.82, and good agreement is observed between the experimental results and the MPACT and KENO results.

The experimental results do not provide detailed power distribution measurements, which emphasizes the value of the fission rate distribution comparisons between MPACT and KENO. Comparisons of the relative fission rate distributions between the two codes at CZP and HZP are shown in Figure 3.83 and 3.84, respectively. These figures include (a) the assembly-averaged fission rate distribution at the plane with the peak power (a quarter core), and (b) the pin-wise relative difference distribution between two codes at the plane

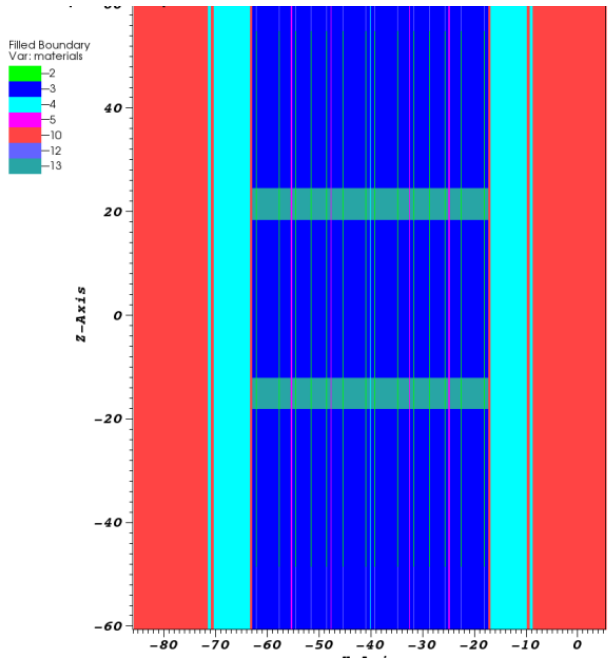

Figure 3.79. MPACT model for axial grids.

Table 3.50. Comparison of critical control rod positions

Case	Temperature (F)	Experiments	MPACT	KENO
CZP	70	37.0	38.2	36.3
HZP	550	71.8	74.4	–

with the peak power (full core). In the CZP peak-power plane shown in Figure 3.83, MPACT systematically underestimates the assembly plane–averaged power by 2.5 to 5.5% relative to KENO. However, the overall shape of the power distribution shows very good agreement between the two codes. As shown in Figure 3.83, the maximum relative difference of 6.5% occurs in the corner pin location of one of the 4 central assemblies, at the same location as in the peak pin power.

In the HZP peak-power plane shown in Figure 3.84, MPACT systematically underestimates the assembly plane–averaged power by up to 2.5% relative to KENO, which is a difference of less than 2σ based on the KENO uncertainty. In fact, only the difference in the four central assemblies exceeds 1σ. The overall shape of the power distribution shows very good agreement between the two codes, with the maximum relative difference of approximately 4.7% occurring in the outermost corners of the core, where pin powers are less than a third of the peak power. Both codes predict that the pin-wise peak powers are located in the center assemblies, and the pin-wise fission rate distributions are compared for the assembly with the peak power in Figure 3.85. It can be seen that the maximum difference is less than 6.5% for CZP and 4% for HZP. The axial relative distributions of fission rate of this peak-power assembly are compared in Figure 3.86, where good agreement can be observed for both CZP and HZP cases. Most of the MPACT and KENO pin powers are within 1σ of the KENO uncertainties. In fact, the relative difference between the KENO and MPACT pin powers for HZP are all well within 1σ, whereas a few relative differences between the KENO and MPACT pin powers for CZP exceed 1σ but are within 1.5σ.

Overall, KENO and MPACT have the same magnitude of discrepancies in both eigenvalues and control rod worth compared with the experimental data. Because better agreements are observed for the HZP condition

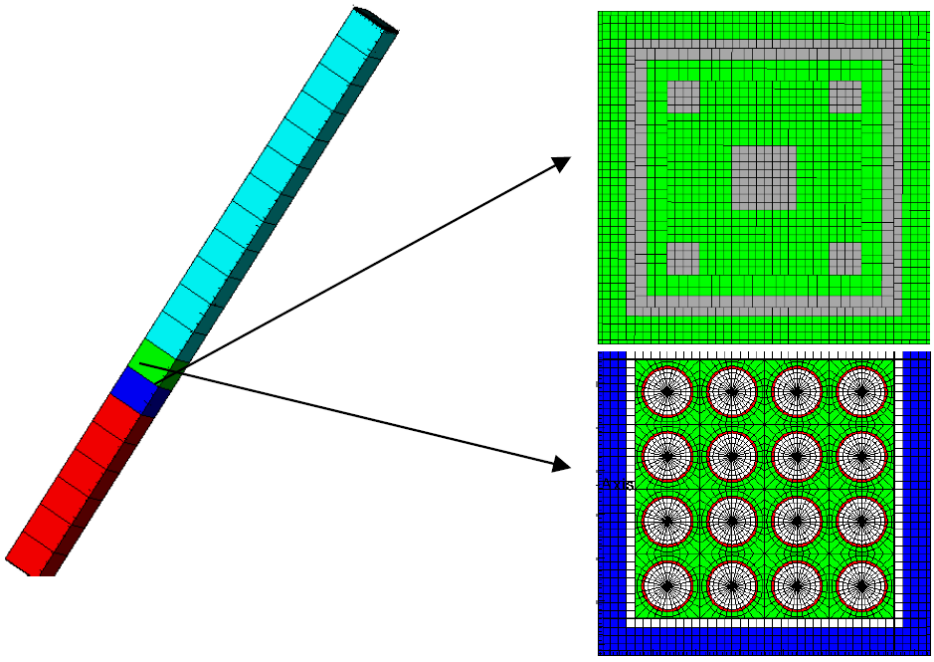

Figure 3.80. MPACT model for flux suppressors.

than for the CZP condition, it appears that some improvements in the nuclear data library might be needed for cold conditions.

The MPACT and KENO results for the SPERT experiments support the following conclusions:

1. The detailed 3D heterogeneous modeling of a complex reactor is feasible for both the deterministic code MPACT and the Monte-Carlo code KENO.
2. Detailed geometry descriptions of in-core components are very important for steady-state validation.
3. The SPERT III E-Core experiment can be used as a benchmark for high-fidelity simulation of light water reactors.
4. Both KENO and MPACT can provide good results for k-eff of both CZP and HZP cases. The fission rates distribution agrees well between KENO and MPACT, except in some regions with very low relative power.

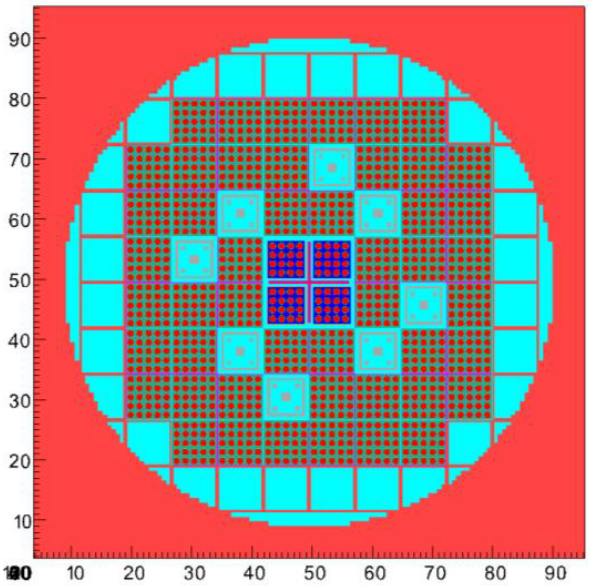

Figure 3.81. MPACT model for middle of active core.

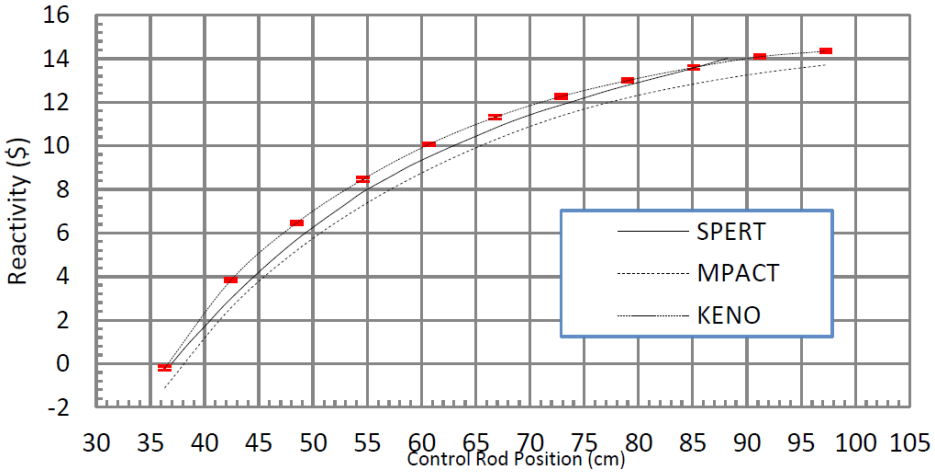

Figure 3.82. Comparison of control rod worth for CZP.

KENO MPACT Rel. Diff. (%)	1.376±0.027 1.339 2.7%	1.688±0.030 1.634 3.2%	1.900±0.032 1.835 3.4%
1.364±0.027 1.327 2.7%	1.967±0.032 1.893 3.8%	2.705±0.038 2.584 4.5%	3.013±0.040 2.874 4.6%
1.678±0.030 1.624 3.2%	2.849±0.039 2.718 4.6%	3.981±0.058 3.785 4.9%	4.135±0.047 3.927 5.0%
2.007±0.033 1.933 3.7%	3.447±0.054 3.283 4.8%	4.302±0.049 4.083 5.1%	5.241±0.067 4.968 5.2%

(a) Assembly-averaged fission rate distribution (plane 5, peak-power plane)

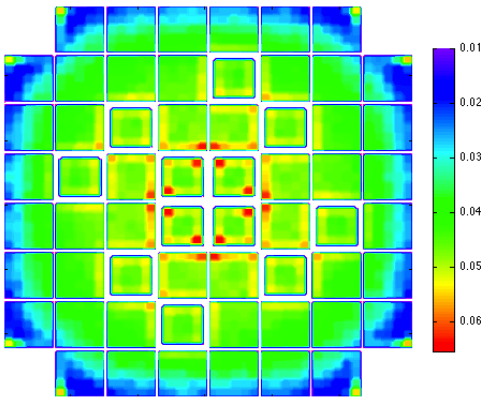

(b) Pin-wise relative difference of fission rate (plane 5, peak-power plane)

Figure 3.83. Comparison of fission rate distribution for CZP.

KENO MPACT Rel. Diff.(%)	0.867±0.021 0.862 0.6%	0.978±0.022 0.975 0.3%	1.108±0.024 1.103 0.5%
.868±0.021 0.863 0.5%	1.043±0.023 1.040 0.4%	1.410±0.027 1.398 0.8%	1.572±0.028 1.556 1.0%
1.000±0.022 .997 0.3%	1.537±0.028 1.521 1.0%	2.354±0.045 2.317 1.6%	2.198±0.034 2.165 1.5%
1.197±0.025 1.190 0.6%	2.050±0.042 2.020 1.5%	2.315±0.035 2.278 1.6%	3.185±0.052 3.114 2.2%

(a) Assembly-averaged fission rate distribution (plane 8, peak-power plane)

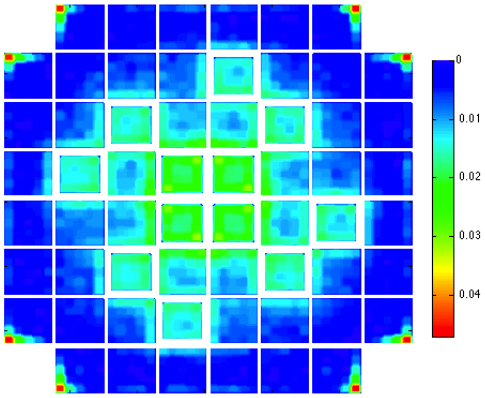

(b) Pin-wise relative differences of fission rate distribution (plane 8, peak-power plane)

Figure 3.84. Comparison of fission rate distribution for HZP.

5.898±0.283 5.578 -5.4%	5.281±0.275 5.012 -5.1%	5.306±0.271 5.029 -5.2%	6.008±0.288 5.616 -6.5%
5.281±0.275 5.01 -5.1%	4.557±0.246 4.353 -4.5%	4.567±0.251 4.358 -4.6%	5.235±0.267 4.965 -5.2%
5.306±0.276 5.027 -5.3%	4.568±0.251 4.357 -4.6%	4.549±0.250 4.347 -4.4%	5.185±0.264 4.93 -4.9%
5.998±0.288 5.615 -6.4%	5.235±0.267 4.964 -5.2%	5.185±0.264 4.929 -4.9%	5.692±0.279 5.403 -5.1%

(a) CZP

KENO MPACT Rel. Diff.	3.321±0.213 3.244 -2.3%	3.117±0.206 3.0502 -2.1%	3.151±0.208 3.0801 -2.3%	3.466±0.222 3.3559 -3.2%
	3.111±0.208 3.0514 -1.9%	2.874±0.198 2.8257 -1.7%	2.912±0.192 2.8593 -1.8%	3.242±0.214 3.1657 -2.4%
	3.151±0.211 3.0815 -2.2%	2.911±0.204 2.8596 -1.8%	2.944±0.203 2.8931 -1.7%	3.266±0.209 3.1952 -2.2%
	3.460±0.218 3.3567 -3.0%	3.242±0.207 3.1659 -2.3%	3.262±0.215 3.1953 -2.0%	3.527±0.219 3.447 -2.3%

(b) HZP

Figure 3.85. Comparison of pin-wise fission rates of the peak power assemblies.

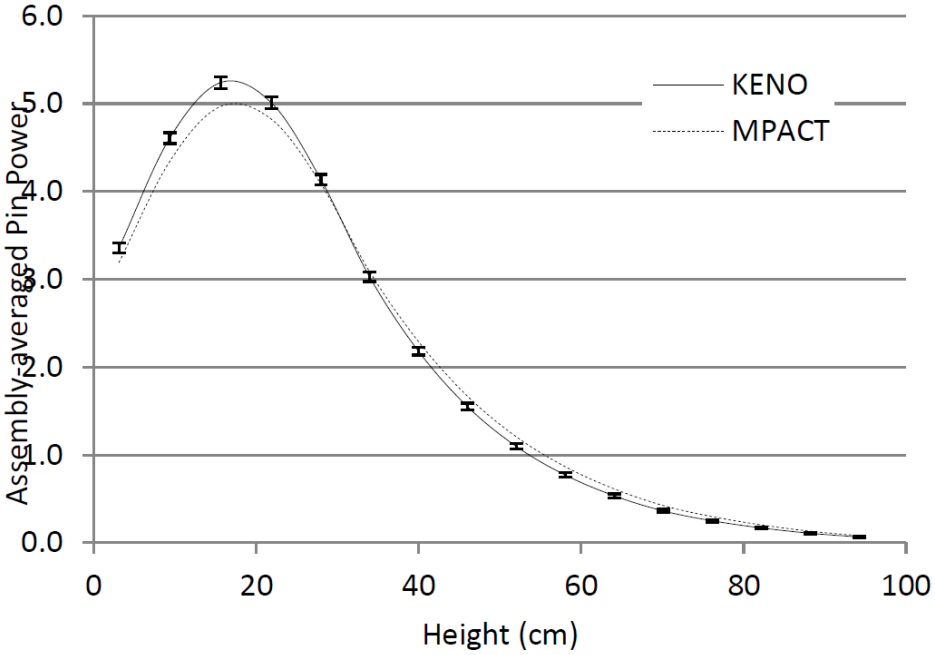

(a) CZP

(a) CZP

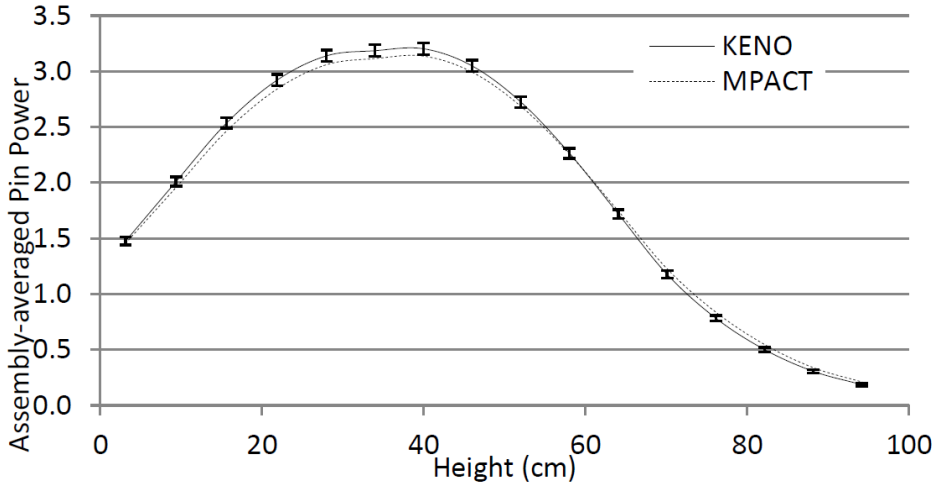

(b) CZP

Figure 3.86. MPACT axial fission rates distribution for SPERT.

3.6.3.4 SPERT E-core transient analysis

The SPERT III E-Core control rod ejection tests consisted of a sequence of CZP, HZP, and HFP tests with various transient rod insertion depths. Superprompt critical tests 86 and 60 were used to perform the initial validation of MPACT for this milestone effort, which used the internal standalone thermal hydraulics, which do not include transient convection capability. Additional SPERT cases will be performed in the future to provide a more comprehensive validation of VERA-CS after CTF is coupled to MPACT. Transient test 86 is a HFP transient in which the initial core inlet temperature is 502°F ± 4°F. The system is also pressurized so that the initial thermal hydraulic condition is within typical PWR operating conditions. In addition, the initial reactor power is approximately 19 ± 1 MW. The withdrawn transient rod worth is \$1.17 ± 0.05, which is simulated by linearly changing the transient rod composition in the withdrawn part of the rod.

Table 3.51. SPERT transient test problems

Test	Initial power (MW)	Pressure (psi)	Inlet temp. (F)	TR rod worth (\$)
60	–	1500 (10.3 MPa)	500 ± 4	1.23 ± 0.05
86	19 ± 1	1500	502 ± 4	1.17 ± 0.05

The SPERT cases were run in MPACT using TCP0 scattering with a nodalization of 0.05 ray spacing and the Chebyshev-Gauss quadrature set with 4 azimuthal and 1 polar angles. The multigroup NEM diffusion kernel was used to perform the axial solution with 20 axial layers. The cross sections for MPACT were provided from the standard 47-group library. The thermal-hydraulics feedback for the transient solution was provided by the internal thermal-hydraulics module in MPACT, which solves transient mass and energy equations. Future work will include coupling of the MPACT transient solver to the subchannel thermal-hydraulics code COBRA-TF. A simple polynomial fitting was used temporarily for the control rod decusping effect, and a more rigorous method based the subplane technique is currently under development [59]. The execution time for Test 86 with 2,880 cores on the Titan compute cluster at ORNL was approximately 2 hours. The power and reactivity calculated by MPACT are shown in Figure 3.87. As indicated, there is reasonable agreement with the measurement data. However, as noted previously, the results here used internal thermal hydraulics, and the final validation will be performed after the CTF transient is validated and coupled to MPACT in VERA-CS in FY17.

Transient test 60 is a HZP transient in which the initial power was about 50 W. Test 60 is more difficult for simulation, because the reactor power increases from 50 to 400 MW within 0.2 s. The transient multi-level (TML) with exponential transformation is used with 5 ms MOC time step, 2.5 ms CMFD time step, and 0.833 PKE time step. The execution time in Titan was approximately 2 hr with 2,880 processors. The MPACT solution is shown in Figure 3.88, and as indicated, the results agree reasonably well with the experimental results. Note that the reactivity measurement data for test 60 only covers the interval shown in the figure. The results of tests 86 and 60 provide confidence in the ability of MPACT to perform control rod ejection simulation for a PWR.

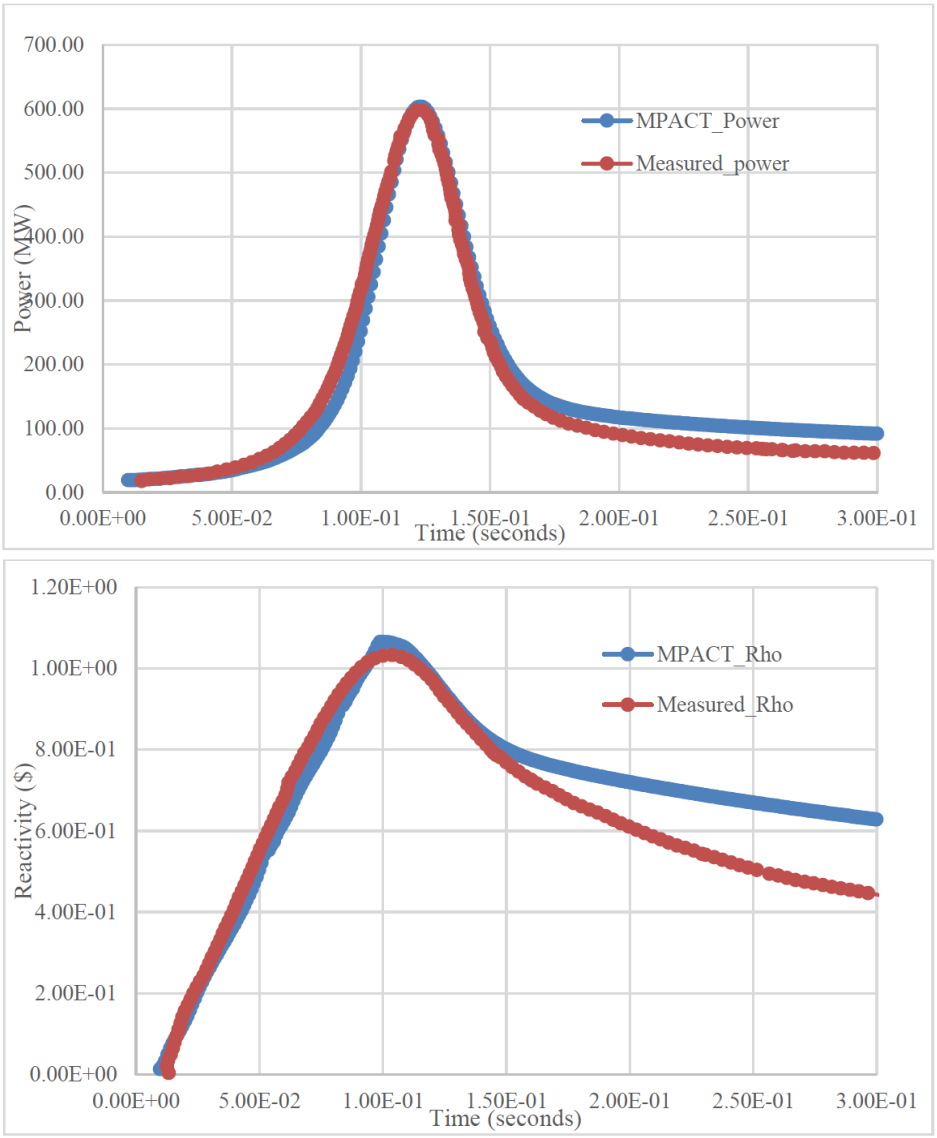

Figure 3.87. MAPCT results for test 86 power (top) and reactivity (bottom).

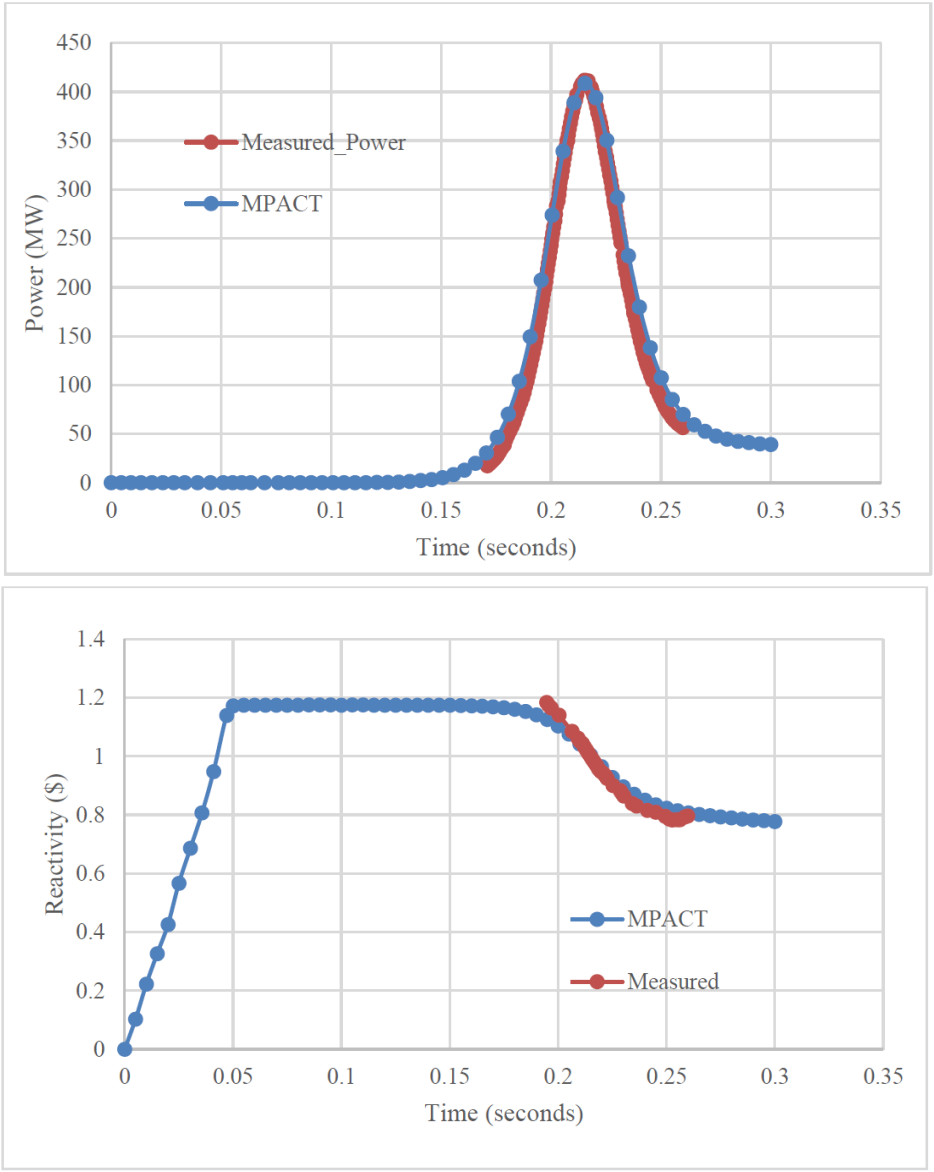

Figure 3.88. MAPCT results for test 60 power (top) and reactivity (bottom).

3.7 PEACH BOTTOM LATTICE VALIDATION

An initial BWR modeling capability was implemented in MPACT, and a preliminary assessment of the capability was performed. This section briefly summarizes some of that work [60], which is based primarily on comparisons to Monte Carlo calculations for multi-assembly problems. Work is anticipated in the future to perform code validation using BWR critical experiments and plant start-up data.

The essential new features implemented in MPACT for the BWR include the following:

- Channel box with rounded corners
- Wide and narrow gaps on the outside of the channel box
- Ability to specify different void/density inside and outside the channel box
- Original equipment manufacturer (OEM) control blade design
- Large water rods that occupy 2×2 pin cells

Other modifications included modification of the input processing, model setup, and meshing. Since MPACT uses the method of characteristics (MOC) for its transport solution algorithm, the actual neutron transport solver required no modification. However, a new meshing capability was implemented at the pin cell level which provided a much more general description of geometry using circles, oriented bounding boxes, and lines that could be placed arbitrarily within the pin cell mesh bounding box. Details on this capability are provided in a paper by Kochunas et al. [60].

The preliminary verification of the BWR capability was performed using several lattices from the Peach Bottom Unit 2 cycle 1 specifications [61]. Models were developed for MPACT using the VERA input, and separate models were also developed with the KENO Monte Carlo model to provide a reference solution. Additionally, a 3D single assembly model was also developed and simulated with multiple control rod positions to verify the 3D control rod positioning.

3.7.1 Comparisons of 2D Peach Bottom Lattices

The MPACT models for the various Peach Bottom lattices are shown in Figure 3.89. The bundles were simulated at HZP. This consisted of having all material temperatures at 600 K, and the water density was 0.736690 g/cc. The MOC discretization of the MPACT models used 0.01 cm spacing, 16 azimuthal angles, and 2 polar angles per octant with the Chebyshev-Yamamoto quadrature.

For MPACT, a new cross section library with 252 groups based on ENDF/B-VII.0 data was used. P2 scattering was also used. KENO performed a continuous energy calculation with ENDF/B-VII.0 cross sections simulating 2,000 active cycles and 100 inactive cycles with 500,000 particles per cycle. The comparisons of the results are given in Tables 3.52 and 3.53 for the unrodded and rodded cases, respectively. For all cases, the uncertainty reported by KENO for k-inf was <3 pcm, and it was <0.05% for any relative fission rate value. Overall, these results show good agreement, but they also suggest some room for improvement. Previous comparisons of MPACT with KENO for PWR lattices had differences that were approximately half of what is observed in the Peach Bottom comparisons. There also appears to be a consistent bias of approximately -100 to -200 pcm for the unrodded and rodded cases, respectively.

Table 3.52. MPACT and Keno comparisons for unrodded Peach Bottom lattices at HZP

Lattice type	Keno k_{inf}	MPACT Δk_{inf} (pcm)	Max diff of fiss rate	RMS fiss rate
1	1.05393	-20	0.28%	0.12%
2a	1.14621	-112	0.55%	0.30%
2b	1.10536	-127	0.53%	0.31%
3a	1.15548	-214	0.54%	0.28%
3d	1.09254	-125	0.57%	0.32%
3e	1.04024	-127	0.62%	0.34%
4 100 mil	1.10087	-90	0.45%	0.24%
4 120 mil	1.09890	-96	0.44%	0.23%
Type 5	1.11378	-90	0.48%	0.23%
Type 6	1.11257	-130	0.43%	0.22%

Table 3.53. MPACT and Keno comparisons for rodded Peach Bottom lattices at HZP

Lattice Type	Keno k_{inf}	MPACT Δk_{inf} (pcm)	Max diff of fiss rate	RMS fiss rate
1	0.78854	-194	0.57%	0.20%
2a	0.90238	-205	0.81%	0.30%
2b	0.85967	-213	0.88%	0.32%
3a	0.89650	-213	0.79%	0.30%
3d	0.87656	-211	0.85%	0.31%
3e	0.81708	-204	0.96%	0.35%
4 100 mil	0.87627	-177	1.03%	0.28%
4 120 mil	0.87370	-177	0.90%	0.25%
Type 5	0.88651	-182	0.99%	0.28%
Type 6	0.88728	-250	0.94%	0.26%

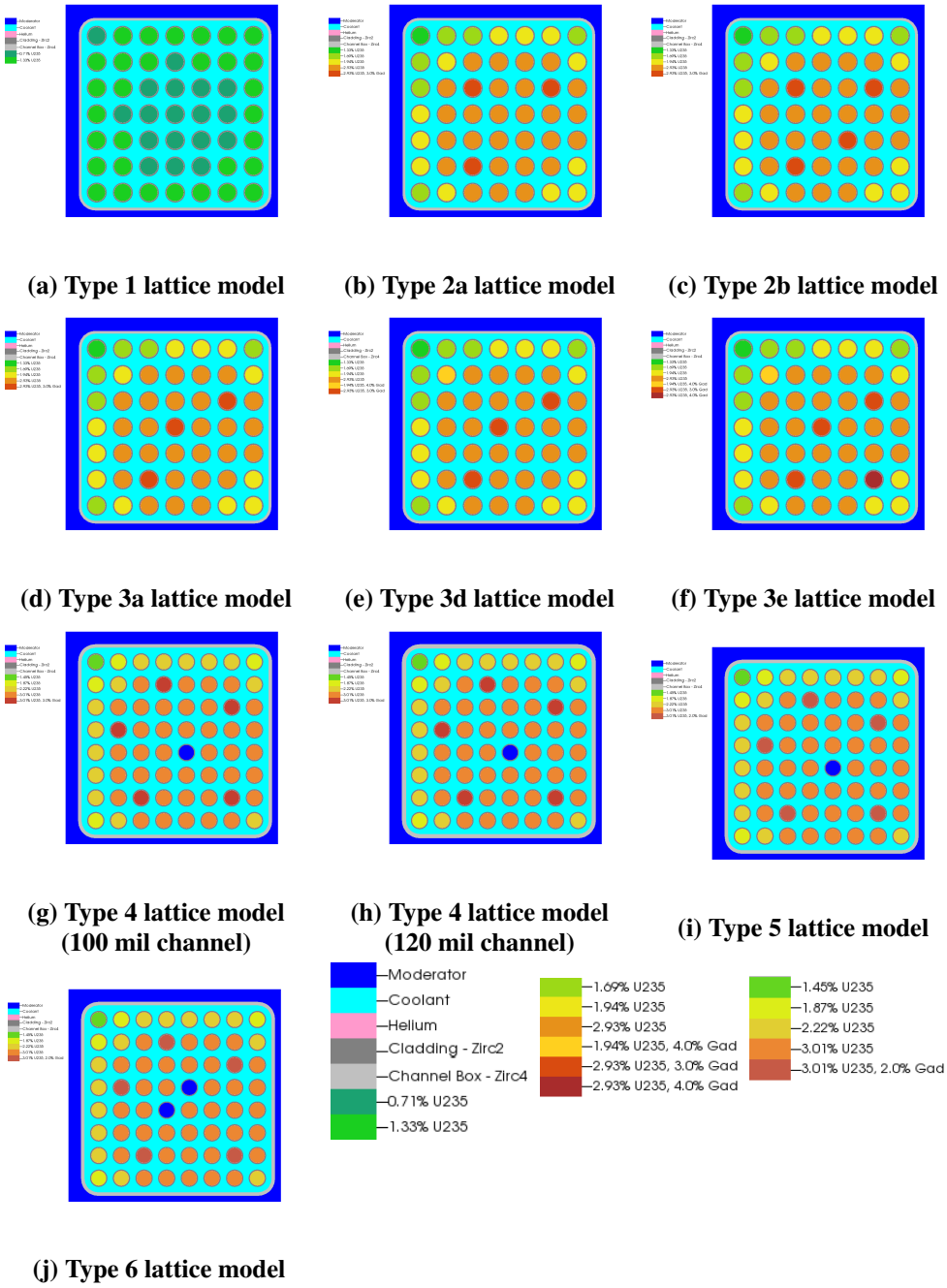

(a) Type 1 lattice model **(b) Type 2a lattice model** **(c) Type 2b lattice model**

(d) Type 3a lattice model **(e) Type 3d lattice model** **(f) Type 3e lattice model**

(g) Type 4 lattice model (100 mil channel) **(h) Type 4 lattice model (120 mil channel)** **(i) Type 5 lattice model**

(j) Type 6 lattice model

Figure 3.89. Selected Peach Bottom lattice models for MPACT.

3.7.2 Comparisons of 3D Peach Bottom Assembly

A set of 3D rodded assembly cases were run in MPACT and in continuous energy KENO for comparison and verification. The type 1 lattice shown in Figure 3.90 was expanded to a full 3D assembly. The model specifies a lower water reflector, a lower core plate, a lower tie plate, a fuel stack, an upper gas plenum, spacer grids, an upper tie plate, an upper core plate, and the control blade. The simulated conditions correspond to HZP. As specified in Larsen [61], the control blade notches are 3 inches wide, and the drive mechanism only moves the blades in 2-notch intervals. Therefore, the cases were run with the control blade at 0, 12, 24, 36, and 48 steps withdrawn, with 48 being the fully withdrawn position.

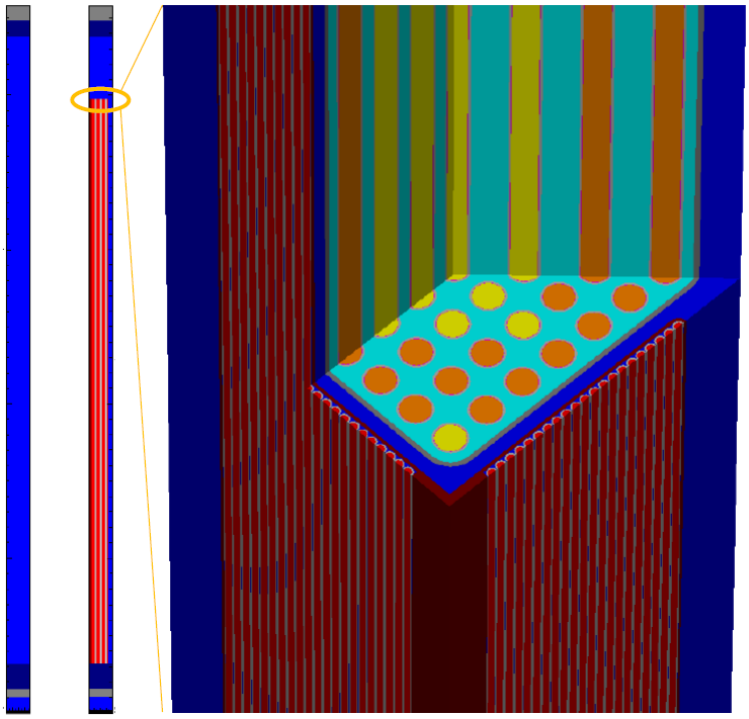

Figure 3.90. MPACT model: Peach Bottom Unit 2 Cycle 1 Type 1 assembly with inserted control blade.

The MPACT cases used the new 51-group library, and the MOC discretization was 0.01 cm, 8 azimuthal, and 2 polar angles per octant. Once again the Chebyshev-Yamamoto angular quadrature was used. These models were also simulated with TCP0 rather than P2, which was used for the lattices. Axially, the model is discretized into 79 planes, with 5.08 cm planes for the fuel. The KENO models used 5 million particles per cycle and simulated 500 inactive cycles and 2,000 active cycles. The results had a maximum statistical uncertainty of 0.7 pcm on k-eff. The uncertainties in the relative pin powers computed from KENO were <0.20% for the fully inserted and fully withdrawn cases. For the partially inserted cases, the statistics of the pins in the rodded regions were very large, although disagreement between the MPACT and KENO results did increase appreciably in these regions. The results of the comparison between MPACT and KENO are given in Table 3.54.

In these models, slightly increased differences can be seen compared to the 2D lattices. The differences are bounded by a 157 pcm difference in reactivity, a 0.74% maximum difference in the relative fission rate, and a 0.26% RMS. Overall, these differences are still quite good, although they are slightly increased over the 2D lattices in terms of the fission rate distributions.

Table 3.54. MPACT and KENO comparisons for Type 1 assembly for different rod positions at HZP

Rod position (steps)	Keno k_{inf}	MPACT Δk_{inf} (pcm)	Max diff of fiss rate	RMS of fiss rate
0	0.78549	-157	0.58%	0.26%
12	1.00887	117	0.67%	0.20%
24	1.03905	-33	0.74%	0.23%
36	1.04657	-59	0.76%	0.24%
48	1.04933	-78	0.74%	0.24%

3.7.3 3D BWR Control Cell

The 3D bundle design was adapted from the fuel loading pattern specification of an Atrium-10, and the large water rod inner diameter is chosen to preserve this bundle fuel–to–moderator ratio. The 3D model was also given 6-inch natural uranium blankets at the top and bottom, and the channel box and an upper plenum region were defined in dimensions consistent with those given in the report by Larsen [61]. Partial length rods, homogenized grid spacers, tie plates, axial reflectors, and core plates were also incorporated into the model. The images of this model are shown in Figure 3.91, and the fast and thermal fluxes are shown in Figure 3.92.

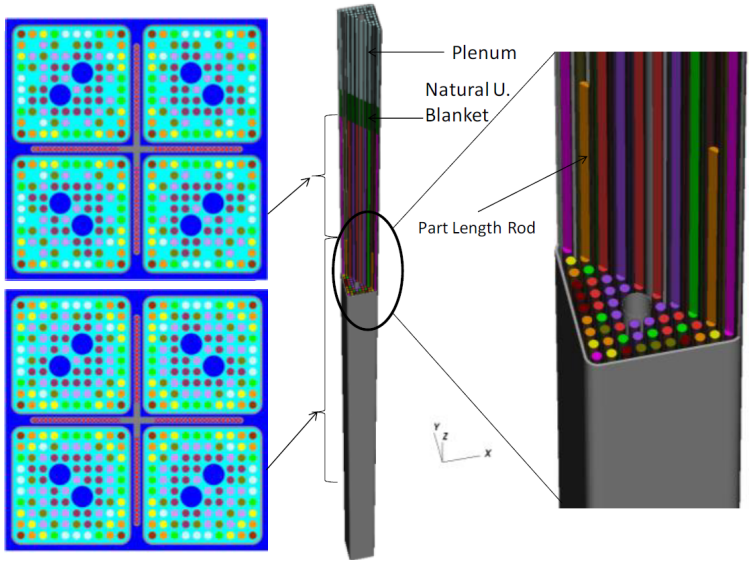

Figure 3.91. Visualization of MPACT geometry for 3D BWR assembly and power.

The model was simulated at hot zero power conditions. The model had an MOC discretization of 0.05 cm ray spacing, 16 azimuthal angles, and 2 polar angles per octant using the Chebyshev-Yamamoto quadrature. The scattering treatment was TCP0, and the 47-group library was used. The model was discretized into 6-inch nodes axially, for a total of 42 planes. The simulation was run in parallel on the Flux cluster at the University of Michigan using 42 processors for full spatial decomposition. The total simulation runtime was 4 minutes and 13 seconds. The convergence criteria for the eigenvalue and flux were set to 5.0e-5, and these criteria were reached after 9 iterations.

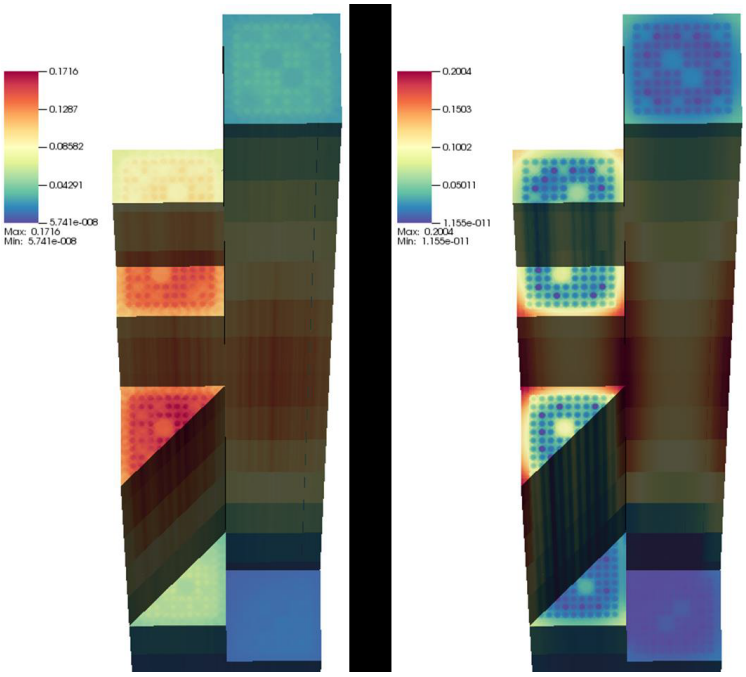

Figure 3.92. Fast flux (left) and thermal flux (right) for 3D control cell.

3.7.4 2D BWR Full Core

The Peach Bottom Cycle 1 loading pattern is shown in Figure 3.93. The core was modeled as 2D at cold zero power with all rods out and no radial reflector. The Cycle 1 loading pattern is asymmetric, which leads to the corresponding asymmetric power distribution shown in Figure 3.94. In this model, the MOC discretization used was 0.05 cm ray spacing with 16 azimuthal and 2 polar angles per octant, with the Chebyshev-Yamamoto angular quadrature. The scattering treatment used was TCP0. The problem was run in parallel on the Falcon cluster at Idaho National Laboratory using 764 processors—one processor for each assembly—for full spatial decomposition. The total runtime of the simulation was 2 minutes and 29 seconds. The convergence criteria for the eigenvalue and flux were set to 1.0e-6 and these criteria were reached after 29 iterations. This is a reasonable computational time for a core calculation, and it indicates that the full 3D BWR model will be computationally feasible.

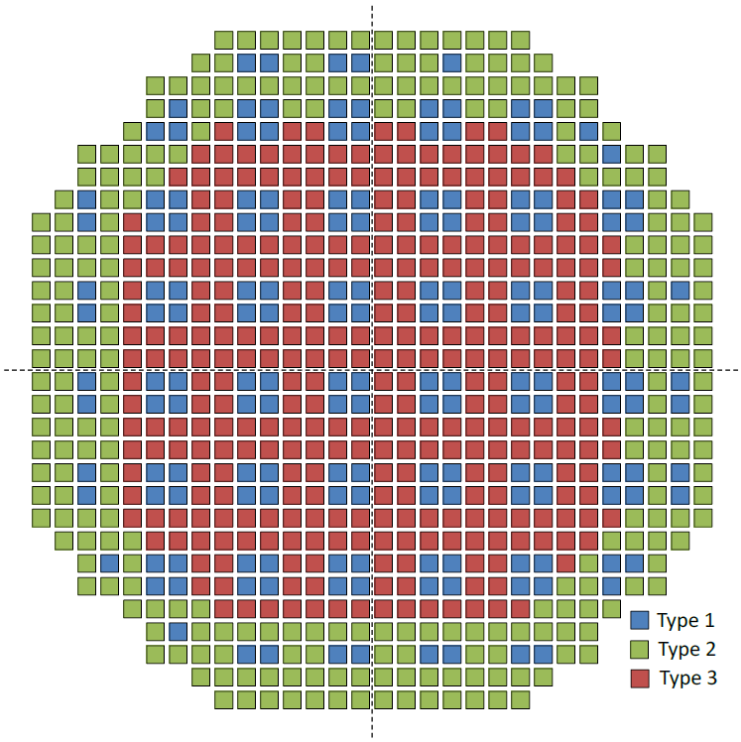

Figure 3.93. Peach Bottom Unit 2 Cycle 1 loading pattern.

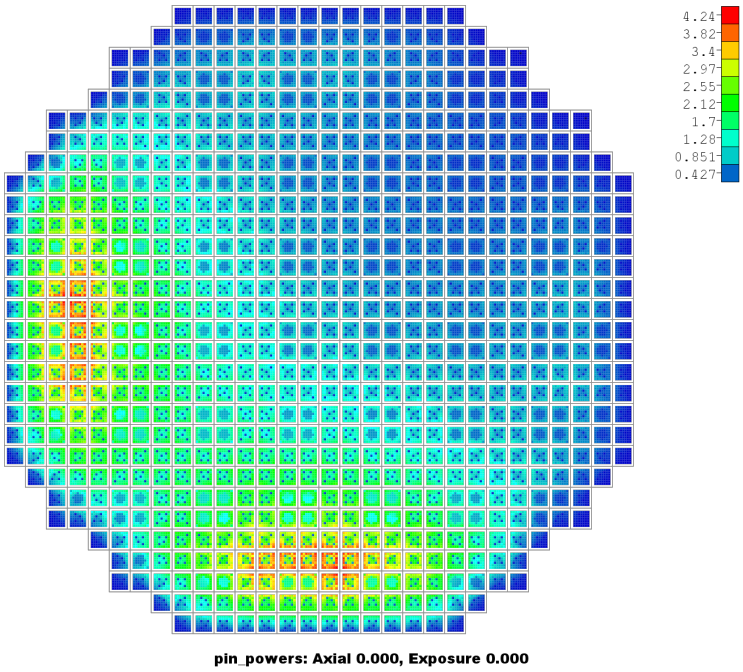

Figure 3.94. Power distribution for 2D Peach Bottom Unit 2 Cycle 1 CZP with all rods out.

3.8 BWR PROGRESSION PROBLEMS

3.8.1 Problem Descriptions

To validate MPACT's neutron transport calculations for boiling water reactors (BWRs), a set of BWR progression problems was developed by Lawing [62]. The problems were patterned after the PWR progression problems developed by Godfrey [6], beginning with simple cases and progressing to larger, more complex cases. The details of these problems are not reproduced here because they are described in extensive detail in Lawing's publicly available report. The problems are briefly described below.

- 2D BWR lattice
  - 8 × 8 Peach-6 bundle from cycle 2 of Peach Bottom unit 2 core with 2 small water rods
  - 8× 8 GE-9 bundle with 1 large water rod
  - 10 × 10 GE-14 bundle with 2 large water rods
  - 10 × 10 GE-14 bundle with 2 large water rods and part length rods (PLRs)
- 2D Mini-Core (4×4) of GE-14 bundles
- 3D GE-14 Single Bundle
  - cold zero power (CZP)
  - hot zero power (HZP)
  - hot full power (HFP) with specified axial void distribution
  - series of 13 blade positions at HZP conditions
- 3D Control Cell (2 × 2)
- 3D Mini-Core (4 × 4) at HFP
  - 4 blades at mixed positions
  - all rods in (ARI)
  - all rods out (ARO)

Depletion calculations for the lattices are performed at various voids; the 2D mini-core is also simulated at several different voids, although it is not depleted. The remaining cases use specified void distributions.

For all calculations, reference results were generated using the Monte Carlo code Serpent 2 [63]. For the 2D calculations and certain 3D calculations, MCNP 6.2 [64] reference results are also available. All results and inputs are available in the BWR progression problem GitHub repository [65].

3.8.2 Results

Results for MPACT are presented by Lawing [62], but the code has been updated significantly since those results were generated. Therefore, updated results are presented below. The tables are produced in the same style as those generated by Lawing [62] to enable easy comparison; the two noteworthy differences are that the Monte Carlo k_{eff} values are not shown and the absolute value of the largest fission rate difference is shown instead of both the minimum and maximum.

3.8.2.1 2D Results

This section presents the results for the 2D calculations. The results for each steady-state problem are shown in the following tables:

- Peach Bottom 6 lattice: Table 3.55
- GE-9 lattice: Table 3.56
- GE-14 lattice: Table 3.57
- GE-14 lattice with PLRs: Table 3.58
- 2D Mini-Core (4×4) of GE-14 bundles: Table 3.59

Figures 3.95 and 3.96 show the results of GE-9 and GE-14 depletion calculations, respectively. No significant differences are observed between these results and those originally presented by Lawing [62]. For all these cases, the results are essentially identical compared to those from Lawing, but they are shown here for completeness.

Table 3.55. Summary of comparison between MPACT and Serpent 2 results for the Peach Bottom 6 lattice

Uncontrolled			
Void (%)	Δk (pcm)	$\Delta P_{i,j}$ (absolute %)	
		Absolute max.	RMS
00	-41	0.49%	1.35%
40	-5	0.37%	1.14%
80	-70	0.22%	0.71%
Controlled			
Void (%)	Δk (pcm)	$\Delta P_{i,j}$ (absolute %)	
		Absolute max.	RMS
00	-171	0.57%	2.01%
40	-76	0.49%	1.88%
80	-38	0.42%	1.61%

Table 3.56. Summary of comparison between MPACT and Serpent 2 results for the GE-9 lattice

Uncontrolled			
Void (%)	Δk (pcm)	$\Delta P_{i,j}$ (absolute %)	
		Absolute max.	RMS
00	-63	0.55%	1.47%
40	-14	0.40%	1.14%
80	-24	0.24%	0.69%
Controlled			
Void (%)	Δk (pcm)	$\Delta P_{i,j}$ (absolute %)	
		Absolute max.	RMS
00	-171	0.72%	2.43%
40	-84	0.58%	2.17%
80	-40	0.43%	1.66%

Table 3.57. Summary of comparison between MPACT and Serpent 2 results for the GE-14 lattice

Uncontrolled			
Void (%)	Δk (pcm)	$\Delta P_{i,j}$ (absolute %)	
		Absolute max.	RMS
00	18	0.55%	1.55%
40	75	0.40%	1.15%
80	41	0.24%	0.70%
Controlled			
Void (%)	Δk (pcm)	$\Delta P_{i,j}$ (absolute %)	
		Absolute max.	RMS
00	-11	0.71%	2.38%
40	56	0.56%	1.91%
80	54	0.42%	1.43%

Table 3.58. Summary of comparison between MPACT and Serpent 2 results for the GE-14 lattice with part length rod

Uncontrolled			
Void (%)	Δk (pcm)	$\Delta P_{i,j}$ (absolute %)	
		Absolute max.	RMS
00	64	0.54%	1.50%
40	126	0.38%	0.97%
80	117	0.20%	0.53%
Controlled			
Void (%)	Δk (pcm)	$\Delta P_{i,j}$ (absolute %)	
		Absolute max.	RMS
00	50	0.66%	2.03%
40	111	0.51%	1.80%
80	119	0.35%	1.29%

Table 3.59. Summary of comparison between MPACT and Serpent 2 results for the 2D Mini-Core

Uncontrolled			
Void (%)	Δk (pcm)	$\Delta P_{i,j}$ (absolute %)	
		Absolute max.	RMS
00	21	0.55%	1.66%
20	50	0.48%	1.68%
60	73	0.33%	1.35%
Controlled			
Void (%)	Δk (pcm)	$\Delta P_{i,j}$ (absolute %)	
		Absolute max.	RMS
00	21	0.56%	1.86%
20	51	0.50%	1.85%
60	63	0.36%	1.78%

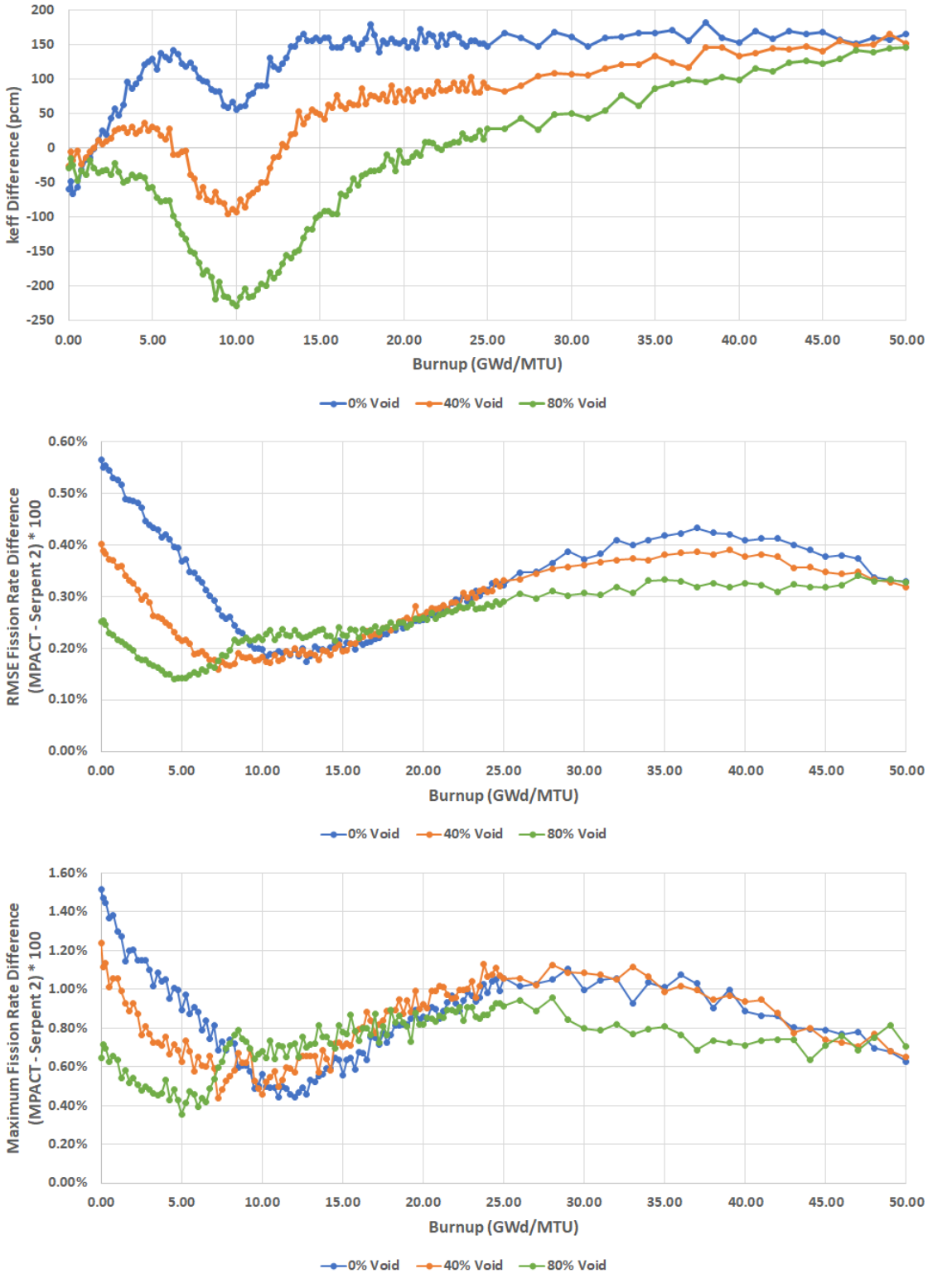

Figure 3.95. Eigenvalue (top), RMSE fission rate (middle), and maximum fission rate (bottom) differences between MPACT and Serpent 2 as a function of burnup for GE-9 depletions at 0%, 40%, and 80% cases.

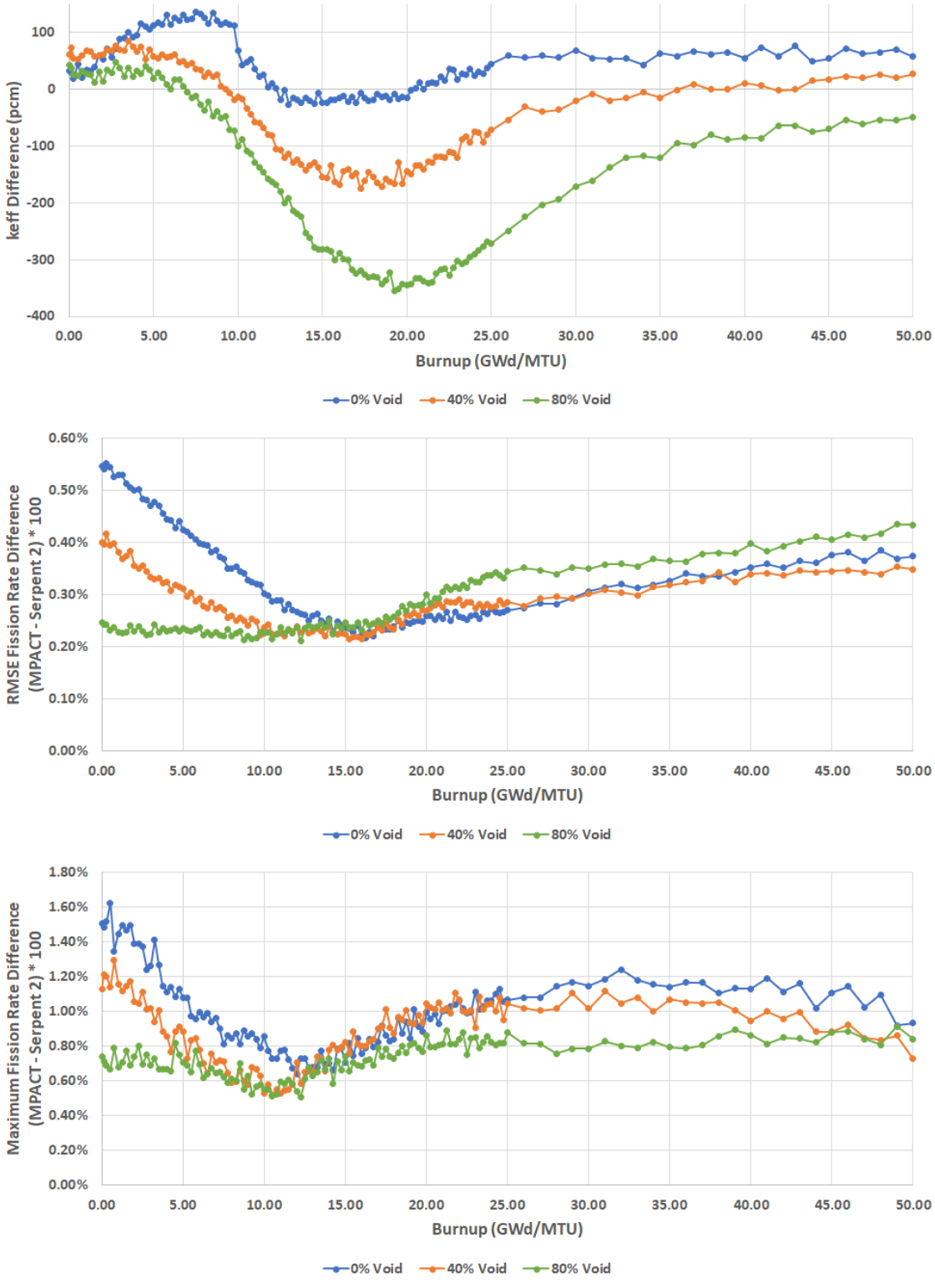

Figure 3.96. Eigenvalue (top), RMSE fission rate (middle), and maximum fission rate (bottom) differences between MPACT and Serpent 2 as a function of burnup for GE-14 depletions at 0%, 40%, and 80% cases.

3.8.2.2 3D Results

The 3D results are shown in the following tables:

- 3D single bundle: Figure 3.60
- 3D controlled bundle: Figure 3.61
- 3D HZP controlled single bundle: Figure 3.62
- 3D Mini Cores: Figure 3.63

In general, these results are 0.5%–2% improved over the results produced by Lawing [62]. This is because an improved axial solver based on the new source expansion nodal method (SENM) solver instead of the nodal expansion method (NEM) solver was used. This new solver uses a combination of polynomials and hyperbolic functions instead of just polynomials, enabling greater resolution of the axial power shape. Although this option is not the default for MPACT, the user is strongly encouraged to use SENM over the default NEM for BWR calculations. For pressurized-water reactors (PWRs), the differences are much less important.

Table 3.60. Summary of comparison between MPACT and Serpent 2 results for the 3D single bundle models

Conditions	Δk (pcm)	$\Delta P_{i,j}$ (absolute %)	
		Absolute max.	RMS
CZP	-12	1.96%	8.66%
HZP	56	1.14%	4.45%
HFP	53	1.54%	5.80%

Table 3.61. Summary of comparison between MPACT and Serpent 2 results for the 3D controlled GE-14 single bundle

Steps withdrawn	Δk (pcm)	$\Delta P_{i,j}$ (absolute %)	
		Absolute max.	RMS
00	7	1.00%	6.14%
04	7	1.02%	6.56%
08	-2	2.01%	16.72%
12	42	1.48%	10.39%
16	61	1.20%	7.23%
20	63	1.01%	5.92%
24	68	0.93%	6.47%
28	63	1.06%	6.46%
32	59	1.15%	5.79%
36	56	1.18%	5.53%
40	55	1.15%	5.08%
44	53	1.12%	4.68%
48	52	1.06%	4.33%

Table 3.62. Summary of comparison between MPACT and Serpent 2 results for the 3D HZP control cell

Case	Δk (pcm)	$\Delta P_{i,j}$ (absolute %)	
		Absolute max.	RMS
HZP control cell	-15	1.55%	14.33%

Table 3.63. Summary of comparison between MPACT and Serpent 2 results for the 3D mini core cases

Blade configuration	Δk (pcm)	$\Delta P_{i,j}$ (absolute %)	
		Absolute max.	RMS
ARI	45	1.12%	7.46%
Mixed blades	64	0.92%	5.47%
ARO	61	0.90%	4.54%

3.9 HATCH CYCLE 1

The Hatch nuclear plant is a BWR with publicly available data for its early cycles. The first cycle has been modeled with Virtual Environment for Reactor Applications (VERA) and compared to available transverse in-core probe (TIP) detector measurements. These results can serve as a multiphysics benchmark for the VERA code system instead of serving only as a simple neutron transport benchmark for MPACT itself.

The options used for MPACT are listed below:

```
[MPACT]
  !Solver Options
  shield_method subgroup-cell
  nodal_method senmp3
  coupling_method simplified

  !Meshing
  automesh_bounds   3 20                    ! min, max
  inter_assembly_gapmeshnum 3 2 3 2 1
  control_blade_meshnum 1 1
  refl_assembly_layers 2

  !Stability
  nodal_group_loop      5
  nodal_inners          10
  nodal_group_start     1
  nodal_inner_tol       1E-5
  nodal_group_tol       1E-5
  nodal_relax_negative  true
  cmfd_rtol             2.0e-3
  cmfd_relax_negative   true
  volume_corr           integral
  moc_source_splitting  full
  moc_min_flux          1E-20
  split_TL_tol          0.0
```

```
[COUPLING]
  rlx_power 0.5
  rlx_tfuel 1.0
  rlx_den   0.8
  bypass_treatment explicit_heating
  bypass_heating 0.0
  channel_box_conduction false
```

The operational history for cycle 1 was erratic, with frequent changes in power and flow. The MPACT model was approximated with 40 state points, as shown in Figure 3.97. Dashed vertical lines show the times at which the TIP detector measurements were taken. The data are available to validate the MPACT detector response, thus indirectly validating the neutron flux calculation.

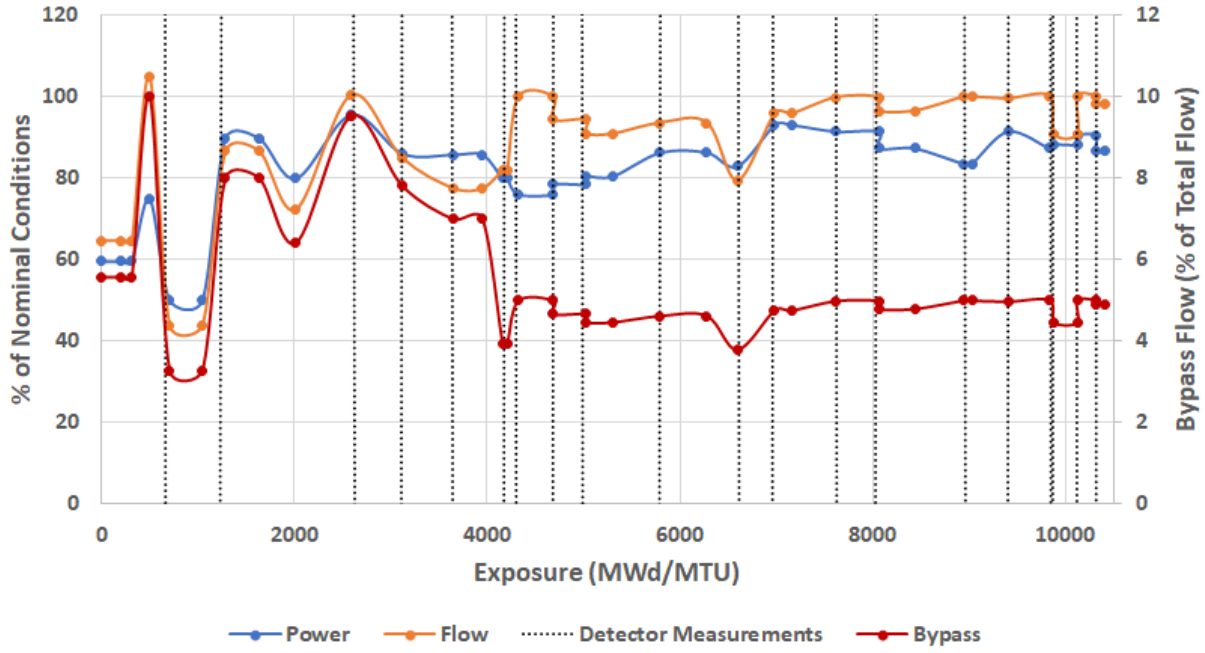

Figure 3.97. Approximation of Hatch Unit 1 cycle 1 operational history used for VERA validation; power and flow are plotted against the left axis, whereas bypass is plotted against the right axis.

Table 3.64. Summary of TIP and k_{eff} results for Hatch Unit 1 cycle 1 validation; results are averaged over all available data points, with standard deviations shown as ±

Error type	Radial	Axial	3D
TIP RMSE	4.69 ± 1.41%	10.81 ± 5.30%	12.95 ± 5.20%
TIP maximum	8.73 ± 4.90%	15.93 ± 7.23%	17.84 ± 6.52%
k_{eff}	–	–	327 ± 303 pcm

Table 3.64 shows average results for the TIP detector measurement comparisons (20 data points) and k_{eff} comparisons (40 data points) over the source of the cycle. The k_{eff} results over the course of the cycle are shown in Figure 3.98. The reactivity is almost always underpredicted, especially in the first half of the cycle. In the second half of the cycle, the errors are smaller—generally approximately -300 pcm or less.

Figure 3.99 shows plots of the TIP comparisons throughout the cycle. The 3D errors are driven by the axial component, especially near the middle of the cycle. At the beginning and end of the cycle, the 3D errors are generally less than 10%. These errors are less significant than those originally obtained using the `bypass_treatment saturated` option. It is expected that future improvements in the thermal hydraulic coupling may improve these results further.

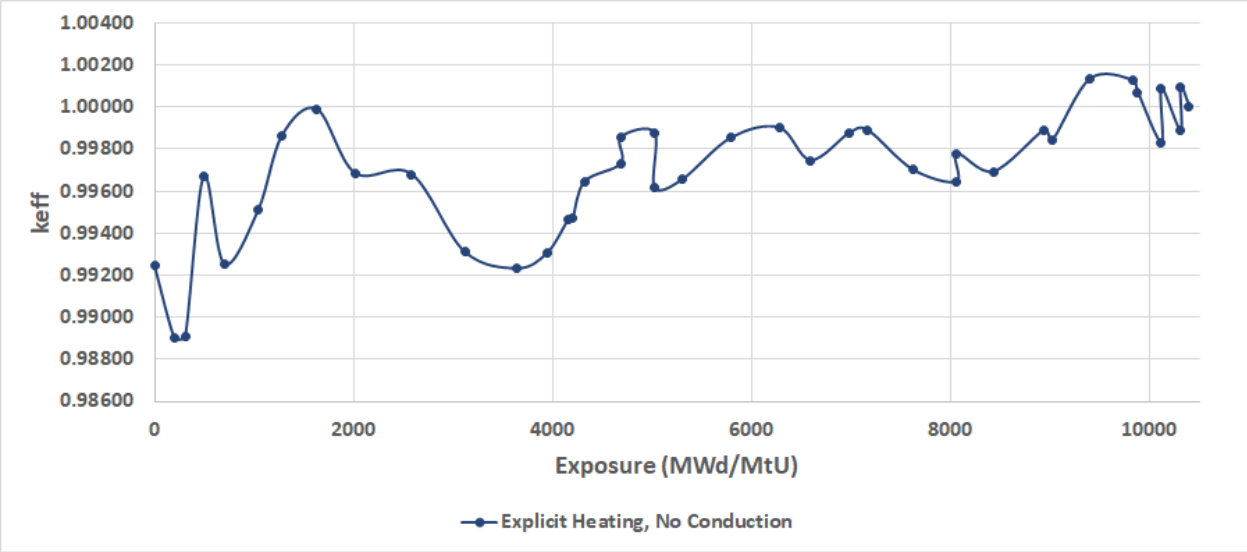

Figure 3.98. Hatch Unit 1 cycle 1 k_{eff} as a function of burnup.

Select flux maps are shown in Figure 3.100. They were selected to be representative of beginning, early, middle, and end of cycle conditions. The 2.584 and 5.024 GWD/MT maps indicate that the power was actually a little more bottom-peaked than predicted by VERA; this is consistent with the axial TIP comparisons being worse than the radial comparisons. The beginning of cycle and end of cycle show overall good agreement.

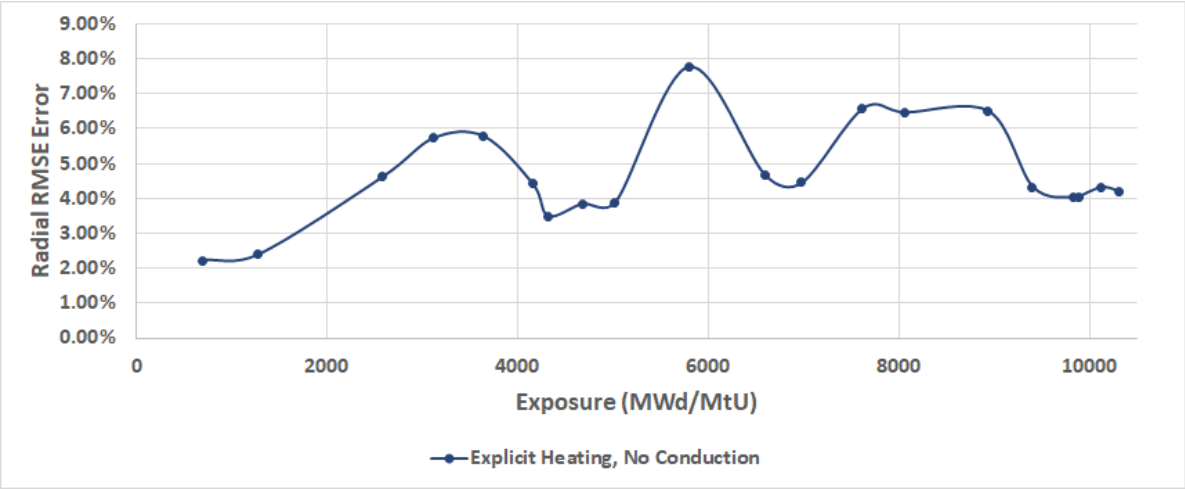

(a) Radial RMSE

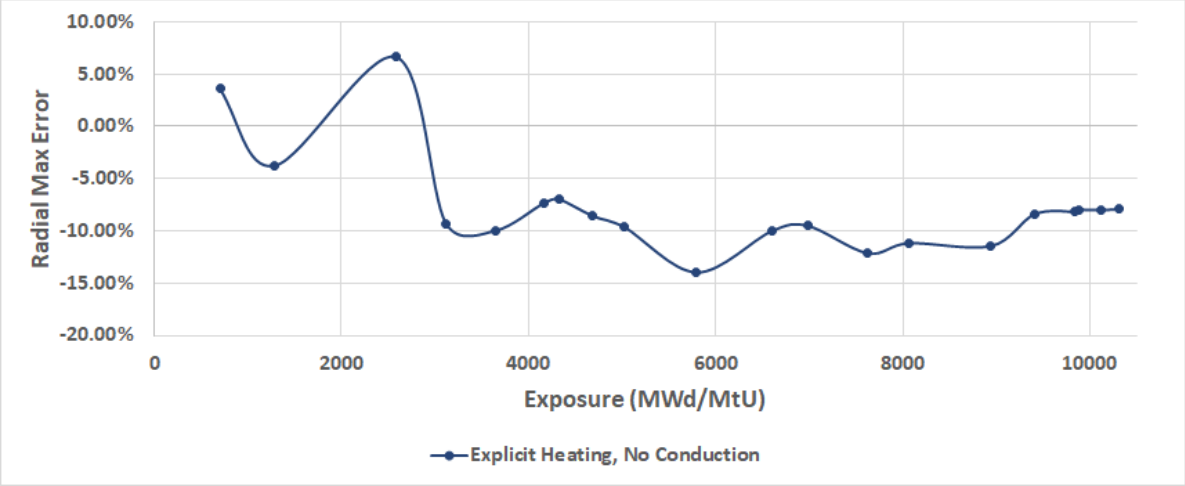

(b) Radial maximum

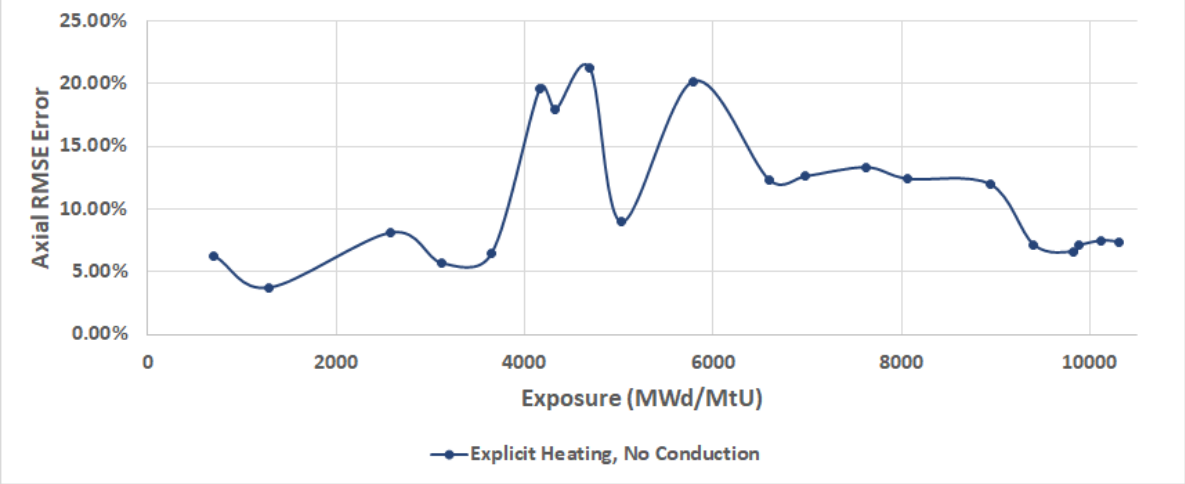

(c) Axial RMSE

Figure 3.99. Hatch Unit 1 cycle 1 TIP detector measurement comparison summary.

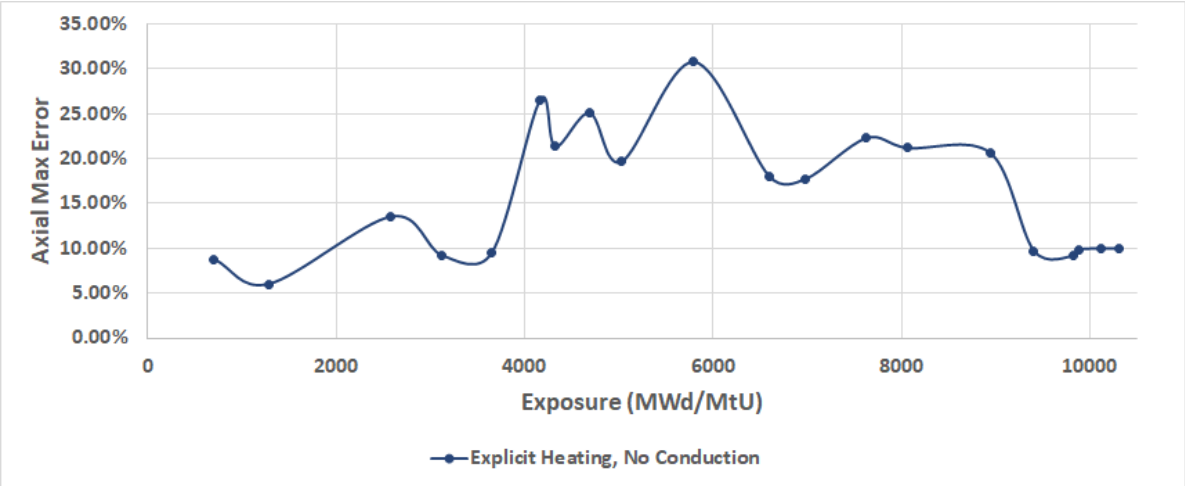

(d) Axial maximum

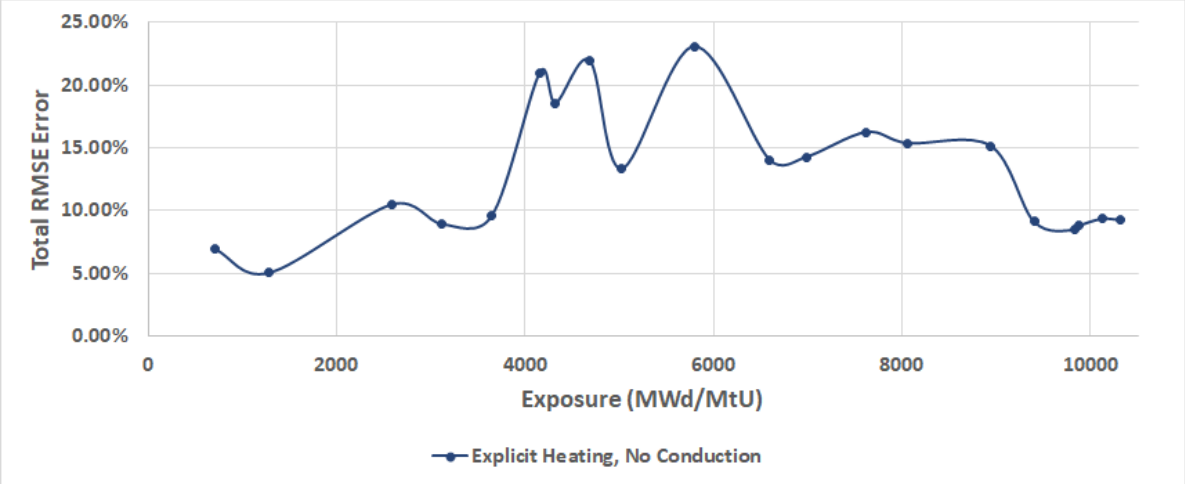

(e) 3D RMSE

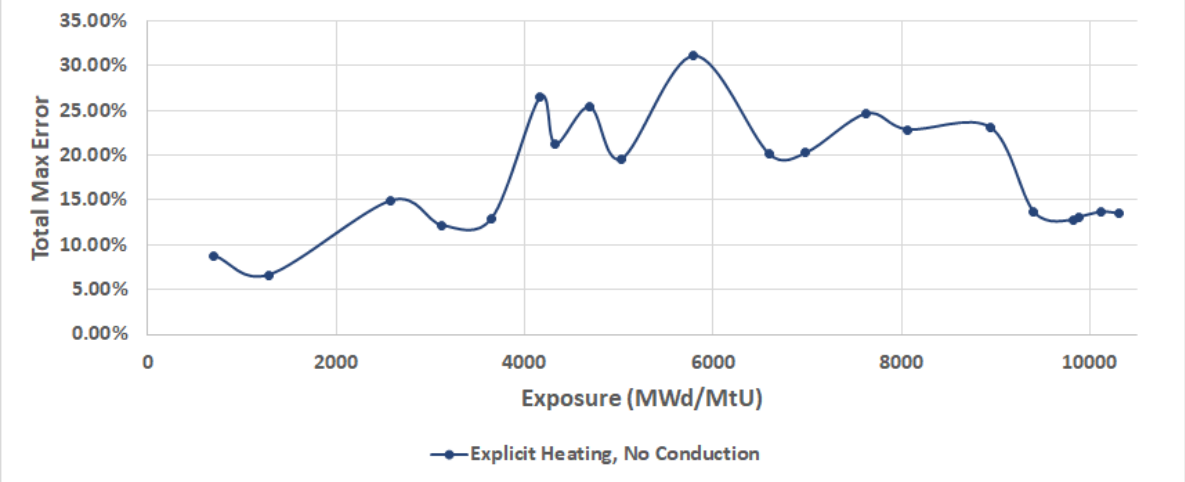

(f) 3D max.

Figure 3.99. Hatch Unit 1 cycle 1 TIP detector measurement comparison summary.

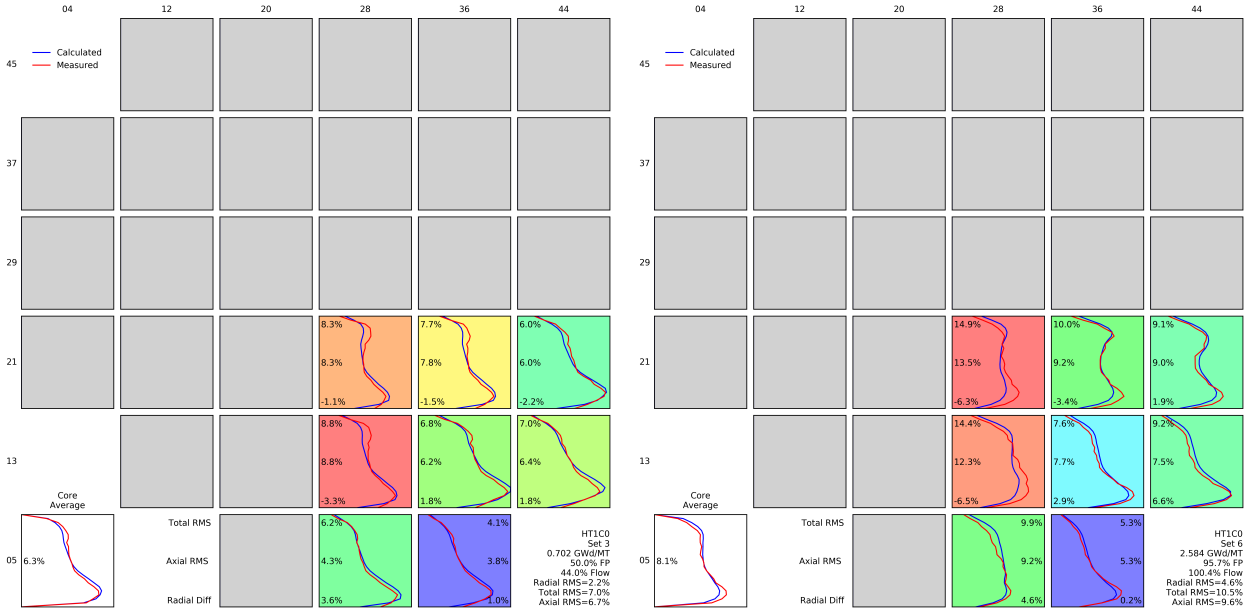

(a) 0.702 GWD/MT **(b) 2.584 GWD/MT**

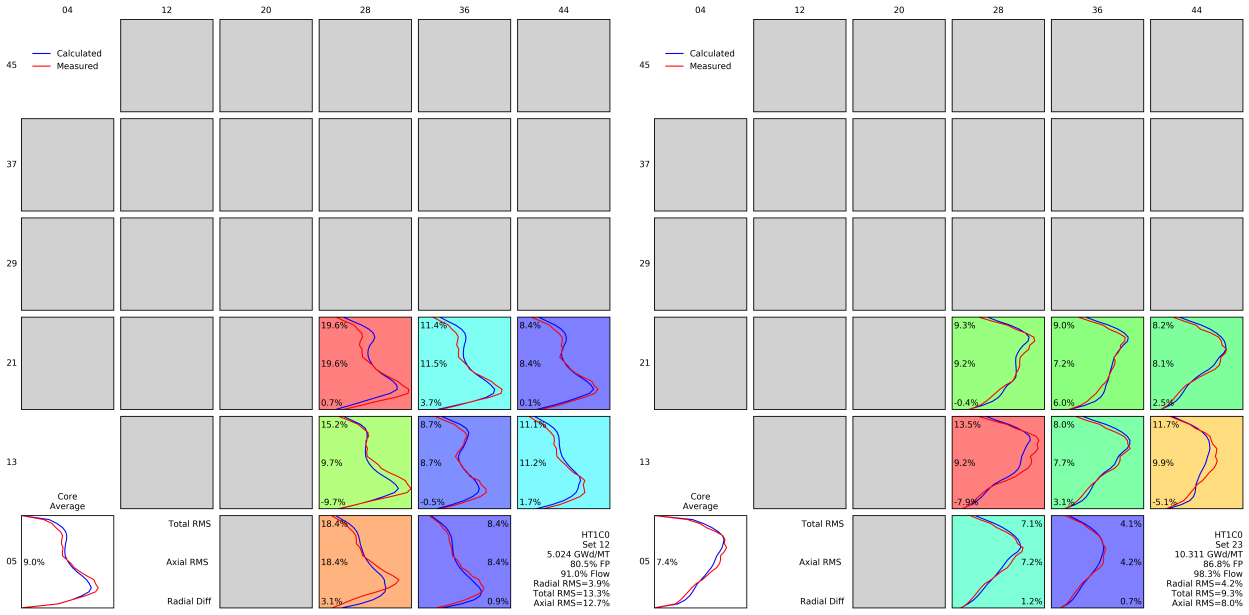

(c) 5.024 GWD/MT **(d) 10.311 GWD/MT**

Figure 3.100. Selected detector measurement maps for Hatch Unit 1 cycle 1.

4. SUMMARY AND FUTURE MPACT V&V WORK

This document summarizes the current state of MPACT V&V and establishes the framework for future MPACT V&V activities. An overview is provided of the verification and validation processes in MPACT, as well as a summary of the status of each component of V&V in the code. As described in the report, the activities in the areas of both source code verification and validation have matured in MPACT.

4.1 CODE VERIFICATION

Some of the specific tasks planned to improve MPACT code verification are outlined below.

4.1.1 Source Code Consistency Testing

As MPACT has matured and the code has grown significantly over the past year, the test coverage has decreased. Improving the test coverage in MPACT will be a priority the future. In particular, some functions do not meet the target goal for MPACT unit test coverage of 80%.

4.1.2 Code Verification Analysis

Mesh convergence analysis: The code verification of MPACT was significantly improved using the Ganapol Benchmark problem.

Method of Manufactured Solutions: The application of MMS was also applied to the Method of Characteristics (MOC), which was improved by using the C5G7 Benchmark problem. In the future, the generalized boundary condition functionality will be implemented in MPACT to enable the implementation of MMS in MPACT.

4.2 CODE VALIDATION

In the area of code validation, work has progressed in all principal validation areas identified by Godfrey [4] in the VERA-CS validation plan, specifically in the areas of critical experiments, measured data from the start-up of operating reactors, and comparison of MPACT results to continuous Monte Carlo.

4.2.1 Critical Experiment

A principal focus of validation work in FY19 was on the IPEN critical physics test to validate the pin resolved capability in MPACT. Additional work will be performed in the future to complete the IPEN benchmark problem, specifically to take advantage of the kinetics validation data.

4.2.2 Core Follow Data

In the future, work will be performed to integrate all the available non-proprietary core follow benchmark data into the MPACT V&V manual.

REFERENCES

[1] B. Collins. Expand Capability and Coverage of MPACT Regression Test Harness. Technical Report RTM Milestone L3RTM.PRT.P10.04, Oak Ridge National Laboratory, 2015.

[2] B. D. Ganapol. *Analytical Benchmarks for Nuclear Engineering Applications: Case Studies in Neutron Transport Theory*. Nuclear Energy Agency, 2008.

[3] AIAA Computational Fluid Dynamics Committee on Standards. Guide for the Verification and Validation of Computational Fluid Dynamics Simulations. Technical Report AIAA-G-077-1998, American Institute of Aeronautics and Astronautics, Reston, VA, 1998.

[4] A. Godfrey. VERA-CS Validation Plan. Technical Report CASL-U-2014-0185-000, Oak Ridge National Laboratory, October 2014.

[5] B. Collins and A. Godfrey. Analysis of the BEAVRS Benchmark Using VERA-CS. Technical Report CASL-U-2015-0076-000, Oak Ridge National Laboratory, April 19 2015.

[6] A. Godfrey. VERA Core Physics Benchmark Progression Problem Specifications. Technical Report CASL-U-2012-0131-004, Oak Ridge National Laboratory, August 29 2014.

[7] J. Wang. Sensitivity Study of MOC Parameters with VERA Benchmark Cases. Master's thesis, Department of Nuclear Engineering and Radiological Sciences, University of Michigan, December 2014.

[8] A. Kolowa. Unit Testing Best Practices. Internet Article, July 1 2009. Retrieved July 23, 2012.

[9] B. Kochunas. MPACT Software Test Plan, Requirements, and Test Report. Technical Report CASL-U-2019-1858-000, Oak Ridge National Laboratory, April 30 2019.

[10] W. L. Oberkampf and T. G. Trucano. Verification and Validation Benchmarks. *Nuclear Engineering and Design*, 238(3):716–743, March 2008.

[11] S. D. Pautz. Verification of Transport Codes by the Method of Manufactured Solutions: the ATTILA Experience. Technical Report LA-UR-01-1487, Los Alamos National Laboratory, 2001.

[12] J. Wang, W. Martin, and B. Collins. Application of the Method of Manufactured Solutions to the 1D SN Equation. In *Proceedings of PHYSOR-16*, Sun Valley, ID, USA, May 2016.

[13] J. Wang, W. Martin, and B. Collins. Order of accuracy of spatial discretization of method of characteristics. In *Proceedings of M&C 2017 - International Conference on Mathematics & Computational Methods Applied to Nuclear Science & Engineering*, Jeju, South Korea, April 2017.

[14] M. A. Smith, G. Palmiotti, T. A. Taiwo, E. E. Lewis, and N. Tsoulfanidis. Two- and Three-Dimensional Results for the C5G7 Benchmark Problem Using the Variational Nodal Method. In *Proceedings of International Conference on Nuclear Technology: Achieving Global Economic Growth While Safeguarding the Environment*, New Orleans, LO, USA, November 2003.

[15] M. Young. *Orthogonal-Mesh, 3D SN with Embedded 2-D Method of Characteristics for Whole-Core, Pin-Resolved Reactor Analysis*. PhD thesis, Department of Nuclear Engineering and Radiological Sciences, University of Michigan, 2016.

[16] B. Collins. Validation of VERA-CS with BEAVRS Cycle 2. Technical Report CASL Milestone L3:PHI.VCS.P13.01, Oak Ridge National Laboratory, September 30 2016.

[17] E. Walker, M. Pilch, S. Stimpson, B. Collins, and S. Palmtag. Axial Solution Verification for MPACT, CTF TH, CTFFuel, and VERA-CS. Technical Report CASL-U-2019-1852-000, Oak Ridge National Laboratory, 2019.

[18] M. Pilch. V&V Guidance and Review. Technical Report CASL L3 Milestone 2577, Oak Ridge National Laboratory, 2019.

[19] W. L. Oberkampf, T. G. Trucano, and C. Hirsch. Verification, Validation, and Predictive Capability in Computational Engineering and Physics. *Applied Mechanics Reviews*, 57(5):345–384, 2004.

[20] T. Downar, S. Palmtag, K. Clarno, and K. Kim. VERA-CS Verification and Validation Plan. Technical Report CASL-U-2017-1287-000, Oak Ridge National Laboratory, April 28 2017.

[21] K. Smith and B. Forget. Challenges in the Development of High-Fidelity LWR Core Neutronics Tools. In *Proceedings of M&C 2013*, Sun Valley, ID, USA, May 5–9 2013.

[22] J. Kulesza, S. Stimpson, A. Gerlach, and D. Jabaay. Babcock and Wilcox Critical Experiment Calculations to Support MPACT Validation. Technical Report CASL-U-2015-0143-000, Oak Ridge National Laboratory, April 24 2015.

[23] S. Palmtag. MPACT Validation with Critical Experiments. Technical Report CASL-U-2017-1388-000, Oak Ridge National Laboratory, July 2017.

[24] N. M. Baldwin et al. Critical Experiments Supporting Close Proximity Water Storage of Power Reactor Fuel. Technical Report B&W-1484-7, Babcock & Wilcox, July 1979.

[25] L. W. Newmann. Urania-Gadolinia: Nuclear Model Development and Critical Experiment Benchmark. Technical Report DOE/ET/34212-41, B&W-1810, Babcock & Wilcox, April 1984.

[26] A. D. Knipe. Specification of the DIMPLE S01 Benchmark Assemblies. Technical Report AEA-TSD-0375, Alternative Reference JDF/DOC-504, AEA Technology, Technical Services Division, November 1994.

[27] B. Yee and B. Kochunas. DIMPLE Modeling with MPACT. Internal Memorandum, Department of Nuclear Science and Engineering, University of Michigan, November 2016.

[28] Z. Dodson, B. Kochunas, K. S. Kim, Y. Liu, B. Yee, and T. Downar. Update to MPACT Modeling of DIMPLE Benchmark Problems. Technical Report CASL-U-2017-1294-000, Oak Ridge National Laboratory, 2017.

[29] Nuclear Energy Agency. Benchmark on the VENUS-2 MOX Core Measurements. Technical Report NEA/NSC/DOC(2000)7, OECD/NEA, 2000.

[30] E. Hellstrand, P. Blomberg, and S. Horner. The Temperature Coefficient of the Resonance Integral for Uranium Metal and Oxide. *Nuclear Science and Engineering*, 8:497–506, 1960.

[31] D. J. Lee, K. Smith, and J. Rhodes. The Impact of ^{238}U Resonance Elastic Scattering Approximations on Thermal Reactor Doppler Reactivity. *Annals of Nuclear Energy*, 36:274–280, 2009.

[32] E. Hellstrand. Measurements of the Effective Resonance Integral in Uranium Metal and Oxide in Different Geometries. *Journal of Applied Physics*, 28:1493–1502, 1957.

[33] A. Godfrey et al. VERA-CS Solutions to the CASL Core Physics Benchmark Problems. In *Proceedings of ANS MC2015 - Joint International Conference on Mathematics and Computation (M&C), Supercomputing in Nuclear Applications (SNA), and the Monte Carlo (MC) Method*, Nashville, TN, April 19–23 2015.

[34] A. Godfrey et al. Watts Bar Unit 2 Startup Results with VERA. Technical Report CASL-2017-1306-000, Oak Ridge National Laboratory, March 31 2017.

[35] U. Mertyurek. Validation of MPACT Depletion Calculations with Radiochemical Assay Data Comparison. Technical Report CASL-X-201X-0XXX-000, Oak Ridge National Laboratory, September 30 2016.

[36] Y. Nakahara, K. Suyama, and T. Suzaki. Technical Development on Burn-up Credit for Spent Fuels [English Translation]. Technical Report JEARI-Tech 2000-071 (ORNL/TR-2001/01, Oak Ridge National Laboratory, January 2002.

[37] R. J. Guenther et al. Characterization of LWR Spent Fuel MCC-Approved Testing Material-ATM-106. Technical Report PNL-5109-106, Pacific Northwest Laboratories, 1988.

[38] C. Alejano et al. Spent Fuel Nuclear Assay Data for Isotopic Validation. Technical Report NEA/NSC/WPNCS/DOC(2011)5, Nuclear Energy Agency, June 2011.

[39] K. Macku, F. Jatuff, M. F. Murphy, O. P. Joneja, C. R. Bischofberger, and R. Chawla. Advanced Foil Activation Techniques for the Measurements of Within-Pin Distributions of 63Cu(n.g)64Cu Reaction Rate in Nuclear Fuel. *Nuclear Instrumentation Methods in Physics Research*, pages 383–400, 2006.

[40] K. Macku, F. Jatuff, M. Murphy, and M. Plaschy. Radial and Azimuthal ^{235}U Fission and ^{238}U Capture Distributions in BWR UO_2 Pins: CASMO-4 and MCNP4 Versus Activation Foil Measurements. *Nuclear Science and Engineering*, 155:96–101, 2007.

[41] T. Williams, R. Chawla, P. Grimm, O. P. Joneja, R. Seiler, and A. Ziver. New Experiments at Zero-Power Facility Using Power Reactor Fuel. In *Proceedings of the International Conference on Physics of Nuclear Science and Technology*, pages 720–727, Long Island, NY, USA, 1998.

[42] J. F. (Ed.) Briesmeister. MCNP – A General Monte Carlo N-Particle Transport Code, Version 4C. Technical Report LA. 13709-M., Los Alamos National Laboratory, 2000.

[43] K. E. Edenius, B. H. Forssen, and D. Knott. CASMO-4, a Fuel Assembly Burnup Program, User's Manual. Technical Report STUDSVIK/SOA-95/1, Studsvik of America Inc., 1995.

[44] L. F. L. Mura, A. dos Santor, D. B. Domingos, P. C. R. Rossi, and R. Jerez. The Experimental Determination of the ^{238}U(n,c) and Total Fission Reaction Rates along the Pellet Radius of the IPEN/MB-01 Reactor. *Annals of Nuclear Energy*, 99:399–409, 2017.

[45] J. B. (Ed.) Briggs. International Handbook of Evaluated Criticality Safety Benchmark Experiments. Technical Report NEA/NSC/DOC(95)03/I, Nuclear Energy Agency, Paris, France, September 2012.

[46] Organisation for Economic Co-operation and Development. International Handbook of Evaluated Reactor Physics Benchmark Experiments. Technical Report NEA/NCS/DOC(2006)1, Nuclear Energy Agency, 2018.

[47] A. Dos Santos et al. *International Handbook of Evaluated Criticality Safety Benchmark Experiments, NEA/NSC/DOC (95)03/I*, chapter LEU-COMP-THERM-077: Critical Loading Configurations of the IEPN/MB-01 Reactor. Nuclear Energy Agency, September 2004.

[48] E. E. Lewis et al. Benchmark on Deterministic Transport Calculations without Spatial Homogenization. Technical report, Nuclear Energy Agency Organisation for Economic Cooperation and Development, 2003.

[49] E. E. Lewis et al. Benchmark on Deterministic Transport Calculations without Spatial Homogenization: MOX Fuel Assembly 3-D Extension Case. Technical report, Nuclear Energy Agency Organisation for Economic Cooperation and Development, 2005.

[50] K. S. Kim. Generation of Transient Data for the ENDF/B-7.0 and ENDF/B-7.1 MPACT Libraries. Technical Report CASL-S-2015-PHI.VCS.P11.02-001, Oak Ridge National Laboratory, October 6 2014.

[51] J. Hykes, R. Ferrer, and J. Rhodes. CASMO5 Analysis of Select IPEN/MB-01 Experiments. In *Proceedings of PHYSOR 2018*, Cancun, Mexico, April 22-26 2018.

[52] A. Santamarina, V. Pascal, G. Truchet, and J-F. Vidal. Validation of LWR reactivity versus reactor period feedback on the delayed neutron data (β_i, λ_i). In *Proceedings of PHYSOR 2018*, Cancun, Mexico, April 22–26 2018.

[53] G. Keepin, T. Wimett, and R. Zeigler. Delayed Neutrons from Fissionable Isotopes of Uranium, Plutonium, and Thorium. *Journal of Nuclear Energy*, 6:1–21, 1957.

[54] R. Tuttle. Delayed-Neutron Data for Reactor-Physics Analysis. *Nuclear Science and Engineering*, 56:37–71, 1975.

[55] R. K. McCardell, D. I. Herborn, and J. E. Houghtaling. Reactivity Accident Test Results and Analyses for the SPERT III E-Core – A Small, Oxide-Fueled, Pressurized-Water Reactor. Technical Report IDO-17281, AEC Research and Development, March 1969.

[56] A. Santamarina et al. The JEFF-3.1.1 Nuclear Data Library Validation Results for JEFF-2.2 to JEFF-3.1.1. Technical Report 22, OECD/NEA Data Bank, JEFF, 2009.

[57] J. Durgone. SPERT III Reactor Facility: E-CORE Revision. Technical Report IDO-17036, AEC Research and Development, 1965.

[58] S. M. Bowman. SCALE 6: Comprehensive Nuclear Safety Analysis Code System. *Nuclear Technology*, 174(2):126–148, 2011.

[59] A. Graham, B. Collins, S. Stimpson, and T. Downar. Subplane Collision Probabilities Method Applied to Control Rod Cusping in 2D/1D. *Annals of Nuclear Energy*, 118:1–14, August 2018.

[60] B. Kochunas et al. Initial BWR Modeling Capability for MPACT. In *Proceedings of M&C 2017 - International Conference on Mathematics & Computational Methods Applied to Nuclear Science & Engineering*, Jeju, South Korea, April 2017.

[61] N. H. Larsen. Core Design and Operating Data for Cycles 1 and 2 of Peach Bottom 2. Technical Report NP-563, Electric Power Research Institute, June 1978.

[62] Chase Lawing, Scott Palmtag, and Mehdi Asgari. BWR Progression Problems. Technical Report ORNL/TM-2020/1792, Oak Ridge National Laboratory, 2021.

[63] J. Leppänen, M. Pusa, T. Viitanen, V. Valtavirta, and T. Kaltiaisenaho. The Serpent Monte Carlo Code: Status, Development, and Applications in 2013. *Annals of Nuclear Energy*, 84:142–150, 2015.

[64] MCNP Users Manual – Code Version 6.2. Technical Report LA-UR-17-29981, Los Alamos National Laboratory, 2017.

[65] C. Lawing. BWR Progression Problems, 2021.

[66] K. M. Case, F. De Hoffman, and G. Placzek. *Introduction to the Theory of Neutron Diffusion*. Los Alamos Scientific Laboratory, Los Alamos, NM, 1953.

[67] J. Wang, W. Martin, and B. Collins. Updates on Method of Manufactured Solutions. Internal Memorandum, CASL, September 24 2016.

[68] MPACT Development Team. MPACT Theory Manual Version 4.3. Technical report, Oak Ridge National Laboratory, 2021. Edited by Ed Larsen, Ben Collins, Brendan Kochunas, Shane Stimpson, and Aaron Graham.

[69] A. Godfrey. Qualify VERA-CS for Multi-Cycle PWR Simulation Capability. Technical Report L1.CASL.P11.02, Oak Ridge National Laboratory, June 30 2015.

[70] H. Horelik et al. Benchmark for Evaluation and Validation of Reactor Simulations (BEAVRS), Release Revision 1.1.1. Technical report, MIT Computational Reactor Physics Group, October 2013.

APPENDIX A. A BENCHMARK SOLUTION FOR MPACT CODE VERIFICATION

APPENDIX A. A BENCHMARK SOLUTION FOR MPACT CODE VERIFICATION

A.1 GANAPOL BENCHMARK RESULTS

Benchmark problem 3.4 in Ganapol's analytical benchmark book [2] has proved itself to be an excellent code verification test problem that can be modeled using MPACT without special coding. It can be included in the MPACT regression suite. As described in Section 2.2.1, the configuration is a homogeneous right circular cylinder that is infinite in height. The homogeneous cylinder has a radius of $r = R$ and a height of $h \to \infty$, with a total cross section of Σ_t, and c secondary neutrons per collision, where $c = \left(\Sigma_s + \nu\Sigma_f\right)/\Sigma_t$.

The benchmark results include the critical rod radius as a function of c, as shown in Figure A.1. Figure A.1 is Table 3.4.4 from [2], and it gives the scalar flux as a function of radius in mean free paths $(1/\Sigma_t)$ for several of the critical rod cases. The first column should be corrected such that r/R ranges from 0.00 to 1.00. Table 3.4.3(b) from [2] provides critical rod radii for a larger range of values of c, but these are not shown in this report.

Table 3.4.4. Critical flux distributions

r/R:c	1.05	1.1	1.6	2.0
0.00E+00	1.00000E+00	1.00000E+00	1.00000E+00	1.00000E+00
0.25E-01	9.29851E-01	9.36052E-01	9.54996E-01	9.59783E-01
0.50E-01	7.33990E-01	7.56084E-01	8.24845E-01	8.42634E-01
0.75E-01	4.52168E-01	4.92189E-01	6.21823E-01	6.56963E-01
0.85E-01	3.26662E-01	3.71791E-01	5.22344E-01	5.64397E-01
0.91E-01	2.49166E-01	2.96040E-01	4.56627E-01	5.02561E-01
0.95E-01	1.95805E-01	2.43013E-01	4.08837E-01	4.57218E-01
0.98E-01	1.53086E-01	1.99922E-01	3.68806E-01	4.18990E-01
1.00E-00	1.17908E-01	1.64122E-01	3.35065E-01	3.86650E-01

Figure A.1. Table 3.4.4 from Ganapol [2].

A.2 MPACT MODEL FOR THE BENCHMARK PROBLEM

The cylinder is modeled as a fuel pin inside a non-scattering square bounding box—a void or a pure absorber—with vacuum boundaries. The critical rod cases give the critical rod size as a function of c. MPACT solved for the eigenvalue k for each of the critical rod radii given in Table 3.4.3(a), where cross sections are chosen to yield the tabulated c. For each of these cases, MPACT should yield $k = 1$ to some precision. This is easily seen by noting that the balance equation for the critical rod for a given value of c is given by $L\varphi = cM\varphi = c\phi/4\pi$, where ϕ is the scalar flux, and $c = \left(\Sigma_s + \nu\Sigma_f\right)/\Sigma_t$. MPACT then solves the following eigenvalue problem with the critical rod radius,

$$L\varphi = \frac{\Sigma_s + \frac{1}{k}\nu\Sigma_f}{\Sigma_t}\frac{1}{4\pi}\phi\,, \tag{A.1}$$

and $k = 1$ is equivalent to finding the critical value of c given the rod radius.

A.3 BOUNDING BOX ASSUMPTION

Although it seems physically plausible that the solution to the rod in a bounding box would be equivalent to solving the bare rod for the case of vacuum boundaries, there may be small effects because the tracks that are incident on the rod are not uniformly and isotropically (U&I) distributed on the rod surface. They are

U&I incident on the bounding box, but they will enter the rod with a non-U&I distribution (in azimuthal and polar angles), depending on the size of the box relative to the rod. This should not be a practical issue for zero incoming fluxes, but this could change the numerical integration along the tracks, possibly causing disagreement with the benchmark results, perhaps in the 6th or 7th digit, for example.

To resolve this question, all the cases were rerun with bounding boxes that preserved the ratio of the bounding box side to the cylinder radius, which was 17. The resulting ks are tabulated in Table A.1, which are identical to the ks tabulated in Table 5.1, thus demonstrating that solving the critical rod problem inside a bounding box was equivalent to solving the bare rod problem.

Table A.1. MPACT k with the ratio bounding box side/radius held constant

c	R	Bounding box size	k	error (pcm)
1.01	13.125516490	223.13	0.9999757	-2.43
1.02	9.043254850	153.74	0.9999783	-2.17
1.05	5.411288290	91.99	0.9999837	-1.63
1.1	3.577391300	60.82	0.9999895	-1.05
1.2	2.287209260	38.88	0.9999967	-0.33
1.3	1.725002920	29.33	1.0000006	0.06
1.4	1.396978590	23.75	1.0000020	0.2
1.5	1.178340850	20.03	1.0000004	0.04
1.6	1.020839010	17.35	0.9999967	-0.33
1.8	0.807426618	13.73	0.9999871	-1.29
2	0.668612867	11.37	0.9999619	-3.81

Furthermore, Monte Carlo simulations were performed to analyze the effect of the bounding box assumption. The geometry studied was an infinite cylinder with radius R = 1 mfp. Case et al. [66] tabulated escape probabilities for infinite rods as a function of radius in mfp. Equation (27) on page 33 gave the exact escape probability in terms of modified Bessel functions of the first and second kinds. Using reciprocity, the exact collision probability can be calculated, which is the probability that a neutron incident U&I on the surface of the infinite rod suffers a collision inside the rod. Monte Carlo was used to model an infinite rod with a radius of 1 mfp that is irradiated with a U&I source of neutrons. One billion source neutrons were emitted into the rod, and the collision probability agreed with the exact solution within 5 decimals. The rod was then put into a bounding box with a U&I source of neutrons on the surface of the bounding box, which is consistent with the MPACT simulations. Two billion source neutrons were emitted on the surface of the bounding box, and approximately 923 million source neutrons entered the rod. The estimated collision probability for those neutrons agreed with the exact result to within 5 decimal points, showing that the bounding box has very little effect on the results within the rod. This provides additional evidence to support the use of the bounding box to analyze the Ganapol benchmark problems.

A.4 MESH CONVERGENCE ANALYSIS

Next, the mesh convergence analysis is included for three discretization parameters, including the radial discretization, ray spacing, and polar angular discretization.

A.4.1 Radial Convergence

The c = 1.01 critical rod case is used as an example. The results are tabulated in Table A.2. Errors are calculated by taking the difference between the eigenvalue k for each individual case and unity. The last column is the assessed rate of convergence.

Table A.2. The error in k vs. number of rings in the fuel

# of rings in fuel	k	error (pcm)	p
10	0.995712	-428.8	1.73
20	0.9987038	-129.62	1.83
30	0.9993816	-61.84	1.87
40	0.9996393	-36.07	1.90
50	0.999764	-23.6	1.92
60	0.9998337	-16.63	1.94
70	0.9998766	-12.34	1.94
80	0.9999048	9.52	1.95
90	0.9999243	-7.57	1.96
100	0.9999384	-6.16	1.96
110	0.9999489	-5.11	1.98
120	0.999957	-4.3	1.98
130	0.9999633	-3.67	1.98
140	0.9999683	-3.17	1.96
150	0.9999723	-2.77	1.97
160	0.9999756	-2.44	–

The convergence curve shows a nice second order radial convergence (up to 160 rings) for $c = 1.01$. However, further study shows a larger c comes with a narrower asymptotic region. For example, when $c = 1.3$, the second order convergence can be observed only up to 30 rings. Past 30 rings, it is evident that other error components begin to contaminate the second order convergence, flattening out the convergence curve earlier. This is understandable, because a larger c comes with a smaller critical radius, where a smaller number of radial discretization is needed to achieve a certain accuracy level. If a constant -0.7 pm error compensation is assumed for the other error components, then the second order convergence can be observed up to 100 rings.

A.4.2 Ray Spacing Convergence

A critical rod case of $c = 1.03$ is used to demonstrate the solution convergence with respect to ray spacing. The following set of discretization parameters is used for the ray spacing convergence analysis.

- Bound box side length = 4 cm
- # radial rings = 80
- # azimuthal slices = 64
- Quadrature set = CHEBYSHEV-GAUSS 64 24
- Convergence criterion = 10^{-7} for both k and ϕ

The results are tabulated in Table A.3, and the convergence curve is plotted in Section 2.2.4.

A constant rate of convergence is not obtained, but MOC never guarantees that. The convergence curve is generally monotonic. Local oscillation exists, which is consistent with the solution verification study in MPACT using Progression Problem 1a. Generally, the convergence curve is nicely converging to the theoretical benchmark.

Table A.3. The error in k vs. ray spacing

ray spacing	k	error (pcm)
0.5	1.0075921	759.21
0.4	1.0060423	604.23
0.3	1.0049383	493.83
0.2	1.0029771	297.71
0.1	1.0011765	117.65
0.09	1.0012963	129.63
0.08	1.0011247	112.47
0.07	1.000989	98.9
0.06	1.0006124	61.24
0.05	1.0004149	41.49
0.04	1.0001499	14.99
0.03	1.0000255	2.55
0.02	1.0000081	0.81

A.4.3 Polar Angle Convergence

To demonstrate the solution convergence with respect to polar angle discretization, the $c = 1.3$ critical rod case is used. The following discretization parameters are used for the polar angle convergence analysis.

- Bound box side length = 4 cm
- # radial rings = 80
- # azimuthal slices = 64
- Quadrature set = CHEBYSHEV-GAUSS 64 varying
- Convergence criterion = 10^{-7} for both k and ϕ

The results are tabulated in Table A.4.

Table A.4. The error in k vs. # of polar angles

# of polar angles	k	error (pcm)	p
3	0.9995324	-46.76	3.40
4	0.999824	-17.6	2.68
5	0.9999033	-9.67	2.14
6	0.9999345	-6.55	1.69
7	0.9999495	-5.05	1.31
8	0.9999576	-4.24	0.76
12	0.9999688	-3.12	0.31
16	0.9999715	-2.85	0.12
24	0.9999728	-2.72	0.04
32	0.9999731	-2.69	0.02
48	0.9999733	-2.67	0.00
64	0.9999733	-2.67	

A constant rate of convergence is not observed with respect to polar angular refinement. This should not be surprising, because the Gaussian quadrature set does not have a constant order.

A.5 CONCLUSIONS

Ganapol's benchmark problem 3.4 [2] has been used as a code verification test for MPACT. The bare rod configuration of problem 3.4 was changed to mimic a square lattice by surrounding the rod with a bounding box with a non-scattering material. Vacuum boundary conditions were imposed on the surface of the bounding box, and several critical rod cases were analyzed with MPACT using the tabulated critical rod radius as a function of c, the mean number of secondaries per collision. MPACT agreed with all cases to within a few pcm. The errors of all cases are shown to be within a few pcm. The convergence behavior was studied. The radial rate of convergence is shown to be second order, which is consistent with second order flat-source approximation. The convergence curves with respect to ray spacing and polar angle quadrature set order were obtained, both of which converge to the analytic solution nicely.

A.6 NEXT STEPS

Table 3.4.4 tabulates the scalar flux as a function of radius for four of the critical rod cases. Because the benchmark results are pointwise results and the MPACT results are integrated over the radial mesh, an effort is being made to integrate the benchmark results over the radial mesh to allow a direct comparison.

APPENDIX B. APPLICATION OF MMS TO SOURCE AND EIGENVALUE PROBLEMS

APPENDIX B. APPLICATION OF MMS TO SOURCE AND EIGENVALUE PROBLEMS

With an example of an Sn 1D problem in FY15, it was demonstrated that MMS can verify the correctness of a numerical algorithm and that of the software implementation for a source problem or an eigenvalue problem [12]. Moreover, it was shown that the order of accuracy is very sensitive to bugs in the code, which supports the fact that the order-of-accuracy test is considered the most rigorous code verification method.

B.1 MMS FOR FIXED SOURCE PROBLEMS TO SN 1D

In FY16, a method was developed which allows the angular error to be separated from the spatial error, thus enabling assessment of the convergence with spatial resolution. The method can be generalized to higher dimensions. The steps and equations to remove the angular error are derived in Wang et al. [12], and the main equation is shown below.

$$\begin{aligned}
\Sigma_j &= \sum_m \psi_{m,j} \cdot w_m - \frac{1}{\Delta V_j} \int_{V_j} \int_{4\pi} \psi\left(\underline{\Omega}, \underline{r}\right) d\Omega dV \\
&= \sum_m \psi_{m,j} \cdot w_m - \frac{1}{\Delta V_j} \int_{V_j} \left[\sum_m \psi_m\left(\underline{r}\right) \cdot w_m \right] dV \\
&\quad + \frac{1}{\Delta V_j} \int_{V_j} \left[\sum_m \psi_m\left(\underline{r}\right) w_m \right] - \frac{1}{\Delta V_j} \int_{V_j} \int_{4\pi} \psi\left(\underline{\Omega}, \underline{r}\right) d\Omega dV \\
&= E_{angular,j} + E_{spatial,j}.
\end{aligned} \tag{B.1}$$

To test the method presented above, a test suite consisting of three problems involving different solution structures was developed to verify the fixed source problems, as shown in Table B.1 [67].

Table B.1. Testing suite for fixed source problems

Problem #	$\psi^b(0,\mu>0)$, $\psi^b(0,\mu<0)$	**c**	$\frac{1}{2}\mathbf{Q_f}$	**Analytical solution (w.r.t. τ)**
1	1,0	0	1	$\psi(\tau,\mu) = \begin{cases} 1 & ,\mu>0 \\ 1-e^{(T-\tau)/\mu} & ,\mu>0 \end{cases}$
2	1,0	0	0.5	$\psi(\tau,\mu) = \begin{cases} 0.5+0.5\cdot^{-\tau/\mu} & ,\mu>0 \\ 1-e^{(T-\tau)/\mu} & ,\mu<0 \end{cases}$
3	MMS boundary*	0.9	MMS source**	$\psi(\tau,\mu) = \psi_0 + \psi_2\tau^2 e^{\mu}$

*The MMS boundary is evaluated at the boundary $\psi^b(0) = \psi_0$, $\psi^b(T) = \psi_0 + \psi_2 T^2 e^{\mu}$

**The MMS source is $Q(\tau,\mu) = \psi_2 \cdot \mu e^{\mu} \cdot 2\tau + \psi_0 + \psi_2 \cdot \tau^2 e^{\mu} - \frac{c}{2}\left[2\psi_0 + \psi_2 \cdot \tau^2\left(e - e^{-1}\right)\right]$

It was shown that the error from each approximation for the independent variables is separable and can be isolated from the overall error so that the order of accuracy with respect to one variable can be revealed as the corresponding grid is refined. This can be clearly shown by comparing the third and last columns in Table B.2.

Table B.2. Errors and order of accuracy in grid refinements in problem #1 with step method (before and after error separation)

Grid points per mfp	Overall error	$p_{overall}$	Angular error	Spatial error	$p_{spatial}$
16	0.05613	1.267	-0.00706	0.06318	0.959
48	0.01395	NaN	-0.00808	0.02203	0.980
144	-0.00061	-2.012	-0.00812	0.00750	0.993
432	-0.00560	-0.239	-0.00812	0.00252	0.997
1296	-0.00728	-0.068	-0.00812	0.00084	0.999
3888	-0.00784	–	-0.00812	0.00028	–

B.2 MMS FOR EIGENVALUE PROBLEMS TO SN 1D

The application of MMS to eigenvalue problems was also investigated. Two approaches were proposed: one using an inhomogeneous manufactured source (MS) approach, and the other using a manufactured cross section (MXS) approach: these two independent approaches were shown to be consistent:

$$(L+T+S) = \frac{1}{k}F\phi + Q_{MMS} \xrightarrow[convergence]{upon} \frac{1}{k}F\phi + \frac{1}{k}\frac{k_{MMS}Q_{MMS}}{\phi_{MMS}}\phi = \frac{1}{k}\left(F + \frac{k_{MMS}Q_{MMS}}{\phi_{MMS}}\right)\phi = \frac{1}{k}F_{MMS}\phi\,. \tag{B.2}$$

Equation (B.2) shows the equivalence between the two approaches, where the blue term is for the MS approach, and the red term is for the MXS approach.

One of the tests performed used the following manufactured solution in Eq. (B.3), which is also plotted in Figure B.1 with a vacuum boundary condition.

$$\psi_{MMS}(\tau,\mu) = \begin{cases} \frac{1}{2}\sin\left(\pi\frac{\tau}{T+2D}\right), & \mu > 0 \\ \frac{1}{2}\sin\left(\pi\frac{\tau+2D}{T+2D}\right), & \mu < 0. \end{cases} \tag{B.3}$$

It was shown that k and the cell-averaged and cell-edged scalar flux both exhibit the same order of accuracy with spatial grid refinement, consistent with the expected order of accuracy (Figure B.2).

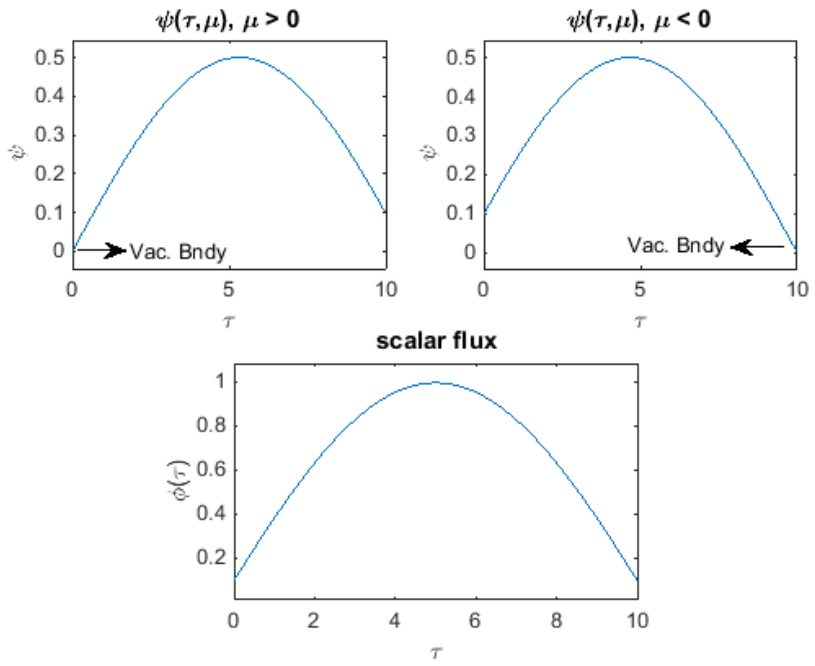

Figure B.1. Manufactured solution with vacuum boundaries.

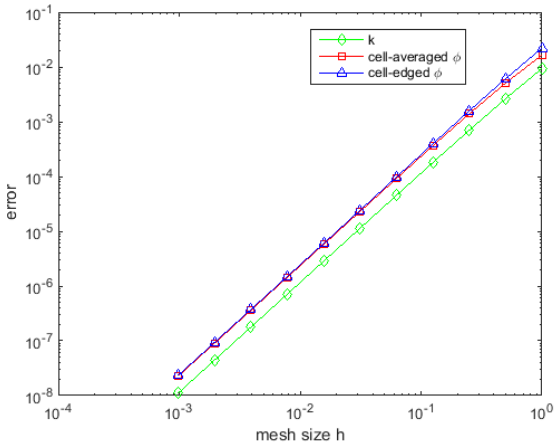

Figure B.2. Error convergence with refined grid (MS approach).

B.3 APPLICATION OF MMS TO AN MOC-BASED TRANSPORT SOLVER

In FY17, preliminary investigation of MMS in 2D MOC clearly showed the complicated and confounding effects in errors from different approximations, demonstrating that a more practical and realistic way to tackle this problem should be to start with simple 1D MOC and then add complexity along the way, which would help reveal each and every error component in a progressive manner. In the occasion described above, both flat source and linear source MOC in a slab geometry were considered. After the 1D MOC, the azimuthal symmetry assumption was relaxed, giving both polar and azimuthal dependencies in the solution of a slab problem. This would enable us to quantify the errors introduced in both angles from a product quadrature set. Having the capability to analyze and separate errors from these two angles, allows the analysis to proceed with the 2D geometry and focus on the added complication from ray spacing.

B.3.1 Spatial Order of Accuracy in 1D MOC

To determine the theoretical order of accuracy of the spatial discretization of MOC in a slab geometry, we start with the 1D Boltzmann transport equation with azimuthal symmetry,

$$\mu \frac{\partial \psi(x,\mu)}{\partial x} + \Sigma_t \psi(x,\mu) = q(x,\mu) \ . \tag{B.4}$$

To simplify the notation, the following coordinate transformation is used. Solving the Boltzmann transport

equation over a canonical cell and averaging it over the cell yield the cell-averaged angular flux,

$$\overline{\psi}(\mu) = \frac{\overline{q}(\mu)}{\Sigma_t} + \frac{\mu}{\Sigma_t z} \cdot \psi(0,\mu) \cdot \left(1 - e^{-\frac{\Sigma_t}{\mu} z}\right) - \frac{e^{\frac{\Sigma_t}{\mu} z}}{\Sigma_t z} \cdot \int_0^z e^{\frac{\Sigma_t}{\mu} z} \cdot q(z',\mu)\, dz' \ . \tag{B.5}$$

The approximating cell-averaged angular flux $\tilde{\overline{\psi}}$ is expressed below, where $\tilde{q}$ approximates q, and $\overline{\tilde{q}}$ is the average of this approximation $\tilde{q}$,

$$\tilde{\overline{\psi}}(\mu) = \frac{\overline{\tilde{q}}(\mu)}{\Sigma_t} + \frac{\mu}{\Sigma_t z} \psi(0,\mu) \left(1 - e^{-\frac{\Sigma_t}{\mu} z}\right) - \frac{e^{-\frac{\Sigma_t}{\mu} z}}{\Sigma_t z} \cdot \int_0^z e^{\frac{\Sigma_t}{\mu} z'} \cdot \tilde{q}(z',\mu)\, dz' \ . \tag{B.6}$$

The error E is defined as the difference between the exact analytical expression of cell-averaged angular flux $\overline{\psi}(\mu)$, as in Equation (B.5), and its approximation $\tilde{\overline{\psi}}(\mu)$, as in Equation (B.6),

$$\begin{aligned} E &= \overline{\psi}(\mu) - \tilde{\overline{\psi}}(\mu) \\ &= \frac{\overline{q}(\mu)}{\Sigma_t} - \frac{\overline{\tilde{q}}(\mu)}{\Sigma_t} - \frac{e^{-\frac{\Sigma_t}{\mu} z}}{\Sigma_t z} \cdot \left[\int_0^z e^{\frac{\Sigma_t}{\mu} z'} \cdot q(z',\mu)\, dz' - \int_0^z e^{\frac{\Sigma_t}{\mu} z'} \cdot \tilde{q}(z',\mu)\, dz' \right] . \end{aligned} \tag{B.7}$$

When different approximations (e.g., FS and LS approximations) are used, the corresponding definition of $\tilde{q}(z')$ is taken, with angular dependence dropped to avoid symbolic entanglements:

$$\tilde{q}(z') = \begin{cases} q^0 & , \quad \text{flat source} \\ q^0 - q^1 \cdot (z' - z^c) & , \quad \text{linear source} \end{cases} . \tag{B.8}$$

It is concluded that flat source MOC is second order accurate, and the linear source MOC is fourth order accurate. The detailed derivation is provided in Wang et al. [13].

A list of the four test cases used in the paper is presented below; each case consists of an assumed flux shape and the corresponding manufactured sources.

Case 1: constant source shape

$$\psi\left(z',\mu\right) = \psi_0 \tag{B.9}$$

$$q_{MMS}\left(z',\mu\right) = \psi_0 \cdot \left(\Sigma_t - \Sigma_s\right) \tag{B.10}$$

Case 2: linear source shape

$$\psi\left(z',\mu\right) = \psi_0 + \psi_1 e^{\mu} \cdot z' \tag{B.11}$$

$$\begin{aligned} q_{MMS}\left(z',\mu\right) =& \psi_0 \cdot \left(\Sigma_t - \Sigma_s\right) + \psi_1 \cdot \mu e^{\mu} \\ &+ \left[\psi_1 \cdot \Sigma_t e^{\mu} - \psi_1 \cdot \frac{\Sigma_s}{2}\left(e - e^{-1}\right)\right] \cdot z' \end{aligned} \tag{B.12}$$

Case 3: quadratic source shape

$$\psi\left(z',\mu\right) = \psi_0 + \psi_2 e^{\mu} \cdot z'^2 \tag{B.13}$$

$$\begin{aligned} q_{MMS}\left(z',\mu\right) =& \psi_0 \cdot \left(\Sigma_t - \Sigma_s\right) + 2\psi_2 \mu e^{\mu} \cdot z' \\ &+ \psi_2 \left[\Sigma_t e^{\mu} - \frac{\Sigma_s}{2}\left(e^{1} - e^{-1}\right)\right] \cdot z'^2 \end{aligned} \tag{B.14}$$

Case 4: non-polynomial source shape

$$\psi\left(z',\mu\right) = \sqrt{z' + 1} \tag{B.15}$$

$$q_{MMS}\left(z',\mu\right) = \frac{\mu}{w\sqrt{z' + 1}} + \left(\Sigma_t - \Sigma_s\right) \cdot \sqrt{z' + 1} \tag{B.16}$$

The orders of accuracy and convergence plots are listed in the table below.

For purely absorbing material, the observed/predicted orders of accuracy are listed in the tables below.

Table B.3. Observed / predicted order of accuracies for purely absorbing material

Approximation	Test cases			
	Constant	Linear	Quadratic	Non-polynomial case (square root)
FS	exact / exact	2nd / 2nd	2nd / 2nd	3rd → 2nd* / 2nd
LS	exact / exact	exact / exact	4th / 4th	4th / 4th

*The arrow indicates the order degradation

For scattering materials, the orders of accuracy are listed in the tables below.

Table B.4. Observed / predicted order of accuracies

Approximation	Test cases			
	Constant	Linear	Quadratic	Non-polynomial case (square root)
FS	exact / exact	2nd / 2nd	2nd / 2nd	2nd / 2nd
LS	exact / exact	exact / exact	4th / 4th	4th / 4th

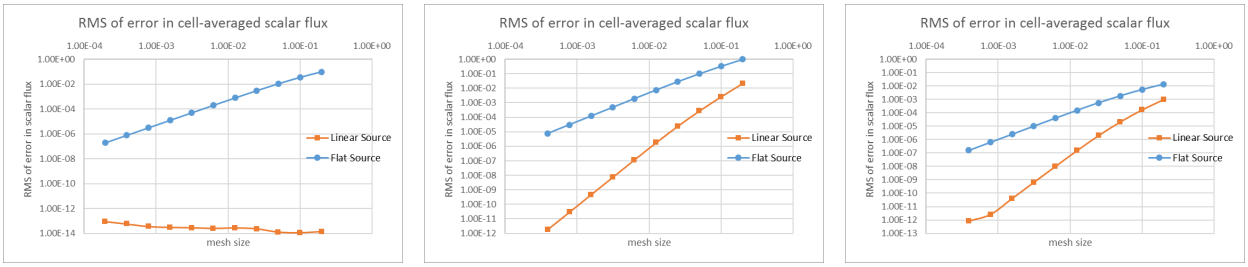

Figure B.3. Order of accuracy and convergence for various source shapes.

B.3.2 1D 2 Angles

When the azimuthal symmetry assumption is relaxed, the problem is reexamined in a 1D slab, where μ represents the cosine value of the polar angle θ, and α represents the azimuthal angle with respect to the positive x direction.

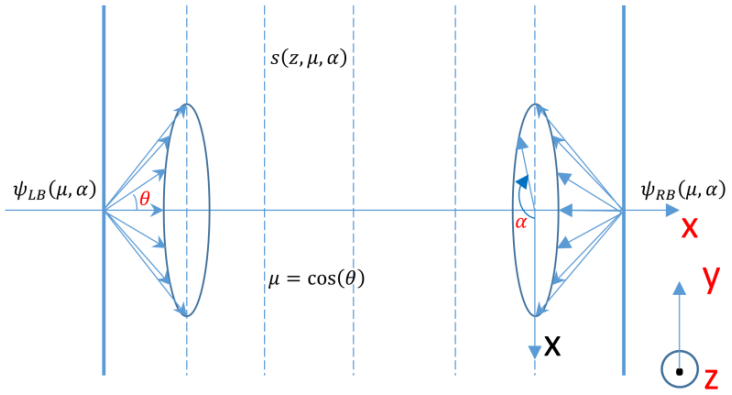

Figure B.4. 1D problem with two angular dependencies.

The 3D Boltzmann transport equation can be reduced to

$$\mu \cdot \frac{d\psi}{dx}(x,\mu\alpha) + \Sigma_t(x) \cdot \psi(x,\mu,\alpha) = Q(x,\mu,\alpha) \ , \tag{B.17a}$$

$$Q(x,\mu,\alpha) = \int_{-1}^{1}\int_{0}^{2\pi} \Sigma_s(x,\mu' \to \mu,\alpha' \to \alpha) \cdot \psi(x,\mu',\alpha')\, d\mu' d\alpha' + S(x,\mu,\alpha) \ , \tag{B.17b}$$

where μ is the polar angle cosine running from -1 to 1, and α is the azimuthal angle running from 0 to 2π.

The characteristic form of this equation is shown below:

$$\frac{d\psi_{m,i}(s)}{ds} + \Sigma_t(x) \cdot \psi_{m,i}(s) = Q_{m,i}(s) \ , \ m = 1, \ldots M = N \cdot I \ , \tag{B.18a}$$

$$Q_{m,i}(s) = \frac{1}{4\pi} \cdot \left[\Sigma_s(x) \cdot \sum_{n}^{N} \sum_{i}^{I} \psi_{n,i}(s) \cdot \omega_{\mu,n} \cdot \omega_{\alpha,i} \right] + S_{m,i}(s) \ , \tag{B.18b}$$

where N and I are the number of polar angles and azimuthal angles, respectively, used in the product quadrature set. The equation is very similar to the typical 1D equation, except that the source now has contributions from both the polar and azimuthal directions.

The equation used to quantify the angular error component can be adapted to the two-angle form:

$$E_{angular,j} = \frac{1}{\Delta X_j} \int_{X_{j-1/2}}^{X_{j+1/2}} \left[\sum_m \omega_m \cdot \psi_m (X) - \int_{4\pi} \psi \left(X, \hat{\Omega} \right) d\Omega \right] dX$$

$$= \sum_n^N \sum_i^I \omega_i \cdot \omega_n \cdot \frac{1}{\Delta X_j} \int_{X_{j-1/2}}^{X_{j+1/2}} \psi_{n,i} (X) \, dX - \int_0^{2\pi} \int_{-1}^{1} \frac{1}{\Delta X_j} \int_{X_{j-1/2}}^{X_{j+1/2}} \psi (X, \mu, \alpha) \, dX d\mu d\alpha \, . \tag{B.19}$$

The angular error removal (AER) procedure is the same as before, which guarantees that both the sources and the converged neutron flux are angular-error-free.

In this case, referred to as *Case FS3*, the manufactured solution has a sinusoidal spatial dependence and more complicated angular dependencies,

$$\psi_{MMS} (x, \mu, \alpha) = \sin \left(\frac{\pi}{X_{end}} \cdot x \right) \cdot e^{\cos(\mu^2)} \cdot e^{\frac{\alpha}{2\pi}} \, . \tag{B.20}$$

The applied quadrature uses two polar angles and four azimuthal angles. Only flat-source MOC for a fixed source problem is used for this case, because the source approximation is not the focus point of investigation here. The order of accuracy (OoA) results are tabulated in Table B.5 and are plotted in Figure B.5, and the second order spatial error convergence is observed after the angular error removal. The eigenvalue problem has similar results and is not presented here.

Table B.5. RMS error convergence of scalar flux for Case FS3 with flat-source MOC (with and without AER)

Mesh size	No AER	OoA	With AER	OoA
1	4.574920	-7.41E-02	5.36E-01	1.8900
0.5	4.815919	-2.05E-02	1.45E-01	1.9713
0.25	4.884791	-5.25E-03	3.69E-02	1.9927
0.125	4.902615	–	9.27E-03	–

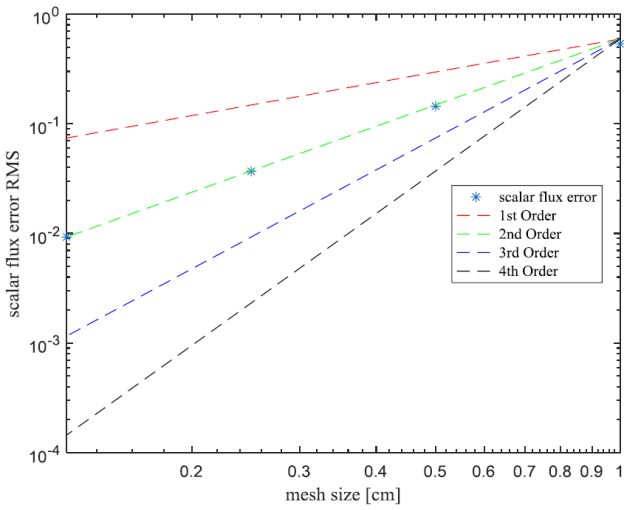

Figure B.5. RMS error convergence of scalar flux for Case FS3 with flat-source MOC.

APPENDIX C. SELF-SHIELDING

APPENDIX C. SELF-SHIELDING

C.1 INTRODUCTION TO SELF-SHIELDING EFFECTS

The term *self-shielding* describes the phenomenon of reduced absorption reaction rates caused by to the depression of the flux. This can occur in two different ways—spatial self-shielding, and energy self-shielding—as illustrated in Figure C.1. *Spatial self-shielding* refers to a condition in which the peripheral region of the fuel can geometrically "shield" the inner region of the fuel, causing reduced reaction rates further into the fuel resulting from the flux shape. *Energy self-shielding* refers to the condition in which the energy spectrum of the flux near the resonance energy will be suppressed.

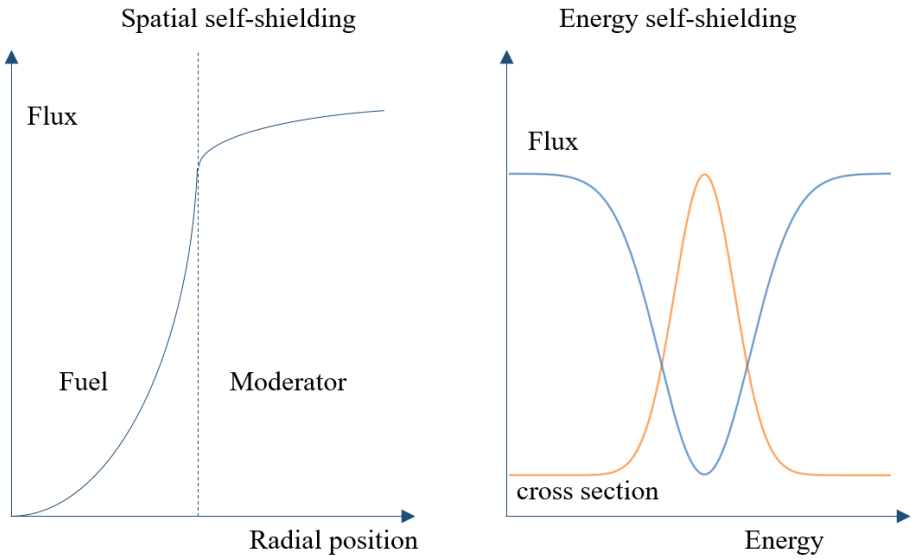

Figure C.1. Spatial and energy self-shielding effects.

C.2 SELF-SHIELDING CONCERN IN GRID REFINEMENT STUDY IN MPACT

To obtain the problem-dependent multigroup cross sections for MPACT, resonance self-shielding calculations are performed before the whole-core MOC calculations. A general grid refinement study solves the same problem, defined by geometry, material, sources, and boundary condition, but only with different grid resolution. With a self-shielding calculation, the material property—namely the multigroup cross sections—is coupled with the grid: for each grid refinement, the cross section is recalculated by the resonance calculation. This results in an updated multigroup cross section for each grid refinement. The specific details of the resonance self-shielding calculation in MPACT are provided in the MPACT Theory Manual [68].

C.3 SELF-SHIELDING CALCULATIONS

For MMS code verification, the self-shielding must be turned off, or the error component must be taken into account.

However, solution verification generally solves a realistic problem on the application model with actual calculation processes. Turning off self-shielding calculation deviates from the purpose of solution verification, which is to estimate the solution error from the code and reveal the observed rate of convergence. However, in this solution verification study, to reveal the rate of convergence with each independent discretization parameter and compare the results with expected convergence rates, self-shielding has been turned off. The

results verified that turning self-shielding off gives more monotonic convergence curves. However, this is at the expense of using self-shielding consistent with the chosen grid, which is beyond the scope of this study and will be addressed in future analyses.

APPENDIX D. MPACT-CTF CORE FOLLOW VALIDATION

APPENDIX D. MPACT-CTF CORE FOLLOW VALIDATION

This appendix summarizes the core follow results for VERA-CS. Because core follow is multiphysics (MPACT-CTF), it is not strictly part of the MPACT single physics validation, and therefore, the coupled code validation is included as an Appendix to the MPACT V&V manual.

D.1 WATTS BAR UNIT 1 RESULTS

D.1.1 Watts Bar Nuclear Unit 1 (WBN1) Cycle 1 Results

The power history for cycle 1 of the Tennessee Valley Authority (TVA) Watts Bar Nuclear Unit 1 (WBN1) is shown in Table D.1. The beginning of cycle power distributions are shown in Figure D.1 for the HZP and HFP core conditions. The depletion results are shown in Table D.2 and Figure D.1. As indicated, the critical boron concentration generally is within 50 ppmB of measurement, as indicated by the black dashed lines in Figure D.2. The in-core detector responses were calculated with MPACT, but the data were not available at the time the CASL-U-2014-0189-000 document was prepared. However, the objective of this milestone was primarily to demonstrate code functionality and not code accuracy. The demonstration of MPACT accuracy was an objective of a 2015 milestone L1.CASL.P11.02 [33] to "Qualify VERA-CS for multi-cycle PWR simulation capability." This milestone used VERA-CS to model WBN1 Cycles 1–12 using TVA plant data (e.g., startup tests, critical borons, flux maps) and actual fuel assembly design data provided by Westinghouse. For these calculations, MPACT was coupled to COBRA-TF for thermal-hydraulics and to ORIGEN for depletion and decay. An improved fuel temperature model based on BISON-CASL was used, together with improved 47g sub-group cross sections. For this milestone, the MPACT results were compared to continuous energy Monte Carlo (SHIFT) results at various points in the burnup cycle. Detailed results were provided for criticality, rod worths, temperature coefficients, boron concentrations, and flux maps to measured data. The results of this milestone provide a substantial validation base for MPACT and are included in Section D.1.2.

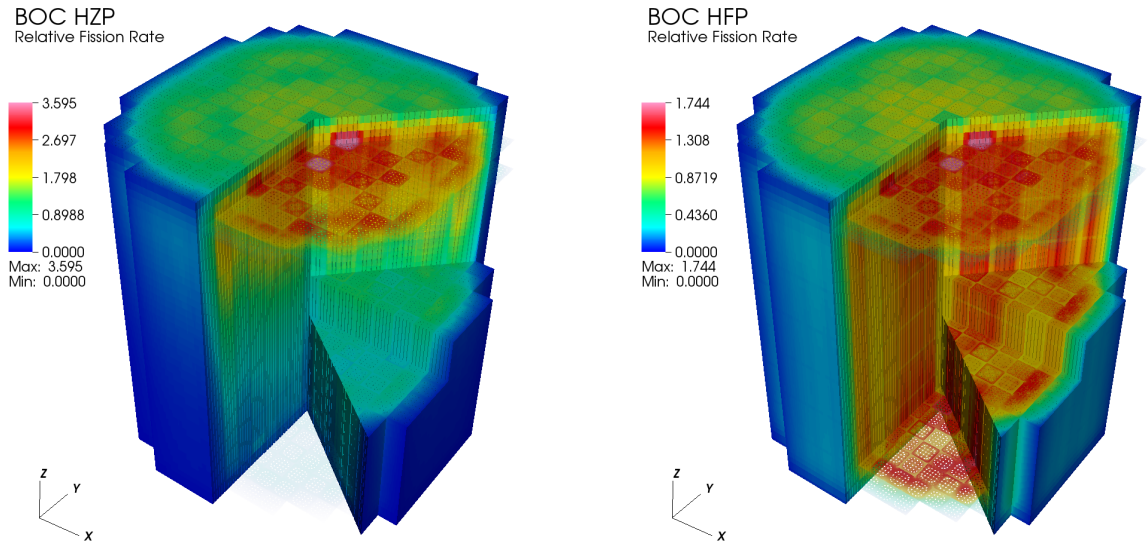

Figure D.1. Core power distribution at BOC HZP (left) and BOC HFP (right).

One of the important features of MPACT that was also verified in VERA Problem 10 was the requirement to shuffle the fuel from Cycle 1 into the Cycle 2 loading pattern, as shown in Figure D.3. The assemblies shown as purple are the fresh feed assemblies being added, and the IFBA and WABA loadings are indicated. All

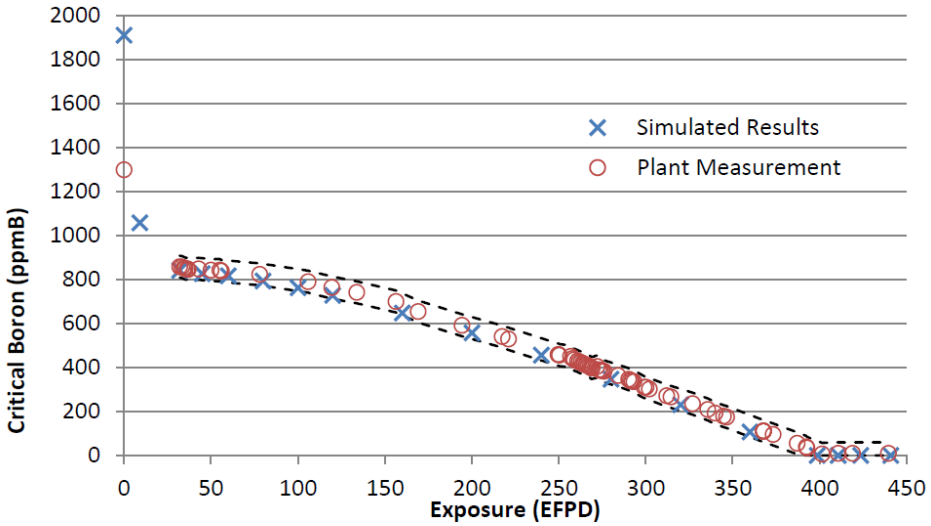

Figure D.2. Comparison of Cycle 1 critical boron.

other assemblies reference their previous x and y label locations in Cycle 1. Figure D.4 shows the pin-wise fuel burnup distribution beginning before shuffling at the end of Cycle 1 (EOC1) up through post-shuffling at the beginning of Cycle 2 (BOC2).

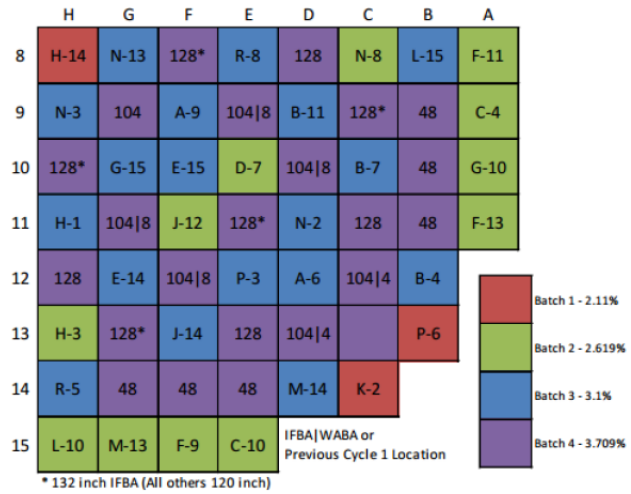

Figure D.3. Problem 10 WBN1 Cycle 2 core loading pattern.

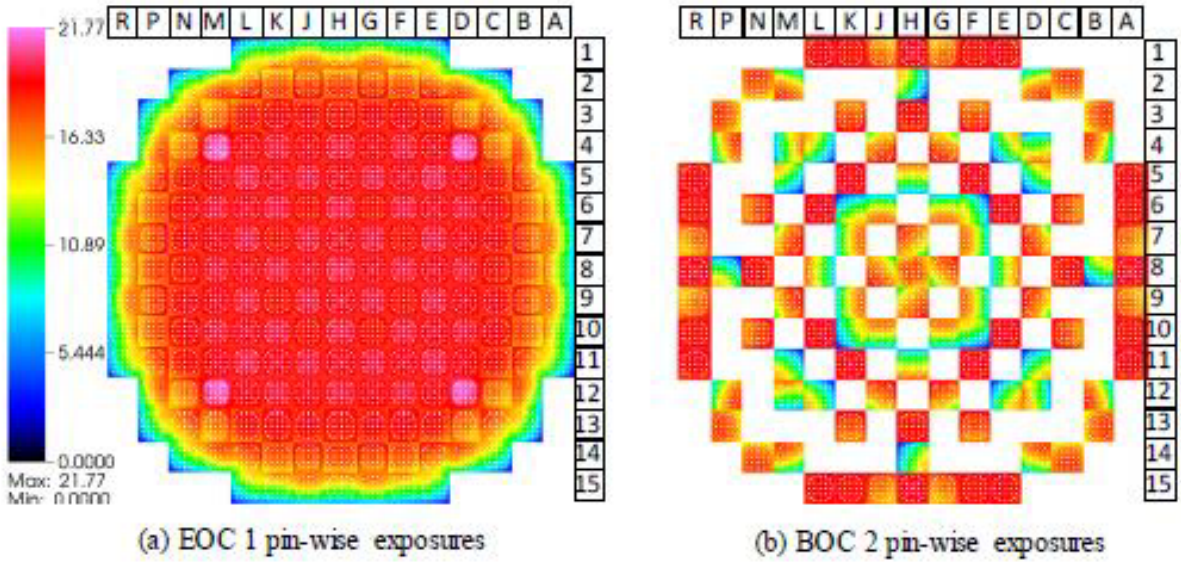

Figure D.4. Watts Bar Nuclear Plant EOC1 to BOC2 fuel rod exposures.

Table D.1. Cycle 1 simulated operating history [6]

Case	EFPDs	Cycle exposure (GWd/MT)	Power (%)	Inlet temp. (F)	Bank D position (steps)
1	0.0	0.000	0.0	557.0	186
2	9.0	0.346	65.7	557.6	192
3	32.0	1.229	99.7	558.1	219
4	50.0	1.920	98.0	558.2	218
5	64.0	2.458	100.0	558.6	219
6	78.0	2.996	99.7	558.7	215
7	92.7	3.531	99.7	558.6	217
8	105.8	4.064	99.8	558.8	220
9	120.9	4.644	99.8	558.4	220
10	133.8	5.139	99.5	557.9	219
11	148.4	5.700	98.0	558.0	214
12	163.3	6.272	95.1	557.9	216
13	182.2	6.998	94.8	557.9	214
14	194.3	7.463	99.8	557.8	220
15	207.7	7.978	93.9	557.5	218
16	221.1	8.492	100.1	558.0	222
17	238.0	9.141	99.7	557.7	220
18	250.0	9.602	100.2	557.6	222
19	269.3	10.344	95.6	557.9	211
20	282.3	10.843	96.4	558.1	215
21	294.6	11.315	93.4	557.4	211
22	312.1	11.987	99.7	557.5	217
23	326.8	12.552	98.0	557.6	215
24	347.8	13.359	99.4	557.7	220
25	373.2	14.334	99.9	557.8	219
26	392.3	15.068	86.9	556.7	202
27	398.6	15.310	99.6	558.0	220
28	410.7	15.775	89.9	557.1	224
29	423.6	16.270	78.8	556.3	228
30	441.0	16.939	64.5	554.9	230
Cycle average			**94.0**	**557.8**	**216.4**

Table D.2. Measured and simulated Cycle 1 states

Simulated						Measured			
Exposure (EFPDs)	**Power (%)**	**Bank D**	**Boron (ppm B)**	**k-eff**	**Fuel temp. (K)**	**Exposure (EFPDs)**	**Power (%)**	**Bank D**	**Boron (ppm B)**
0	1.0E-06	219	1,909.54	1.00000	291.7	**0**	0		1,299
9	65.7	219	1,057.87	1.00000	756.9	–	–	–	–
32	99.7	219	841.79	1.00000	873.4	**32**	99.7	219	858
45	97.7	219	825.59	1.00000	866.0	**42.8**	100	215	848
60	97.7	219	816.29	1.00000	865.8	**55.9**	99.9	214	839
80	97.7	219	793.05	0.99999	865.3	**78**	99.9	208	823
100	97.7	219	762.39	1.00000	864.8	**105.8**	99.8	217	790
120	97.7	219	727.34	1.00000	864.4	**119.4**	99.8	212	763
160	97.7	219	646.76	1.00000	863.6	**156.4**	99.9	218	700
200	97.7	219	556.52	0.99999	862.8	**194.3**	98.9	215	592
240	97.7	219	455.65	1.00000	862.1	**249.6**	99.9	216	458
280	97.7	219	346.24	1.00000	861.4	**284**	99.9	218	363
320	97.7	219	229.35	1.00000	860.9	**314.5**	99.5	214	266
360	97.7	219	107.17	1.00000	860.5	**367.7**	100	216	111
398.6	97.7	219	1.0E-07	0.99873	860.1	**401.4**	99.6	217	7
410.7	89.9	219	1.0E-07	0.99720	833.3	**410.7**	89.9	216	9
423.6	78.8	219	1.0E-07	0.99667	796.0	**418.8**	83.4	228	9
441	64.5	219	1.0E-07	0.99564	750.0	**439.5**	65.3	227	9

D.1.2 Multi-Cycle Results

In June, 2015 work was completed by A. Godfrey on depleting Cycles 1–12 of WBN1 [69]. This successfully demonstrated the ability of MPACT and VERA-CS to model the entire operating history of the WBN1 plant, which is currently in its 20th year and 13th fuel cycle. A rigorous benchmark was also performed using a significant amount of operating data provided by TVA, implementing the same rigorous analyses that are used for the validation and licensing of industrial methods. These data include criticality measurements, physics testing results, critical soluble boron concentrations, and measured in-core neutron flux distributions. This section summarizes selected results from that report [69].

Each MPACT/VERA-CS calculation was performed after reloading the core and shuffling the fuel from the previous cycle (except Cycle 1). The previous fuel compositions were decayed by ORIGEN over the time span of the refueling outage, also resulting in the complete decay of ^{135}Xe and buildup of ^{149}Sm. The calculations were performed without thermal hydraulics feedback, in quarter-core symmetry, and the MOC ray spacing was significantly decreased by 10× to improve the accuracy of neutron transport near the very thin IFBA coating. The differences between the measured critical boron concentrations and the calculated values with VERA-CS are shown in Figure D.5.

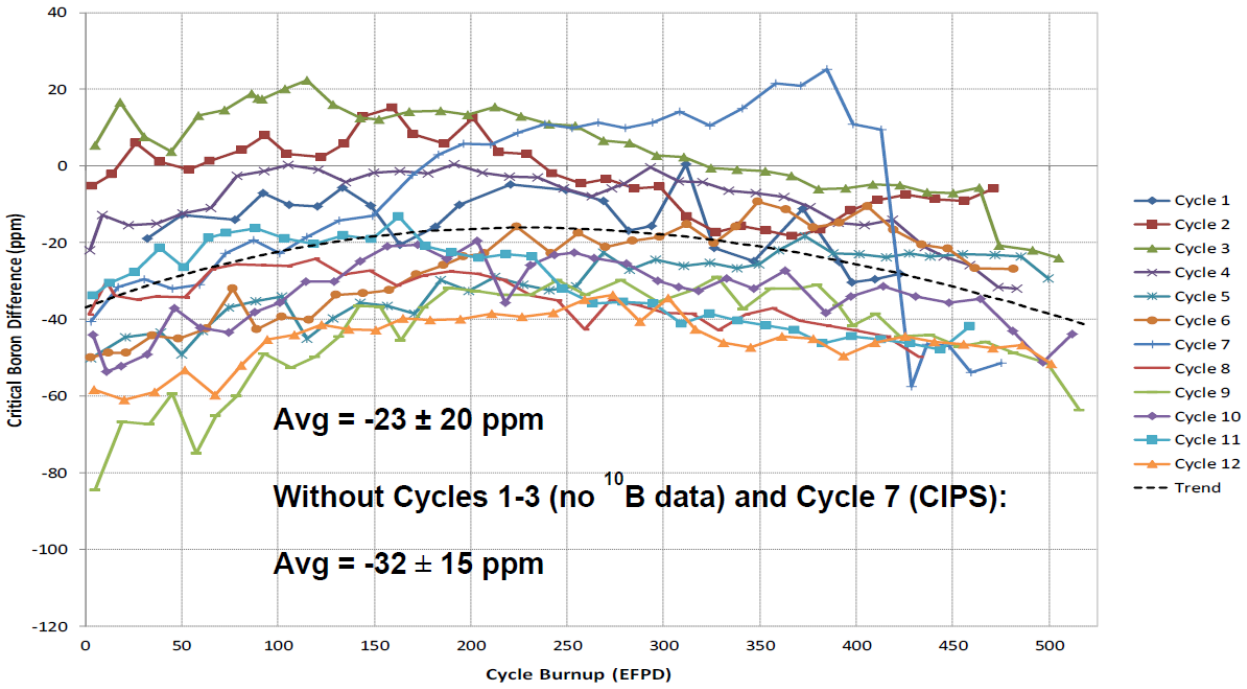

Figure D.5. Difference between critical boron and the MPACT/VERA-CS prediction.

As indicated, the average BOC critical boron difference is about 23 ppm. As noted in Godfrey's technical report [69], the prediction of Cycle 7 is particularly poor, which is likely a result of the occurrence of CRUD induced power shift (CIPS). Godfrey [69] also notes that some other factors have been identified which account for the differences in Cycles 6–12, such as the presence of tritium production "TPBARs"; because of the classified nature of these components, their absorber loading is approximate. Godfrey also presents results [69] for the predicted vs. measured control bank reactivity worths (CBWs) at the beginning of each fuel cycle as part of the startup test procedures. The measured values from WBN1 have been provided by TVA as part of the zero power physics test results transmittals. The individual rod worths, which are most useful for code validation, are provided in the report. The total rod worth errors for all of the WBN1 cycles

are shown here in Figure D.6 to demonstrate what agreement could be obtained if MPACT/VERA-CS were used for startup testing predictions following the same methodologies that were used for current industrial methods licensed by the US Nuclear Regulatory Commission (NRC).

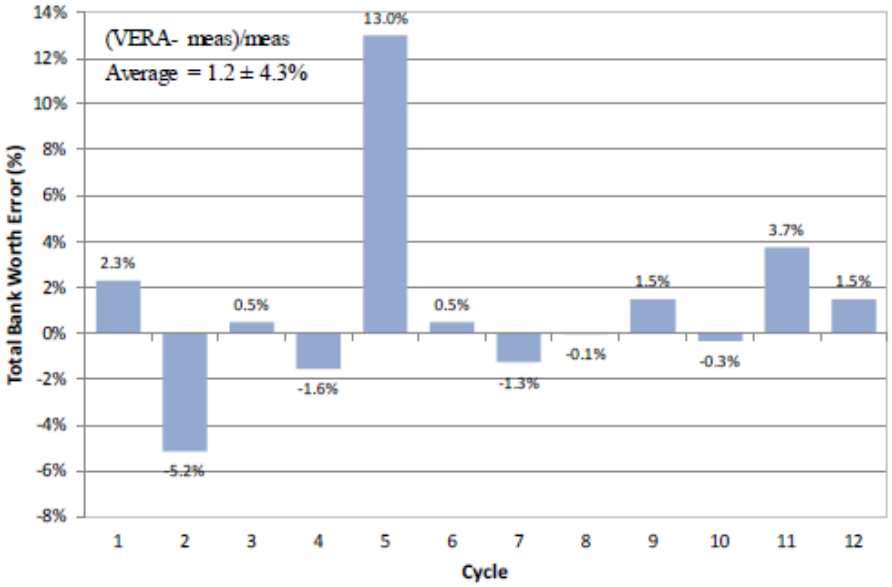

Figure D.6. BOC HZP total CBW errors.

Detailed flux map comparisons were also performed over all twelve cycles of depletion: 183 flux maps were selected for comparison to calculations from MPACT/VERA-CS as presented in Godfrey's report [69]. A sample flux map comparison is shown in Figure D.7 below. The image is depicts the southeast quadrant of the reactor core, with locations containing at least one operable symmetric instrument containing data. The data are presented as a simplified axial plot of the measured (red) and calculated (blue) signals at 61 axial locations. The value of the 3D RMS difference of the 61 locations is shown in the upper right of each instrumented location in that string. The lower right corner shows the difference in radial powers for that instrument × 100. Values above 5% are highlighted in red. Another simplified axial plot of the 1D average axial shape of the operable instruments is shown at the bottom right, with corresponding RMSs. The box to the right provides the cycle, exposure, power level, and radial (2D) and total (3D) RMS values for the entire distribution. The difference in measured and calculated axial offset is also provided.

A summary of the flux map comparisons from [69] and shown in Table D.3 indicates that VERA-CS can calculate the measured power distributions reasonably well, especially given the fuel temperature limitations, larger reactivity differences, and known quadrant power tilts. The radial power distribution RMS is only 1.8%, with errors tending to be 50% higher in the first 6–8 GWd/MTU of the cycles. For the latter half of the cycles, the 2D RMS approaches 1.25% for all cycles. A plot of the 3D total RMS during the cycle exposure is shown in Figure D.3.

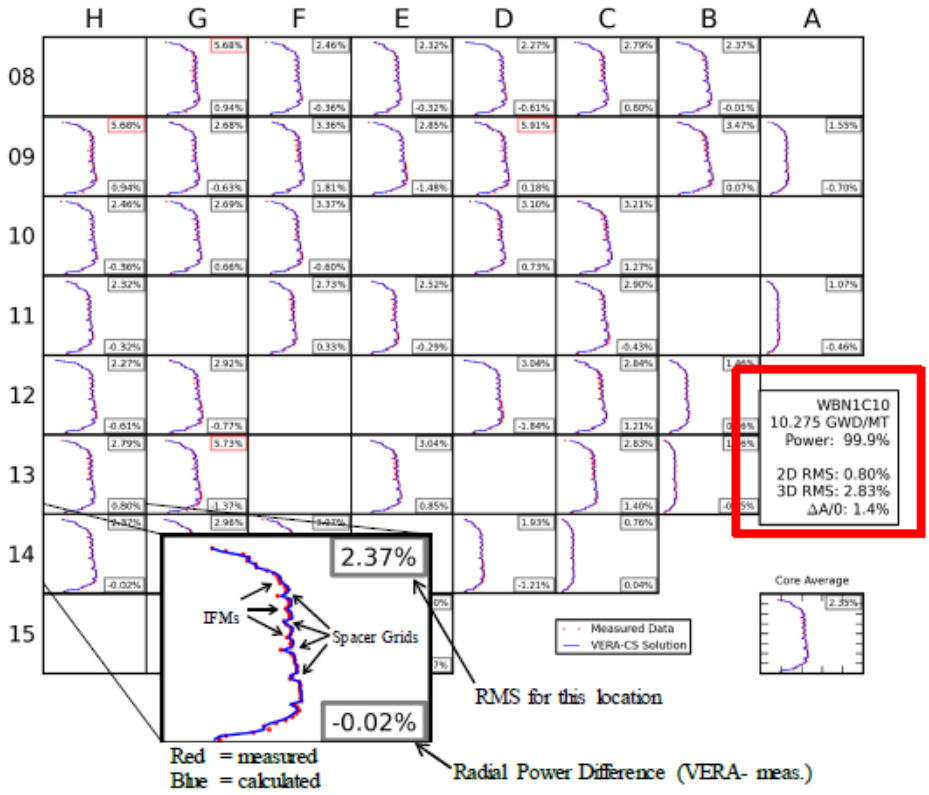

Figure D.7. Sample HFP flux map: middle of cycle 10.

Table D.3. Summary of flux map comparisons for Cycles 1–12 of WBN1.

Cycle	Count	ΔAO	1D RMS	2D RMS	3D RMS	2D max	Det max	3D max
1	13	-1.17	2.55	1.10	3.29	3.37	7.25	27.28
2	13	0.08	1.11	1.60	2.70	3.99	7.29	31.79
3	19	0.45	1.87	1.67	2.92	5.95	8.34	42.03
4	19	0.52	2.14	1.77	3.23	4.82	8.37	40.74
5	19	1.04	2.33	2.05	3.64	8.02	9.61	38.74
6	18	1.38	2.60	1.92	3.77	6.15	9.60	41.77
7	18	1.79	5.17	1.74	6.73	5.94	15.70	33.31
8	15	-0.35	3.03	1.77	4.00	7.67	10.27	43.63
9	19	1.32	2.41	2.35	3.94	10.03	11.88	41.72
10	16	-0.43	2.79	1.56	3.64	7.55	9.62	38.15
11	6	0.25	1.52	1.88	2.77	7.36	7.85	21.51
12	8	-0.43	2.23	2.47	3.72	11.54	12.32	37.15
Total	**183**	**0.50**	**2.75**	**1.85**	**3.93**	**11.54**	**15.70**	**43.63**
St. Dev.		**0.85**	**0.98**	**0.32**	**1.05**			

*Note that the axial shapes for each detector in Cycles 4–12 are approximate

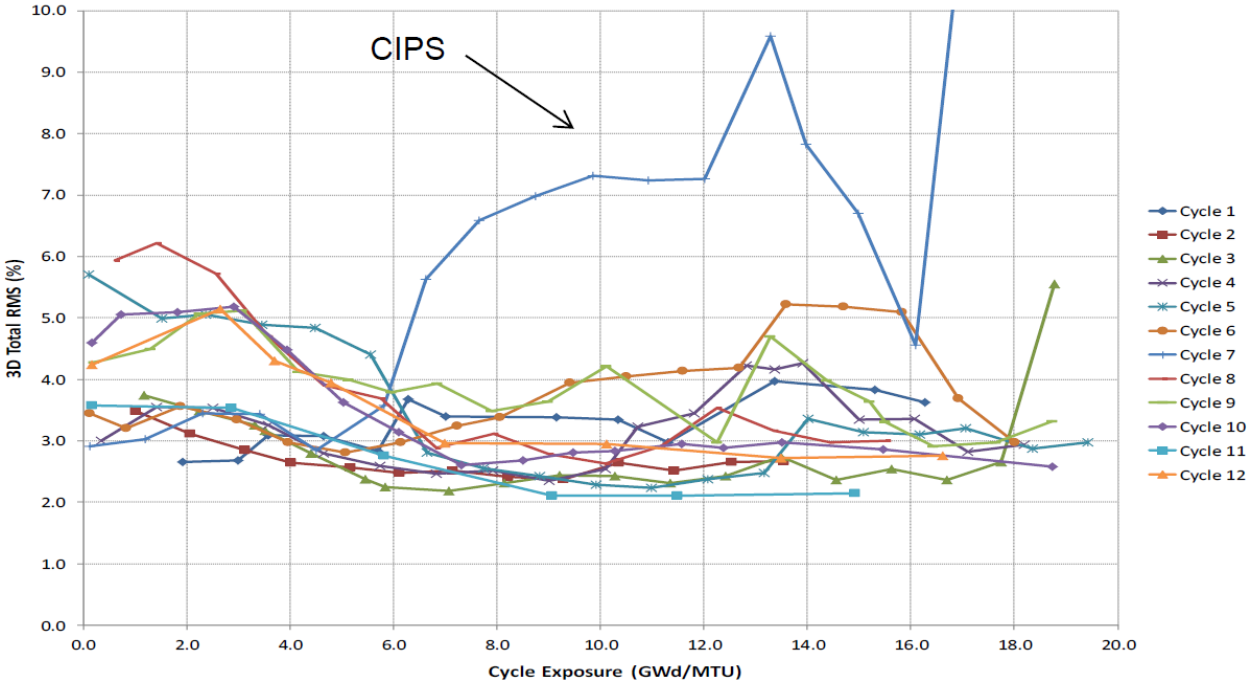

Figure D.8. Summary of 3D total RMS for Cycles 1–12 of WBN1.

D.1.3 Summary of WBN1 Results

An overall summary of the MPACT/VERA-CS benchmarking results for Watts Bar Cycles 1–12 is shown in Table D.4. Generally, these results demonstrate successful application of MPACT and VERA-CS for the depletion and benchmarking of twelve fuel cycles of a commercial PWR, which confirms the ability of MPACT and VERA-CS to represent realistic, detailed reactor core models and to perform simulations in a reasonable turnaround time. Although there is still some room for improvement in the results, these comparisons to measured data are acceptable, and they provide an important contribution to the validation base of the MPACT code.

Table D.4. Summary of MPACT/VERA-CS benchmarking results for Watts Bar Cycles 1–12.

Measurement	Mean ± 1 sigma†	Runtime per cycle‡
BOC HZP critical boron	-9±24 ppm	1.75 hours
BOC HZP bank worth	1.2±4.3%	3.33 hours
BOC HZP ITC	-0.8±0.7 pcm/°F	0.75 hours
HFP boron letdown	-24±19 ppm	21.9 hours
HFP flux maps – radial – total	1.8±0.3% RMS 3.5±0.4% RMS	–

†Suspect measurements or known anomalies are excluded from this summary
‡The typical number of compute cores is 4,307

D.2 BEAVRS BENCHMARK

The Benchmark for Evaluation and Validation of Reactor Simulations (BEAVRS) is a publicly available reactor specification provided by the Massachusetts Institute of Technology (MIT) Computational Reactor Physics Group [70]. The three-region core loading and fuel enrichments are also similar to WBN1; however,

there are some differences in the lattice pattern and discrete burnable absorber types. The benchmark contains two cycles of detailed geometry and measurements from an unnamed utility's PWR, but the BEAVRS reactor is a traditional Westinghouse 4-loop PWR that is very similar to WBN1. The measured data provided for BEAVRS include Cycles 1 and 2 zero power physics testing (ZPPT) results, power escalation and HFP measured flux maps, and HFP critical boron concentration measurements for both cycles. The power history for each cycle is provided, but the regulating bank history is not.

Because BEAVRS is a public release from an unnamed utility, its data are limited, and support is not readily available for problems or questions. Also, it is unlikely to be continued to any more cycles, which limits the long-term value that could be gained (as opposed to benchmarking against a plant that is still operating, in cooperation with an end user). Nevertheless, this benchmark is becoming an industry standard for validation of advanced codes, and Cycle 1 of BEAVRS was performed with MPACT [5], and a PHI milestone was completed in FY16 to validate MPACT for Cycle 2 of BEAVRS [16]. The following sections provide a brief summary of the results from CASL-U-2015-0076-000 on the Cycle 1 depletion.

D.2.1 BEAVRS Cycle 1

One of the principal issues in modeling Cycle 1 of BEAVRS was the complexity of the plant's power history. In Figure D.9, the actual power history is shown in blue, and the average power used in MPACT is shown in red. The simplified power history captured the three major outages and the power down period at end of cycle, and it aligns with the 16 flux maps throughout the cycle. Some the key results are summarized in Table D.5, and the pin power distribution calculated by MPACT at three statepoints in the cycle is shown in Figure D.10. A comparison of the flux measurements predicted by MPACT with the measured data is shown in Figure D.11 for a flux map at the middle of cycle. The detailed data for all 16 statepoints are provided in the report by Collins and Godfrey [5]. In general, the results for cycle 1 are in good agreement with the plant data, and they provide an important addition to the MPACT validation base.

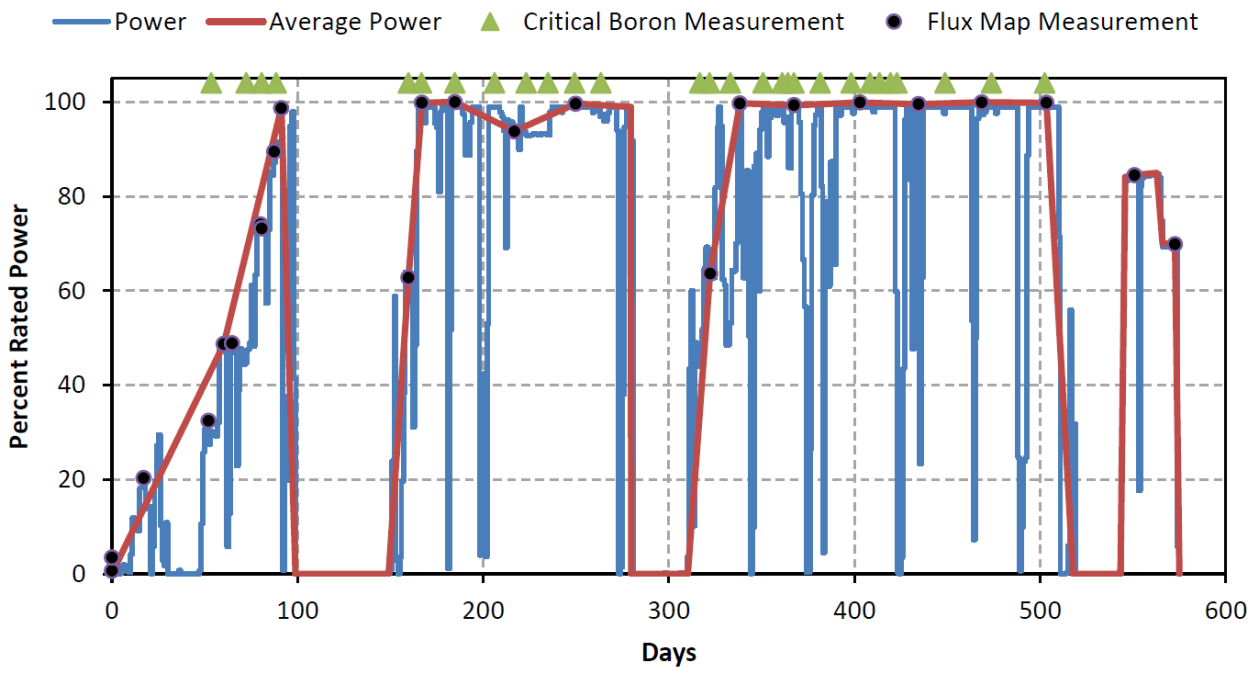

Figure D.9. Actual and simplified power history used in the MPACT BEAVRS model [5].

Table D.5. Summary of key results for the MPACT calculation of BEAVRS cycle 1

Exposure		Power	Boron			Flux map comparisons		
GWD/MT	EFPDs	(%)	Meas.	Calc.	Diff.	Radial RMS	3D RMS	Delta A/O
0	0	0	975	958	17	2.44%	5.14%	-2.23%
0.268	6.4	48.69	703	696	7	–	–	–
1.023	24.5	98.67	626	601	25	1.71%	4.54%	-0.46%
1.184	28.4	0	633	–	–	–	–	–
1.187	28.5	0	633	–	–	–	–	–
1.296	31.1	62.78	638	652	–	3.49%	5.46%	-2.20%
1.507	36.1	99.78	610	601	9	0.99%	3.14%	-0.52%
2.163	51.9	99.98	623	582	40	1.35%	3.02%	-0.22%
3.297	79.1	93.78	580	563	17	0.85%	3.11%	1.22%
4.614	110.6	99.6	532	503	29	0.91%	3.79%	-1.63%
5.713	137	98.9	479	452	27	–	–	–
5.734	137.5	0	478	–	–	–	–	–
5.779	138.6	0	476	–	–	–	–	–
6.013	144.2	63.65	461	–	–	1.08%	4.46%	-2.65%
6.491	155.7	99.7	444	415	30	1.28%	4.36%	1.55%
7.508	180.1	99.3	384	353	31	0.90%	3.47%	0.95%
8.701	208.7	99.86	310	284	26	1.00%	3.55%	0.98%
9.804	235.1	99.51	248	218	30	–	–	–
11.085	265.8	99.91	162	135	27	1.21%	4.01%	-0.75%
12.342	296	99.79	70	50	20	1.27%	3.73%	-1.01%
12.677	304	0	52	–	–	–	–	–
12.694	304.4	0	51	–	–	–	–	–
12.74	305.5	84.1	49	51	-2	–	–	–
12.916	309.7	84.48	39	53	-14	1.45%	4.34%	1.79%
13.31	319.2	84.94	18	17	1	–	–	–
13.411	321.6	70	13	40	-27	–	–	–
13.604	326.2	69.86	2	28	-26	1.48%	4.59%	1.00%
13.645	327.2	0	0	–	–	–	–	–

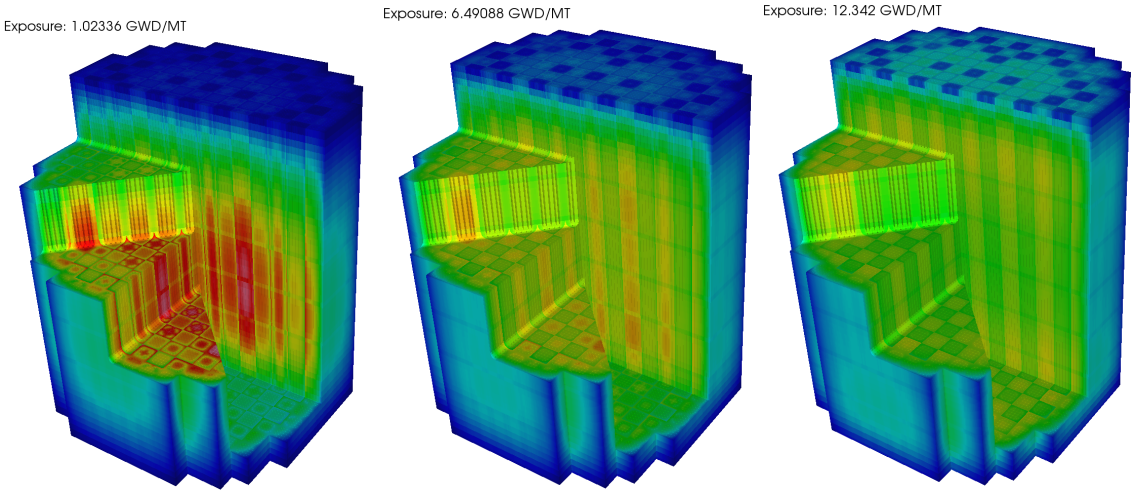

Figure D.10. Pin power distribution during Cycle 1 of BEAVRS [5].

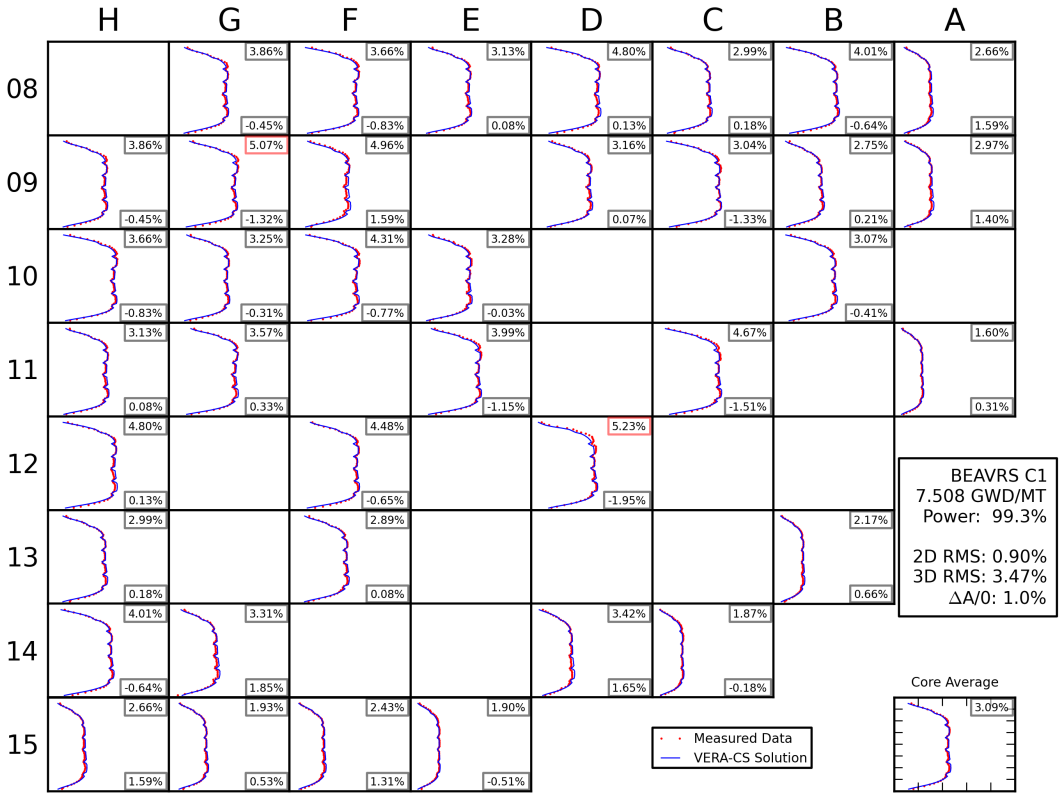

Figure D.11. Comparison of BEAVRS Cycle 1 flux maps to MPACT results.